DISSERTATION

submitted to the
Combined Faculties for the Natural Sciences and for Mathematics
of the Ruperto-Carola University of Heidelberg, Germany
for the degree of
Doctor of Natural Sciences

presented by
Dipl.-Phys. Malte Ellerbrock
born in Hamburg

Oral examination: 11. February 2004

Measurement of the Neutral Current Cross Section and Search for Contact Interactions with the H1 Experiment at HERA

Referees: Prof. Dr. Franz Eisele
Prof. Dr. Johanna Stachel

Kurzfassung

Eine Messung des inklusiven Wirkungsquerschnittes für den neutralen Strom der tief-inelastischen e^+p-Streuung und eine anschließende Suche nach Elektron-Quark Kontakt-Wechselwirkungen werden vorgestellt.
Die Analyse beruht auf Daten, die in den Jahren 1999 und 2000 bei einer Schwerpunktsenergie von $\sqrt{s} \approx 319$ GeV mit dem H1-Experiment bei HERA aufgezeichnet wurden. Umfangreiche systematische Verbesserungen werden bei der Rekonstruktion der Ereignisse mit neutralem Strom bei hohen Viererimpulsüberträgen Q^2 erreicht. Die präzise Messung des gestreuten Elektrons alleine mit dem Kalorimeter wird etabliert. Die einfach- und doppelt-differentiellen Wirkungsquerschnitte $d\sigma/dQ^2$ und $d^2\sigma/dx\,dQ^2$ werden im Bereich $200 \leq Q^2 \leq 30000$ GeV^2 und $0.0032 \leq$ Bjorken $x \leq 0.65$ gemessen. Die Ergebnisse sind in guter Übereinstimmung mit der QCD-Vorhersage des Standardmodells.
Die Kompatibilität des gemessenen Wirkungsquerschnittes mit dem Standardmodell und dessen Erweiterungen wird mit Hilfe einer neuartigen χ^2-Anpassung quantifiziert, die die Abhängigkeit von der Form der Proton-Partondichten stark reduziert. Es werden keine signifikanten Anzeichen für neue Physik gefunden. Die Analyse liefert eine obere Grenze auf den Quarkradius von $R_{\text{quark}} < 1.1 \times 10^{-18}$ m (CL=95%) und untere Ausschlussgrenzen auf Skalen von Elektron-Quark-'Compositeness' im Bereich von 1.5 bis 4.8 TeV. Die Ergebnisse sind vergleichbar mit denen anderer Analysen, die bei HERA, LEP oder am TeVatron durchgeführt wurden.

Abstract

A measurement of the inclusive neutral current cross section for deep inelastic e^+p scattering and a subsequent search for electron-quark contact interactions are presented.
The analysis is based on data taken in 1999 and 2000 at a centre-of-mass energy of $\sqrt{s} \approx 319$ GeV with the H1 experiment at HERA. Substantial systematic improvements are achieved for the reconstruction of neutral current events at large four-momentum transfer Q^2. The precise measurement of the scattered electron using solely calorimetric information is established. The single and double differential cross sections $d\sigma/dQ^2$ and $d^2\sigma/dx\,dQ^2$ are measured in the range of $200 \leq Q^2 \leq 30000$ GeV^2 and $0.0032 \leq$ Bjorken $x \leq 0.65$. The results are in good agreement with the Standard Model QCD prediction.
The compatibility of the cross section measurement with the Standard Model and extensions beyond is quantified using a novel χ^2 fit, which strongly reduces the dependence on the shape of the proton parton densities. No significant indications of new physics are found. The analysis yields an upper bound on the quark radius of $R_{\text{quark}} < 1.1 \times 10^{-18}$ m (CL=95%) and lower limits on electron-quark compositeness scales ranging from 1.5 to 4.8 TeV. The results are comparable to those of other analyses performed at HERA, LEP or TeVatron.

For my parents
and my sister

Contents

Chapter 1

Introduction

Within the last decades, the Standard Model of elementary particle interactions has become the accepted theory to describe experimental observables in high energy physics. In the framework of the Standard Model, matter consists of quarks and leptons as fundamental particles, each of them appearing in three families. Interactions between the particles are based on the strong and electroweak forces and are mediated by the exchange of gauge bosons.

The Standard Model has been tested in many aspects and to some extent with impressing accuracy. Up to now, it has successfully accomplished all extensions to new energy regimes which have been opened for experimental research by upgraded or new accelerators. Nevertheless, the Standard Model cannot be the final theory of fundamental interactions, since it leaves too many experimental facts unexplained and since it has some basic fundamental problems which have to show up at high energies. To name a few of them:

- The Standard Model contains many free parameters which are not predicted by theory but must be measured by experiments. Why can't the Standard Model predict e.g. a particle's mass?
- Fermions appear in three families of identical structure. Why are there exactly three generations of quarks and leptons?
- The open hierarchy problem: Why does electroweak unification happen already at the 100 GeV scale far below the so-called Planck scale where the unification of all interactions is expected?
- How does gravity fit into all of this?

All experiments are therefore also looking for deviations from the Standard Model predictions, and today there is at least one experimental fact which requires an extension of the Standard Model, namely the finite mass of neutrinos as discovered by oscillation experiments. Other deviations have been observed, e.g.:

- The measurement of the magnetic moment of the muon disagrees about 2.5σ from the Standard Model prediction.
- The determinations of the electroweak mixing angle from the observation of leptonic and hadronic Z^0 decays differ almost 3σ.

These are still compatible with statistical fluctuations and therefore not convincing enough to declare the break down of the Standard Model.

Thus, there are both experimental and theoretical reasons which motivate the search for new physics. Since the Standard Model is a rather successful theory, primarily extensions of the Standard Model are considered.

The consequences arising from new physics are expected to be observable in the extreme kinematic regions, at highest energies and momentum transfers. The experiments at the ep storage ring HERA are well suited to test some of these models since they explore the highest centre-of-mass energy available for deep inelastic scattering with a lepton and a quark in the initial state. It was in fact one of the intentions and design goals of the H1 experiment to look for physics beyond the Standard Model.

Direct signals like new particles pointing to the existence of new physics have not been observed at HERA so far. On the other hand, the search for indirect effects arising from new physics extends to kinematic regions which are currently not directly accessible. At HERA, the best way to look for deviations from the Standard Model apart from searches for new particles is the precise measurement of the inclusive neutral current cross section at high x and Q^2. Theoretically, this cross section is well described in the Standard Model. Experimentally, it offers clean signatures and precise kinematics mainly on the basis of the scattered electron.

The subject of this thesis is the measurement of the inclusive neutral current ep cross section at large momentum transfers with data from the H1 experiment and the subsequent investigation for electron-quark contact interactions associated with scales far beyond the HERA centre-of-mass energy. The main emphasis is put on the precise determination of the neutral current cross section including the comprehensive treatment of the systematic uncertainties. The results are used in a novel fit to derive an upper bound on the radius of light quarks and lower limits on electron-quark compositeness scales.

The thesis is organised as follows:

- Chapter 2 presents a theoretical overview of deep inelastic ep scattering and the measurement of the inclusive neutral current cross section within the Standard Model.

- Chapter 3 describes the concept of electron-quark contact interactions and their relation to Standard Model neutral current ep scattering.

- The HERA collider and the H1 experiment are introduced in chapter 4.

- Chapter 5 represents the main part of the data analysis and explains the event identification and reconstruction. Importance is attached to the energy and position measurement of the scattered electron exploiting the full capabilities of the H1 Liquid Argon calorimeter.

- Chapter 6 presents the event selection and summarises the data sample used for the cross section measurement.

- Chapter 7 contains the cross section determination. It describes the relevant systematic uncertainties and their implications on the cross section measurement. The cross section result is presented and compared to the H1 publication.
- The interpretation of the cross section result is performed in chapter 8. In a statistical analysis based on a χ^2 fit, the compatibility of the cross section measurement with the Standard Model prediction is tested. In addition, limits are derived on the quark radius and scales of various compositeness models.
- In chapter 9 this thesis concludes with a summary of the cross section and contact interaction results and gives an outlook.

Chapter 2

Standard Model Deep Inelastic ep Scattering

The Standard Model framework provides a precise description of deep inelastic scattering processes with high momentum transfers.

This chapter deals with the phenomenology of deep inelastic electron[1]-proton (ep) scattering at HERA. The fundamental scattering process is introduced together with the relevant kinematic quantities as well as important methods used for the kinematic reconstruction. The Standard Model cross section and its decomposition into proton structure functions and coupling terms is reviewed.

For a more comprehensive description of Standard Model deep inelastic scattering is referred to e.g. [1, 2] and [3, 4].

2.1 Kinematics of Neutral Current Events

The HERA machine at the DESY laboratory in Hamburg provides collisions of electrons with an energy of 27.5 GeV with protons with an energy of 920 GeV. The fundamental process is the interaction of an electron with a quark or anti-quark inside the proton. This process is depicted in leading order by the Quark-Parton Model (QPM) which assumes that the proton[2] consists of point-like partons which don't interact with each other and which share the total proton momentum. The QPM was originally introduced by Feynman to interpret the scaling behaviour of the structure functions.

In interactions with high momentum transfers between the electron and the proton, the partons behave as free particles and the electron scatters incoherently off single partons. Therefore, deep inelastic ep scattering is also known as elastic eq scattering.

The interaction is schematically displayed in figure 2.1. The electron e with four momentum k enters the scattering process from the left, the proton p with four momentum P from the right hand side. The electron scatters off a parton inside the proton, and a lepton leaves with four momentum k'. The incident parton carries the fractional four momentum x of the proton. The interaction between the electron and

[1] If not explicitly stated, the lepton is always denoted as electron independent of its charge.

[2] The Quark-Parton Model does in general apply for nucleons.

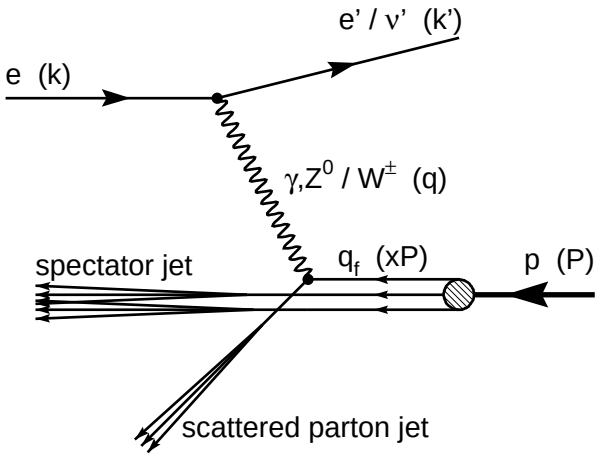

Figure 2.1: Illustration of leading order deep inelastic ep scattering. The four momentum vectors are given in parentheses.

the parton is mediated by the exchange of a virtual gauge boson which transfers the four momentum $q = k - k'$. The scattered parton hadronises and produces a jet. The same happens to the remaining partons of the proton which proceed along the proton direction and form the so-called remnant or "spectator" jet.

Depending on the charge of the boson the process is named neutral current (NC) or charged current (CC) interaction. This analysis deals with inclusive neutral current deep inelastic ep scattering, i.e. a photon (γ) or Z^0 boson is exchanged and the electron remains unchanged:

$$e(k) + p(P) \quad \longrightarrow \quad e'(k') + X \ . \tag{2.1}$$

The particle's four momenta are given in parentheses. X denotes the hadronic final state which represents the sum of all final state particles apart from the scattered electron.

A convenient and commonly used set of lorentz invariant kinematic variables to describe the process of equation 2.1 is defined by:

$$Q^2 \ = \ -q^2 = -\left(k - k'\right)^2 \ , \tag{2.2}$$

$$x \ = \ \frac{Q^2}{2\left(P \cdot q\right)} \ , \tag{2.3}$$

$$y \ = \ \frac{P \cdot q}{P \cdot k} \ . \tag{2.4}$$

The virtuality Q^2 is the negative of the four momentum squared which is transferred by the virtual boson. Q^2 specifies the transverse resolving power of the probe with wavelength $\lambda = 1/Q$ [3]. The Bjorken scaling variables x and y are non-dimensional and take on values between zero and one. In the infinite momentum frame, where the proton moves with infinite momentum and the proton mass can be neglected, x can be interpreted as the momentum fraction of the proton which is carried by the struck

[3] If not explicitly given, $\hbar = c = 1$ is used throughout.

parton. In the proton rest frame, the inelasticity y corresponds to the relative energy fraction transferred from the electron to the proton.

Deep inelastic scattering (DIS) denotes interactions which have $Q^2 \gg M_p^2$ (deep) and $W^2 \gg M_p^2$ (inelastic) where M_p is the proton mass and W is the centre-of-mass energy of the $\gamma^* p$ system.

The centre-of-mass energy $\sqrt{s}$ of the total ep scattering process is given by $s = (P + k)^2 \approx 4E_e E_p$, where E_e and E_p are the beam energies of the electron and the proton, respectively. At HERA, $\sqrt{s} = 319$ GeV defines the largest mass of a particle that can be produced on-shell.

Neglecting the lepton and proton masses yields the important relation

$$Q^2 = s \cdot x \cdot y \ . \tag{2.5}$$

Thus, at a fixed centre-of-mass energy $\sqrt{s}$, the kinematics of the scattering process is completely described by two independent variables.

Kinematic Plane

Figure 2.2 shows the kinematic plane in Q^2 and x, defining the kinematic phase space accessible at HERA. The kinematic limit is given by the diagonal line for $y = 1$, restricting the measurements to the lower right half plane. A change in centre-of-mass energy corresponds to a parallel translation of this limit, and lines of constant y run parallel to the diagonal (cf. equation 2.5).

Since the HERA centre-of-mass energy of $\sqrt{s} = 319$ GeV is large compared to fixed target experiments, HERA provides extensive access to both the extremely low x and the very high Q^2 kinematic regions. The HERA DIS data of H1 and ZEUS cover the approximate ranges of $1 < Q^2 < 5{\times}10^4$ GeV^2 and $10^{-5} < x < 0.65$. The measurements of the fixed target experiments expand the coverage of the kinematic plane to the lower right corner. They provide valuable data with high statistics at highest x where the HERA experiments suffer from limited statistics.

This analysis covers the kinematic range of high $Q^2 \gtrsim 200$ GeV^2 and $y > 0.05$, corresponding to the upper right corner in figure 2.2. Approaching the kinematic limit of HERA allows sensitive searches for substructure of the quarks and for production of new particles with masses up to $\sqrt{s} = 319$ GeV.

2.2 Neutral Current Cross Section

This section presents the cross section definition as applied in this analysis. For the subsequent apposition of additional contact interaction terms (cf. section 3.2), the cross section is fractionised down to the level of parton densities of the proton and electroweak couplings.

The data used in this analysis were taken with longitudinally unpolarised electrons scattering off unpolarised protons. However, these days the HERA collider starts to provide a longitudinally polarised lepton beam for ep interactions. Polarisation is a powerful option to search for physics beyond the Standard Model and, as the case may

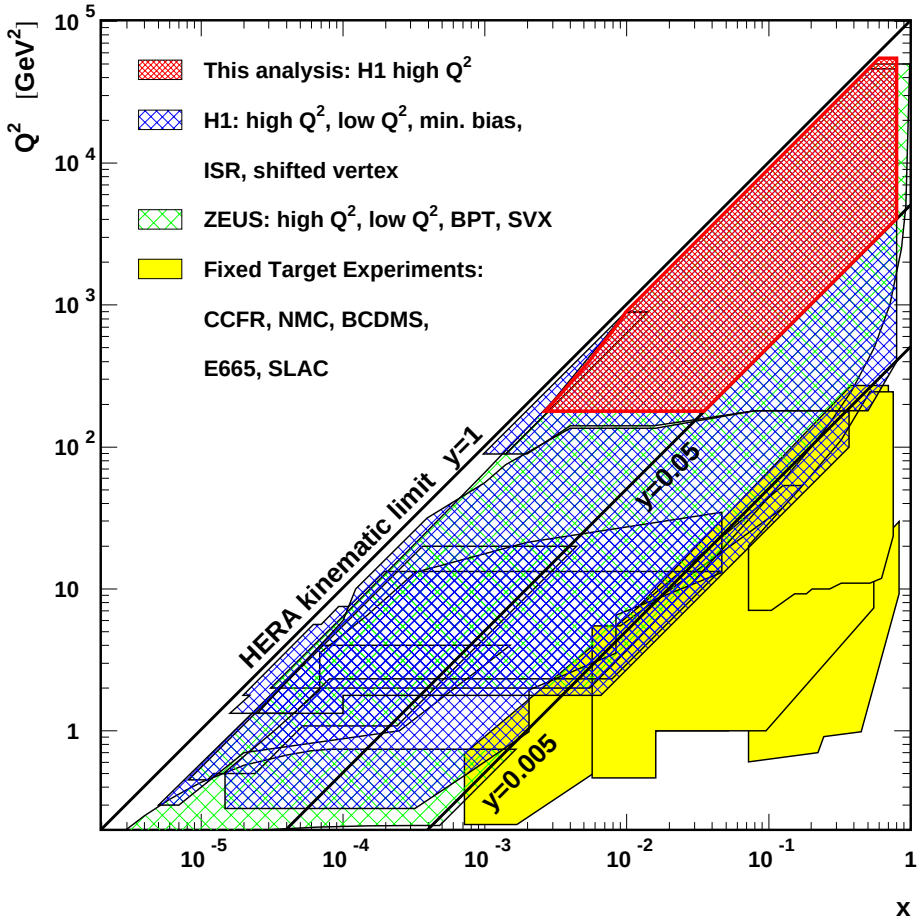

Figure 2.2: The kinematic plane of Q^2 and x accessible at HERA, showing the coverage of this analysis (red, fine grid), of the HERA experiments H1 and ZEUS, and of some fixed target experiments. See text for further explanations.

be, to verify and/or identify the source of new processes. Since also needed later on for the implementation of general contact interaction terms, the cross section for ep scattering with a lepton beam of arbitrary longitudinal polarisation is described in this section.

The cross section of neutral current deep inelastic scattering depends on two independent variables which characterise the scattering process and is usually given as function of Q^2 and x. In general, a measured cross section contains the information on the fundamental scattering process plus additional radiative corrections (δ^{rad}):

$$\frac{d^2\sigma}{dx\,dQ^2} = \left(\frac{d^2\sigma}{dx\,dQ^2}\right)_{\text{Born}} \cdot \left(1+\delta^{\text{rad}}\right) \quad . \tag{2.6}$$

The so-called Born cross section only includes the lowest order $\mathcal{O}(\alpha^2)$ contribution of the electroweak interaction and is discussed in detail below. Terms of higher orders in the coupling constant α represent radiative corrections to the Born cross section. They don't carry additional information on the electron-quark interaction and will be addressed in section 2.3.

2.2.1 Born Cross Section and Structure Functions

The Born cross section represents the fundamental measure for fermion-fermion interactions.

The neutral current scattering process is illustrated in figure 2.1 in lowest order QCD, $\mathcal{O}(\alpha_s^0)$, where a photon (γ) or Z^0 boson is exchanged between the electron and a parton inside the proton. Higher order QCD contributions will be discussed in section 2.2.3.

The Standard Model Born cross section for deep inelastic neutral current ep scattering with an arbitrarily polarised lepton beam is typically written as

$$\frac{d^2\sigma}{dx\,dQ^2}\left(e^{\pm}p\to eX\right) = \frac{2\pi\alpha^2}{x\,Q^4}\left[Y_+\,\widetilde{F}_2\big(x,Q^2\big) \mp Y_-\,x\widetilde{F}_3\big(x,Q^2\big) - y^2\,\widetilde{F}_L\big(x,Q^2\big)\right] \quad , \quad (2.7)$$

where $\alpha = e^2/4\pi$ is the electromagnetic coupling constant to be taken at $Q^2 = 0$ GeV^2. The essential Q^{-4} dependence of the cross section accommodates for the Rutherford-type scattering behaviour being characteristic for elastic scattering of point-like charged particles. The term in square brackets accounts for the details of the ep interaction: The three nonnegative generalised structure functions $\widetilde{F}_2(x,Q^2)$, $x\widetilde{F}_3(x,Q^2)$ and $\widetilde{F}_L(x,Q^2)$ contain the parton information of the proton and the couplings between the fermions and the exchanged boson. The $\mp$ sign of the $x\widetilde{F}_3$ term governs the opposite contribution to the cross section for e^+p and e^-p scattering. The kinematic coefficients $Y_\pm = 1 \pm (1-y)^2$ take care of the helicity dependences of the electroweak interactions.

The $e^\pm$ beam polarisation λ ($\lambda \in [-1,1]$), where $\lambda = 0$ for unpolarised leptons and $\lambda = -1(+1)$ for left-handed (right-handed) incoming leptons, enters implicitly via the structure functions. It should be pointed out already here that $\widetilde{F}_2$ and $x\widetilde{F}_3$ remain constant only for an unpolarised lepton beam but change in magnitude for finite lepton beam polarisation when switching between e^+ and e^- lepton beams.

The longitudinal structure function $\widetilde{F}_L$ describes the absorption of a longitudinally polarised vector boson and vanishes for point-like spin one-half particles in the limit of negligible quark masses and intrinsic transverse momenta in the proton. However, QCD effects as gluon radiation lead to a small contribution of $\widetilde{F}_L$ in the kinematic region of small x and highest y. Since this analysis is restricted to $y < 0.9$ and covers very high momentum transfers which require considerably large values of x, $\widetilde{F}_L$ yields a minor contribution to the cross section and is neglected in the following discussion of the structure functions. However, $\widetilde{F}_L$ may in principal be decomposed in a similar way as will be shown for $\widetilde{F}_2$. Certainly, the $\widetilde{F}_L$ contribution is taken into account in the cross section calculations performed in this analysis.

The structure functions are decomposed according to the fact that the cross section contains the absolute square of the sum of the amplitudes of the contributing electroweak matrix elements,

$$\frac{d^2\sigma}{dx\,dQ^2} \propto \left| \right|^2 \quad . \quad (2.8)$$

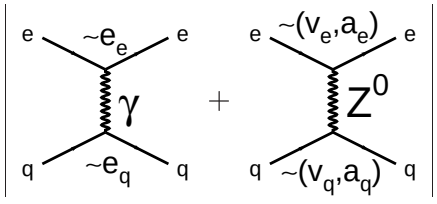

The exchanged γ (Z^0) couples with the charges e_e and e_q (vector/axial vector couplings v_e/a_e and v_q/a_q) to the electron and quark, respectively, where the fermion's couplings to the Z^0 are defined as

$$\begin{aligned} v_f &= T_{3,f} - 2e_f \sin^2(\theta_W) \ , \\ a_f &= T_{3,f} \ . \end{aligned} \tag{2.9}$$

$T_{3,f}$ is the third component of the weak isospin of the fermion and θ_W is the Weinberg angle, relating the $W^\pm$ mass to the Z^0 mass via $\sin^2(\theta_W) = 1 - M_W^2/M_Z^2$ (on-shell scheme).

Following the prescription of 2.8, the generalised structure functions can be separated into the contributions arising from the pure γ and the pure Z^0 exchange as well as from the γZ^0 interference:

$$\begin{aligned} \widetilde{F}_2 &= F_2^\gamma - (v_e \pm \lambda a_e)\, \kappa_Z \; F_2^{\gamma Z} + (v_e^2 + a_e^2 \pm \lambda\, 2 v_e a_e)\, \kappa_Z^2 \; F_2^Z \ , \\ x\widetilde{F}_3 &= - (a_e \pm \lambda v_e)\, \kappa_Z \; xF_3^{\gamma Z} + (2 v_e a_e \pm \lambda(v_e^2 + a_e^2))\, \kappa_Z^2 \; xF_3^Z \ . \end{aligned} \tag{2.10}$$

The explicit indication of the x and Q^2 dependences are omitted for simplicity. The $\pm$ and $\mp$ signs refer to the charge of the $e^\pm$ beam, while the polarisation enters through λ. In this notation, the couplings v_e and a_e of the lepton to the Z^0 are always those of the electron particle for both e^+p and e^-p scattering.

The factor κ_Z denotes the ratio of the couplings and propagators of the Z^0 to those of the photon,

$$\kappa_Z = \kappa_Z\big(Q^2\big) = \frac{1}{4 \sin^2(\theta_W) \cos^2(\theta_W)} \frac{Q^2}{Q^2 + M_Z^2} \approx 1.41 \frac{Q^2}{Q^2 + M_Z^2} \ . \tag{2.11}$$

Therefore, the relative magnitudes of the cross sections corresponding to (γ,γZ^0,Z^0) exchange behave like (1,κ_Z,κ_Z^2), depending on Q^2 as displayed in figure 2.3.

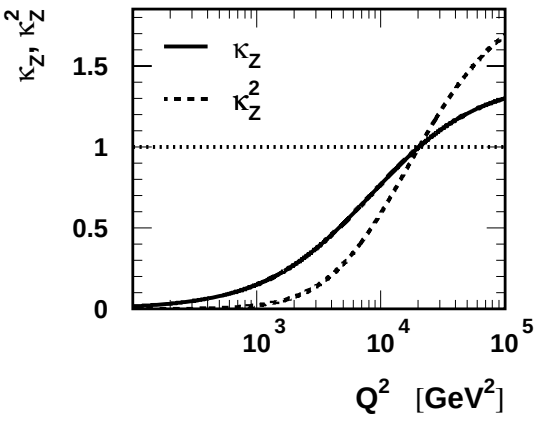

Figure 2.3: Q^2 dependence of κ_Z, the ratio of the couplings and propagators of the Z^0 to those of the photon, and of κ_Z^2.

The structure functions F_2^γ, $F_2^{\gamma Z}$, F_2^Z, $xF_3^{\gamma Z}$ and xF_3^Z of equation 2.10 characterise solely the proton as seen by a neutral current, independent of what the counterpart of the interaction (here the electron) is. The electromagnetic structure function F_2^γ originates from pure photon exchange and is the dominant contribution to the cross section in the bulk of the kinematic phase space accessible at HERA. The structure

functions $F_2^{\gamma Z}$ (F_2^Z) and $xF_3^{\gamma Z}$ (xF_3^Z) represent the γZ^0 interference (pure Z^0) terms of $\widetilde{F}_2$ and $x\widetilde{F}_3$, respectively. The γZ^0 interference contribution is noticeable already at intermediate Q^2 values of a few 1000 GeV^2. However, both γZ^0 and Z^0 exchange yield important contributions to the cross section only at very large Q^2 typically beyond $M_Z^2 \approx 8000$ GeV^2. The different structure function contributions to the cross section are presented in figure 2.4 as function of x for large $Q^2 \geq 2000$ GeV^2 by comparing them to the cross section of pure photon exchange. The x dependence reflects both

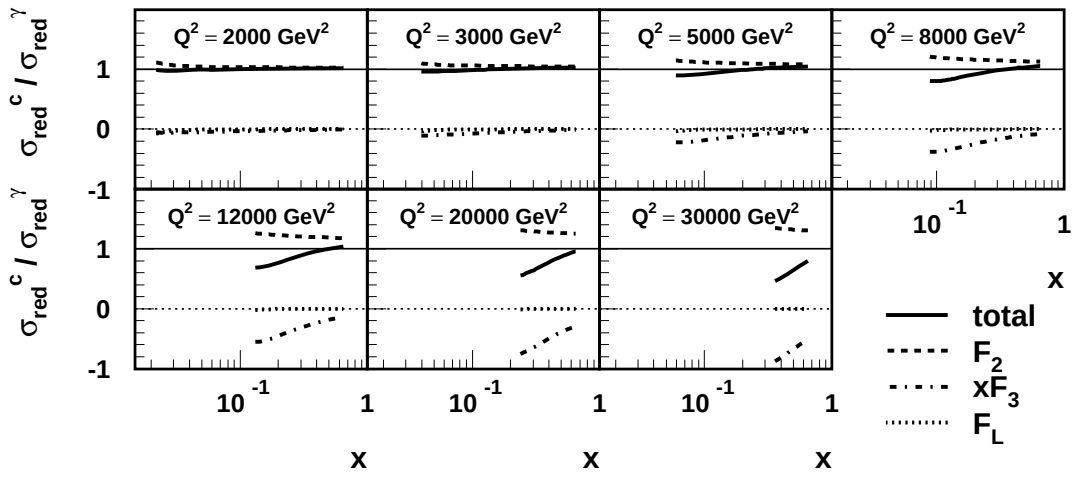

Figure 2.4: Cross section contributions σ_{red}^c of the structure functions $\widetilde{F}_2$ (dashed), $x\widetilde{F}_3$ (dash-dotted) and $\widetilde{F}_L$ (dotted) as well as the total NC cross section (solid line), normalised to the cross section of pure photon exchange σ_{red}^γ. The cross sections have been derived from the H1 1997 PDF Fit (cf. section 2.5).

the magnitude of the structure functions themselves and the different weights of the y dependent coefficients of the structure functions which govern the composition of the cross section (cf. equation 2.7).

Since there are no assumptions on the proton structure, the definition of equation 2.10 provides the most general form of the proton structure functions for the electroweak boson exchanges.

The single differential cross section

The single differential cross section as function of Q^2 is obtained by integration of equation 2.7 over the allowed kinematic phase space:

$$\left.\frac{d\sigma}{dQ^2}\right|_{Q_0^2} = \int_x \left.\frac{d^2\sigma}{dx\,dQ^2}\right|_{Q_0^2} dx \ . \tag{2.12}$$

The reduced cross section

For the representation and discussion of the data, a modification of the double differential cross section, the so-called reduced cross section, is defined by

$$\begin{aligned} \widetilde{\sigma} &= \left(\frac{d^2\sigma}{dx\,dQ^2}\right)_{\text{red.}} = \frac{x\,Q^4}{2\pi\alpha^2}\frac{1}{Y_+}\frac{d^2\sigma}{dx\,dQ^2} \\ &= \widetilde{F}_2\big(x,Q^2\big) \mp \frac{Y_-}{Y_+}\cdot x\widetilde{F}_3\big(x,Q^2\big) - \frac{y^2}{Y_+}\cdot \widetilde{F}_L\big(x,Q^2\big) \ . \end{aligned} \tag{2.13}$$

The propagator term as well as the couplings are divided out to obtain essentially the effects of the parton distribution functions. In most of the kinematic range the relation $\widetilde{\sigma} \approx \widetilde{F}_2$ holds to a good approximation.

2.2.2 Structure Functions in the Quark-Parton Model

The QCD Quark-Parton Model provides a connection between structure functions and parton densities. In this picture, the structure functions of equation 2.10 are related to the couplings of the neutral current to the quarks as well as to the quark and anti-quark momentum densities of the proton:

$$\begin{aligned} \Big[F_2^{\gamma}, F_2^{\gamma Z}, F_2^{Z}\Big] &= x\sum_f \left[e_f^2, 2e_f v_f, v_f^2 + a_f^2\right] \ \big(q_f + \overline{q}_f\big) \ , \\ \Big[xF_3^{\gamma Z}, xF_3^{Z}\Big] &= \qquad x\sum_f \left[2e_f a_f, 2v_f a_f\right] \ \big(q_f - \overline{q}_f\big) \ . \end{aligned} \tag{2.14}$$

The sums run over all quark flavours f. The function $q_f(x,Q^2)$ is the probability density to find a quark of flavour f in the proton with fractional momentum x and at a scale Q^2. The F_2 part of the cross section depends on the total quark content of the proton while the xF_3 part is sensitive to the valence quark distributions. The parton densities of the proton cannot be derived from first principles but have to be determined by experiment. However, they are universal and don't depend on the specific process. Further information about parton density functions are presented in section 2.5.

For the investigation of additional interactions beyond the Standard Model, e.g. of various contact interaction scenarios, it is convenient to separate the generalised structure functions into the quark densities $q_f(x,Q^2)$ and the overall coupling terms. Considering leptons of pure left- or right-handed chirality, the combination of equations 2.10 and 2.14 yields:

$$\begin{aligned} \widetilde{F}_2^{L,R}(x,Q^2) &= \quad x\sum_f \left[q_f(x,Q^2) + \overline{q}_f(x,Q^2)\right] \ \left\{\left|V_q^{L,R}(Q^2)\right|^2 + \left|A_q^{L,R}(Q^2)\right|^2\right\} \ , \\ x\widetilde{F}_3^{L,R}(x,Q^2) &= \mp x\sum_f \left[q_f(x,Q^2) - \overline{q}_f(x,Q^2)\right] \ \left\{-\lambda'\,2\,V_q^{L,R}(Q^2)\,A_q^{L,R}(Q^2)\right\} \ , \end{aligned} \tag{2.15}$$

with the electroweak coupling terms

$$\begin{aligned} V_q^{L,R}(Q^2) &= e_q \ - \ (v_e \pm \lambda' a_e)\,v_q\,\kappa_Z(Q^2) \ , \\ A_q^{L,R}(Q^2) &= \quad - \ (v_e \pm \lambda' a_e)\,a_q\,\kappa_Z(Q^2) \ . \end{aligned} \tag{2.16}$$

Again, the $\pm$ signs refer to the $e^{\pm}$ beam, while the pure polarisation enters with $\lambda' = \mp 1$ for the L, R states. Note that the $\mp$ sign of $x\widetilde{F}_3$ in equation 2.15 cancels the $\mp$ sign of the cross section contribution (cf. equation 2.7).

The generalised structure functions for arbitrary lepton beam polarisation λ can be obtained by a linear combination of the structure functions given in equation 2.15.

In this notation, V_q and A_q represent the vector and axial-vector couplings of the neutral current to the parton inside the proton. It is deduced from equation 2.15 that $\widetilde{F}_2$ respects parity operations while $x\widetilde{F}_3$ contains the parity violating part of the interaction.

2.2.3 Higher Order QCD Corrections

So far, the neutral current cross section has been discussed for leading order QCD. This picture assumes that quarks are the only constituents of the proton. However, experimental results indicated that quarks carry only about half of the hadron momentum and that there must be additional constituents [5] which in QCD are identified with the gluons.

QCD is an essential ingredient of the Standard Model. It is well tested in hard processes where the transferred momentum is large compared to any other scale involved. In this kinematic regime, perturbative QCD is based on the factorisation of the inclusive cross section into partonic subprocesses and parton distribution functions $q(x, Q^2)$ [6]. The Q^2 dependence of the parton distribution functions at fixed values of x is governed by the DGLAP[4] evolution equations [7, 8, 9], whereas the x dependence is not predicted by theory.

In analogy to the renormalisation of the coupling constant α_s, $q_0(x)$ can be regarded as unmeasurable, raw distribution. The collinear singularities are absorbed into these raw distributions at a factorisation scale μ. The corresponding renormalised distribution $q(x, \mu^2)$ cannot be determined perturbatively since it contains long range contributions of the strong interaction. Therefore, $q(x, \mu^2)$ has to be extracted from experimental structure function data (cf. section 2.5).

A fundamental property of QCD is the possibility to separate between short and long range contributions to physical cross sections at high momentum transfers. This factorisation is valid in all orders perturbation theory and provides a unique method to deal with logarithmic singularities. In addition, there are finite (non logarithmic) contributions. The set of these finite contributions, being factorised and absorbed into the quark density functions, defines the renormalisation scheme.

In the DIS[5] scheme [10], all gluon contributions are absorbed into the renormalised quark distributions. Thus, the structure function $F_2(x, Q^2)$ is defined as in equation 2.14 to all orders in α_s, only the parton densities may change. The structure functions $xF_3(x, Q^2)$ and $F_L(x, Q^2)$ get corrections for all contributions of higher orders.

In the $\overline{MS}$[6] scheme [11], which is more commonly used in practice, only the divergent contribution and an omnipresent $(\ln(4\pi) - \gamma_E)$ term are factorised out. Here, all

[4] Dokshitzer-Gribov-Lipatov-Altarelli-Parisi
[5] Deep Inelastic Scattering
[6] Modified Minimal Subtraction

three structure functions receive corrections in higher orders.

The cross section calculations in this analysis are performed in NLO QCD to $\mathcal{O}(\alpha_s)$. The corresponding structure functions are derived from the respective parameterisations of the proton parton density distributions (cf. section 2.5) as given in the HECTOR [12] program package.

2.3 QED Radiative Corrections

In the previous discussion of kinematics and cross sections only leading order $\mathcal{O}(\alpha^2)$ terms of the electroweak interaction have been considered. However, the real data contain contributions of higher orders in α, arising from the exchange or emission of additional bosons and from the self energies of the particles involved.

The cross section measurements have to be corrected for these effects since the higher order contributions depend on the interaction process and partly even on the detector acceptance and on experimental cuts of the analysis procedure.

In case of NC scattering, the radiative corrections are classified according to the contributing Feynman diagrams [13]:

- **Leptonic corrections** yield the dominant contributions and account for an additional photon attached to the lepton line. One differentiates between:
  - Initial state radiation (ISR): The incoming electron radiates a real photon which most likely escapes detection through the beam pipe. The consequence is a change in the electron-proton centre-of-mass energy and therefore different kinematics compared with the original process.
  - Final state radiation (FSR): The outgoing electron radiates a real photon. Most probably the photons are emitted under small angles leading to the detection of the electron and the photon as a single particle. These events are thus mostly indistinguishable from events without radiation. Since wide angle radiation is suppressed, FSR yields small corrections compared to ISR.
  - Vertex correction and self energies: The former considers photons which are radiated off the incoming electron and absorbed again by the outgoing electron, while the latter accounts for the radiation and reabsorption on the external lepton line. These processes cannot be observed experimentally.

- **Quarkonic corrections** consider additional photons attached to the quark line analogous to the leptonic contributions. However, due to the large quark masses and the fractional charge of the quarks, they are strongly suppressed compared to the electron side.

- **Lepton-quark interference corrections** account for the interference of the leptonic and quarkonic bremsstrahlung processes and for $\gamma\gamma$ and γZ box diagram contributions. Since they depend on the quark masses and the quark charge again, these corrections are also small compared to the leptonic corrections.

- **Purely weak corrections** represent all other diagrams that don't contain additional photons. These include the self energy of the photon which yields the most important correction to the NC cross section. It is connected with the so-called running of the electromagnetic coupling constant $\alpha = \alpha(Q^2)$ which decreases by approximately 6% at $Q^2 = M_Z^2$ compared to $\alpha(0) \approx 1/137$. In addition, the weak corrections contain the Z self energy, the γZ mixing, the weak lepton and quark vertex corrections and box diagrams with two W or Z bosons.

The radiative corrections can be separated into electromagnetic and purely weak contributions,

$$1 + \delta^{\text{rad}} = \left(1 + \delta^{\text{QED}}\right) \cdot \left(1 + \delta^{\text{weak}}\right) \ . \tag{2.17}$$

The former are commonly called QED corrections (δ^{QED}) and contain the leptonic and quarkonic corrections, their interference as well as the self energy of the photon. The weak corrections (δ^{weak}) correspond to processes with the Z or W boson.

The QED radiative corrections are precisely predicted by theory and provide a sizeable contribution to the measured cross section. Figure 2.5 shows the QED radiative corrections to the neutral current cross section as obtained in the Leading Log Approximation from the HELIOS [14] program which is implemented in the HECTOR [12] package. The corrections are presented in bins of the double differential cross section as measured in this analysis and include the $y > 0.05$ requirement. The two most commonly used reconstruction methods, e and $e\Sigma$ (cf. section 2.4), are compared with and without the $(E - p_z) > 35$ GeV requirement applied in the current analysis. The corrections rise towards low x, corresponding to large values of y. The effects are large, of the order 10%, due to the steep Q^2 dependence of the NC cross section which leads to large kinematic migrations. The impact of the $(E - p_z)$ cut, which rejects NC events with an ISR photon of energy $E_\gamma > 10$ GeV, is observed by the kink in the curves of the e method.

The cross section measurement is corrected for radiative effects implicitly by using Monte Carlo simulations which include radiation effects (cf. section 4.4). The HERACLES [15] event generator includes the QED radiation processes explained above.

Weak radiative corrections

The weak corrections δ^{weak} to the neutral current cross section are typically less than 1% and never more than 3% [16]. They are not corrected for in the cross section measurement which is therefore given by (cf. equation 2.6):

$$\frac{d^2\sigma}{dx\,dQ^2} = \left(\frac{d^2\sigma}{dx\,dQ^2}\right)_{\text{Born}} \cdot \left(1 + \delta^{\text{weak}}\right) \ . \tag{2.18}$$

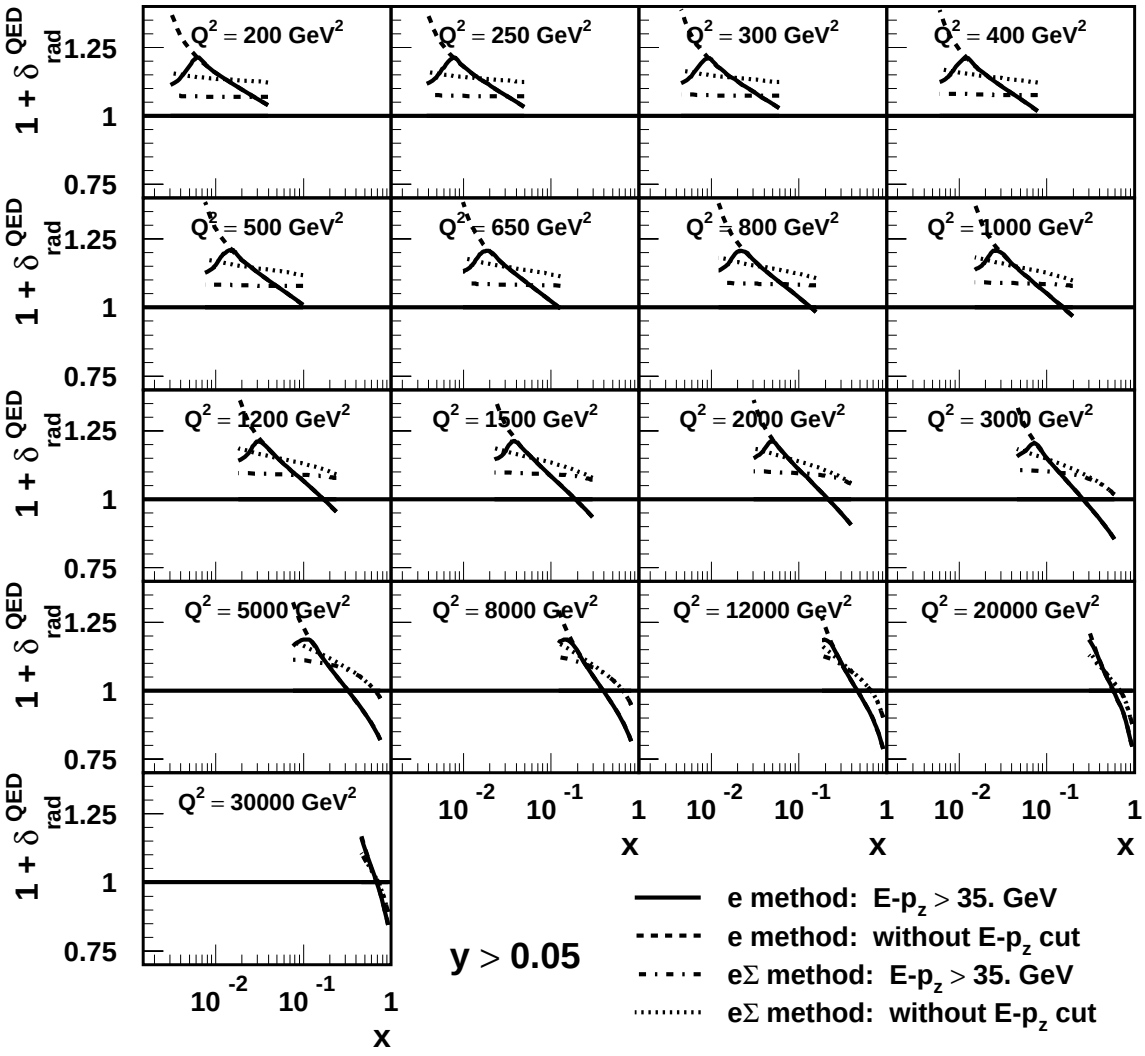

Figure 2.5: QED radiative corrections to the double differential NC cross section $d^2\sigma/dx\,dQ^2$ in the kinematic phase space of the present analysis. The corrections are shown for the e and $e\Sigma$ reconstruction methods each with and without the $(E - p_z) > 35$ GeV requirement.

2.4 Reconstruction of Event Kinematics

The measurement of the differential cross sections (cf. chapter 7) requires the precise reconstruction of the event kinematics.

In neutral current ep scattering at HERA, both the scattered electron and the hadronic recoil system can be measured. The scattered electron is usually described by its energy E'_e and scattering angle θ_e[7]. Since the hadronic jet from the spectator partons escapes detection through the beam pipe, the following variables are commonly

[7] At HERA, polar angles θ are measured with respect to the proton beam direction which defines the positive z axis and the so-called forward direction.

used to describe the hadronic final state:

$$(E - p_z)_{had} = \sum_h (E_h - p_{z,h}) \ , \tag{2.19}$$

$$p_{T,had} = \sqrt{\left(\sum_h p_{x,h}\right)^2 + \left(\sum_h p_{y,h}\right)^2} \ . \tag{2.20}$$

The sums run over all objects of the hadronic final state. $(E - p_z)$ is the so-called longitudinal energy momentum balance, p_T is the transverse momentum. By construction, the former is relatively insensitive to losses through the forward beam pipe. Both variables are combined to define the inclusive hadron angle γ_{had},

$$\tan \frac{\gamma_{had}}{2} = \frac{(E - p_z)_{had}}{p_{T,had}} \ . \tag{2.21}$$

In the QPM, γ_{had} corresponds to the quark scattering angle θ_q presumed the hadronic final state is massless.

Measuring with a perfect detector, energy and momentum conservation require the total $(E - p_z)_{tot}$ and $p_{T,tot}$[8] of the scattered electron and the hadronic final state to be equal to the values of the initial beam particles.

$$\begin{aligned} (E - p_z)_{tot} &= 2 \cdot E_e = 55 \text{ GeV} \ , \\ p_{T,tot} &= 0 \ . \end{aligned} \tag{2.22}$$

However, real experiments suffer from acceptance losses and resolution effects which lead to deviations.

At given energies of the incoming electron (E_e) and proton (E_p) and therefore at fixed centre-of-mass energy $\sqrt{s} = 2\sqrt{E_e \cdot E_p}$, the kinematics of the ep interaction is completely described by any two independent variables. Neutral current events provide four independent measurements, two of each of the electron and proton. The redundancy offers several methods of kinematic reconstruction. The choice of the reconstruction method defines the sources of systematic errors and the size of radiative corrections. Since only two of the kinematic variables Q^2, x and y are independent, usually Q^2 and y are reconstructed, being closely related to the measured observables, and x is determined from equation 2.5.

The electron method (e method) uses the electron variables to determine Q^2, x and y. Since in neutral current interactions at high Q^2, the scattered electron can be reconstructed much easier and more reliable compared to the hadronic final state, the e method is of absolute importance and provides the basis for all other reconstruction methods. Furthermore in use are the Σ and $e\Sigma$ methods, which have the advantage to consider to some extent the effects of initial state radiation, and the double angle method (2α method), which is rather insensitive to energy calibration issues. Pure hadronic reconstruction suffers from large measurement uncertainties and is not considered here.

[8] $p_{T,tot}$ is the absolute value of the vectorial sum of electron and hadronic final state p_T.

Initial state radiation from the incoming electron is the most severe effect spoiling the kinematic reconstruction. In principle, the properties of the radiated photon can be reconstructed from the overdetermined system of four measuring quantities in neutral current interactions, leading to an adaption of the centre-of-mass energy. However, all reconstruction methods discussed here always apply the full centre-of-mass energy, since the benefit from being completely independent of initial state radiation cannot compensate the loss in resolution associated with the reconstruction of the electron entering the hard interaction [17].

In the following, the reconstruction methods are discussed which are relevant for this analysis. Also presented are the uncertainties on the kinematic variables as determined from standard error propagation.

All kinematic formulae are given as function of the measured quantities E'_e and θ_e of the electron as well as $(E-p_z)_{had}$ of the hadronic final state. Since the transverse momentum p_T of the hadronic final state is more difficult to measure and suffers e.g. from beam pipe losses, it doesn't enter the methods considered. For simplicity, $(E-p_z)_e \equiv E'_e(1-\cos\theta_e)$ and $(E-p_z)_{tot} \equiv (E-p_z)_e+(E-p_z)_{had}$ and $\Sigma_{had} \equiv (E-p_z)_{had}$.

Electron (e) Method

The e method is the main method used in this analysis and reconstructs the kinematics solely from the energy E_e and the polar angle θ_e of the scattered electron:

$$y_e = 1 - \frac{(E-p_z)_e}{2E_e} , \tag{2.23}$$

$$Q^2_e = \frac{p^2_{T,e}}{1-y_e} = 4E_eE'_e\cos^2\frac{\theta_e}{2} , \tag{2.24}$$

$$x_e = \frac{Q^2_e}{s\cdot y_e} . \tag{2.25}$$

Their measurement errors are given as[9]:

$$\begin{aligned}
\frac{\delta y_e}{y_e} &= -\frac{1-y_e}{y_e}\frac{\delta E'_e}{E'_e} \oplus -\frac{1-y_e}{y_e\,\tan\theta_e/2}\,\delta\theta_e , \\
\frac{\delta Q^2_e}{Q^2_e} &= \frac{\delta E'_e}{E'_e} \oplus -\tan\frac{\theta_e}{2}\,\delta\theta_e , \\
\frac{\delta x_e}{x_e} &= \frac{1}{y_e}\frac{\delta E'_e}{E'_e} \oplus \left[-\tan\frac{\theta_e}{2} + \frac{1-y_e}{y_e}\cot\frac{\theta_e}{2}\right]\delta\theta_e .
\end{aligned} \tag{2.26}$$

This method provides an excellent resolution in Q^2 for the entire kinematic phase space accessible at HERA and good precision in x and y at moderate and high values of y. However, due to the $1/y$ behaviour of the errors this method suffers from imperfections in the reconstruction of y and especially of x at low y values. That is why $y_e > 0.05$ is required in this analysis (cf. chapter 6).

[9] $A \oplus B \equiv \sqrt{A^2+B^2}$; the sign of A and B indicates the direction of the bias.

Sigma (Σ) and eSigma ($e\Sigma$) Methods

The Σ method accounts to some extent for potential photons radiated from the initial electron escaping undetected through the beam pipe. In addition to the electron variables, the $(E-p_z)_{had}$ of the hadronic final state is used to reconstruct the total $(E-p_z)_{tot} = (E-p_z)_e + (E-p_z)_{had}$ which replaces the nominal value of $2E_e$ in the formula of the e method.

$$y_\Sigma = \frac{(E-p_z)_{had}}{(E-p_z)_{tot}} , \tag{2.27}$$

$$Q^2_\Sigma = \frac{p^2_{T,e}}{1-y_\Sigma} , \tag{2.28}$$

$$x_\Sigma = \frac{Q^2_\Sigma}{s \cdot y_\Sigma} . \tag{2.29}$$

The difference in $(E-p_z)$ can be allocated to an initial state photon with energy $E_\gamma = E_e - \frac{1}{2}\left[(E-p_z)_e + (E-p_z)_{had}\right]$, changing the centre-of-mass energy available for the hard ep interaction to $s' = 2\,(E_e - E_\gamma)\,E_p = \frac{(E-p_z)_{tot}}{2E_e} \cdot s$. However, as explained above, x is calculated using the full centre-of-mass energy, leaving some remaining sensitivity of the Σ method to initial state radiation. The measurement errors are:

$$\begin{aligned}
\frac{\delta y_\Sigma}{y_\Sigma} &= -(1-y_\Sigma)\frac{\delta E'_e}{E'_e} \oplus -\frac{1-y_\Sigma}{\tan\theta_e/2}\,\delta\theta_e \oplus (1-y_\Sigma)\frac{\delta\Sigma_{had}}{\Sigma_{had}} , \\
\frac{\delta Q^2_\Sigma}{Q^2_\Sigma} &= (2-y_\Sigma)\frac{\delta E'_e}{E'_e} \oplus \left[-\tan\frac{\theta_e}{2} + \frac{1-y_\Sigma}{\tan\theta_e/2}\right]\delta\theta_e \oplus y_\Sigma\,\frac{\delta\Sigma_{had}}{\Sigma_{had}} , \\
\frac{\delta x_\Sigma}{x_\Sigma} &= (3-2y_\Sigma)\frac{\delta E'_e}{E'_e} \oplus \left[-\tan\frac{\theta_e}{2} + \frac{2(1-y_\Sigma)}{\tan\theta_e/2}\right]\delta\theta_e \oplus (2y_\Sigma-1)\frac{\delta\Sigma_{had}}{\Sigma_{had}} .
\end{aligned} \tag{2.30}$$

Compared to the e method, the Σ method provides a better resolution in x and y at low and moderate values of y.

Since the e method provides the optimal resolution in Q^2 surpassing also the Σ method [18], the $e\Sigma$ method is introduced which reconstructs Q^2 from the e method and x from the Σ method.

$$y_{e\Sigma} = \frac{2E_e}{(E-p_z)_{tot}} \cdot y_\Sigma , \tag{2.31}$$

$$Q^2_{e\Sigma} = Q^2_e , \tag{2.32}$$

$$x_{e\Sigma} = \frac{Q^2_{e\Sigma}}{s \cdot y_{e\Sigma}} = x_\Sigma . \tag{2.33}$$

The errors in $Q^2_{e\Sigma}$ and $x_{e\Sigma}$ are given by the respective entries of equations 2.26 and 2.30. The error in $y_{e\Sigma}$ is

$$\frac{\delta y_{e\Sigma}}{y_{e\Sigma}} = -2(1-y_{e\Sigma})\frac{\delta E'_e}{E'_e} \oplus -\frac{2(1-y_{e\Sigma})}{\tan\theta_e/2}\,\delta\theta_e \oplus (1-2y_{e\Sigma})\frac{\delta\Sigma_{had}}{\Sigma_{had}} . \tag{2.34}$$

The $e\Sigma$ method provides good resolution and is the best overall solution to reconstruct the kinematics in a unified way in the entire kinematic range accessible at HERA including the very low y region.

However, in the kinematic range relevant for this analysis, i.e. at high Q^2 and at least moderate y, the Σ and $e\Sigma$ methods are completely dominated by the electron quantities. In addition, the electron method provides a clear and simple access to the systematic error treatment since it is independent of the properties of the hadronic final state. Therefore, the electron method is used for the primary reconstruction of the event kinematics. The $e\Sigma$ method will only be used for cross-checks to give confidence that the energy measurements and the radiative corrections are under control.

Double Angle (2α) Method

The double angle method uses the electron scattering angle θ_e and the inclusive hadron angle γ_{had} to reconstruct the kinematics.

$$y_{2\alpha} = \frac{\tan\gamma_{had}/2}{\tan\gamma_{had}/2 + \tan\theta_e/2} , \tag{2.35}$$

$$Q^2_{2\alpha} = 4E_e^2 \cdot \frac{\cot\theta_e/2}{\tan\gamma_{had}/2 + \tan\theta_e/2} , \tag{2.36}$$

$$x_{2\alpha} = \frac{Q^2_{2\alpha}}{s \cdot y_{2\alpha}} . \tag{2.37}$$

The angle measurement is to first order independent of the energy calibration of the detector, but local inhomogeneities in the energy reconstruction may lead to distortions.

In the picture of the Quark-Parton Model, the energies of the electron and quark are related to their angles by the total p_T and $(E - p_z)$ balance of neutral current events. The measurement of the angles θ_e and γ_{had} therefore allows to predict the transverse momentum and the energies of the electron and the quark.

$$\begin{aligned} p_{T,2\alpha} &= \frac{2 \cdot E_e}{\tan\frac{\theta_e}{2} + \tan\frac{\gamma_{had}}{2}} , \\ E_{e,2\alpha} &= \frac{1}{\sin\theta_e} \cdot p_T , \\ E_{q,2\alpha} &= \frac{1}{\sin\gamma_{had}} \cdot p_T . \end{aligned} \tag{2.38}$$

Due to the assumption of a perfect $(E - p_z)$ balance, the 2α method is extremely sensitive to initial state radiation. Thus, this method is used in this analysis exclusively for energy calibration purposes.

2.5 Parton Density Functions of the Proton

A knowledge of the partonic structure of the proton is of particular importance for the interpretation of hard scattering ep data. The parton density functions (PDFs), which build up the structure functions of the proton, contain long range contributions of the NC interaction. Thus, they cannot be derived from first principles but have to be extracted from experimental data.

The PDFs have been parameterised by so-called global analyses using a wide range of DIS and related hard scattering data which cover large areas of the kinematic phase space. Since the Q^2 dependence is well known and given by the DGLAP equations, the x dependence of the PDFs is parameterised at some low scale $Q_0^2 \approx 1\ \mathrm{GeV}^2$. A common ansatz is of the form

$$x\,q(x,Q^2) = A\,x^B\,(1-x)^C \cdot P(x)\ , \tag{2.39}$$

with a polynomial function $P(x)$. Positive values of B and C assure that the PDFs vanish for $x \to 0$ and $x \to 1$. The PDFs are developed at fixed x from Q_0^2 to a given scale Q^2 using the DGLAP evolution equations. The parameters A, B, C, etc. are determined from a fit by comparing the cross sections predicted by these PDFs with those actually measured in experiment. The main constraints come from DIS fixed target data and, since available, from the DIS data of the HERA experiments.

Up to a few years ago, the parameterisations of PDFs did not contain error estimates and data analyses compared the effects of different PDF sets to estimate their errors. These days the experimental data have reached a level of precision which demands for improvements in the uncertainty determination. However, the global analyses have been confronted with conceptual difficulties in providing complete error estimates [25]. According to their origin, the systematic uncertainties on PDFs are separated into so-called experimental and theoretical errors:

- Experimental errors contain the uncertainty due to the statistical and systematic errors of the experimental input data. The latest parameterisations (e.g. CTEQ6.1 [19, 20] and MRST2001 [21, 22]) provide experimental uncertainties on their PDFs. Following the eigenvector-basis approach to the Hessian method [19, 22, 23], they produce additional PDF sets corresponding to fit parameters (e.g. A, B, C, ...) which describe the $\Delta\chi^2$ behaviour in the vicinity of the χ^2 minimum of the central fit. Since the χ^2 minimum is mapped in the plus and minus directions along the eigenvectors of the error matrix, the PDF sets are linear independent w.r.t. the fit parameter space. Therefore, uncertainties of any quantity related to the PDFs, e.g. of the NC cross section, are accessible by standard error propagation of the differences imposed by each plus/minus pair of the error PDF sets. The resulting uncertainties on the NC e^+p cross section are shown in figure 2.6 for the CTEQ6.1 and MRST2001 PDF sets. Since the PDF fits suffer from theoretical difficulties and experimental inaccuracies [22, 24], the PDF analyses derive their error sets from the e.g. $\Delta\chi^2 = 20$ or 100 contours. Thus, the magnitude of the errors is somehow arbitrary. However, the errors show the expected increase towards low x and especially at highest x reflecting the availability of experimental data. Contrary to that, the errors are rather independent of Q^2.

- Theoretical errors include uncertainties arising from e.g. the selection of data used in the fit, the estimates of higher order QCD contributions and the input assumptions placed on the PDF fit [25, 26]. The latter reflects primarily the ignorance of the form of the x dependence of the PDFs at the initial scale.

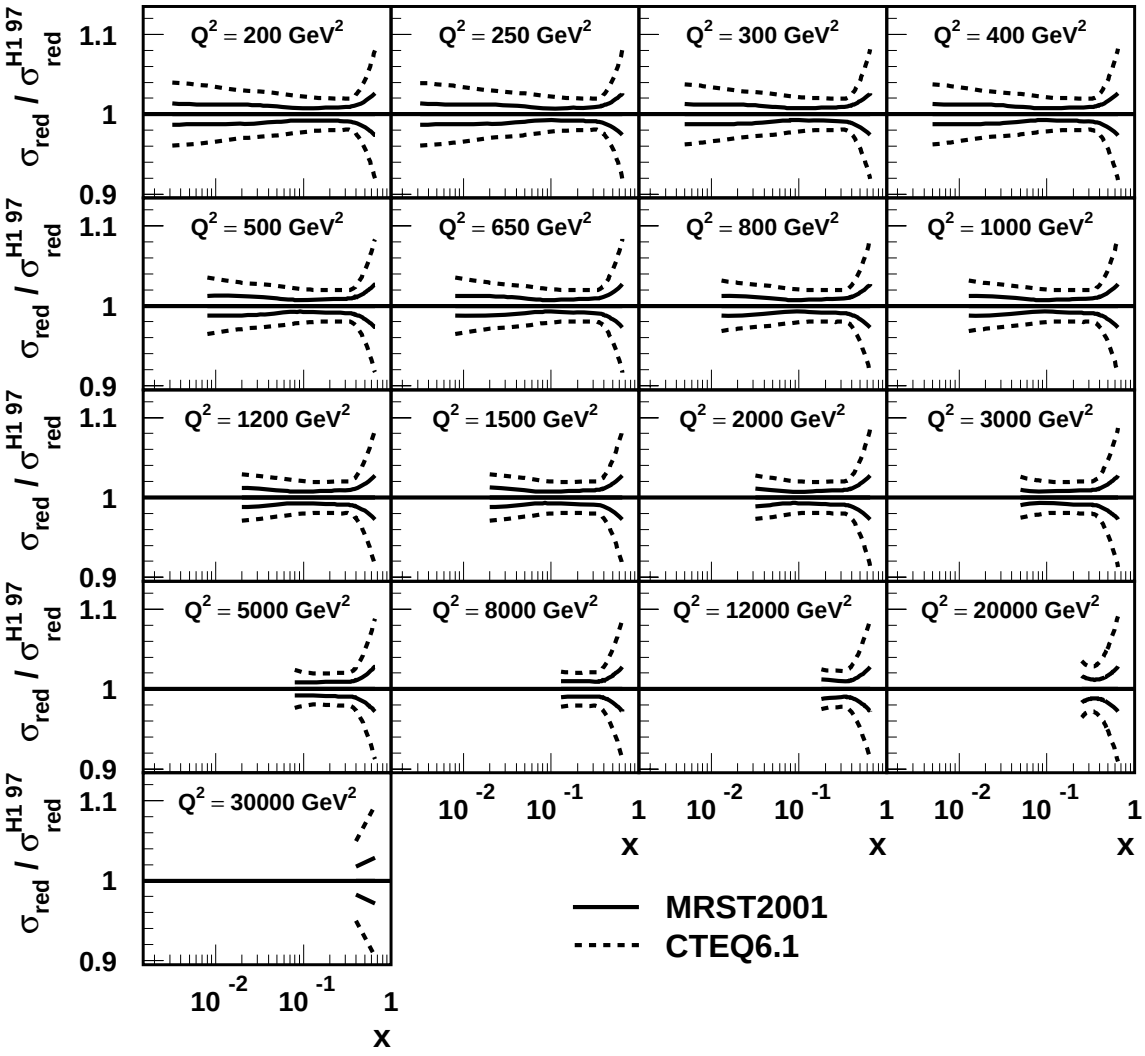

Figure 2.6: Cross section uncertainties for the MRST2001 and CETQ6.1 PDF sets, imposed by 'experimental' PDF uncertainties.

Compared to the experimental errors, the theoretical ones are even more difficult to obtain and currently subject to intensive discussions. However, it is expected that the theoretical errors may yield the dominant contributions to the total PDF uncertainties.

As a consequence, the goal of this analysis is to be rather independent of details of the PDF input, especially of its x parameterisation. This will affect the contact interaction fits to the data presented in chapter 8.

The PDF sets used in this analysis are briefly introduced in the following:

- The **H1 1997 PDF Fit** [27] is based on the H1 inclusive high Q^2 NC and CC cross section data of 1994 to 1997, on H1 low Q^2 data of 1994 as well as on proton and deuteron data from the BCDMS [28] and NMC [29] experiments. This PDF is used for the cross section measurement, since it provides a good description of

the H1 data while not depending on the 1999-2000 H1 data which are subject of this analysis.

- The **H1 2000 PDF Fit** [16] is completely independent of data from other experiments. It relies solely on the H1 inclusive cross section data of 1994 to 2000. Since these include the 1999/2000 NC high Q^2 data which are subject of this analysis, this recent fit of H1 is used for cross-checks only.

- The **CTEQ5** parameterisations [30] is the oldest PDF set used in this analysis. It is based on a wide range of data available in 1999. H1 data only give a marginal contribution by the low Q^2 F_2 data of 1994.

- The **CTEQ6.1** PDF set [19, 20] is an extension of CTEQ5 applying improved fit methods. It uses more recent data, including the 1998/1999 H1 e^-p data at last. In addition to the central fit, this package contains 40 PDF sets for uncertainty studies providing the plus and minus sets of 20 eigenvector representations.

- The **MRST1999** PDF set [31] is the result of a global analysis similar to that of CTEQ5. However, it includes a little more recent data and in particular the H1 inclusive cross section data taken until 1997.

- The **MRST2001** PDF parameterisations [21, 22] is comparable to the CTEQ6.1 set regarding the data used in the fit. In addition to the central fit result which corresponds to an α_s value of 0.119, this package provides PDF sets of fits with α_s being lowered and raised by the experimental uncertainty of 0.002. Finally, it contains 30 error PDFs corresponding to the respective plus and minus sets for each of 15 eigenvector representations.

To get an estimate of the differences between the PDF sets, the corresponding cross sections are compared in figure 2.7. Typical differences are of a few percent. They partly exceed the range of the experimental systematic uncertainties quoted by the latest PDF versions of MRST and CTEQ (cf. figure 2.6), indicating some missing contributions arising from theoretical issues. A remarkable pattern is observed at $x \approx 0.25$ where the cross sections of all global analyses take almost the same value of about 2% above the prediction by the H1 1997 PDF Fit.

It should be stressed that the high Q^2 data sets don't have a significant influence on the structure function fit results which are mainly constrained from the high statistics data at low Q^2 values. However, correlated systematics may impose small dependences of the parton densities from the data at highest Q^2.

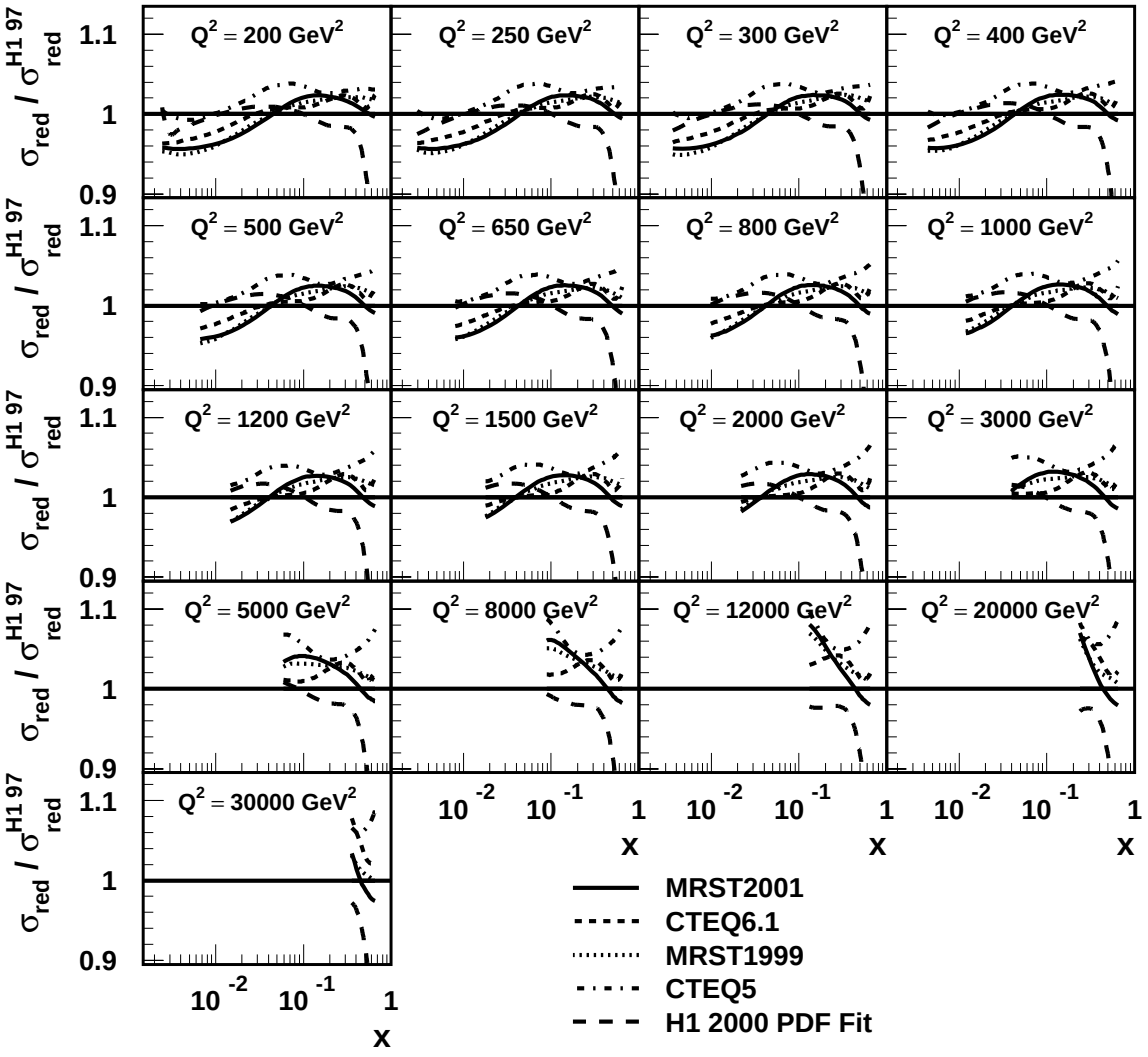

Figure 2.7: NC cross sections derived from different PDF sets. They are normalised to the cross section obtained from the H1 1997 PDF Fit.

Chapter 3

Physics Beyond the Standard Model

The previous chapter dealt with the neutral current high Q^2 cross section being a sensitive probe to validate the Standard Model and to prove consistency within this model up to the extreme kinematic regions accessible at HERA. At the same time, the neutral current cross section provides a precise and versatile measurement to look for new physics phenomena. In fact, considering interference effects of Standard Model processes with the virtual exchange of new, heavy particles or composite objects, scales of new physics can be tested which are far above the HERA centre-of-mass energy.

The neutral current cross section measurement extends up to very high values of $Q^2 \approx 50000$ GeV^2. According to the Heisenberg uncertainty principle, i.e. $\Delta p \cdot \Delta x \gtrsim \hbar$, the ep interaction probes spatial structures with a resolution of up to

$$\Delta x \approx \frac{\hbar\, c}{\sqrt{Q^2}} \approx \frac{200 \text{ GeV} \cdot 10^{-18} \text{ m}}{\sqrt{50000 \text{ GeV}^2}} \approx 0.9 \times 10^{-18} \text{ m} , \tag{3.1}$$

that is where potential signs of new physics may become observable.

The Standard Model describes the interactions between elementary particles by the exchange of gauge bosons. So far established are the massless photon γ as well as the heavy Z^0 and $W^{\pm}$ bosons. The fundamental fermions (leptons and quarks) and gauge bosons (photons and Z^0 bosons) are assumed to be point-like with no substructure. Popular, model independent extensions of the Standard Model can be performed by the introduction of so-called contact interactions, which could be explained e.g. by compositeness, leptoquarks, supersymmetry, large extra dimensions, etc. and which introduce new physics scales in the TeV range.

The purpose of the present analysis is to investigate the inclusive double differential neutral current cross section for the effects of a finite quark radius and various compositeness models of contact interactions.

3.1 Form Factors and Quark Radius

The Standard Model regards the leptons and quarks to be point-like without spatial extension. This assumption can be tested particularly in neutral current ep interactions,

since the gauge boson exchange is sensitive to the electroweak charge distributions of the participating particles. From a classical point of view, the neutral current cross section should decrease with Q^2 for an extended object compared to point-like particles, since at sufficient resolving power the exchange bosons interact only with parts of the distributed charge. This behaviour is commonly described by a form factor ansatz for a spherical charge distribution [32],

$$\frac{d^2\sigma}{dx\,dQ^2} = \frac{d^2\sigma^{SM}}{dx\,dQ^2} \cdot \left|f(Q^2)\right|^2 \ , \text{ with } f(Q^2) = 1 - \frac{1}{6}\,R^2\,Q^2 \ . \tag{3.2}$$

Here, the quark radius R is taken as the root of the mean squared radius of the electroweak charge distribution, $R = \sqrt{\langle r^2 \rangle}$. In principle, a form factor may be assigned to both lepton and quark. However, since the current limits on the electron radius are beyond the reach of HERA, the electron is assumed to be point-like as well as the photon and Z^0 boson. According to equation 3.1, the typical resolution is expected to be of $\sim$1 fm.

3.2 Contact Interactions

There are many models beyond the Standard Model which predict new effects at scales in the TeV energy range. New currents or heavy bosons at scales far beyond the electroweak symmetry breaking scale, representing new physics, could produce indirect effects in deep inelastic ep scattering by virtual exchange. The interference of these interactions with the Standard Model fields would lead to residual contact interactions which may be observed as deviations in the event rates and consequently in the cross sections. These modifications are expected to be stronger and therefore cleaner to detect the higher the resolution of the probe is. Hence, the neutral current ep cross section offers an ideal measurement to look for these effects since it reaches the highest accessible Q^2 values with appropriate, finite statistics. The HERA ep collider is especially suited for the investigations of $(e\overline{e})(q\overline{q})$ contact interactions since it provides the world's highest centre-of-mass energy with both types of the participating particles in the initial state. In particular the initial electron allows a relatively clean measurement. In comparison, the TeVatron $(p\overline{p})$ colliding experiments suffer from the difficulties of having two hadrons as the inital state, even though exploiting a higher centre-of-mass energy.

3.2.1 Introduction

In analogy to Fermi's interpretation of weak interactions, indirect signatures of particle masses and scales Λ_X far beyond the currently available centre-of-mass energies, $\sqrt{s}$, can be described in the low energy approximation, i.e. $\Lambda_X \gg \sqrt{s}$, as point-like four fermion contact interaction. As illustrated in figure 3.1, the contributing Feynman diagrams with the appropriate propagator terms contract into a four-fermion interaction with remaining effective coupling g_X^2/Λ_X^2.

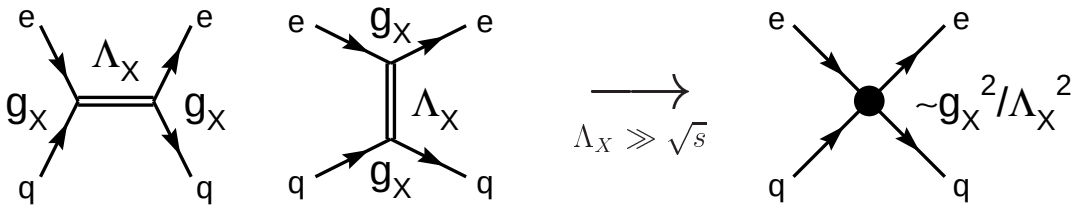

Figure 3.1: Feynman diagrams for neutral current ep scattering via a new interaction, contracting in the low energy approximation into an effective four-fermion contact interaction with coupling g_X^2/Λ_X^2.

The effects of heavy particles or composite objects beyond the scale of electroweak symmetry breaking can be analysed theoretically by introducing an effective lagrangian $\mathcal{L}_{CI}$ which is added to the Standard Model lagrange function,

$$\mathcal{L} = \mathcal{L}_{SM} + \mathcal{L}_{CI} \ . \tag{3.3}$$

If one accepts the Standard Model as the correct low energy effective lagrangian, new interactions in principle should respect the $SU(3)_c \times SU(2)_l \times U(1)_y$ invariance as well. However, just implying $SU(3)_c \times U(1)_y$ symmetry[1], the most general form of independent lagrange contributions can be expressed in terms of the three lorentz invariant fermion bilinear forms of scalar-scalar (S), vector-vector (V) and tensor-tensor (T) type interactions [33, 34, 35]:

$$\mathcal{L}_{CI} \ = \ \mathcal{L}_S + \mathcal{L}_V + \mathcal{L}_T \ , \tag{3.4}$$

$$\mathcal{L}_S \ = \ \sum_q \ \{ \, \eta_S^q (\overline{e}_L e_R)(\overline{q}_L q_R) + \eta_{S'}^q (\overline{e}_L e_R)(\overline{q}_R q_L) \, \} + \text{h.c.} \ , \tag{3.5}$$

$$\begin{aligned} \mathcal{L}_V \ = \ \sum_q \ \{ \quad & \eta_{LL}^q (\overline{e}_L \gamma_\mu e_L)(\overline{q}_L \gamma^\mu q_L) \ + \ \eta_{LR}^q (\overline{e}_L \gamma_\mu e_L)(\overline{q}_R \gamma^\mu q_R) \\ & + \ \eta_{RL}^q (\overline{e}_R \gamma_\mu e_R)(\overline{q}_L \gamma^\mu q_L) \ + \ \eta_{RR}^q (\overline{e}_R \gamma_\mu e_R)(\overline{q}_R \gamma^\mu q_R) \ \} \ , \end{aligned} \tag{3.6}$$

$$\mathcal{L}_T \ = \ \sum_q \ \{ \, \eta_T^q (\overline{e}_L \sigma_{\mu\nu} e_R)(\overline{q}_L \sigma^{\mu\nu} q_R) \, \} + \text{h.c.} \ . \tag{3.7}$$

The sums run over all quarks and anti-quarks q. The indices L and R denote the respective left and right handed helicities of the fermions.

The contributions of scalar and tensor terms, which contain helicity flip operations between the fermions, are proportional to the fermion mass and therefore strongly suppressed at HERA [35]. In addition, these contributions are restrained by strong exclusion limits from low energy experiments measuring helicity suppressed rare decays [36, 37]. They are therefore neglected in the following.

[1] In theories where the Z^0 and $W^\pm$ bosons are composite objects, the $SU(2)_l \times U(1)_y$ group may not necessarily have a fundamental meaning.

Thus, the most general form of a chiral invariant lagrange contribution for contact interactions in neutral current scattering reads [38]:

$$\mathcal{L}_{CI} \approx \mathcal{L}_V = \sum_q \{ \quad \eta^q_{LL}(\overline{e}_L\gamma_\mu e_L)(\overline{q}_L\gamma^\mu q_L) \; + \; \eta^q_{LR}(\overline{e}_L\gamma_\mu e_L)(\overline{q}_R\gamma^\mu q_R) \\ + \; \eta^q_{RL}(\overline{e}_R\gamma_\mu e_R)(\overline{q}_L\gamma^\mu q_L) \; + \; \eta^q_{RR}(\overline{e}_R\gamma_\mu e_R)(\overline{q}_R\gamma^\mu q_R) \; \} \; . \tag{3.8}$$

In this description, the strength of the contributing contact interactions is parameterised by independent coupling coefficients

$$\eta^q_{ab} \equiv \epsilon^q_{ab}\frac{g^2}{\Lambda^{q\;2}_{ab}} \; . \tag{3.9}$$

The indices a and b denote the helicities L or R of the electron and quark, respectively, g is the overall coupling strength, Λ^q_{ab} represents the scale of the contact interaction and $\epsilon^q_{ab}=\pm 1$ defines a sign for the interference with the Standard Model amplitude.

In principle, the parameters η^q_{ab} could be (pairwise) different for all quark types $q\in(u,d,s,c,b)$ and for all helicity combinations $a,b\in(L,R)$. However, in deep inelastic ep scattering at high Q^2 the u and d quark contributions completely dominate. Contact interaction terms arising from the second- and third-generation sea quarks are strongly suppressed by the respective parton density functions in the proton, since the kinematic range of high Q^2 requires at least moderate x values.

For the present analysis, quark flavour symmetry is assumed, i.e. the coefficients η^q_{ab} are independent of the family and are distinguished only for up- and down-type quarks:

$$\begin{aligned} \eta^u_{ab} \quad &\equiv \quad \eta^u_{ab} \; = \; \eta^c_{ab} \qquad\qquad , \\ \eta^d_{ab} \quad &\equiv \quad \eta^d_{ab} \; = \; \eta^s_{ab} \; = \; \eta^b_{ab} \; . \end{aligned} \tag{3.10}$$

Due to the strong dominance of the first quark generation, the contact interaction limits presented in this analysis are rather insensitive to this assumption[2]. Contributions from the top quark are negligible at HERA due to its high mass.

Therefore, the four respective helicity combinations for the up- and down-type quarks yield eight independent parameters giving rise to many different scenarios of contact interactions.

The cross section can only be calculated to leading order $\mathcal{O}(\alpha_s)$ since contact interactions as defined above are a non-renormalisable effective theory. Therefore, the NLO Standard Model cross section as described in chapter 2 is weighted by the leading oder cross section ratio

$$w = \frac{\left(\dfrac{d^2\sigma}{dx\,dQ^2}\right)^{LO}_{\text{SM+CI}}}{\left(\dfrac{d^2\sigma}{dx\,dQ^2}\right)^{LO}_{\text{SM}}} \; . \tag{3.11}$$

[2]The situation is similar at the TeVatron where contact interaction limits are derived from lepton-pair production that also depends on the proton density functions. In contrast, the contact interaction analyses at LEP are sensitive to the process $e^+e^- \to$ hadrons and the resulting limits depend strongly on flavour symmetry assumptions.

Radiative corrections due to real photon emission (cf. section 2.3) are expected to cancel in this ratio to a large extent.

The ansatz of equation 3.8 can be easily applied to any new phenomenon and allows a model independent approach to study various kinds of contact interactions, e.g. (eq) compositeness, leptoquarks, large extra dimensions or new currents mediated by heavy gauge bosons. In this analysis the data are investigated for $(e\overline{e})(q\overline{q})$ contact interactions of various compositeness scenarios.

3.2.2 Implementation of Contact Interactions

The previous section introduced the phenomenology of contact interactions. The lagrange contribution of equation 3.8 together with the coupling coefficients η^q_{ab} of equation 3.9 lead to the following extension of the Standard Model neutral current coupling terms $V_q^{L,R}(Q^2)$ and $A_q^{L,R}(Q^2)$ as defined in equation 2.16:

$$\begin{aligned}
V_q^L(Q^2) &= e_q - (v_e \mp a_e)\, v_q\, \kappa_Z\,(Q^2) + \frac{Q^2}{8\pi\alpha}\,(\eta^q_{LL} + \eta^q_{LR}) \;, \\
V_q^R(Q^2) &= e_q - (v_e \pm a_e)\, v_q\, \kappa_Z\,(Q^2) + \frac{Q^2}{8\pi\alpha}\,(\eta^q_{RL} + \eta^q_{RR}) \;, \\
A_q^L(Q^2) &= \quad - (v_e \mp a_e)\, a_q\, \kappa_Z\,(Q^2) + \frac{Q^2}{8\pi\alpha}\,(\eta^q_{LL} - \eta^q_{LR}) \;, \\
A_q^R(Q^2) &= \quad - (v_e \pm a_e)\, a_q\, \kappa_Z\,(Q^2) + \frac{Q^2}{8\pi\alpha}\,(\eta^q_{RL} - \eta^q_{RR}) \;.
\end{aligned} \tag{3.12}$$

The $\pm$ and $\mp$ signs refer to the $e^\pm$ type of the lepton beam particle.

As can be seen from equations 2.7, 2.15 and 3.12, the effect of a contact interaction on the neutral current cross section depends on the specific scenario. There are two general terms contributing in addition to the Standard Model prediction. One is proportional to $\eta^2 \sim 1/\Lambda^4$ and enhances the cross section at very high Q^2. The other one is proportional to $\eta \sim 1/\Lambda^2$ and originates from the interference with the Standard Model amplitude, which can have either signs to enhance or suppress the cross section at intermediate Q^2 values. Although the additional contact interaction terms in equation 3.12 are independent of the lepton beam particle, the interference contributions are different for e^+p and e^-p scattering. It is important to note that contact interactions modify the Standard Model cross section at all x and Q^2. The effects depend mainly on Q^2 but also on x at fixed Q^2 due to the different particle density contributions in the structure functions F_2 and xF_3 (cf. equation 2.15) and due to the different y dependences of the coefficient functions $Y_\pm$ multiplying the structure functions in equation 2.7.

3.2.3 Substructure of Leptons and Quarks – Compositeness

Originally, contact interactions have been equated with the association of substructures of electrons and quarks. Starting from the electron and from the up and down quarks, the subsequent discoveries of the remaining fermions initiated the speculation

that leptons and quarks were composite objects, composed of more fundamental particles called preons [39]. In these models, the scale Λ characterises the strength of the interaction which binds the preons within the fermions.

In general, contact interactions comprise only one scale Λ for all couplings and don't distinguish between up and down type quarks, further reducing the variety of coupling combinations to

$$\begin{aligned} \eta^u_{ab} &= \eta^d_{ab} \quad \equiv \quad \eta_{ab} = \epsilon_{ab}\frac{g^2}{\Lambda^2} \ , \\ \text{with} \quad \epsilon^u_{ab} &= \epsilon^d_{ab} \quad \equiv \quad \epsilon_{ab} \ . \end{aligned} \tag{3.13}$$

Equation 3.13 assures $SU(2)$ invariance which requires $\eta^u_{RL} = \eta^d_{RL}$ [37]. Finally, four coupling terms η_{ab} or rather $\epsilon_{ab} \in [0, \pm 1]$ remain in addition to the overall scale Λ to define the various contact interaction scenarios. The overall coupling constant is by convention set to $g^2 = 4\pi$.

The 26 chiral structures of compositeness models investigated in this analysis are defined in table 3.1. Each row provides a relative coupling combination between the ϵ_{ab}

coupling	ϵ_{LL}	ϵ_{LR}	ϵ_{RL}	ϵ_{RR}
LL	1	0	0	0
LR	0	1	0	0
RL	0	0	1	0
RR	0	0	0	1
VV	1	1	1	1
AA	1	-1	-1	1
VA	1	-1	1	-1
$LL - LR$	1	-1	0	0
$LL + RL$	1	0	1	0
$LL + RR$	1	0	0	1
$LR + RL$	0	1	1	0
$LR + RR$	0	1	0	1
$RL - RR$	0	0	1	-1

Table 3.1: Chiral structures of compositeness models for contact interaction couplings. Each row corresponds to two different contact interaction scenarios of opposite interference sign w.r.t. the Standard Model amplitudes. The table gives the coupling combinations for models denoted by the '+' superscript, e.g. LL^+. The models of opposite overall interference behaviour, e.g. LL^-, are defined by reversed signs.

which serves for two different models of opposite overall interference behaviour w.r.t. the Standard Model amplitudes.

Low energy experiments which measured parity violating transition amplitudes in caesium atoms [37, 40, 41] have put very restrictive constraints on parity violating contact interactions, e.g. on scenarios of pure chiral couplings (LL, LR, RL, RR). Nevertheless, these contact interaction types will be considered in this analysis, since they

are of simplest, elementary form and since at HERA, they are investigated at much higher energy scales. The strong limits from the low energy experiments don't affect parity conserving contact interaction scenarios, i.e. which comply with

$$\eta^q_{LL} + \eta^q_{LR} - \eta^q_{RL} - \eta^q_{RR} = 0 \ . \tag{3.14}$$

Besides the types of pure chiral coupling, all other contact interaction scenarios defined in table 3.1 obey equation 3.14 and therefore preserve parity. Note that each line in this table represents two scenarios, one for $\epsilon = +1$ and one for $\epsilon = -1$, denoted as e.g. LL^+ and LL^-, respectively.

The modifications of the Standard Model double differential cross sections due to contact interactions are displayed in appendix B for the scenarios defined above. Compositeness scales mainly affect the Q^2 dependence of the cross section. In general, a steep rise with Q^2 is found for positive interference signs, while negative interference leads to a typical interference pattern. Moreover, the effects of contact interactions increase towards large x.

Some contact interaction scenarios lead to ambiguities in the resulting cross sections: For models which have negative interference with the Standard Model amplitudes, at a certain, finite scale Λ the cross section observable may be indistinguishable from the Standard Model prediction. Here, the destructive SM×CI interference term cancels approximately the pure CI×CI term, e.g. for the AA model with $\Lambda^- \approx 4$ GeV. In addition, some models yield comparable effects on the cross section for both interference signs of the same coupling combination, e.g. the VA coupling combination.

Chapter 4

The H1 Experiment at HERA

The analysis of this thesis is based on data which were taken with the H1 experiment at the HERA *ep* collider. This chapter introduces the HERA collider and the detector components of the H1 experiment which are relevant for the investigation of neutral current events at large momentum transfers.

4.1 The HERA Collider

The HERA[1] *ep* collider is located at the DESY[2] laboratory in Hamburg, Germany. It consists of two storage rings, one for electrons (or positrons) and one for protons, which have a circumference of 6.4 km and are situated in a tunnel about 10-15 m below the surface. The HERA facility with the main accelerator ring and the pre-accelerator system is shown in figure 4.1. The beams are accumulated and pre-accelerated in

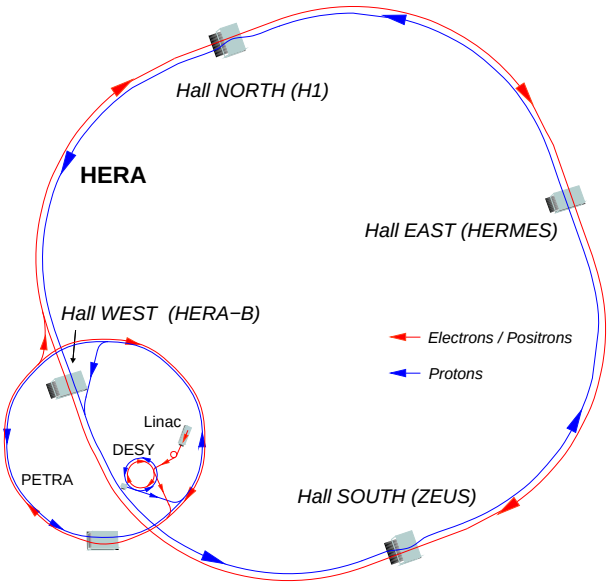

Figure 4.1: The HERA collider facility and its pre-accelerator system.

[1] Hadron-Elektron-Ring-Anlage
[2] Deutsches Elektronen-Synchrotron

several steps before the electrons and the protons are injected in opposite directions into the HERA machine. Bending magnets in the curved sections keep the beams on a circular orbit, while the straight sections are equipped with acceleration stations and focussing magnets. The beams are collided head-on in two interaction regions occupied by the experiments H1 and ZEUS. There are two additional fixed target experiments, HERA-B and HERMES, which use only one of the beams. Due to the RF voltage used for the acceleration electrons and protons appear in up to 220 bunches of 10^{10} to 10^{11} particles each. The time between two bunch crossings is 96 ns. The longitudinal bunch length is about 60 cm, leading to an approximately Gaussian distribution of interaction points along the beam line with a width of about 10 cm.

During the data taking period 1999-2000, HERA was operated with $E_e = 27.5$ GeV positrons and $E_p = 920$ GeV protons, providing a centre-of-mass energy of $\sqrt{s} \approx 319$ GeV. Typical electron currents of 40 mA and proton currents of 90 mA yielded a peak luminosity of about 1.5×10^{31} cm^{-2}s^{-1}, which corresponds to the design value. The annual integrated luminosity provided by HERA since 1992 and the one accumulated by H1 are displayed in figure 4.2. From 1992 to 2000, the H1 experiment has recorded

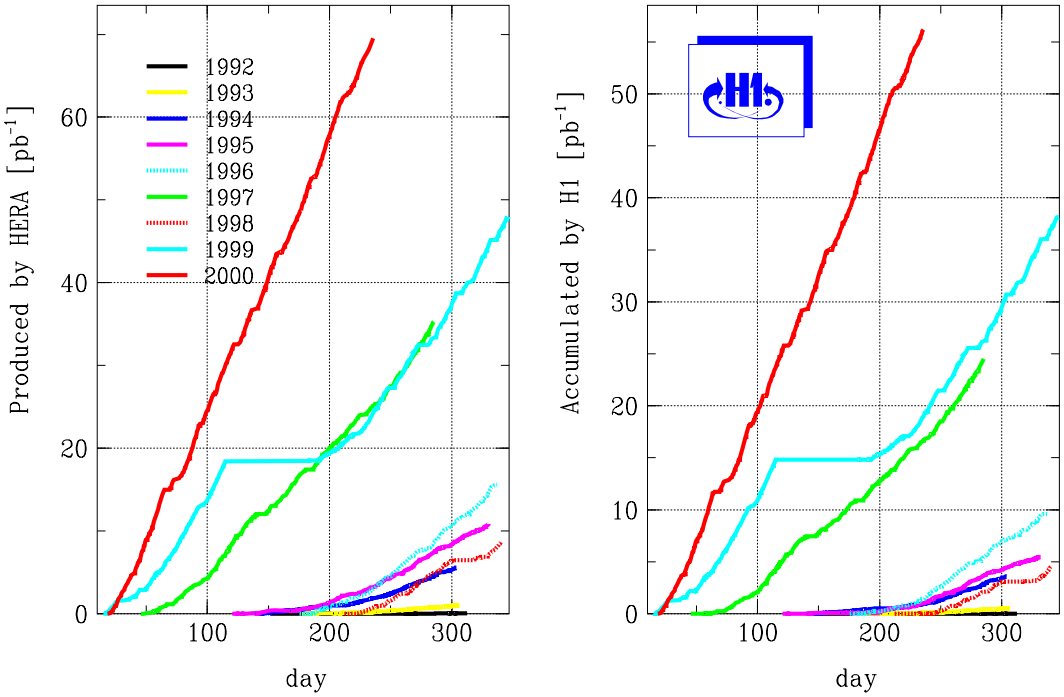

Figure 4.2: Annual integrated luminosity as function of time. The left figure shows the integrated luminosity provided by HERA, the luminosity accumulated by the H1 experiment is shown on the right.

data corresponding to an integrated luminosity of about 120 pb^{-1}. The present analysis is based on data from the second half of 1999 and the year 2000.

In September 2000, HERA operation was shut down to allow for a major luminosity upgrade of the HERA machine and the colliding beam experiments. Currently, the start-up of the HERA-II run proceeds promising an increase of luminosity by a factor of five.

4.2 The H1 Detector

The H1 detector was designed on the basis of the HERA physics program, which includes the precise measurement of the proton structure, tests of the Standard Model and searches for new physics. The multi-purpose detector serves to measure the energy and direction of particles emerging from ep interactions. Emphasis is placed on accurate lepton and in particular electron identification and calorimetric measurement as well as on high granularity and resolution for hadronic jet measurements. To allow for the recognition of missing transverse energy, the detector provides hermetic coverage of almost the complete solid angle of 4π with some unavoidable losses due to the feed through of the beam pipe.

A right-handed Cartesian coordinate system is used to describe points within the H1 detector. The origin is placed at the geometrical centre of the central tracking chambers which defines the nominal interaction point. The z-axis points in the proton beam direction, the y-axis points vertically upwards. The x-y plane is referred to as the transverse plane. The forward and backward directions denote the regions of $z > 0$ and $z < 0$, respectively. The polar angle θ is measured w.r.t. the proton beam direction and the azimuthal angle ϕ is defined w.r.t. the positive x-axis. The pseudorapidity η is sometimes used instead of the polar angle which are related by $\eta = -\ln(\tan\theta/2)$.

A schematic view of the H1 detector is shown in figure 4.3. The individual detector components are mounted concentrically around the beam line. Due to the different beam momenta and the corresponding strong boost of the ep centre-of-mass system in the proton direction, the detector design is asymmetric with respect to the interaction point, with enhanced instrumentation in the forward direction.

The interaction region is covered by silicon detectors in the central and backward directions to assist the measurement of particle tracks and detect secondary vertices. They are followed by the central and forward tracking detectors to measure the trajectories and momenta of charged particles. The tracking system is enclosed in a large calorimeter system which consists of the Liquid Argon calorimeter in the central and forward directions and is supplemented in the backward region by the Spaghetti calorimeter. Both of them are divided into an electromagnetic and hadronic section and measure the positions and energies of neutral and charged particles. They also allow for the separation of electromagnetically interacting particles and hadrons and thus for the identification of electrons. An additional plug calorimeter is installed in the forward direction close to the beam pipe. The Liquid Argon calorimeter is surrounded by a superconducting coil which provides a homogeneous magnetic field of 1.15 T parallel to the beam axis. The field lines are closed by the iron return yoke which is instrumented with streamer tubes to detect muons and to measure energy leakage from hadrons not fully contained in the calorimeters. The forward muon detector consists of drift chambers and a toroidal magnet to identify and measure the momentum of penetrating muons in the forward direction. The luminosity system is placed in the negative z-direction close to the beam pipe.

A detailed description of the H1 detector can be found in [42, 43]. In the following only the components important for the present analysis are described.

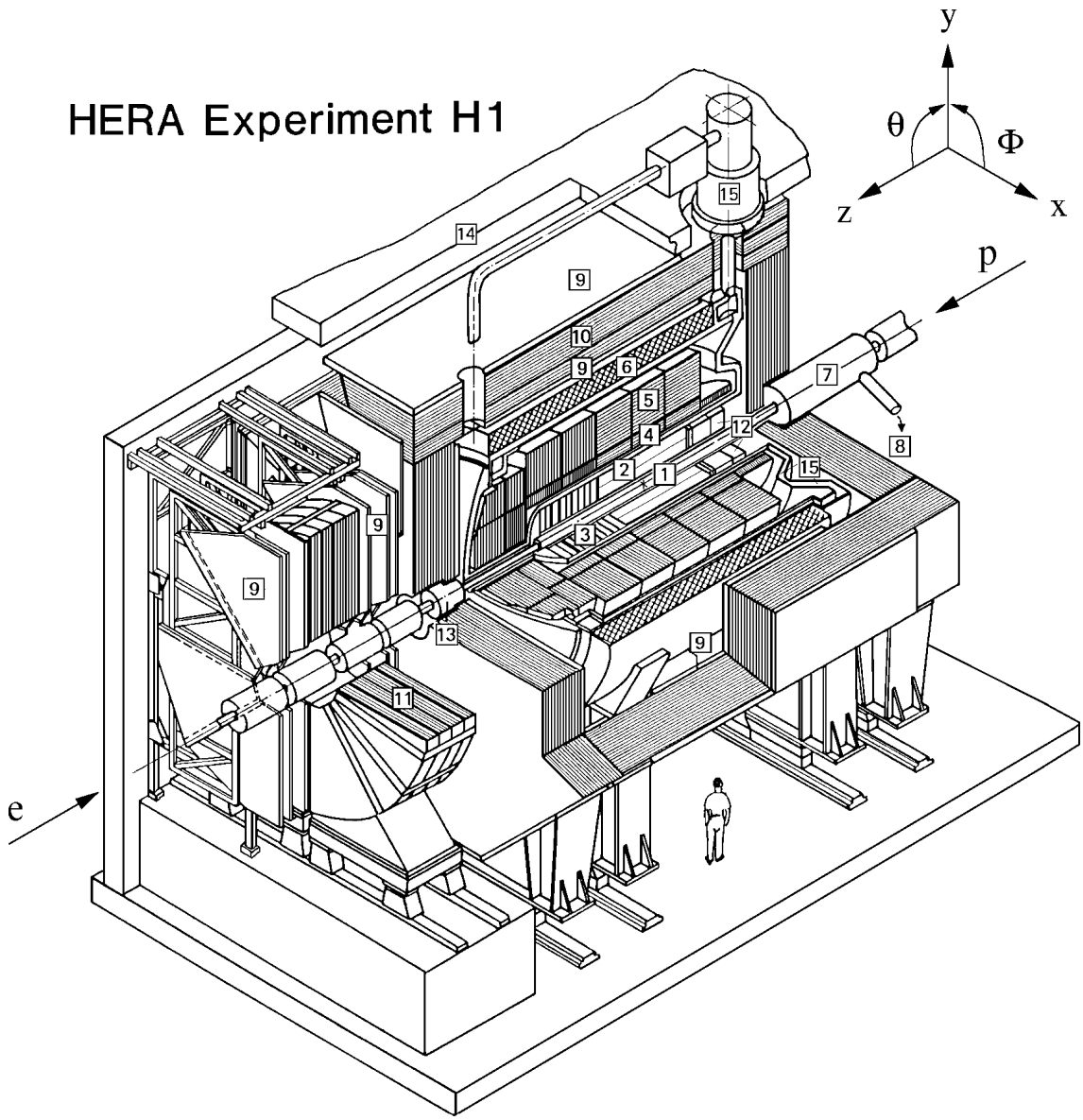

1	Beam pipe and beam magnets	9	Muon chambers
2	Central tracking chambers	10	Instrumented iron
3	Forward tracking system	11	Muon toroid magnet
4	Electromagnetic LAr calorimeter (lead)	12	Warm calorimeter (Spacal)
5	Hadronic LAr calorimeter (stainless steel)	13	Plug calorimeter
6	Superconducting coil	14	Concrete shielding
7	Compensating magnet	15	Liquid Argon cryostat
8	Helium cryogenics		

Figure 4.3: Schematic view of the H1 detector. The H1 coordinate system is indicated in the top right corner.

4.2.1 Liquid Argon Calorimeter

The Liquid Argon (LAr) calorimeter is the most important detector component for the present analysis. It provides the identification and measurement of the scattered electron and the main part of the measurement of the hadronic final state of neutral current high Q^2 events. The LAr calorimeter covers the polar angle range of $4^\circ \leq \theta \lesssim 154^\circ$ and is housed in a single cryostat. The superconducting solenoid is located outside of the cryostat to minimise the amount of inactive material in front of the calorimeter.

The LAr technique offers the advantages of good stability, ease of electronic calibration, good homogeneity of the response and fine granularity. These properties allow for the identification of electrons and the precise measurement of their energies and positions as well as the accurate measurement of the hadronic energy flow. The structure of the LAr calorimeter and its energy measurement are described below. Detailed information can be found in [44].

The plug calorimeter, which covers the very forward region between the LAr calorimeter and the beam pipe, is not used in this analysis.

Structure of the LAr calorimeter

The LAr calorimeter is a sampling calorimeter which consists of an inner, fine grained electromagnetic section followed by a coarser hadronic part. Figure 4.4 shows a vertical cut along the beam axis of the LAr calorimeter. It is divided along the z-direction into eight self-supporting wheels, named according to their position w.r.t. the proton beam: Backward Barrel (BBE), Central Barrel (CB1, CB2, CB3), Forward Barrel (FB1, FB2), Outer Forward (OF) and Inner Forward (IF). The BBE consists of an electromagnetic section only, the OF only of two hadronic sections. In ϕ-direction, each wheel is further segmented into eight identical units, the so-called octants. Figure 4.5 shows a transverse cross section of a central barrel wheel with the typical octagon structure. In the BBE the structure of the octants is bent at the edges leading to a 16-fold polygonal surface of the calorimeter front. The insensitive areas at the connection points of the modules are called "z-cracks" between the wheels and "ϕ-cracks" between the octants.

The LAr calorimeter is built up of absorber plates supplemented by high voltage and read-out electrodes. The interspaces between the plates are filled with liquid Argon as active medium. To obtain a uniform energy resolution, the orientation of the plates is arranged such that the angle of incidence of particles originating from the ep interaction point is always larger than 45°. The electromagnetic section consists of 2.4 mm lead absorber plates. The LAr gap thickness is 2.35 mm on average. The absorption length of the electromagnetic part varies between 20 and 30 radiation lengths (X_0) in the central and forward directions, respectively. The absorber material in the hadronic section consists of 19 mm thick stainless steel plates with a double gap of 2.4 mm filled with liquid Argon. The total amount of absorbing material of the calorimeter corresponds to about 5 to 8 hadronic interaction lengths (λ).

The LAr calorimeter is segmented into about 44000 read-out cells to enable a good spatial resolution of deposited energies. The segmentation is coarse in the backward

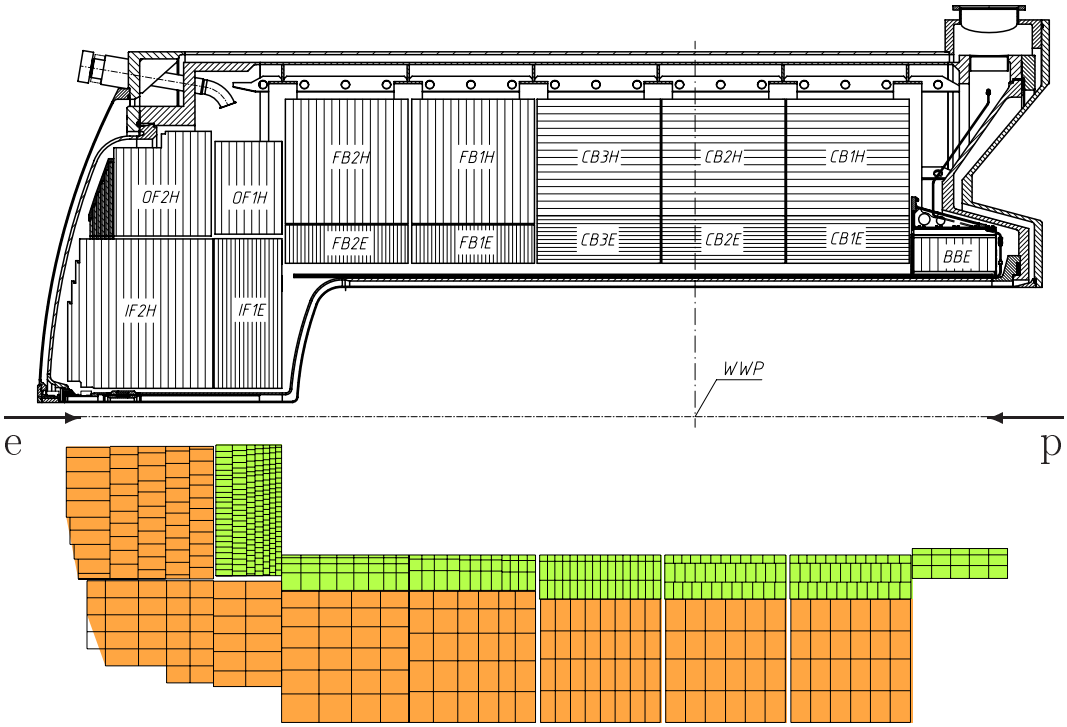

Figure 4.4: Longitudinal cross section of the LAr calorimeter. The upper half shows the sampling structure with the orientation of absorber plates. The read-out cell structure is indicated in the lower part. "WWP" denotes the nominal interaction point.

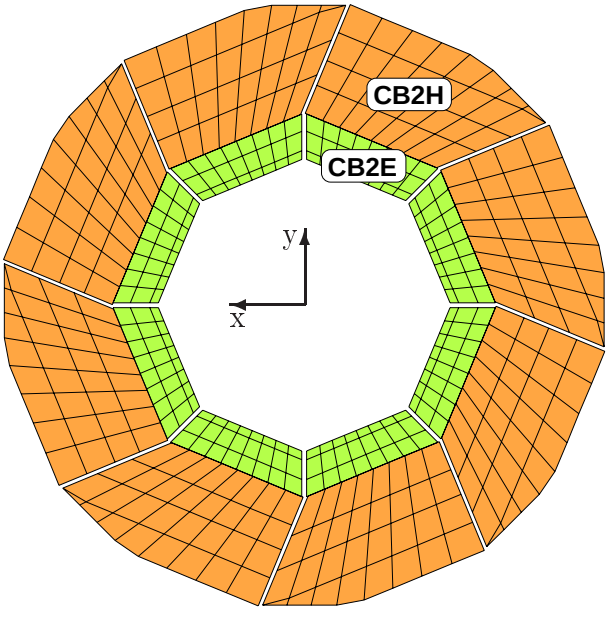

Figure 4.5: Transverse cross section of a central barrel (CB2) wheel of the LAr calorimeter viewed along the proton beam direction.

part and becomes finer towards the forward direction (cf. lower part of figure 4.4). As seen from the *ep* interaction point, the number of layers increases from three to six in the electromagnetic section and from four to six in the hadronic section. In terms of the Molière radius[3], R_M, which is a measure of the transverse extension of electromagnetic showers, the typical transverse size of the cells varies between $2.5R_M$ in the backward region and $1.0R_M$ in the forward part. The fine granularity allows for both a precise position measurement of electromagnetically interacting particles and a clean separation of electromagnetic and hadronic showers. The latter provides the basis for an efficient electron identification.

Energy measurement with the LAr calorimeter

Using a LAr calorimeter technique the energy measurement relies on the absorption of the total energy of the primary particle by a cascade of secondary particles [45]. Part of the energy – about 10% for electromagnetic showers – is deposited in the LAr gaps by ionisation. The charge is collected with charge sensitive amplifiers from the read-out pads. In test beam measurements [46, 47] calibration constants were determined for each cell geometry to convert the measured charge into energy units. The electronic noise contribution depends linearly on the capacitance of the complete read-out chain which is mainly given by the cell size. For a single cell the noise amounts to an equivalent energy of about 10 to 30 MeV. The accumulation of all cells would thus yield a substantial contribution to the energy measurement of the LAr calorimeter. However, noise suppression algorithms are applied and reduce the noise contribution to a large extent without significant effects on the real energy measurements. Further correction factors entering the charge to energy conversion are: the charge collection efficiency at nominal high voltage operation, which is measured from high voltage curves using cosmic or halo muons; corrections for local variations of the size of cracks or absorbers, which are obtained from Monte Carlo simulations. Finally, the energy reconstruction combines groups of cells to so-called clusters which approximately correspond to the energy depositions of single particles.

The LAr calorimeter is non-compensating, i.e. the deposited charge is smaller for hadrons than for electrons of the same energy. The signal ratio of electrons to pions, the so-called e/π ratio, is about 1.35 for 10 GeV particles and decreases logarithmically with energy. Large π^0 fluctuations in hadronic showers thus yield a non-linear energy response and significant non-Gaussian contributions to the energy measurement. This deficit is compensated using a software energy weighting technique. The method relies on the fine segmentation of the LAr calorimeter which allows to identify the electromagnetic components within hadronic showers. Details on the energy weighting are discussed in section 5.8, which presents an improved algorithm developed in parallel to this thesis.

CERN test beam measurements [46, 47] for the LAr calorimeter modules revealed

[3]The Moliere radius, R_M, is a characteristic constant of a material describing its electromagnetic interaction properties, and is related to the radiation length by $R_M = X_0 \cdot E_s/E_c$, with the radiation length X_0, a scale energy $E_s \approx 21$ MeV, and the critical energy E_c [92]. R_M is a good scaling variable in describing the transverse dimension of electromagnetic showers.

an energy resolution of

$$\sigma_{em}(E)/E = 12\%/\sqrt{E[\mathrm{GeV}]} \oplus 1\% \tag{4.1}$$

for electrons and photons and

$$\sigma_{had}(E)/E = 50\%/\sqrt{E[\mathrm{GeV}]} \oplus 2\% \tag{4.2}$$

for charged hadrons. The in situ calibration of the electromagnetic and hadronic energy scale is performed with real ep data in the present analysis (cf. sections 5.7 and 5.8).

4.2.2 Spaghetti Calorimeter

The Spaghetti calorimeter (Spacal) [48] supplements the calorimetric measurement in the backward direction covering the polar angle range of $153° < \theta < 177.5°$. In the present analysis it is used to complete the measurement of the hadronic final state in the backward region.

The Spacal was designed to provide an accurate measurement of the scattered electron of low Q^2 neutral current DIS events ($1 \lesssim Q^2 \lesssim 150$ GeV^2). It is a sampling calorimeter made of lead as absorber material and scintillating fibres as active component. Incident particles develop into a shower in the lead and accompanying charged particles cause scintillation of the fibres. The light is collected and read out by photomultiplier tubes.

The Spacal consists of an electromagnetic and a hadronic section made of 0.5 mm and 1.0 mm diameter scintillating plastic fibres with a lead-to-fibre volume ratio of 2.3 : 1 and 3.4 : 1, respectively. The electromagnetic section contains 1192 cells of transverse size of 40.5×40.5 mm^2 providing a spatial resolution of a few mm for electrons. The active material corresponds to 28 radiation lengths. The electromagnetic energy resolution was obtained in test beam measurements [49] to be $\sigma_{em}(E)/E \approx 7\%/\sqrt{E[\mathrm{GeV}]} \oplus 1\%$. The absolute energy scale is known to a precision of 1.0%.

The hadronic section consists of 136 cells with size 119×119 mm^2. In total, the Spacal is two interaction lengths deep.

The Spacal provides coarse hadronic energy measurement and precise time information which is used on the first trigger level to suppress background events.

4.2.3 Tail Catcher Calorimeter

The iron yoke of the main solenoid surrounds all major detector components of the H1 experiment. It serves as hadronic tail catcher, measuring hadronic energy leaking out of the LAr and Spacal calorimeters, and for the measurement of penetrating muons.

The iron system consists of ten iron layers, each 7.5 cm thick, which are instrumented with a total of 16 layers of limited streamer tubes. Five layers are equipped with strip electrodes running perpendicular to the wires. The digital information of the wires and strips allow for the reconstruction of tracks in the iron, which are used for the identification of muons. The spatial resolution of these tracks is of the order of

5-15 mm. The detector is subdivided into the forward endcap, the barrel and the backward endcap, which cover different polar angle regions and have different orientations of the wires and strips.

In order to measure hadronic energy leaking out of the main calorimeters, eleven layers of the instrumented iron are equipped with read-out electrodes (pads), which have a typical size of 40×50 cm in the barrel part and 28×28 cm in the endcaps. The signals of the consecutive five inner and six outer pads are added and thus provide two-fold energy sampling in depth. The energy measurement is based on the analog read-out of the pad signals. Details on the calibration, long-term stability and energy scale are discussed in [50]. The main energy contributions of the tail-catcher to the total calorimetric energy measurement comes from the directions close to the beams and from the transition region between LAr and Spacal calorimeter. The energy resolution was obtained in test beam measurements [51] to be $\sigma(E)/E \approx 100\%/\sqrt{E[\mathrm{GeV}]}$.

4.2.4 Inner Tracking System

The inner tracking system is designed to measure the momenta and angles of charged particles and to provide fast trigger signals. The trajectories of particles are determined by combining the signals of different sub-detectors. The momenta are obtained from the curvature of the tracks within the magnetic field provided by the superconducting solenoid magnet. In the present analysis the tracking system serves for the reconstruction of the ep interaction vertex.

The components of the inner tracking system are shown in figure 4.6. Due to the high track multiplicity in the forward direction, which is a result of the different beam

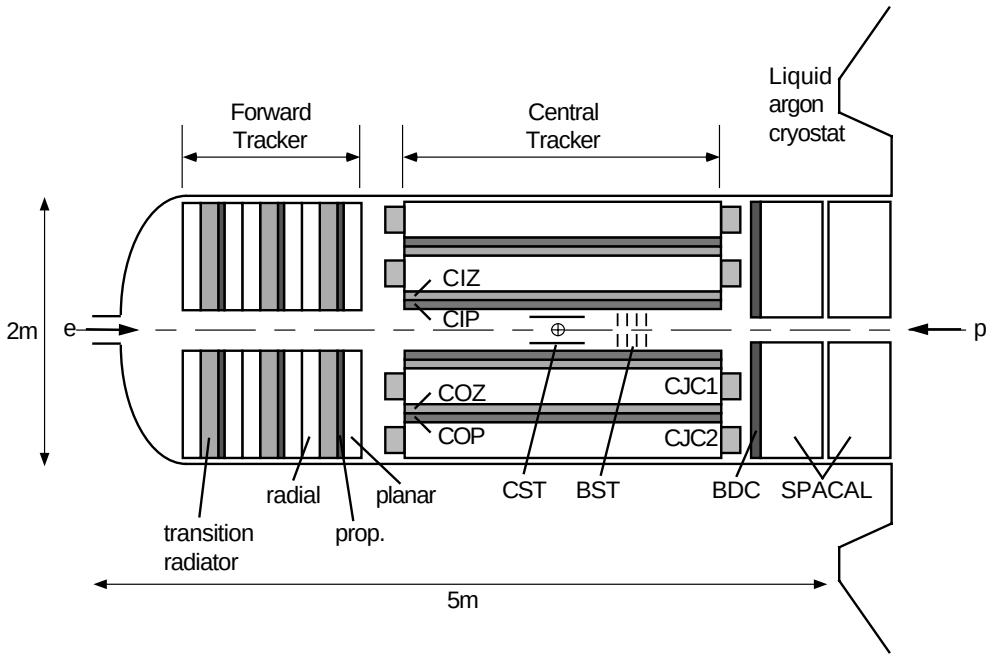

Figure 4.6: Longitudinal cross section of the inner tracking system.

energies, the tracking system is divided into central and forward tracking devices. The backward drift chamber (BDC), which completes the coverage in the backward region, is not used in the present analysis.

Central tracking chambers

The central tracking detector covers the angular range $15° < \theta < 165°$ with full azimuthal acceptance. Figure 4.7 shows a transverse cross section of the central tracking chambers, which are mounted concentrically around the beam pipe. The following chambers are installed:

- Central silicon tracker (CST) consisting of two detector layers (not shown).
- Central inner and outer multi-wire proportional chambers (CIP and COP), each consisting of two detector layers.
- Inner and outer central jet chambers (CJC1 and CJC2). The CJC1 (CJC2) consists of 30 (60) cells with 24 (32) sense wires parallel to the z axis.
- Central inner and outer z-drift chambers (CIZ and COZ) equipped with wires perpendicular to the beam axis. The CIZ (COZ) consists of 15 (24) so-called "rings" of drift cells along z with four signal wire layers per cell.

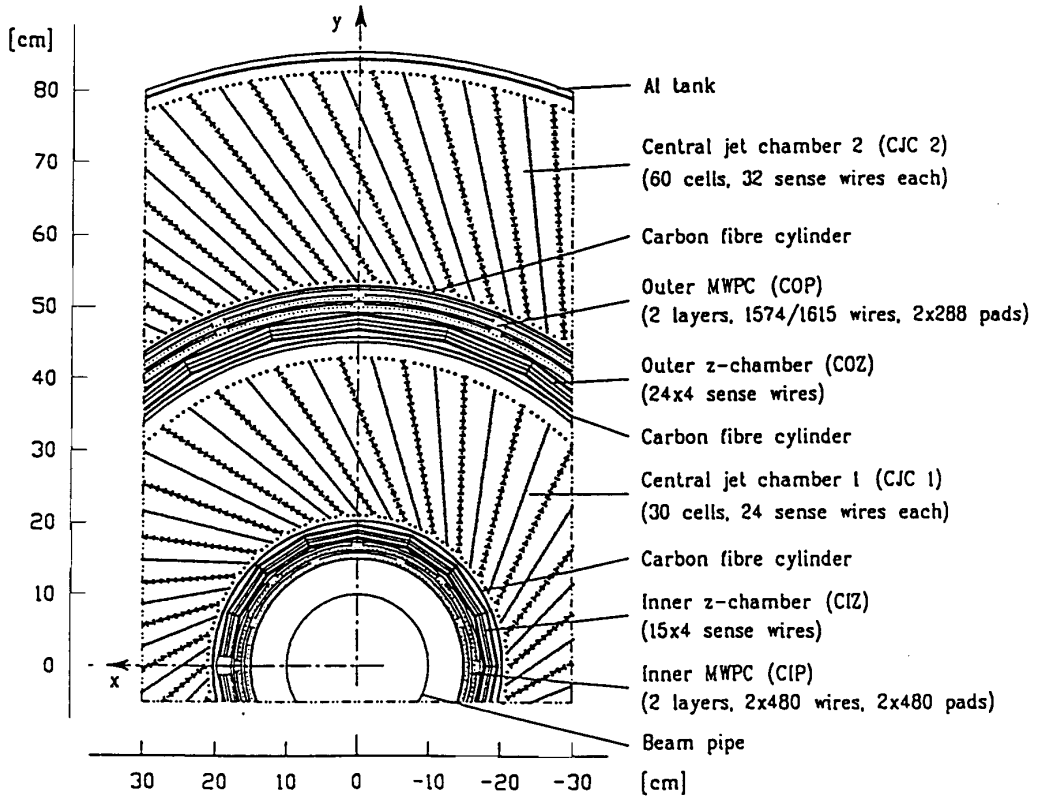

Figure 4.7: Transverse cross section of the central tracking chambers.

The primary components of the tracking system are the two jet-type drift chambers CJC1 and CJC2, denoted as CJC. They measure the r-ϕ-coordinate of the particle tracks with a precision of $\sigma_{r\phi} \approx 170$ μm. The z-coordinate is measured by comparing the collected charge on the two ends of the wire, resulting in a rather coarse resolution of $\sigma_z \approx 2.5$ cm. A much better precision of $\sigma_z \approx 400$ μm is achieved with the assistance of the z-chambers CIZ and COZ.

The tracking system achieves a momentum resolution in the coordinate transverse to the magnetic field of $\sigma(p_T)/p_T \approx 0.008 \cdot p_T[\text{GeV}]$.

Forward tracking chambers

The forward tracking system extends the polar angle coverage of the central tracking system down to $\theta \approx 7°$. It consists of three identical super-modules, each containing three planes of planar drift chambers (rotated by 60° against each other), a multi-wire proportional chamber, a transition radiation detector and a radial drift chamber. The forward tracking system allows for the reconstruction of the ep interaction vertex for events where no tracks are found within the acceptance of the central tracking system.

Proportional chambers

Integrated into the tracking system are layers of multi-wire proportional chambers, which cover the polar angle range between 5° and 175° with full azimuthal acceptance. They provide a fast timing signal with time resolution below the time difference between HERA bunch crossings, fast track information to be used on the first trigger level, and supplementary track elements for the track reconstruction.

4.2.5 Time-of-Flight Detectors

The Time-of-Flight (ToF) system [52] is used to reject proton beam induced background. So-called beam-gas and beam-wall events, where protons interact with the residual gas inside the beam pipe or with the beam pipe wall, yield a large contribution to the non-ep background.

The ToF systems consists of several scintillator arrays located in the backward region of the H1 detector. They are mounted perpendicular to the beam pipe and provide precise time information of traversing particles. At the position of the ToF-walls, the signal of proton induced background events is separated in time from real ep collisions by the time-of-flight of beam protons from the ToF plane to the ep interaction region and the emerging final state particles back from the interaction point to the ToF-wall. Based on the precisely known time structure of ep collisions, time windows are set to reject non-ep background.

The precise time resolution of the Spacal calorimeter provides additional time information which is used in an analogous way as for the ToF system.

4.2.6 Luminosity Measurement

The measurement of the luminosity yields an important ingredient to a cross section determination. The instantaneous luminosity $\mathcal{L}$ connects the interaction rate dN/dt with the cross section σ of a given process:

$$\frac{dN}{dt} = \mathcal{L} \cdot \sigma \ . \tag{4.3}$$

The total number of events is related to the integrated luminosity $L = \int \mathcal{L}\, dt$, which is given in units of inverse picobarn, pb^{-1}. Thus the measurements of integrated luminosity and number of events allows for the determination of a cross section.

At H1 the luminosity is measured with the Bethe-Heitler process of small-angle bremsstrahlung [53], $ep \to e'\gamma p$. The cross section of this reaction is calculable to high precision and diverges for photons radiated collinear to the electron. The large cross section enables a precise measurement of the event rate and thus of the luminosity using equation 4.3.

Figure 4.8 shows the luminosity system [54] of the H1 experiment. It consists of the electron tagger (ET) located at $z_{ET} = -33.4$ m and the photon detector (PD) at $z_{PD} = -102.9$ m. Both detectors are segmented crystal Čerenkov counters with high radiation resistance and good energy, coordinate and time resolution.

The scattered electron from the Bethe-Heitler process, which has a reduced momentum compared to the beam electrons, is deflected by a magnet system and measured in the electron tagger. The photon is predominantly scattered under small angles and

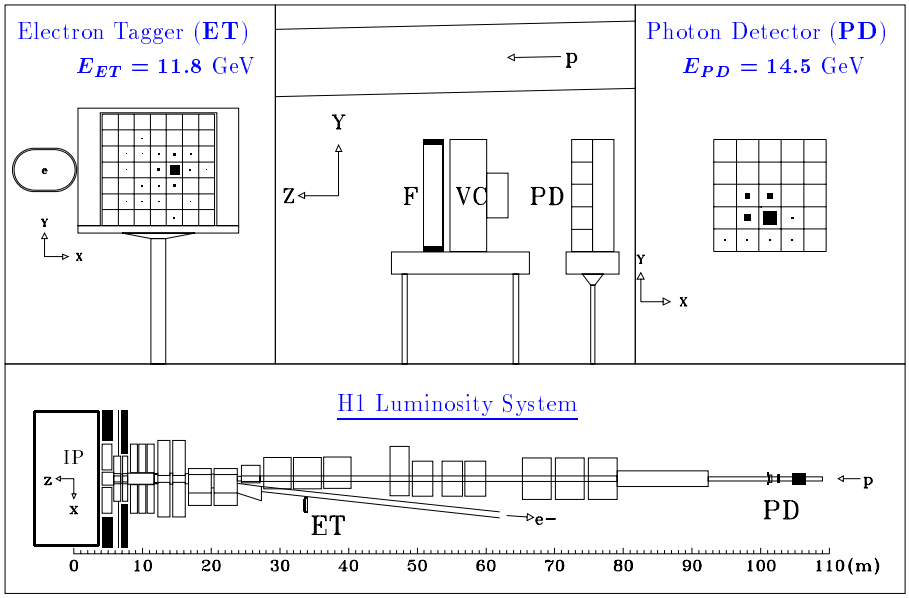

Figure 4.8: The luminosity system of the H1 experiment. In the upper part, the electron tagger (left) and the photon detector (right) are shown with a typical bremsstrahlung event. The lower part shows both detectors with respect to the ep beam lines and the interaction point (IP).

leaves the upwards bent proton beam pipe before hitting the photon detector. The photon detector is shielded from synchrotron radiation by a lead filter (F). A water Čerenkov veto counter (VC) recognises events with photons interacting in the lead absorber, which are rejected for precise energy measurements. The electron and photon detectors are permanently calibrated during data taking constraining the energy sum $E_{ET} + E_{PD}$ to the electron beam energy E_e.

For the online measurement of the luminosity the 'coincidence' method is used, which requires the simultaneous detection of Bethe-Heitler electrons and photons. However, due to smaller systematic uncertainties, the 'single photon' method is applied for the offline determination of the final value of the integrated luminosity. In this case, the luminosity is measured solely from the rate of detected photons,

$$L = \frac{N_{BH}^{ep}(E_\gamma > E_{min})}{\sigma_{BH}(E_\gamma > E_{min})} \ , \tag{4.4}$$

where $N_{BH}^{ep}(E_\gamma > E_{min})$ and $\sigma_{BH}(E_\gamma > E_{min})$ denote the number of selected Bethe-Heitler events with an photon energy E_γ larger than a minimum energy E_{min} and the corresponding cross section, respectively. Important corrections to the event number are trigger efficiencies, the acceptance of the photon detector and pile-up effects. The final systematic uncertainty of the luminosity measurement is typically of the order of 1%.

In addition to the luminosity measurement the luminosity system also serves for the identification of photoproduction events ($Q^2 < 0.01$ GeV^2) and DIS events with an additional photon from initial state QED radiation.

4.3 Trigger System and Data Acquisition

The trigger system of the H1 experiment consists of a series of fast filters designed to accept only desired events during data acquisition. Events with significant detector signals occur at a rate of about 100 kHz. However, they predominantly arise from non-*ep* background processes such as cosmic muons or beam-wall interactions as well as from the uninteresting part of *ep* interactions typically of very large cross sections. While rejecting these events, the trigger has to efficiently recognise potential interesting interactions to allow for the investigations of rare, low cross section processes, for instance of high Q^2 interactions. In addition, the trigger controls the dead time of the detector, since the complete read-out of the detector takes some time in which no further events can be observed.

The trigger system is divided into four levels (L1 to L4). The first level trigger (L1) provides a decision in about 2 μs on whether an event should be kept or not. The basis are coarse detector information of fast availability, e.g. timing, energy sums, vertexing and event topology, which define trigger elements of individual subdetector components. These trigger elements are logically combined into 128 subtriggers. In the meantime, the total detector information is stored continously in a pipeline buffer. If any of the subtrigger conditions is fulfilled, the pipeline is stopped, and the event is passed to the second level trigger (L2). Here, the signals of different detector components can be connected to provide topological information about the event. The

full detector information is available on the next trigger level (L4), which performs a partial reconstruction of the whole event to verify the decision of the previous levels. The events accepted by L4 are written to tape with a typical rate of 10-20 Hz.

Finally, the accepted raw data are subject to the full event reconstruction. The events are classified according to different physics categories, what is also known as L5 classification.

The data are taken in so-called runs, which are time intervals of almost constant experimental conditions. A luminosity fill denotes the period between two HERA fillings of electrons or protons.

Triggering neutral current high Q^2 events

The triggering of neutral current high Q^2 events is mainly based on the prominent, localised energy deposition of the scattered electron in the LAr calorimeter.

The LAr calorimeter provides input to the central trigger by so-called big tower (BT) sums. The signals of the 44000 calorimeter read-out channels (pads) are merged into electromagnetic and hadronic trigger cells (TC) which consist of 16 and 4 pads, respectively. The signals of the trigger cells are combined into projective trigger towers (TT) and further into 256 big towers, which point to the interaction vertex [44, 55].

Important for the triggering of neutral current events are the LAr trigger elements LAr_electron_1 and LAr_electron_2 which are activated by an energy deposition above threshold in the electromagnetic section of a big tower. In the LAr barrel region, they have different thresholds of about 5 GeV for LAr_electron_1 and 3.5 GeV for LAr_electron_2. The thresholds are increased to about 30 GeV in the IF region to account for beam induced background.

The related subtriggers relevant for the present analysis are the following:

s67 is based the LAr_electron_1 trigger element and is the main and most efficient subtrigger for neutral current high Q^2 events. The high threshold of about 5 GeV in the LAr barrel allows relatively loose additional timing and veto requirements to activate this subtrigger. The timing condition can be supplied by the LAr calorimeter or by the central or forward tracking system.

s75 combines the LAr_electron_2 trigger element with the requirement of at least one high p_T track measured in the central tracking chambers.

s71 is mainly based on track information. The only LAr requirement is a deposit of at least 1 GeV (LAr barrel) in the direction of a prominent track found by the proportional chambers. Since the LAr condition is rather weak, this subtrigger can be considered as independent of the LAr trigger elements.

All these subtriggers require in addition timing information to determine the bunch crossing time and some veto conditions which are mainly based on timing information, e.g. by the veto walls or the time of flight system. A more detailed description of trigger elements and neutral current subtriggers is provided in [56].

The subtriggers s67 and s75 are used to trigger NC events while s71 serves as monitor trigger to determine the trigger efficiency (cf. section 6.3). These subtriggers

are not affected by prescale factors, which are introduced to reduce the high rates of some subtriggers in order to limit the dead time of the detector.

4.4 Monte Carlo Simulation

In order to measure a cross section of a given process, it is of absolute importance to understand the detector response in all aspects related to the measurement of this process. This is a non-trivial task for an apparatus as complex as the H1 detector. There are correlations between several detector effects and also physics influences, the detector acceptance depends on radiation effects, for instance. In addition, the detector contains by construction locally different amounts of dead material. Therefore, Monte Carlo simulations have been proven useful, which include the structure and functionality of the detector.

Event generation

The generation of DIS ep events is based on the prediction of the corresponding differential cross sections. High Q^2 neutral current DIS events are generated using the DJANGO program package [57] which is an interface of the programs HERACLES [15] and LEPTO [58]. The HERACLES program generates $ep \to e'X(\gamma)$ events including the Born process and the $\mathcal{O}(\alpha)$ QED radiative corrections (cf. section 2.3). The LEPTO program includes higher order QCD effects using the colour dipole model [59] as implemented in the ARIADNE program [60] for the description of parton showers. The Lund string fragmentation [61] as implemented in the JETSET program [62] is used to obtain the complete hadronic final state. Detailed investigations of these generators concerning HERA ep interactions can be found in [63, 64].

The events are generated using the out-dated MRSH proton parton density functions [65] and thus reweighted to the cross section prediction according to the parton densities of the H1 1997 PDF Fit [27] (cf. section 2.5). Each event is scaled by the ratio of the full NLO cross section calculated with the new parton density parameterisation to the cross section which has been used by the generator. It is worthwhile to note that both cross sections have to be evaluated according to the kinematics of the hard interaction at the hadron vertex where the parton densities actually enter the calculation.

The generated neutral current DIS high Q^2 events correspond to an integrated luminosity of $L = 165$ pb^{-1}. For $Q^2 > 500$ GeV^2 additional data set were generated, accounting to at least ten times the data luminosity.

The following processes were generated in order to predict the background contributions to the neutral current DIS events (cf. section 6.5): Photoproduction (γp) events are generated by the PYTHIA program [62] using the GRV LO parton densities [66] for the proton and the photon. The generation of elastic QED-Compton events is based on the COMPTON program [67]. Lepton-pair events are generated using the LPAIR generator [68, 69].

Simulation of the H1 detector

A detailed simulation of the H1 detector, H1SIM [70], has been implemented using the GEANT program package [71]. It contains the geometry and the material properties of the entire detector system. The parameters were determined in test beam measurements and optimised using real *ep* data.

The detector response is simulated for the generated events by tracking the generated particles through the detector. This step includes e.g. the generation of secondary particles and the shower development in the calorimeter material. In the standard simulation, called H1FAST [72], electromagnetic and hadronic showers are simulated using parameterisations of the shower shape which depend on averaged geometry and material information. For energy calibration and systematic studies Monte Carlo events were also simulated with the so-called detailed simulation, which accurately traces each particle track down to a minimal cut-off energy. In a second step, the response of the active detector components, e.g. sense wires and calorimeter cells, is simulated.

Finally, real data noise patterns of the LAr calorimeter and other detector components, which were recorded using a random trigger, are superimposed to the genuine physics signals. In addition, the trigger response is simulated to some extent.

The simulation is completed by subjecting the events to the same reconstruction program as the data.

Chapter 5

Event Identification and Reconstruction

In this chapter the event identification and reconstruction is described which provides the basis for an accurate cross section measurement.

Neutral current DIS events of large four momentum transfer Q^2 have the very clean signature of a prominent electromagnetic cluster in the LAr calorimeter caused by the scattered electron and a hadronic final state which compensates the transverse momentum of the electron. Since the kinematic quantities of the ep interaction are reconstructed solely from the scattered electron (cf. section 2.4), the electron identification as well as the precise measurements of the electron energy and scattering angle are essential for this analysis and will be explained in detail. The following items are discussed in this chapter:

- Determination of the interaction vertex.
- Electron identification.
- Reconstruction of the electron centre of gravity.
- Alignment of the LAr calorimeter.
- Electron angle measurement.
- Electron energy calibration.
- Measurement of the hadronic final state.

This chapter also deals with systematic uncertainties which are separated into a correlated and an uncorrelated part w.r.t. the cross section measurement. In addition to a good description of the data by simulation, this analysis focusses on the absolute precision of the measurements.

5.1 Introductory Remarks

Important properties of the detector performance and of the simulation relevant for this analysis are discussed.

5.1.1 Electromagnetic Shower Shapes

The Monte Carlo programs simulate the detector response of electromagnetic showers and consequently of electron cluster candidates in the LAr calorimeter with the so-called H1FAST option, using a parameterisation of the shower shape variables (cf. section 4.4).

Significant deficits between data and simulation have been observed in the description of transverse and longitudinal shower extensions and consequently of the energy density and the number of cells of electromagnetic clusters. The transverse and longitudinal dispersions of the electron cluster, σ_R and σ_L, are defined by

$$\sigma_R = \sqrt{< r^2 > - < r >^2} \;, \quad \sigma_L = \sqrt{< l^2 > - < l >^2} \;, \tag{5.1}$$

where

$$< x^n > = \frac{1}{\sum_i w_i} \sum_i w_i \, x_i^n \;, \quad w_i = \frac{E_i}{V_i}$$

is the n^{th} moment of the distance x between the shower centre of gravity and the cell i weighted by the cell energy density E_i/V_i. r and l represent the respective projections of x transverse and parallel to the shower axis. σ_R and σ_L are shown in figure 5.1 for the CB2 wheel. Since the shower size grows with increasing energy and since the

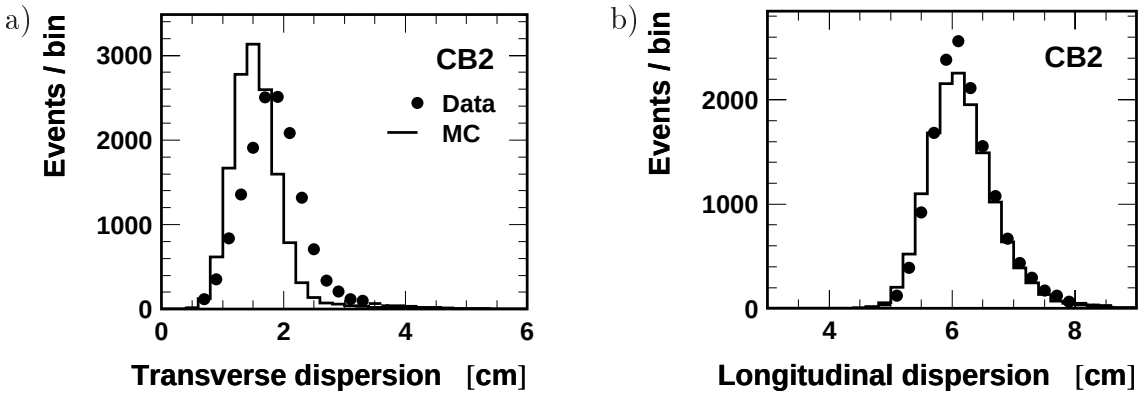

Figure 5.1: Comparison between data and simulation of transverse (a) and longitudinal (b) shower extensions of the electron cluster in the CB2 wheel.

wheels differ in geometry and slightly in material constants, table 5.1 quantifies the peak values and the widths of the transverse and longitudinal dispersions separately for each wheel of the barrel part of the LAr calorimeter. The disagreement between data and simulation in mean value and width of the transverse dispersion is at the 10% level. In the CB2 wheel it even reaches 20% for the mean and 30% for the width. Considerable deviations are also observed for the width of the distribution of the longitudinal dispersion. Compared to the real data, the simulated showers are significantly more compact, especially in the transverse direction.

The parameters which define the electromagnetic shower shapes in the simulation were tuned with test beam data and checked with real data just after the HERA start

Wheel	transverse dispersion						longitudinal dispersion					
	peak [cm]			width [cm]			peak [cm]			width [cm]		
	Data	MC	Δ[%]	Data	MC	Δ[%]	Data	MC	Δ[%]	Data	MC	Δ[%]
BBE	1.990	1.828	+8.9	0.528	0.467	+13.1	6.433	6.323	+1.7	0.711	0.666	+6.7
CB1	1.916	1.787	+7.2	0.482	0.434	+11.1	6.179	6.097	+1.3	0.480	0.521	−8.0
CB2	1.794	1.503	+19.4	0.449	0.346	+30.0	6.119	6.092	+0.4	0.445	0.485	−8.2
CB3	1.672	1.512	+10.6	0.359	0.317	+13.4	6.113	6.091	+0.4	0.516	0.540	−4.5
FB1+2	1.950	1.772	+10.1	0.440	0.376	+17.2	6.316	6.220	+1.5	0.708	0.739	−4.2

Table 5.1: Wheel-wise mean and width of the peak fits to the transverse and longitudinal dispersions for data and simulation (MC). For both dispersions, the typical precision of the mean (width) of the fit is $\lesssim 0.25\%$ ($\lesssim 1\%$) in BBE-CB2, $\lesssim 0.5\%$ ($\approx 2\%$) in CB3, and $\approx 1.5\%$ ($\approx 8\%$) in FB1+2. Δ denotes the relative difference between data and simulation.

up with low statistics. Recently, these parameters have been adjusted in a dedicated analysis [73] using the precise data available in the meantime. Since this investigation had not been completed during the data analysis period of this thesis, the old detector simulation is used for the present cross section measurement.

The differences of the electromagnetic shower shapes in data and simulation are identified and well understood. They mainly influence the electron cluster reconstruction and the energy calibration. However, both are performed individually for data and simulation. The corresponding systematic errors are under control as will be presented in the following sections.

5.1.2 Performance of the Tracking Chambers

The central drift chambers of the H1 detector measure the trajectories of charged particles providing trigger information and allowing momentum measurement, particle identification and the reconstruction of the primary vertex. Unfortunately, the CJC was not 100% operational in all sectors throughout the data taking period. The performance of the tracking system can be monitored with neutral current data events which are selected by requiring a scattered electron which is clearly identified by its cluster shape and event kinematics. Using the z and ϕ position of the electron cluster, the local performance of the tracking system is quantified by the fraction of electron clusters which have an associated track. Figure 5.2 shows the track link efficiencies separately for CJC1 and CJC2 versus ϕ as function of time. The average track link efficiency is about 95% for the combined central jet chambers, but there are data taking periods where broken wires prevented operation of complete sectors of the jet chamber.

The Monte Carlo simulation is performed with perfect tracking conditions. Since the defects of the tracking system are difficult to describe with the required accuracy, the tracking system is used in this analysis exclusively to reconstruct the primary interaction vertex.

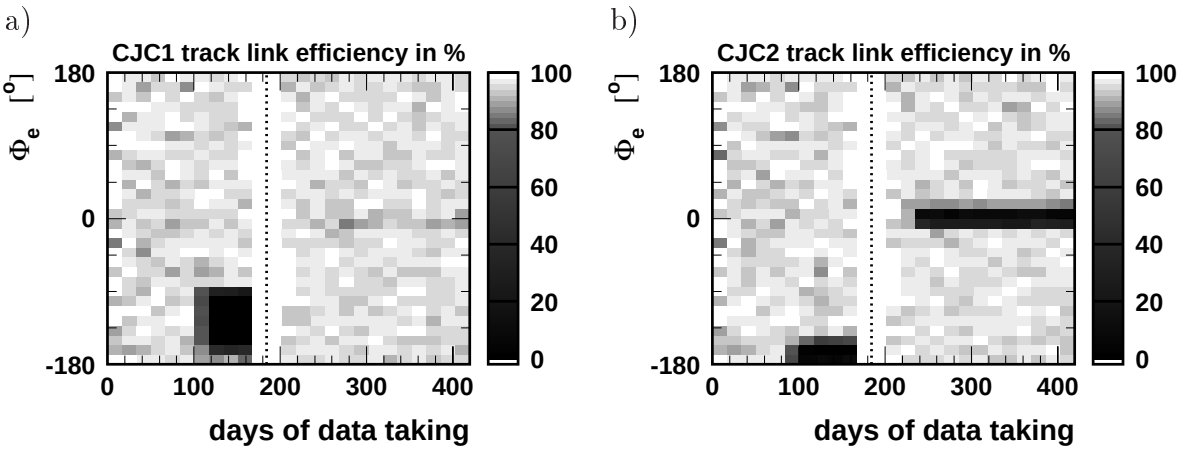

Figure 5.2: Electron track link efficiencies of the CJC1 (a) and CJC2 (b) chambers as function of electron azimuth angle ϕ_e and days of data taking. The 1999/2000 transition is marked by the dotted line.

5.2 Determination of the Interaction Vertex

The determination of the event interaction vertex is important for the precise reconstruction of the event kinematics and for the suppression of non-ep-collision background. In fact, the reconstruction of the event vertex enables a more precise determination of the event kinematics compared to using the average run vertex. There are also effects which depend indirectly on the z vertex position. For instance, the fiducial volume[1] definition relies on the impact point of the electron trajectory on the surface of the LAr calorimeter which is obtained by interpolation between the vertex and the electron cluster position (cf. section 6.3).

The interaction vertex is reconstructed with tracks from charged particles in the event which are measured with the tracking system of the H1 detector (cf. section 4.2.4). Figure 5.3 shows the z vertex resolution as obtained in simulation. The CJC

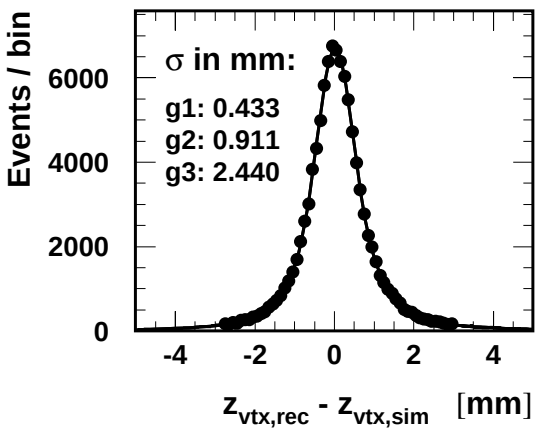

Figure 5.3: z vertex resolution of simulated events, obtained by comparing reconstructed and simulated z vertex positions. The sum of three Gaussian distributions (g) is fitted to the distribution, reflecting the dependence of the z vertex resolution on the contributing tracking detectors (CJC,CIZ,COZ). The corresponding widths are given and have an accuracy of about 2%.

[1] The fiducial volume defines the active volume of the LAr calorimeter and excludes inefficient LAr calorimeter trigger regions.

alone provides a single track z resolution of the order of 2.5 cm. For events with multiple tracks, the z vertex resolution scales approximately with $1/\sqrt{N_{track}}$. However, the majority of events have at least some tracks which generate hits in the z chambers (CIZ, COZ). Depending on whether only one or both z chambers contribute to the track measurements, the z vertex resolution is improved up to about 0.5 mm.

Since the CIZ and COZ chamber efficiencies are not accurately modelled within the simulation, differences in the z vertex resolution between data and simulation are expected. However, as investigated in [74], z vertex resolution effects are only of minor importance for the cross section result. In contrast, the description of the absolute z vertex distribution of the data by simulation is essential to obtain an accurate, unbiased cross section measurement. Furthermore, the simulation needs to reproduce the vertex finding efficiency of the data.

Vertex finding efficiency

The vertex finding efficiency is determined using a clean neutral current event sample. Apart from the primary vertex all neutral current selection cuts are applied (cf. chapter 6). In the case where no primary vertex has been found, the event quantities are calculated using the nominal vertex position at the origin of the H1 coordinates. In addition, the events have to be well balanced in longitudinal and transverse momentum to suppress non-ep-collision and photoproduction background. Events with two electron candidates are rejected to remove QED-Compton background. The vertex finding

N_e	$= 1$
$p_{T,calo}$	< 5 GeV
$50 < E - p_z$	< 60.5 GeV

Table 5.2: Additional selection requirements for the determination of the vertex finding efficiency.

efficiency of data and simulation is shown in figure 5.4 as function of y_Σ (cf. section 2.4). The lower the values of y_Σ, the more forward concentrates the hadronic activity, partly escaping the acceptance of the tracking system.

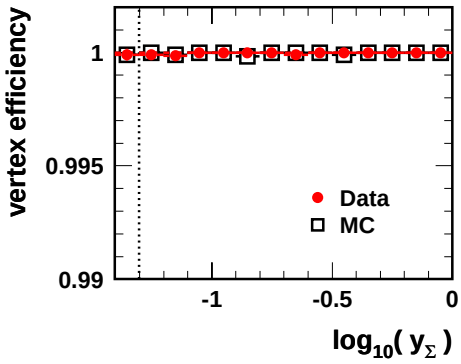

Figure 5.4: Vertex finding efficiency as function of y_Σ. The dotted line indicates the $y = 0.05$ lower limit of the cross section measurement.

The primary interaction vertex is found reliably in the entire kinematic range of the present cross section measurement. The inefficiency is certainly below 0.1% and thus negligible.

Most of the events have a reconstructed track associated with the scattered electron which solely could determine the primary vertex. However, since the primary vertex is reconstructed from the tracks of all charged particles in the event, including those of the hadronic final state, a very efficient reconstruction of the event vertex is achieved even in the case where no electron track has been measured. The hadronic final state is broadly distributed within a cone of typical radius of one in the pseudorapidity-azimuth plane[2] which is in general larger than the local inefficiencies of the tracking system. In addition, the $y > 0.05$ requirement keeps at least part of the activity of the hadronic final state within the acceptance of the central tracking system. In fact, more than 99.8% of the data events have a primary vertex reconstructed with at least one track from the CJC. The remaining events rely on the vertex reconstruction using the forward tracking system. In 0.7% of the data events, the primary vertex is determined solely from the electron track.

The primary vertex efficiency is stable throughout the total running period and independent of the position of the scattered electron. It has been verified, that the vertex efficiency is not affected by the varying experimental conditions of the central tracking system.

Shape of the z Vertex Distribution

The z vertex distribution is spread out around the nominal interaction point due to extended bunches of the proton beam. The mean z vertex position changes in time and in general with each machine fill depending on the beam settings of the accelerator. For fixed beam conditions, the z vertex distribution is approximately Gaussian.

The Monte Carlo events are simulated with a Gaussian z vertex distribution of fixed width centred at the nominal interaction point. The simulation is reweighted to the z vertex distribution of the data, preserving the overall normalisation of the Monte Carlo sample. To account for correlations with other time dependent detector effects, the reweighting is performed separately for each of the five run ranges in which the data are split (cf. section 6.2). Figure 5.5 shows the results for each period. Figure 5.6 displays the overall z vertex distribution of data and simulation after the adjustment. Also shown is the corresponding ratio between data and simulation. Apart from an overall shift in the normalisation, the simulation reproduces the z vertex distribution of the data well.

In summary, the Monte Carlo simulation provides a good description of the reconstruction of the primary interaction vertex.

[2] $R = \sqrt{\Delta\eta^2 + \Delta\phi^2} = 1$

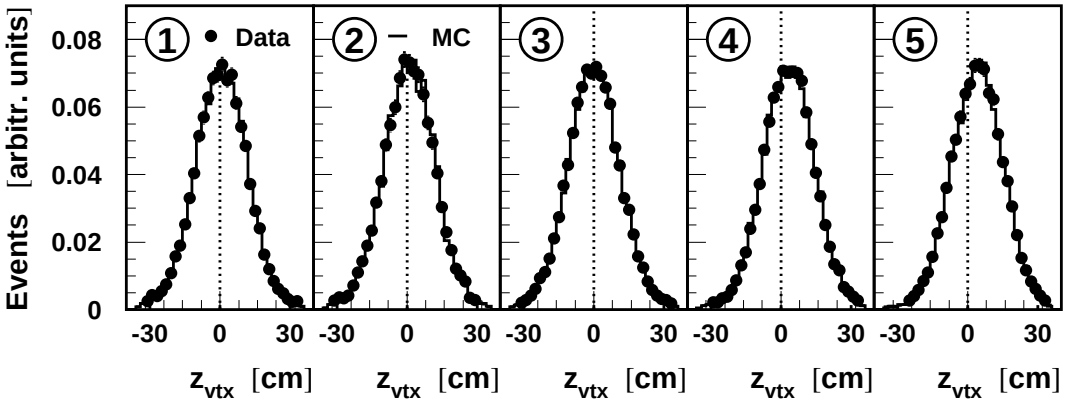

Figure 5.5: Shape of the z vertex distributions for data and simulation after the z vertex reweighting of the simulation. The distributions are shown for each of the five run ranges of different experimental conditions (cf. table 6.2).

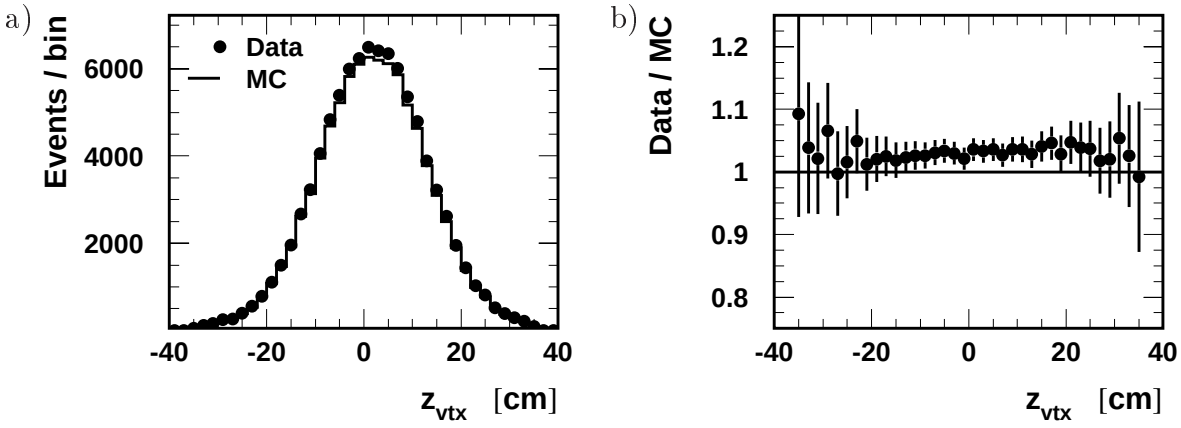

Figure 5.6: a) The z vertex distribution for data (full points) and simulation (histogram) after the z vertex reweighting. The simulation is normalised to the luminosity of the data. The ratio data to simulation is shown in (b).

5.3 Electron Identification

In neutral current events with large momentum transfer $Q^2 \gtrsim 150$ GeV^2, electrons are scattered into the acceptance of the LAr calorimeter. The electron identification is based solely on calorimeter information and benefits from the fine granularity of the LAr calorimeter. Electron candidates are identified as isolated and compact electromagnetic energy clusters of well defined shower shape. The electron finding algorithm QECFWD [75] is used for this analysis and briefly described in the following.

An initial candidate is defined by a cone of 7.5° around any prominent energy cluster. The cone starts one meter in front of the cluster on the line connecting the interaction vertex with the centre of gravity of the cluster. The candidate consists of all cells of the electromagnetic section and the first layer of the hadronic section within this cone.

To allow a clean separation from hadronic activity, electron shower estimators are

Estimator	Description	Requirement
ETOT	total energy	> 8 GeV
NCEL	number of cells	> 3
EAEM	energy fraction in first 2 layers (3 in IF) of the electromagnetic section	$> 0.94 + 0.05 \cos(2\theta_0)$
EAHN	energy fraction of N most energetic cells, N=4(BBE-CB2),8(CB3-FB2),12(IF)	$> f(\theta_0)$, cf. figure 5.7a
EATR	transverse dispersion [cm]	$< f'(\theta_0)$, cf. figure 5.7b
EAIF	energy fraction in isolation cone ($R = 0.25$) carried by electron candidate	> 0.95
EAHD	hadronic energy in isolation cone	< 300 MeV or EAIF > 0.98

Table 5.3: Electron identification requirements based on cluster estimators as used by QECFWD. f and f' are functions shown in figure 5.7 and depend on the cluster polar angle θ_0 calculated with the nominal interaction point position.

introduced as described in table 5.3. The electron candidates are required to meet the following conditions: There must be a prominent energy deposition in the calorimeter (estimators ETOT, NCEL) to separate from random noise and low energetic hadrons. As expected for electromagnetically interacting particles, the shower has to develop early in the calorimeter and deposit most of its energy in the electromagnetic section[3] (EAEM). The cluster has to be compact both in the longitudinal and transverse directions (EAHN, EATR). Finally, the electron candidate is tested for calorimetric isolation w.r.t. energy depositions behind and around the electron candidate within a cone of $R = 0.25$[4] (EAIF, EAHD). The isolation requirement suppresses the neutral pion contribution in the hadronic final state.

The requirements on the shower shape of the electron candidate are detailed in table 5.3. The cut functions f and f' of EAHN and EATR are shown in figure 5.7.

Due to the improper simulation of the electromagnetic shower shape (cf. section 5.1.1), estimators which are sensitive to the shower extension have been carefully studied. Largest differences are observed in the transverse dispersion (estimator EATR), which was already shown in figure 5.1 for the CB2 wheel. However, as can be seen from the data distributions in figure 5.7b, the requirement imposed on the estimator EATR provides some safety margin. The fraction of simulated neutral current events affected by the cut is small and in general amounts to less than 0.5%. Small differences between data and simulation in the distribution of the estimator EAHN can also be attributed to the different shower shape descriptions.

In summary, the electron finding algorithm is optimised to provide an efficient electron recognition. Background contributions passing the electron identification are

[3] In the electromagnetic section of the LAr calorimeter, the radiation length X_0 corresponds to about 1.6 cm. The first two layers (three in IF) correspond to about 10-15 X_0 depending on the polar angle.

[4] The distance $R = \sqrt{\Delta\eta^2 + \Delta\phi^2}$ is defined in the η-ϕ plane with $\eta = -\ln(\tan\frac{\theta}{2})$.

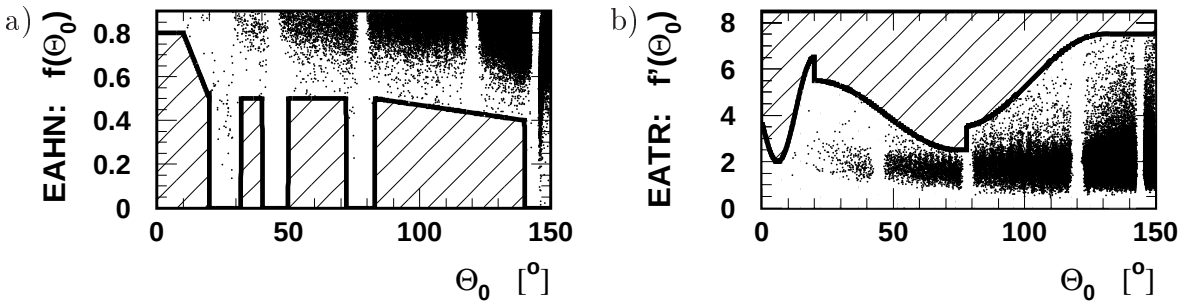

Figure 5.7: Polar angle dependent cluster shape requirements of the electron identification on the electron shower estimators EAHN (a) and EATR (b), cf. table 5.3. θ_0 denotes the polar angle of the electron candidate w.r.t. the nominal interaction point. Also shown are the entries of the data used for the cross section measurement. Electron candidates with estimator values in the hatched regions are rejected.

rejected by kinematical requirements. Therefore, the demands on single estimators are relatively loose. High separation power is achieved by the sum of all estimators. Thus, the electron identification remains rather independent of the detailed description of the electron shower by simulation.

The systematic uncertainty due to the different description of the shower shapes is included in the errors quoted for the overall efficiency. The systematic error is increased for $z > 0$ cm, corresponding to $\theta_0 < 90°$, where the data distribution of the transverse dispersion comes closer to the cut boundaries (cf. figure 5.7b).

All other electron shower estimators of the data are well described by the simulation. As an example, figure 5.8 shows the energy fraction in the first layers of the calorimeter and the electron cluster contribution to the total energy in an isolation cone around the electron candidate.

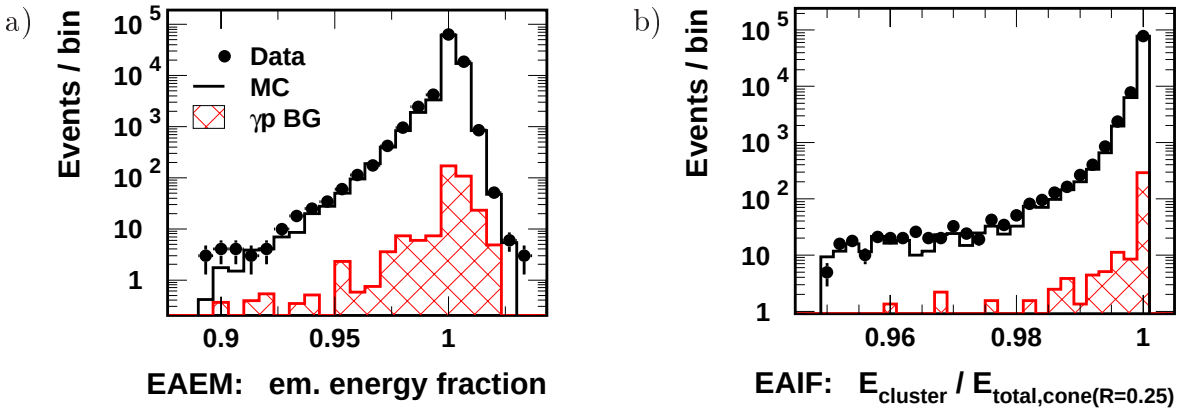

Figure 5.8: Examples of calorimeter cluster estimators used for the electron identification. a) shows the electromagnetic energy fraction, b) the ratio of the electron cluster energy to the total energy in an isolation cone with $R = 0.25$ around the electron.

The electron identification provides a clean sample of events which have a compact energy deposition in the LAr calorimeter which most likely originates from an electromagnetically interacting particle. In case of multiple electron candidates, the scattered electron is taken to be the candidate with the highest transverse momentum.

For an accurate cross section determination, the simulation has to describe the electron finding efficiency of the data.

Electron finding efficiency

The electron identification is based on cluster shape estimators to distinguish a pure electromagnetic interacting particle from hadronic activity. To study the efficiency of the electron finding algorithm, a track based electron finder is used which is independent of any details in the cluster shape.

The cone jet algorithm PXCONE [76, 77] is applied with radius $R = 0.5$ and minimum transverse energy $E_T = 5$ GeV to identify all jet-like calorimeter clusters in the event without any previous classification of electron candidates or the hadronic final state. If at least two jets are found, the two jets of highest p_T are investigated for tracks of basic quality within an isolation box of $\Delta\eta = 1$ and $\Delta\phi = 90°$ in the η-ϕ plane around the respective jet. This box definition is motivated by the topology of neutral current events, where in leading order α_s the hadronic final state is located opposite to the electron in the transverse plane. In addition, typical hadronic jets have an extension of one in the η direction. A jet is classified as electron jet candidate if there is exactly one track found in the isolation zone of this jet. The electron jet is treated as a normal electron candidate and inherits all kinematic quantities from the energy clusters of the jet.

Since cluster shape information cannot be used to suppress hadronic backgrounds, relative stringent requirements are imposed to define a very clean data sample as monitor. The selection is summarised in table 5.4. The kinematic range is restricted to

E_{ejet}	> 11 GeV
y_{ejet}	$\in [0.05; 0.9]$
$D_{jet,track} = \sqrt{\Delta\eta^2 + \Delta\phi^2}$	< 0.2
$\lvert\frac{1}{p_{T,ejet}} - \frac{1}{p_{T,track,ejet}}\rvert$	< 0.02
$N_{track,opposite\ ejet}$	> 1
$E - p_z$	> 35 GeV
$p_{T,calo}$	< 20 GeV
no background found by topological cosmic and halo finders	

Table 5.4: Selection to define the monitoring data sample for the determination of the electron identification efficiency. The subscript 'ejet' denotes electron jet variables.

that of the final analysis. The track of the electron jet is required to match within errors the calorimeter depositions in η and ϕ directions as well as in transverse momentum p_T. There must be at least two tracks associated with the jet in the opposite hemisphere to represent hadronic activity. This favours events with clean topology of

(leading order α_s) neutral current interactions and rejects e.g. QED-Compton backgrounds. Further background rejection is achieved by the use of halo and cosmic muon topological pattern finders (cf. section 6.5). The remaining background contribution is negligible ($\lesssim 0.2\%$) as found from simulation.

The electron finding efficiency for data and simulation is displayed in figure 5.9 as function of the z and ϕ impact position of the electron jet on the surface of the LAr calorimeter. In general, the efficiency is very high reaching 98% and above in the

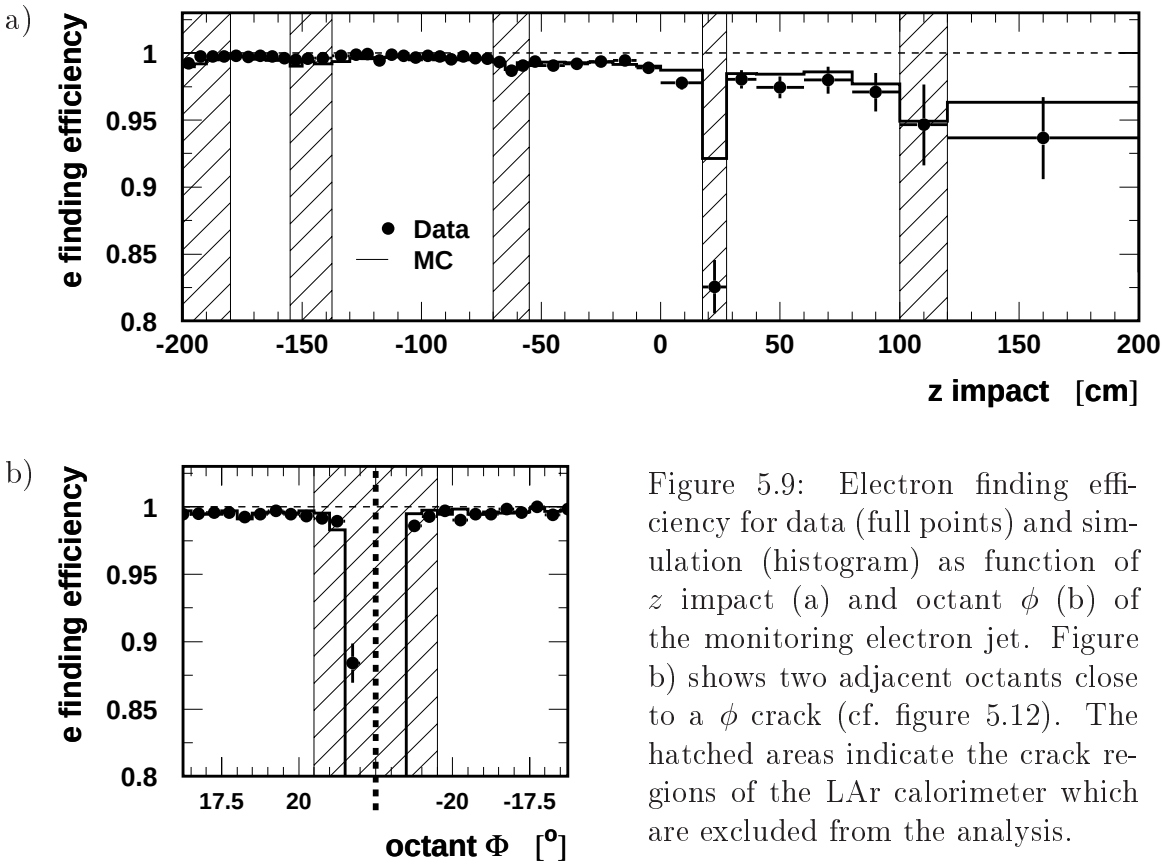

Figure 5.9: Electron finding efficiency for data (full points) and simulation (histogram) as function of z impact (a) and octant ϕ (b) of the monitoring electron jet. Figure b) shows two adjacent octants close to a ϕ crack (cf. figure 5.12). The hatched areas indicate the crack regions of the LAr calorimeter which are excluded from the analysis.

central barrel region. In the vicinity of the z and ϕ cracks of the LAr calorimeter, the electron identification is less efficient. In these regions, the electron has to pass inactive material from the support structure of the calorimeter. In the ϕ cracks and in the z crack between the CB2 and CB3 wheels, the electron may even enter the hadronic section without prior interactions. The coarse granularity of the hadronic part of the LAr calorimeter does not allow an efficient separation of electromagnetic particles from hadronic activity. Therefore, the z and ϕ crack regions are excluded from the cross section analysis[5] as indicated in figure 5.9.

In the remaining fiducial volume, the electron identification efficiency observed for data is well described by the simulation within the statistical uncertainty. However,

[5]The rear part of BBE ($z < -180$ cm) and the z cracks between BBE/CB1 ($z \approx -150$ cm) and CB1/CB2 ($z \approx -60$ cm) are excluded mainly due to uncertainties in the position determination and due to the deterioration of the electron energy resolution.

for $z > 0$ cm, the data tend to lie systematically below the Monte Carlo prediction. This small effect may be attributed to the dependence of the electron finder estimator EATR (cf. table 5.3) on the different shower shapes in data and simulation.

Thus, the systematic error on the electron identification is assigned to be 0.5% for $z_{imp} < 0$ cm and 2% for $0 \leq z_{imp} < 100$ cm.

Due to the tracking requirement the electron jet finder can be used to monitor the original electron finder only in the angular range covered by the central tracking device. For the more forward region of electron impact position $z_{imp} > 100$ cm, the electron identification has to rely mainly on the predictions of the simulation. The corresponding systematic uncertainty is taken from [16] to be 2%.

In addition, simulated neutral current events have been used to check the reliability of the electron identification. In less than 0.2% of the events a cluster of the hadronic final state is misidentified as the scattered electron.

Additional Electron Isolation

The preceding electron identification already yields electrons of high purity. However, there is still background mainly from photoproduction processes where typically a neutral pion cluster is misidentified as an electron. These events often show additional energy around the electron candidate arising from the hadronic final state contribution. To reduce this background, the electron cluster is required to fulfil additional isolation. In a cone with $R = 1$ around the electron, the transverse energy sum $E_{T,had,cone(e)}$ of calorimetric depositions apart from the electron candidate is allowed to be at maximum 10% of the electron transverse momentum $p_{T,e}$. Figure 5.10 shows the ratio $E_{T,had,cone(e)}/p_{T,e}$ for data, simulation and γp background. As obtained from simulation, the isolation requirement reduces the background contribution from 1.0% to below 0.4%. The rejected events are found over the entire polar angular range and predominantly at high y as expected for γp background.

In the data, 3.7% of the events are rejected by the isolation cut. Correcting the data for background contributions as obtained from simulation, the inefficiency imposed by this cut is 3.3% in the data compared to 3.5% in simulated NC events.

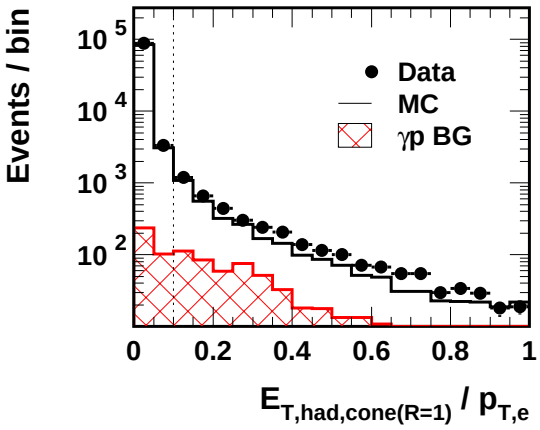

Figure 5.10: Distribution of transverse energy $E_{T,had,cone(e)}$ in a cone with $R = 1$ around the electron normalised to the transverse momentum $E_{T,had,cone(e)}/p_{T,e}$ of the electron. The additional isolation cut is indicated by the dotted line. Simulations of neutral current events (MC) and photoproduction background (γp BG) are normalised to the luminosity of the data.

This requirement strongly reduces the photoproduction background and causes only minor signal inefficiencies. In fact, the background rejection power is compatible to that of the requirement of a track associated with the cluster.

Differences between data and simulation are accounted for in the systematic uncertainty on the remaining background contribution (cf. section 6.5).

Electron Track Requirement

With the preceding electron identification and after standard kinematic constraints (cf. chapter 6), neutral current events have a clear signature and very low background contamination in the central detector region.

Since about 30% of the background events have a track linked to the electron candidate, an additional track requirement would not further reduce the background significantly enough to compensate for the difficulties introduced by a track link requirement.

In the forward detector region, where a track measurement may help to distinguish scattered electrons from photons originating from the hadronic final state, the tracking system doesn't provide sufficient information for a reliable track reconstruction. Due to the large amount of inactive material in front of the forward tracker, secondary tracks are caused by photon conversion. In addition there are many fake tracks originating from hadronic interactions.

The background contribution is nevertheless small because the kinematic requirement of $y_e < 0.9$ implies large energies for electrons scattered into the forward part of the detector (cf. equation 2.25). These electron energies are much larger than typical energies from photons originating from the hadronic final state or competing processes. This kinematic constraint ensures sufficient electron identification efficiency also in the forward region.

Thus, neutral current events are selected without requiring a track associated with the electron cluster.

5.4 Reconstruction of the Electron Centre of Gravity

The precise measurement of the electron scattering angle is important both for the reconstruction of the kinematics and for the reliable definition of the fiducial volume of the detector. In the usual neutral current high Q^2 analyses of the H1 experiment [16, 27, 78], the electron angle θ_e is measured by the positions of the electron cluster in the LAr calorimeter and the z vertex. ϕ_e is taken from the track which is required to be associated with the electron candidate.

Since there is no electron track link required in this analysis, both electron angles θ_e and ϕ_e have to be reconstructed from electron cluster information of the LAr calorimeter. This section presents the procedure to achieve an accurate measurement of the electron cluster centre of gravity position in the ϕ and z directions.

The cluster position has to be reconstructed from the cells of the LAr calorimeter containing energy depositions from the electron shower. In general, the centre of gravity is defined as the weighted sum of single cell contributions,

$$\vec{x} = \frac{\sum\limits_{cells} w_i \, \vec{x}_i}{\sum\limits_{cells} w_i} \ , \tag{5.2}$$

where the vector $\vec{x}_i$ is the cell position, typically the cell centre. w_i is a weighting function depending on the energy E_i or the energy density E_i/V_i of the cell deposition.

The cells represent the smallest units of the LAr calorimeter and have a typical size in the central barrel part of about 7.5 cm along z and of 10(5) cm in the CB1/2(CB3) wheels in the ϕ direction. Table 5.5 gives parameters of the electromagnetic section of the LAr calorimeter and basic material constants. The mean extension of a cell D is

LAr calorimeter, electromagnetic section				
			Wheel	D/R_M
R_M	$\simeq$	3.6 cm	CB1/2	2.4
X_0	$\simeq$	1.6 cm	CB3	1.4
E_c	$\simeq$	9.5 MeV	FB1/2	1.8
λ_I	$\simeq$	31 cm	IF	1.0

Table 5.5: Parameters of the electromagnetic section of the LAr calorimeter [79]. R_M, X_0, E_c and λ_I denote the mean Molière radius, radiation length, critical energy and interaction length, respectively, D is the mean extension of the cells, related to the mean surface D^2.

comparable or even larger than the Molière radius R_M, which is a typical measure of the transverse extension of electromagnetic showers initiated by electrons or photons. Thus, an electromagnetic particle deposits its energy in a few cells only and one expects effects of the granularity on the measurement of the cluster position.

To good approximation, the average transverse energy profile of an electromagnetic shower can be described by the superposition of two Gaussian distributions, representing the compact core of the shower and a contribution from the shower tails [80]. When moving the mean of a Gaussian energy distribution across the intersection of two cells as sketched in figure 5.11, the energy fraction in one cell is given by a tanh-like function. A centre of gravity of a shower calculated with equation 5.2, using a weight w_i proportional to the cell energy E_i, shows a tanh-like correlation between the reconstructed position and the true location. In case of a large fraction of the shower energy deposited in a single cell, the centre of gravity is reconstructed close to the centre of that cell and the true position cannot be properly measured. As the true shower position moves closer to the border of the cell, sufficient energy is shared between the cells and the position becomes measurable.

The standard reconstruction of the electron cluster position uses the cell weight $w_i = \sqrt{E_i}$ to calculate the cluster centre of gravity (cf. equation 5.2), which to some extent

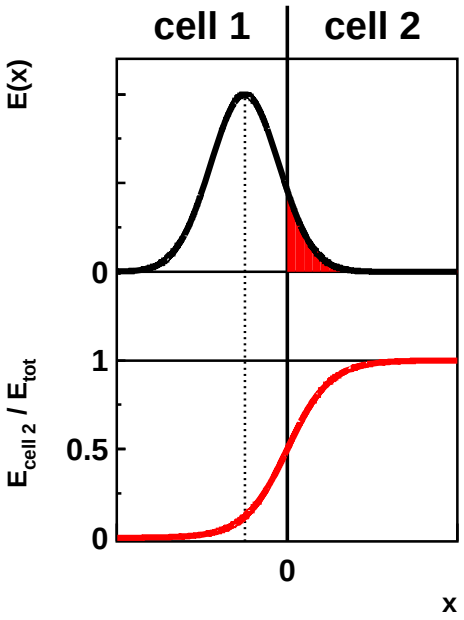

Figure 5.11: Sketch of moving a Gaussian energy distribution across the boundary of cells 1 and 2 (upper part). The energy deposited in cell 2 is filled red, and the energy fraction recorded in cell 2 is shown as function of the mean value x of the Gaussian by the red tanh-like curve (lower part).

favours the tail contributions. Nevertheless, both the ϕ and the z measurements show a pronounced tanh-like behaviour and systematic shifts of the reconstructed position compared to the true one, as demonstrated in the following subsections.

There have been attempts to improve the reconstruction by applying a logarithmic weighting function which further enhances low energetic contributions. The logarithmic weighting solution of the form $w_i = c + \log(E_i/E_{tot})$ is successfully applied in the Spacal calorimeter. In the LAr calorimeter only minor improvements are observed.

Methods which provide a considerable reduction of the core contribution imply a strong dependence on the low energy cells at the border of a cluster and are therefore sensitive to low energy fluctuations and noise.

This analysis pursues an alternative approach to reconstruct the electron position:

1. At first, a temporary centre of gravity is calculated in the standard way of equation 5.2 using a weight which yields a strong correlation between reconstructed and true positions.
2. The correlation is parameterised by a tanh-like ansatz and used in a second step to correct the temporary position.

The correction procedure is applied in the barrel part of the LAr calorimeter only. In the very forward direction (IF) the centre of gravity is determined solely from the $w_i = \sqrt{E_i/V_i}$ weighted cell positions. This weight is more intuitive than the original $w_i = \sqrt{E_i}$ weight, since the energy density considers the different cell sizes of different layers. In addition Monte Carlo investigations revealed a slightly improved spatial resolution compared to the original $\sqrt{E_i}$ weight. It is also not necessary to apply any further correction in the IF region. The transverse shower profile extends over many cells, since the granularity improves while the shower size increases due to higher electron energies. In addition, there is no precise reference position available, since the IF region is beyond the acceptance of the CJC.

Motivated by the cell geometry of the LAr calorimeter the corrections are determined separately for the ϕ and z directions. Correlations between both directions have been studied and found to be negligible.

The reference position for the correction is taken from vertex fitted tracks associated with the electron cluster. The tracks are extrapolated to the temporary cluster position, considering the curvature in the magnetic field. The track requirements which assure a precise reference position are listed in table 5.6. They select a track of good quality

I	radial track length	l_{track}	$>$ 20 cm	
II	track-cluster match	$\left\lvert \frac{1}{p_{T,track}} - \frac{1}{p_{T,cluster}} \right\rvert$	$<$ 0.02	
III	track isolation	$p_{T,other\ tracks,R=1}/p_{T,track}$	$<$ 10%	
IV	z chambers contribute	$N_{hit,CIZ}$ and $N_{hit,COZ}$	$>$ 1 each	(for z only)

Table 5.6: Selection requirements for the electron tracks which provide the reference position for the correction of the electron centre of gravity.

(I) which definitely belongs to the scattered electron (II,III). For the z reference, both z chambers are needed to provide sufficient precision (IV). Events with final state radiation are suppressed (II) to guarantee that the track points exactly to the cluster.

5.4.1 The ϕ Reconstruction

In the ϕ direction the LAr calorimeter is composed of eight identical octant stacks. Within each octant, the angle ϕ_{octant} is defined according to figure 5.12. All octants are mapped on top of each other and ϕ_{octant} is the remaining azimuthal angle. As sketched in figure 5.12, the cells of different layers are perfectly projective for all wheels in the LAr calorimeter barrel. Different are the number of cells per octant, eight in the BBE-CB2 and 16 in the CB3-FB2 wheels, and the layer structure (cf. figure 4.4).

For electromagnetic clusters with a transverse extension being smaller or comparable to the cell size, the correlation between $\phi_{cluster}$ and ϕ_{track} is sketched in figure 5.13

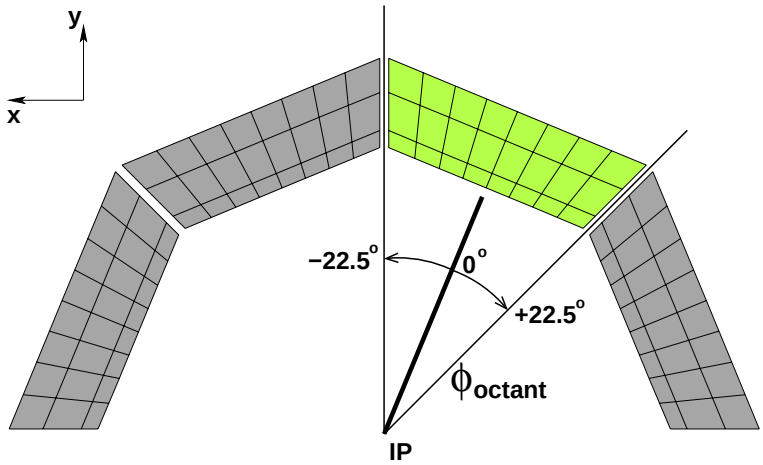

Figure 5.12: Cross section in the (x, y) plane of the electromagnetic section of the LAr calorimeter CB2 wheel (upper half part only). The octant ϕ definition is sketched for an exemplary octant, starting with $\phi_{octant} = 0°$ at the centre of an octant and reaching the ϕ crack centres at $\pm 22.5°$. IP is the nominal interaction point.

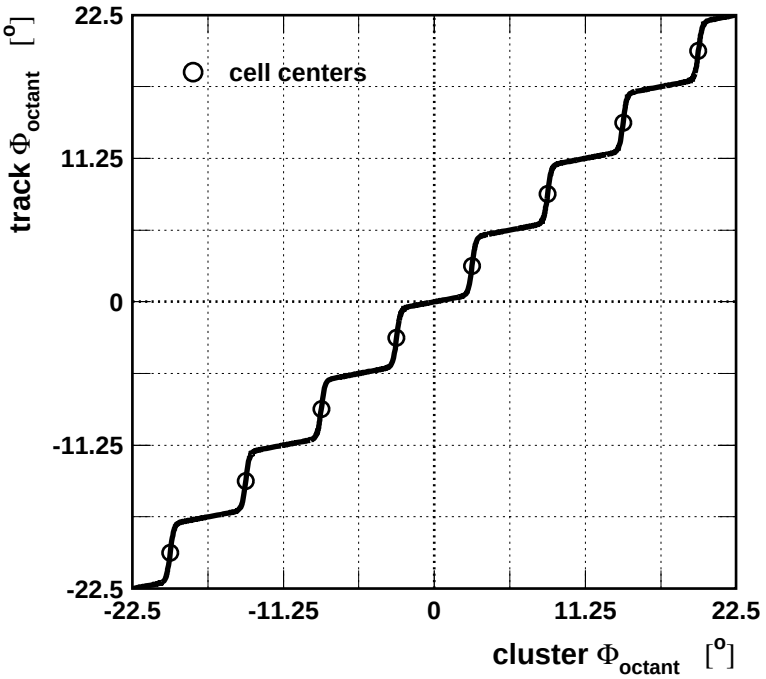

Figure 5.13: Sketch of the correlation between $\phi_{cluster}$ and ϕ_{track} as expected in the BBE-CB2 wheels. The cell centres are marked by circles, the cell boundaries by the grid.

as an example for the BBE-CB2 wheels which have eight cells per octant. Each of the eight cells within an octant contribute with a tanh-like relation. The position of a shower entering at the intersection of two cells can be reconstructed accurately (small slope) since the energy is almost evenly distributed between the two cells. However, particles which hit the calorimeter in the vicinity of the centre of a cell deposit their energy mainly in a single cell and are always reconstructed close to the cell position (steep slope). In this case, small energy depositions in the neighbouring cells cannot contribute strong enough to provide a good correlation.

Standard cluster ϕ reconstruction

For the standard reconstruction of the electron centre of gravity, using the $w_i = \sqrt{E_i}$ cell weight, the correlation of $\phi_{cluster} - \phi_{track}$ versus $\phi_{cluster}$ is displayed in figure 5.14 for data and simulation in the CB2 wheel.

The maximum difference of $\phi_{cluster} - \phi_{track}$ is larger in the Monte Carlo events which is due to the different transverse shower extensions in data and simulation.

Furthermore, the data show an overall sine-like modulation while the simulation is flat. This structure may indicate towards a small defect in the geometry description of the real calorimeter, where cells close to the centre of an octant seem to be a little compressed. Since this effect is found to be identical in all octants, it cannot depend on the alignment of the LAr calorimeter w.r.t. the tracking detectors. Moreover, the cool-down of the calorimeter to LAr temperature (cf. section 5.5) seems to be excluded from causing this effect, since radial and transverse contractions should compensate each other in ϕ. The origin of this effect is unknown.

This type of $\phi_{cluster} - \phi_{track}$ versus $\phi_{cluster}$ correlation is observed almost identically also for the other wheels of the LAr barrel. The only change is the doubling in

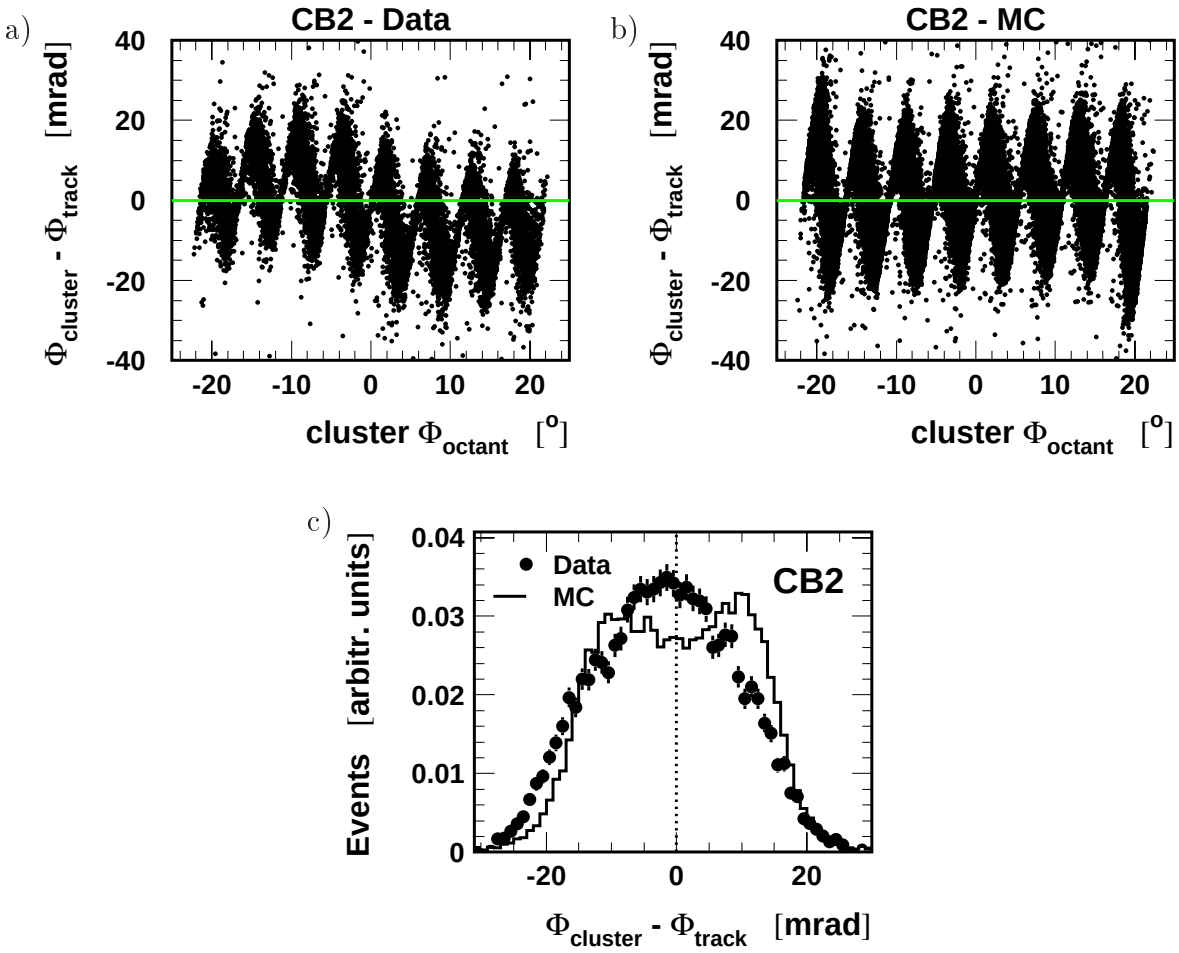

Figure 5.14: Correlation between cluster and track ϕ measurements for data (a) and simulation (b) in the CB2 wheel using the standard $\phi_{cluster}$ reconstruction. c) contains the respective projections of a) and b) onto the y axis.

periodicity for the CB3 and FB wheels, which contain 16 instead of eight cells per octant. Despite the fine granularity, the effect is still sizeable in these wheels. Otherwise, only small differences are found between the wheels which can be attributed to the enlargement of the shower extension with increasing energy.

Figure 5.14c shows the projection of the ϕ correlation for the CB2, revealing the poor resolution of the standard calorimetric ϕ reconstruction. The cluster ϕ resolution is quantified in table 5.7 (left column) in terms of the rms values for all wheels of the LAr barrel and for data and simulation.

Improved ϕ reconstruction method

In the correction procedure of this analysis, the temporary $\phi_{cluster}$ is determined using the linear weight $w_i = E_i/V_i$ of the cell energy density. This provides a strong correlation and offers the advantage of being independent of the shower development in the radial or z directions. The resulting correlations are shown in figure 5.15 for all

LAr wheel	rms of $\phi_{cluster} - \phi_{track}$ in [mrad]			
	standard reco.		new procedure	
	Data	MC	Data	MC
BBE	8.58	9.90	7.81	9.07
CB1	10.46	10.82	6.76	7.88
CB2	11.09	11.21	6.69	7.22
CB3	7.07	4.29	2.86	2.86
FB1/2	4.21	4.46	3.49	4.19

Table 5.7: Wheel-wise resolution of the electron cluster ϕ measurement for data and simulation using the standard reconstruction of the cluster centre of gravity (columns 2,3) and the new correction procedure (columns 4,5).

wheels of the barrel. The overall properties are identical to those already discussed for the standard reconstruction. However, the linear weight provides steeper dependences, especially close to the cell centres.

The correlations are parameterised as function of the temporary $\phi_{cluster}$ coordinate, ϕ_{temp}, using a tanh ansatz for each cell i described by the following parameters (cf. figure 5.13):

P^{const} : overall vertical shift w.r.t. track ϕ, corresponds to the alignment of the wheel regarding rotation around the z axis.

P^{shift} : overall horizontal shift w.r.t. cluster ϕ, accounts for bias between positive and negative octant ϕ.

P_i^{slope} : slope of the asymptotic part of the tanh at the cell borders.

P_i^{height} : offset provided by the tanh, i.e. distance between asymptotes.

P_i^{stretch} : stretch/squeeze of the tanh, yields (together with P_i^{slope}) the slope of the tanh at the cell centre.

P_i^{centre} : zero crossing of the tanh function, representing the cell centre.

Exploiting the symmetry in octant ϕ w.r.t. the centre of an octant, the cell-wise parameters are governed by the constraints[6]

$$\begin{aligned} P_i^{\text{height}} &= P_{n_{oct}-i}^{\text{height}} , \\ P_i^{\text{stretch}} &= P_{n_{oct}-i}^{\text{stretch}} , \\ P_i^{\text{center}} &= -P_{n_{oct}-i}^{\text{center}} , \end{aligned} \tag{5.3}$$

with n_{oct} as largest cell number in the ϕ direction within an octant, i.e. 7 for BBE-CB2 and 15 for CB3-FB2. The slope parameters are found to be identical for all cells, leaving 15 (27) parameters for each of the BBE-CB2 (CB3-FB2) wheels. The final correction functions have the following form:

$$\begin{aligned} \phi_{final} &= P^{\text{const}} + P^{\text{slope}} \cdot \phi_{temp} \\ &\quad + \sum_{i=0}^{n_{oct}} P_i^{\text{height}} \cdot \tanh\Big[P_i^{\text{stretch}} \left(\phi_{temp} - P^{\text{shift}} - P_i^{\text{center}} \right) \Big] \ . \end{aligned} \tag{5.4}$$

[6]The cell numbering starts with 0 at lowest octant ϕ.

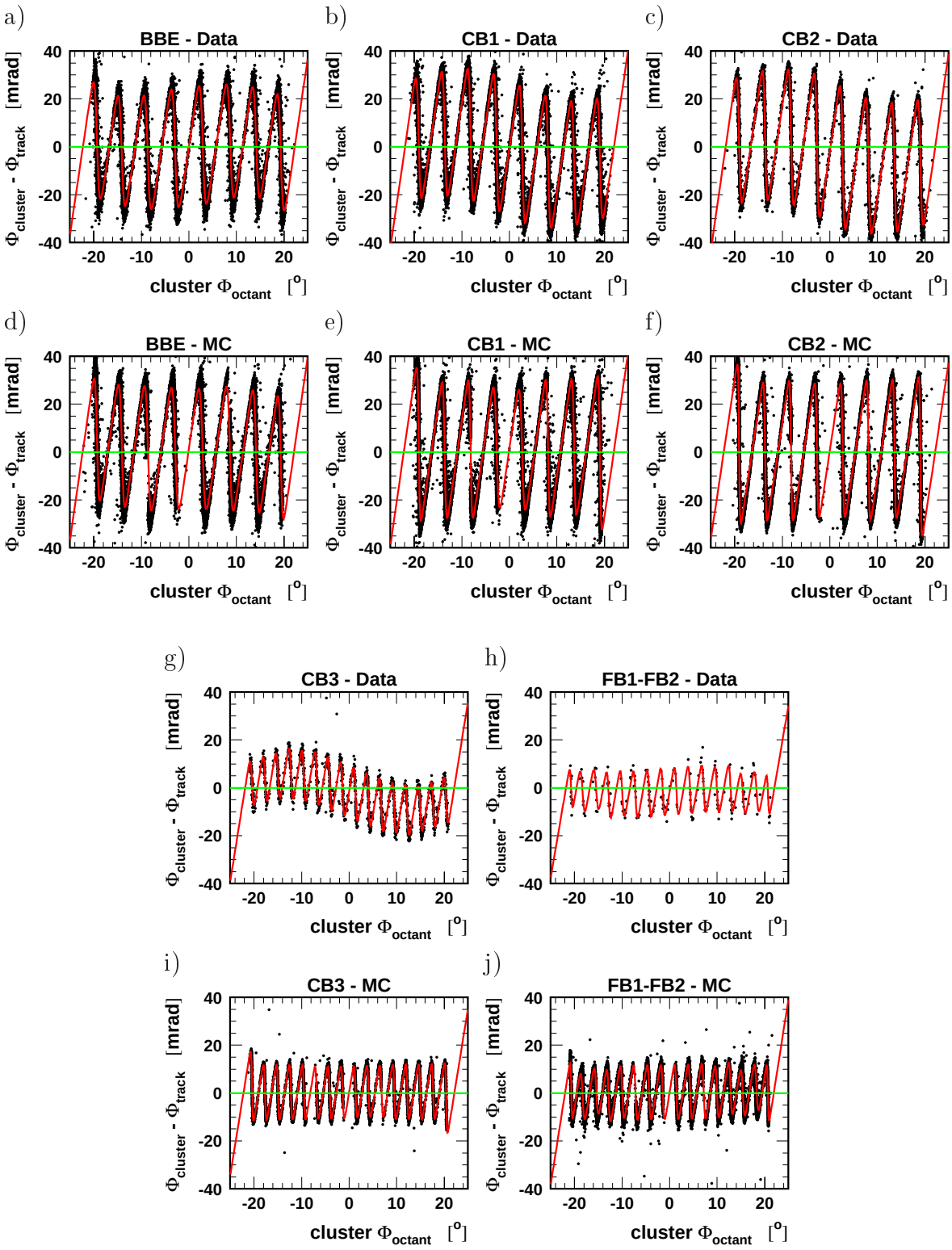

Figure 5.15: Wheel-wise electron $\phi_{cluster} - \phi_{track}$ as function of $\phi_{cluster}$ for data (a,b,c,g,h) and simulation (d,e,f,i,j). The red, solid curves show the corresponding correction functions obtained from a fit to the distributions.

In simulation, no differences have been observed for the FB1 and FB2 wheels. Since the same is true within available statistics for the data, the correction is performed for the combined FB1 and FB2 wheels.

The parameters are determined simultaneously from a fit to all events passing the selection requirements. To account for limited statistics in the data, the parameters are combined in the fit for each pair of cells for the CB3-FB2 wheels. The resulting correction functions are indicated in figure 5.15 by the solid curves. They provide a good description of the correlations. The addition of extra parameters to the fit does not improve the result, whereas a further reduction of parameters, e.g. by introducing further constraints, yields a significantly worse description of the data.

The procedure uses the internal LAr coordinates to be independent of outside influences, especially of alignment corrections which may change in time. P^{const} corresponds to an alignment parameter. It is used in the fit but set to zero for the application of the final ϕ correction. The alignment of the LAr calorimeter w.r.t. the tracking system (cf. section 5.5) is performed subsequently using the improved cluster positions.

Result of the ϕ reconstruction

The procedure described above corrects the cell size effects as well as underlying biases individually for data and simulation. Figure 5.16 shows the final resolution of the cluster ϕ measurement for each wheel and separately for data and simulation. The distributions of the BBE-CB2 wheels have two contributions, a narrow core and a wide tail, which are related to the shower positions being close to the cell intersections and nearby a cell centre, respectively. This clear distinction is found for both data and simulation and is due to the fact that the lateral shower extension is much smaller than the cell distances. In addition, the more compact shower shape of the simulation is observed in the tails of the distribution which are broader and yield larger contributions compared to the data. In the CB3-FB2 wheels the tail contributions are drastically reduced mainly due to the higher cell granularity in ϕ. The comparison with the standard reconstruction method (histogram in figure 5.16) reveals the large improvements obtained with the current procedure.

The distributions are parameterised by the superposition of two Gaussian distributions. As summarised in table 5.8 the cluster ϕ resolution is about 2-3 mrad for the core and typically 8 mrad for the tails. As verified by the simulation, the resolution of the track measurement yields a negligible contribution, since the events are required to have an electron track of rather good quality.

In the BBE-CB2 wheels, it is almost impossible to resolve the cluster positions close to a cell centre because of insufficient contributions from neighbouring cells. Alternative cell weights do not improve the results.

A precise measurement of the ϕ coordinate is primarily needed for the application of the fiducial volume cuts (cf. section 6.3): Firstly, a ϕ crack cut of $\pm 2^\circ$ around the crack is required for the cross section analysis to assure reliable electron identification (cf. section 5.3). This corresponds to a cut line within the first quarter (half) of the outermost cell for the BBE-CB2 (CB3-FB2) wheels. Using cell information from the neighbouring octant, the cluster ϕ measurement extends even closer to the ϕ crack than

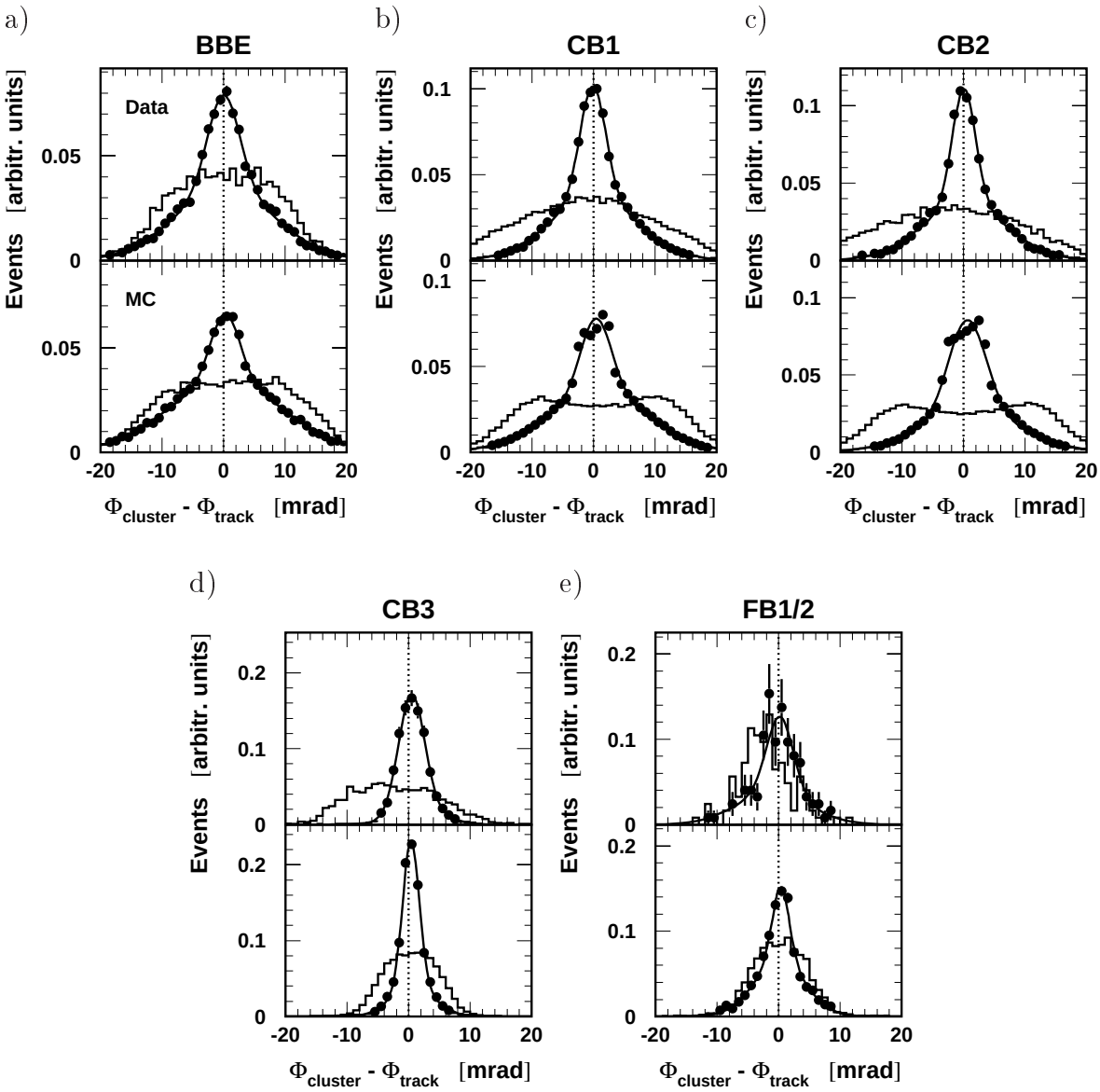

Figure 5.16: Resolution of the final cluster ϕ measurement for the wheels of the LAr barrel BBE-FB2 (a-e). Data (simulation) are shown in the upper (lower) half of each figure. The lines represent the sum of two Gaussians fitted to the distributions. The corresponding widths are given in table 5.8. The distributions for the original ϕ reconstruction are shown as histograms.

$\pm 2°$. Secondly, inefficient LAr trigger regions are rejected. Since, the trigger cells are composed of arrays of LAr cells, this cut is by definition placed on the cell boundaries.

The results have been verified by performing the same procedure to the $e^- p$ data from 1998-1999. Apart from the alignment parameter P^{const}, the correction functions agree well for the $e^+ p$ and $e^- p$ data sets, including the sine-like overall modulation of the data. In addition, no p_T dependence of the fit parameters has been observed, i.e. there is no influence visible from the curvature of the electron trajectory within the magnetic field. This also proves the reliability of the track extrapolation.

Wheel	Cluster ϕ resolution [mrad]			
	Narrow core		Wide tail	
	Data	MC	Data	MC
BBE	2.58±0.12	2.37±0.11	8.16±0.13	9.45±0.09
CB1	2.07±0.05	2.55±0.04	7.14±0.07	8.53±0.05
CB2	1.89±0.07	3.06±0.03	7.00±0.12	8.40±0.06
CB3	2.39±0.06	1.89±0.02	–	–
FB1/2	2.65±0.50	1.41±0.09	13.7±38.6	4.25±0.07

Table 5.8: Resolution of the cluster ϕ measurement for data and simulation in the barrel wheels of the LAr calorimeter. The corresponding fits of the sum of two Gaussians are shown in figure 5.16. The $\Delta\phi$ distributions of CB3 are well described by a single Gaussian.

The remaining differences between data and simulation are due to the different descriptions of electromagnetic shower shapes (cf. section 5.1.1). They could in principle be resolved by e.g. smearing the $\phi_{cluster}$ angle in data. However, downgrading the data to agree with the simulation is rather questionable. Since future analyses are supposed to use simulations with improved shower parameterisation, no further attempt is made to improve here. Nevertheless, the current $\phi_{cluster}$ reconstruction yields large improvements compared to the original method.

With the current achievements, the reconstruction of the electron centre of gravity provides an accurate ϕ measurement and keeps the analysis independent of an electron track requirement.

5.4.2 The z Reconstruction

The precise z reconstruction of the electron cluster centre of gravity is more important for the analysis than the ϕ measurement, since the related polar angle θ_e directly enters the calculation of Q^2 (cf. equation 2.25) which is a steeply falling distribution.

The reconstruction of the z coordinate is performed in a similar way as the ϕ reconstruction. However, the procedure in z is more complicated because the shower direction in general is not at all perpendicular to the calorimeter surface. In addition, the cell arrangement is not cleanly projective w.r.t. to the nominal interaction point.

To provide a precise reference position in z, the z chambers are required to contribute to the electron track measurement (cf. table 5.6). Since part of the CIZ rings located at positive z were not operational during the 1999-2000 data taking period, the data provide insufficient statistics for the CB3 and more forward wheels. In this region, the correction is based solely on simulated events.

The corresponding cell structure of the electromagnetic part of the LAr calorimeter is shown in the (r, z) plane in figure 5.17. Typical cell sizes in z are 12 cm in the BBE, 7.5 cm in the CB1 and CB2, and 5 cm in the CB3 wheel. Since the cells are distributed in a more irregular way w.r.t. the shower direction, a precise z measurement may be expected just from the temporary centre of gravity derived from the weighted cell positions according to equation 5.2. However, as shown in figure 5.18 for the standard

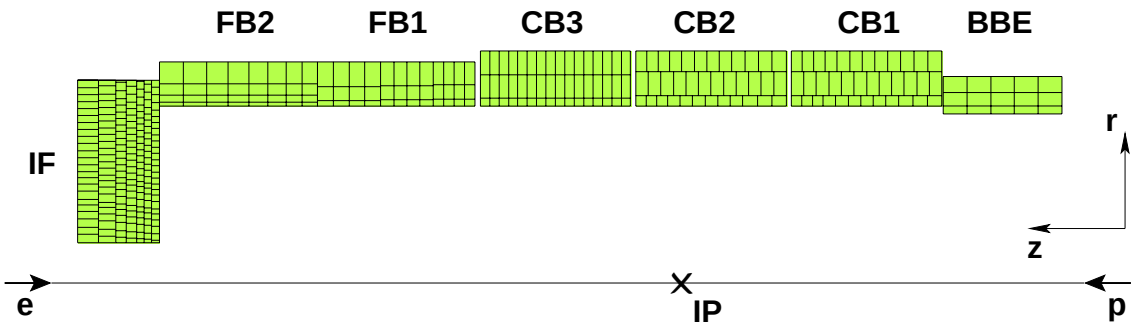

Figure 5.17: Longitudinal cross section of the electromagnetic section of the LAr calorimeter (upper half part only). IP is the nominal interaction point.

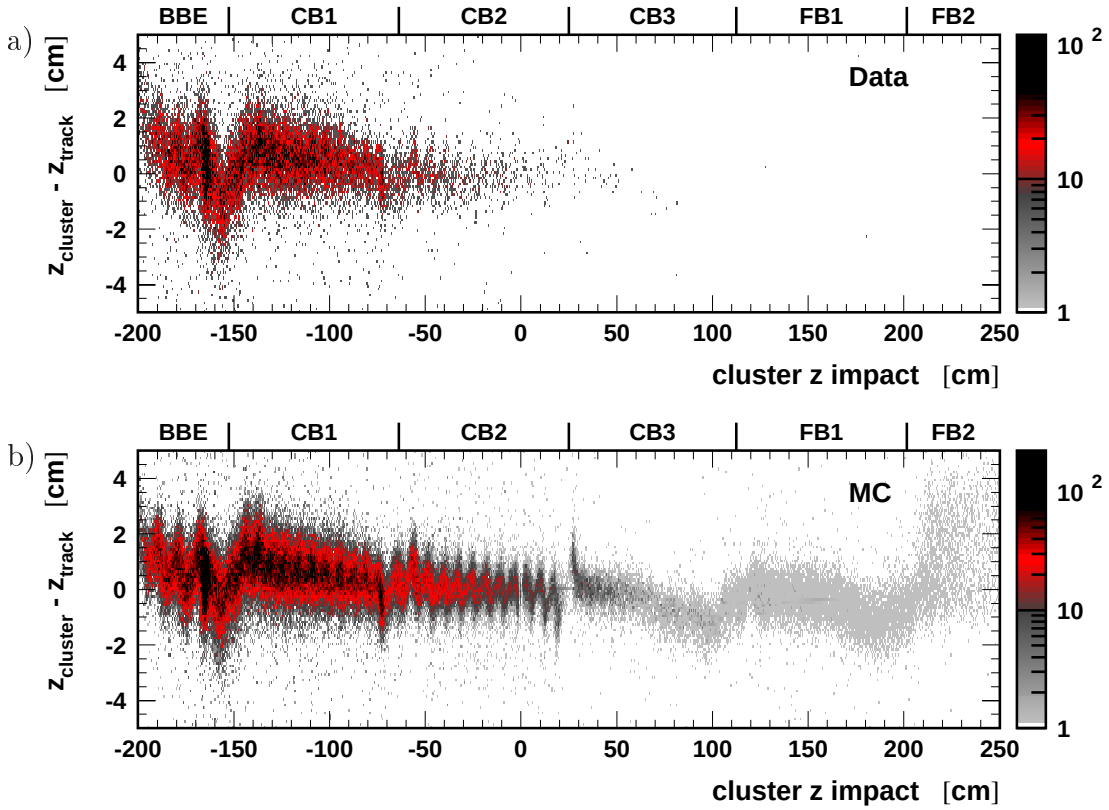

Figure 5.18: Electron $z_{cluster} - z_{track}$ difference as function of $z_{cluster}$ using the standard cluster reconstruction for data (a) and simulation (b). The colour code represents an arbitrary scale of number of events, whereas the relative normalisation is the same for data and simulation. For the simulation, non-zero entries below one are shown in light gray. The LAr wheels and the cracks in-between are indicated at the top.

reconstruction, the cell structure of the LAr calorimeter is clearly visible also in the z direction. Especially in the CB1 and CB2 the pattern represents the cells of the second layer (k=1)[7], which on average contains most of the electron shower energy.

[7] Cell layers are numbered by k starting at 0.

Furthermore, disturbances of the cluster z measurement are observed in the vicinity of the z cracks as soon as part of the cluster energy is lost in the crack. The structure at $z \approx -155$ cm is in addition due to the change of the LAr geometry when crossing from the CB1 to the BBE wheel. Compared to the CB wheels, the BBE is displaced about 10 cm more inwards leaving an edge of the calorimeter surface (cf. figure 5.17).

Layer-wise corrections were not successful.

Improved z reconstruction procedure

The correction procedure is closely related to that in ϕ. The main difference compared to the ϕ coordinate is the missing symmetry in z. Thus, there is no analogue to the P^{shift} parameter.

The track z versus cluster z correlations are parameterised as function of the temporary $z_{cluster}$ coordinate, z_{temp}, in terms of the cells j of the second layer (k=1) using the following parameters:

P^{const} : overall shift w.r.t. track z, yields alignment correction.

P_j^{slope} : slope of the asymptotic part of the tanh at the cell borders.

P_j^{height} : offset provided by the tanh, i.e. distance between asymptotes.

P_j^{stretch} : stretch/squeeze of the tanh, yields (together with P_j^{slope}) the slope of the tanh at the cell centre.

P_j^{dcentre} : offset to the nominal z coordinate of cell j; defines position of tanh zero crossing, representing the cell centre.

The corresponding correction functions are given by

$$\begin{aligned} z_{final} \;=\; & P^{\text{const}} + \sum_{j=0}^{j_{cell}} P_j^{\text{slope}} \cdot \Delta z_j + P_{j_{cell}}^{\text{slope}} \cdot (z_{temp} - z_{center,j_{cell}}) \\ & + \sum_{j=0}^{n_{cell}} P_j^{\text{height}} \cdot \tanh\Big[P_j^{\text{stretch}} \Big(z_{temp} - z_{center,j} - P_j^{\text{dcentre}} \Big) \Big] \;, \end{aligned} \tag{5.5}$$

where j_{cell} is the cell number of the cell which contains z_{temp}, Δz_j is the distance between the centres of adjacent cells, and $z_{center,j}$ is the nominal z coordinate of cell j.

The parameters are determined simultaneously from a fit to all events passing the selection requirements. Apart from the BBE wheel, the P_j^{slope}, P_j^{height}, P_j^{stretch} and P_j^{dcentre} parameters are combined for each pair of cells in the fit to reduce the number of free parameters.

This procedure cannot provide any information on the z alignment of the LAr calorimeter w.r.t. the tracking devices, since there is no symmetry like in the ϕ direction. However, to provide access to the alignment in z, which is an important information to be used e.g. for the reconstruction of the hadronic final state, the tracking coordinates of the data were shifted wheel-wise in z such that the uncorrected distributions between cluster and track agree in data and simulation. Only those regions have been used where data and simulation show very similar structures, mainly far away from cracks.

First of all, the cell weight is optimised which is used for the temporary z calculation. The cell weight is searched for which provides the lowest sensitivity to the cell structure,

leading to the smallest local corrections. To estimate the local deviations due to the cell size effects, only the overall modulation (slope) is corrected using the parameters P^{const} and P_j^{slope} but setting $P_j^{\text{height}} \equiv 0$ in equation 5.5. This is studied wheel-wise for different cell weights using simulated events to have large statistics. The resulting widths of the $z_{cluster} - z_{track}$ distributions are presented in table 5.9. For all methods

LAr wheel	Gaussian width of $\Delta z = z_{cluster} - z_{track}$ after slope correction for simulation [cm]			
	Cell weight w_i for COG determination			
	$\sqrt{E_i}$	$\sqrt{E_i/V_i}$	E_i/V_i	$c + \log$
BBE	0.86	0.87	0.72	1.00
CB1	0.70	0.68	0.76	0.63
CB2	0.56	0.54	0.88	0.42
CB3	0.41	0.41	0.33	0.39
FB1	0.48	0.50	0.37	0.49
FB2	0.65	1.02	0.49	0.73

Table 5.9: Width of electron $\Delta z = z_{cluster} - z_{track}$ in cm from simulation after slope correction only, using different weights w_i for the determination of the temporary cluster centre of gravity (COG, see text for explanation). The abbreviation $c + \log$ stands for $const + \log[(E_i/V_i)/(E_i/V_i)_{max}]$, where the constant has been optimised for each wheel to provide best resolution. Typical errors on the width range from 1% in BBE-CB2 to 5% in the FB2.

the fraction of events located outside of the 3σ range around the mean value are of the order of 1% and never exceed 2%. Therefore, the width of the Δz distributions is a good estimator to determine the best z reconstruction method.

The linear E_i/V_i weight provides the best resolution for the BBE, CB3 and FB wheels and $w_i = \sqrt{E_i/V_i}$ is applied in the CB1 and CB2 wheels. Since the logarithmic cell weight, $(c + \log)$ [8], yields sharp local deviations between $z_{cluster}$ and z_{track} in some z regions, this method is disfavoured.

The previous results of the Monte Carlo study were cross-checked with data for the BBE-CB2 wheels. The widths in data are slightly broader, but the relative behaviour between wheels and weighting methods is in agreement with the observations for the simulation.

The final correlation distributions and the corresponding parameterisations of the correction function are shown in figure 5.19. The parameterisations provide a good description of the correlations and account for the cell size effects as well as for overall trends and local biases. The latter are found predominantly in the vicinity of the z cracks.

For the application of the correction, the functions pass smoothly from one wheel to another, even though events with electrons in the crack regions are rejected from the analysis. For $z > 270$ cm, the final correction approximates $z_{final} = z_{cluster}$ which is taken for $z > 290$ cm.

[8] $c + \log \equiv const + \log[(E_i/V_i)/(E_i/V_i)_{max}]$

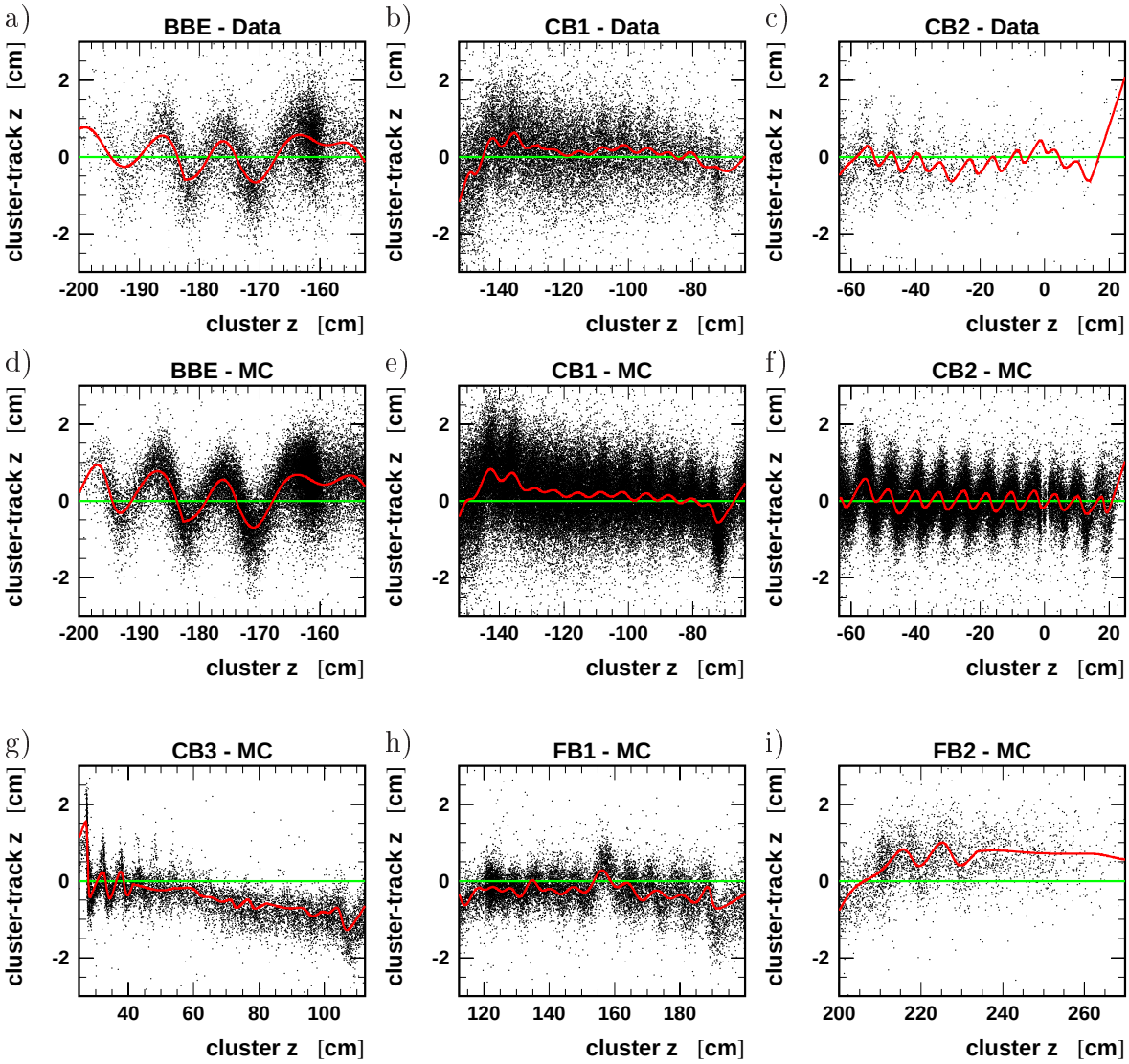

Figure 5.19: Wheel-wise electron $z_{cluster} - z_{track}$ as function of $z_{cluster}$ for data (a,b,c) and simulation (d,e,f,g,h,i). The red, solid curves show the corresponding correction functions obtained from a fit to the distribution.

Result of the z reconstruction

Figure 5.20 shows the final resolution of the cluster z measurement for each wheel. Clear improvements are observed w.r.t. the standard z reconstruction. The distributions of all wheels are approximately Gaussian and the fraction of events beyond $\pm 3\sigma$ is only between 1 and 3%.

The z resolution for each wheel is quantified in table 5.10 and represents the width of a Gaussian function obtained from a fit to the distributions as shown in figure 5.20. The z resolutions are of the order of 5 mm. In the BBE, the resolution in data is significantly worse compared to the simulation. However, the impact on the θ_e determination is negligible due to the large angle. Good agreement between data and simulation is observed in the CB1 and CB2 wheels. In the more forward region, the correction used for the simulation is also applied to the data.

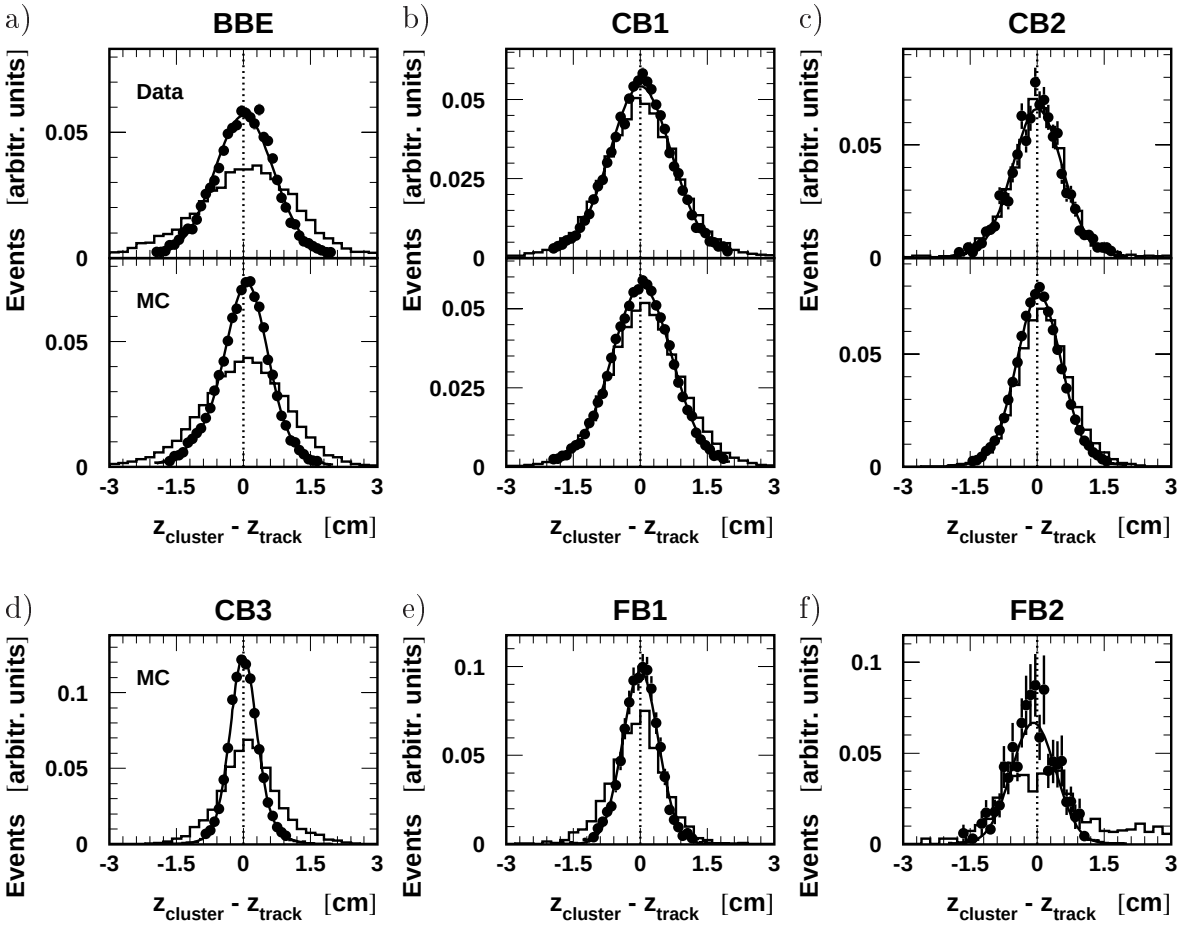

Figure 5.20: Resolution of the final cluster z measurement for the wheels of the LAr barrel BBE-FB2 (a-f). For the BBE-CB2 wheels (a-c), data (simulation) is shown in the upper (lower) half of each figure. For the CB3-FB2 wheels (d-f), only simulation is shown. The lines represent a Gaussian fit to the distributions. The corresponding widths are given in table 5.10. The histograms show the resolution for the standard COG reconstruction with cell weights $w_i = \sqrt{E_i}$.

Wheel	Cluster z resolution [cm]	
	Data	MC
BBE	0.638±0.010	0.513±0.005
CB1	0.691±0.009	0.670±0.005
CB2	0.540±0.021	0.487±0.003
CB3	–	0.309±0.005
FB1	–	0.368±0.016
FB2	–	0.476±0.050

Table 5.10: Resolution of the cluster z measurement for data and simulation in the barrel wheels of the LAr calorimeter. The corresponding Gaussian fits are shown in figure 5.20.

As discussed for the ϕ reconstruction, the best z resolution is obtained for events where the shower axis is located on the intersection of two cells. Therefore, the borderlines of the z crack cuts are placed on the cell borders of the second layer ($k = 1$).

Compared to previous analyses, the current reconstruction of the electron cluster centre of gravity provides an improved z measurement. It is based on the correction of both cell size effects and overall modulations which are typical for the calculation of the centre of gravity. The gain is an improved precision of the electron scattering angle as will be presented in section 5.6.

Although the adaptation of the simulation to the electromagnetic shower development in real data will reduce the systematic differences between data and simulation, a further correction as described above will be required to measure the electron scattering angle with highest possible absolute precision.

With additional statistics expected from HERA-II, the precision of the cluster ϕ and z determination with the method described may be clearly improved in the CB3 and FB area.

5.5 Alignment of the LAr Calorimeter

The precise reconstruction of the event kinematics requires the exact relative alignment of the different detector components. In this analysis, the knowledge of the relative position of the LAr calorimeter and the central tracking system is crucial. The latter measures the interaction vertex for each event (cf. section 5.2) and defines the coordinate system.

During the assembly of the LAr calorimeter, the wheels were pushed successively into the cryostat where they reside on supporting rails without a fixed connection among each other. The cool down to LAr temperature at about 72K causes changes in the relative position between the wheels. The tracking system provides the reference frame for the H1 experiment and the coordinates of the LAr calorimeter wheels are adjusted accordingly.

First of all, the initial coordinates of the LAr calorimeter already incorporate the contraction due to the cool-down. The LAr calorimeter stack positions have been mapped at room temperature outside the cryostat. It is assumed that in ϕ direction the shrinkage is symmetric and a correction is needed in z only,

$$z_{cold} = 23.67\text{cm} + (z_{warm} - 23.67\text{cm}) \cdot (1 - 0.0027) \; . \tag{5.6}$$

The LAr calorimeter is aligned to the tracking system using real data of high quality. The procedure is based on the position of the scattered electron from neutral current events which have an associated track measured within the CJC and z chambers. The position of the electron cluster measured in the LAr calorimeter (cf. section 5.4) is compared to the track extrapolated to the cluster. All selected data points are used in a fit to determine the six parameters of translation and rotation simultaneously for each object to be aligned. Rotations are defined w.r.t. axes running through the centre of the corresponding object. To avoid large correlations between the alignment parameters, the fit accounts for non-uniform octant-wise event distributions which may arise particularly from spatial inhomogeneities in the track efficiency.

The alignment is performed individually for each LAr wheel with sufficient statistics, i.e. for the BBE, CB1 and CB2 wheels. The CB3, FB1 and FB2 wheels are combined

for the alignment procedure. Due to low statistics and missing acceptance of the central tracking system, the forward wheels 6 and 7 (IF1/2, OF1/2) are not subject to alignment corrections.

The alignment parameters derived from the fit and the corresponding errors are presented in table 5.11 The large data sample provides sensitivity in the sub-mm and

		Wheel-wise alignment constants for data			
		BBE	CB1	CB2	CB3-FB
translations	Δx [mm]	-0.37 ± 0.09	-0.32 ± 0.06	-1.40 ± 0.12	-2.04 ± 0.33
	Δy [mm]	-0.53 ± 0.09	-0.47 ± 0.06	-0.30 ± 0.11	0.51 ± 0.32
	Δz [mm]	-0.03 ± 0.13	0.88 ± 0.05	2.33 ± 0.06	-0.38 ± 0.18
rotations	α_x [mrad]	-1.48 ± 0.20	-0.31 ± 0.07	-1.34 ± 0.07	-0.39 ± 0.24
	β_y [mrad]	0.52 ± 0.20	0.71 ± 0.07	-0.54 ± 0.07	0.45 ± 0.24
	γ_z [mrad]	1.06 ± 0.06	1.61 ± 0.03	2.56 ± 0.07	2.17 ± 0.20

Table 5.11: Alignment constants of the LAr calorimeter relative to the central tracking system. The parameters have been derived simultaneously from a fit comparing the positions of the electron cluster centre of gravity to that of the extrapolated electron track.

-mrad range, respectively. Obvious differences in the alignment parameters are determined for different wheels. Although a lot of parameters are significantly different from zero, most of the corrections are small and have negligible influence on the cross section measurement.

For the data, the alignment corrections are applied to the reconstructed centre of gravity of the electron as well as, on cell level, to the hadronic final state. As expected, no significant correction parameters are observed in simulated events.

The effect of the alignment is illustrated in figure 5.21 exemplary for the ϕ measurement. After the correction, the calorimetric ϕ measurement coincides with the track

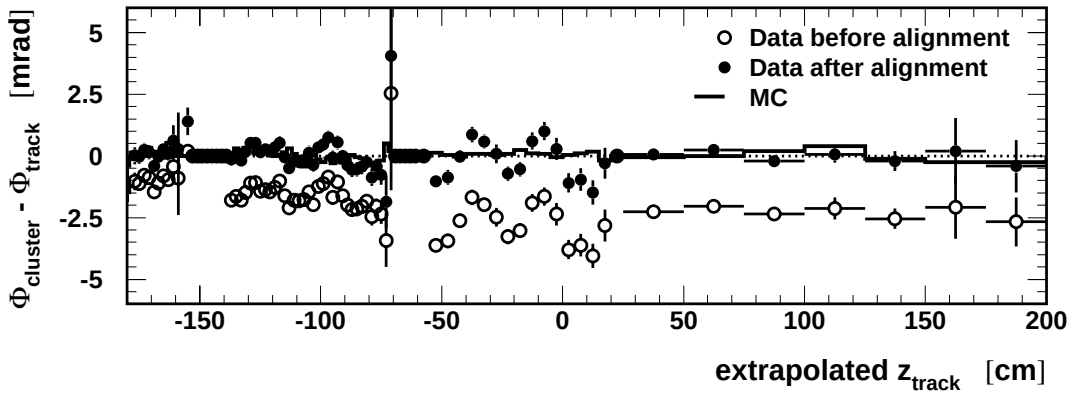

Figure 5.21: LAr calorimeter alignment distribution $\phi_{cluster} - \phi_{track}$ as function of z_{track} being extrapolated to the electron centre of gravity. Shown are the data distributions before (open points) and after (full points) the alignment correction as well as simulation (histogram).

prediction for data and simulation.

The alignment parameters were found to be independent of the transverse momentum of the electron. This indicates a correct track extrapolation to the electron centre of gravity and excludes effects due to the curvature of the electron in the magnetic field.

With the current statistics, the forward part of the LAr calorimeter (CB3 and more forward wheels) can only be checked overall. Since shifts and rotations in the well measurable backward wheels are smaller or at most comparable to respective 3 mm and 3 mrad effective changes, this accuracy is also assumed for the relative position of the forward wheels. Due to the long lever arm of about 3m, the angular measurement of electrons in the IF is rather insensitive to the exact positions of the LAr calorimeter modules.

5.6 Electron Angle Measurement

The angles θ_e and ϕ_e of the scattered electron directly enter the reconstruction of the event kinematics. They are determined solely from the positions of the electron cluster centre of gravity (cf. section 5.4) and the interaction vertex (cf. section 5.2), providing a robust, uniform method in the entire kinematic range.

The ϕ measurement was presented in subsection 5.4.1. A precision of about 3 mrad is reached in the regions at the intersections of the cells and close to the cracks, which are important for defining the fiducial volume.

The θ_e angle is derived from the cluster and vertex positions. The precision of the θ_e measurement is studied by comparison to the θ angle measured with the track associated with the electron. To provide an appropriate reference, the track has to be reconstructed with contributions from the outer z chamber and the vertex has to be constrained by at least three tracks. Figure 5.22 shows the mean value of $\theta_{cluster} - \theta_{track}$ as function of the z impact position. On average, the data are well described

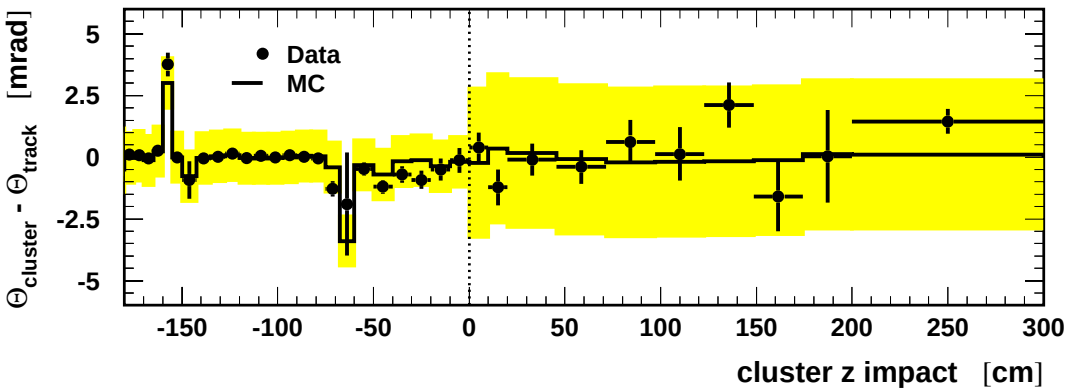

Figure 5.22: Precision of the electron polar angle θ_e as determined from the cluster centre of gravity. A track with z chamber information is taken as reference. The yellow band around the Monte Carlo histogram indicates the quoted systematic uncertainty.

by simulation. In the backward wheels, the θ reconstruction relies mainly on the determination of the COG of the electromagnetic shower, while in the forward LAr wheels the accuracy is mainly limited by the knowledge of alignment.

As discussed in section 5.4, there are small remaining differences in the resolution of the cluster position which are partly propagated to the θ determination. However, Monte Carlo studies confirmed the results of [74] that the relative agreement between data and simulation is of secondary importance compared to the absolute precision of the polar angle measurement. This gives confidence to quote the systematic error on the polar angle of the scattered electron to be $\delta\theta_e = 1$ mrad for $z < 0$ and $\delta\theta_e = 3$ mrad for $z > 0$.

Thus, the calorimetric θ_e measurement yields a precision of the order of the design value for the H1 LAr calorimeter.

Beam tilt correction

The angles θ and ϕ discussed so far are given in H1 detector coordinates. For the determination of the event kinematics, the angles have to be taken with respect to the ep beam axis. The latter is inclined by a small angle of $\mathcal{O}$(mrad) w.r.t. the H1 coordinates depending on the beam optics. Figure 5.23 shows the so-called beam tilt in the x and y directions as function of HERA machine fills. The beam tilt correction is applied to the data to obtain the final electron angle measurements. The Monte Carlo events are simulated without beam tilt.

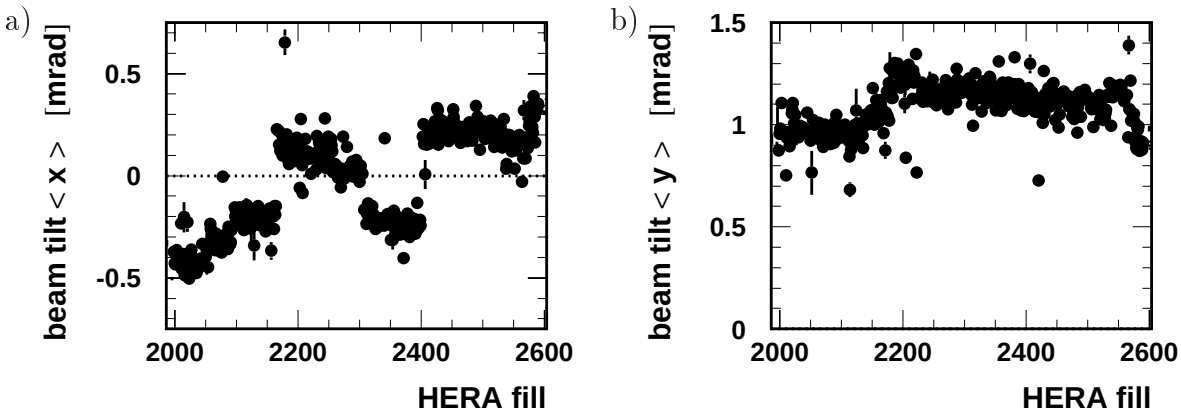

Figure 5.23: Inclination of the ep beam w.r.t. the z axis of the H1 detector coordinates as function of HERA luminosity fills. The so-called beam tilt is given for the x (a) and y (b) directions.

5.7 Electron Energy Calibration

The electron energy measurement provides the main input to the reconstruction of the event kinematics and yields the dominant contributions to the systematic uncertainties.

Aim of the electron energy calibration is to provide an accurate electromagnetic energy scale and resolution as well as a good description of the data by the simulation. Since the electron energy spectrum is sensitive to the quark densities in the proton, the Monte Carlo has to be generated with appropriate structure functions describing the data. Throughout this analysis, Monte Carlo events are based on the H1 1997 PDF fit (cf. sections 2.5 and 4.4).

In the kinematic range of this analysis, the electron is scattered into the acceptance of the LAr calorimeter. This section describes the determination of the electromagnetic energy scale of the LAr calorimeter, focussing again on the backward and central barrel wheels (BBE-CB3) where the data provide sufficient statistics.

The electron energy calibration is based on the overdetermined kinematics of neutral current events. The measured cluster energy E'_e is compared to the energy $E_{e,2\alpha}$ predicted by the double angle method (cf. section 2.4). The latter uses the measurements of the electron scattering angle θ_e and of the inclusive hadron angle γ_{had} and is to a good approximation independent of the calorimetric electron energy measurement.

To provide a clean NC event sample and to assure sufficient precision of the reference scale, in addition to the standard NC event selection (cf. chapter 6) the following selection requirements are imposed:

- Exactly one electron and one jet, representing a "perfect" leading order NC event topology. The jet identification is based on the cone jet algorithm PXCONE [76, 77] which defines jets as energy deposits within a cone of radius $R = 1$ in the (η, ϕ) plane with a minimum E_T of 5 GeV and a maximum overlap fraction between adjacent cones of 0.75.
- $\gamma_{had} > 11.5°$ ensures full containment of a jet with a typical jet radius of $R = 1$ in the LAr calorimeter to provide a precise reference energy predicted by the double angle method (see below).
- $y_\Sigma < 0.3(0.5)$ for $z_{imp} \leq (>)25$ cm, i.e. for electrons in the BBE-CB2 (CB3 and more forward) wheels yields a precise reference energy (see below).
- $45 < E - p_z < 65$ GeV reduces effects of initial state radiation.
- The ϕ and z cracks are excluded.

Double angle reference energy

The double angle method relies on the measurement of the electron scattering angle θ_e and the inclusive hadron angle γ_{had}. The accurate determination of the former were described in section 5.6. In figure 5.24a, the resolution of the γ_{had} measurement is studied with simulated events. For $\gamma_{had} > 11.5°$, most parts of the hadronic final state are contained within the LAr calorimeter acceptance and the reconstructed inclusive hadron angle provides sufficient precision. The implication on the double angle energy

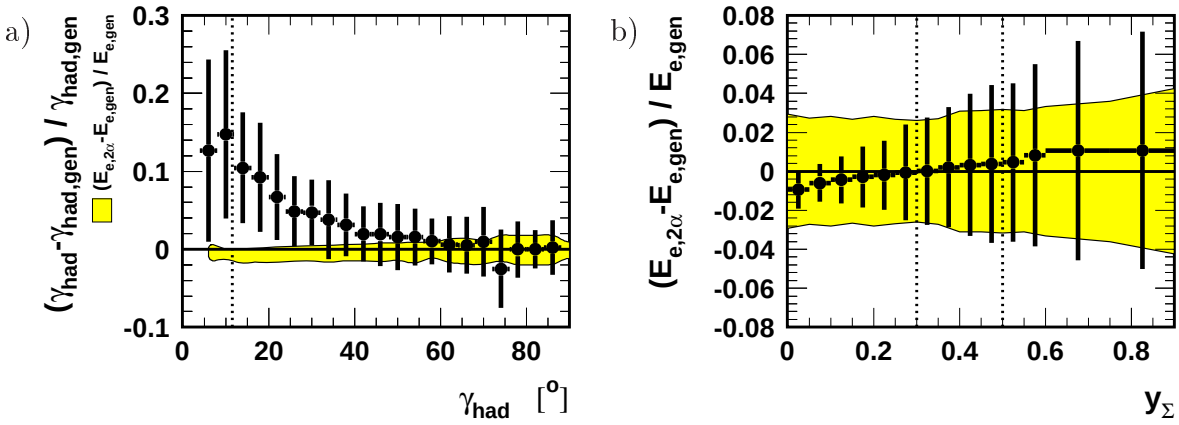

Figure 5.24: a) Resolution of the inclusive hadronic angle γ_{had} as function of γ_{had}. The yellow band shows the resolution of the double angle electron energy. b) y_Σ dependence of the electron energy as predicted by the double angle method. The yellow band describes the resolution of the calorimetric energy measurement. In both figures, the points indicate the mean values of Gaussian peak fits and the vertical error bars show the corresponding widths. The dotted lines indicate the respective $\gamma_{had} > 11.5°$ and $y_\Sigma < 0.3(0.5)$ requirements for the electron energy calibration.

$E_{e,2\alpha}$ is indicated by the shaded band which shows the relative energy resolution $(E_{e,2\alpha} - E_{e,gen})/E_{e,gen}$. The y dependence of the electron energy reconstructed with the double angle method is investigated in figure 5.24b. Comparing the double angle energy to the generated electron energy $E_{e,gen}$, the resolution of the double angle method is less than 2% for $y_\Sigma < 0.3$. In this kinematic range, the double angle prediction provides much higher energy resolution than the calorimetric electron energy measurement, illustrated by the yellow band in figure 5.24b. For the CB3 and more forward wheels, the cut is relaxed to $y_\Sigma < 0.5$ to enlarge statistics. However, the energy prediction by the double angle method is still more precise than the statistical accuracy of the data. At high y, the accuracy of the double angle prediction suffers from the less precise reconstruction of γ_{had} and from the larger impact of radiation effects.

Within the selection, as described above, there is a remaining bias of the double angle energy at low y and low γ_{had} of up to 1% compared to the true electron energy (cf. figure 5.24). The bias is corrected for, since the electron energy calibration aims for an accuracy of the absolute energy scale of below 1%. To allow the application of the electron energy calibration to any NC event selection and in particular to the final cross section data sample, the average bias of the double angle energy is corrected as function of the z impact position of the electron. The corresponding ratio of double angle energy to generated electron energy is shown in figure 5.25. In the FB1 and more forward region, a constant value of 0.99 is used. The correction as derived from simulation is applied to the double angle prediction of the electron energy for data and Monte Carlo events.

Thus, the double angle electron energy provides an appropriate reference scale to investigate both the absolute energy measurement and the energy resolution of the electromagnetic LAr calorimeter.

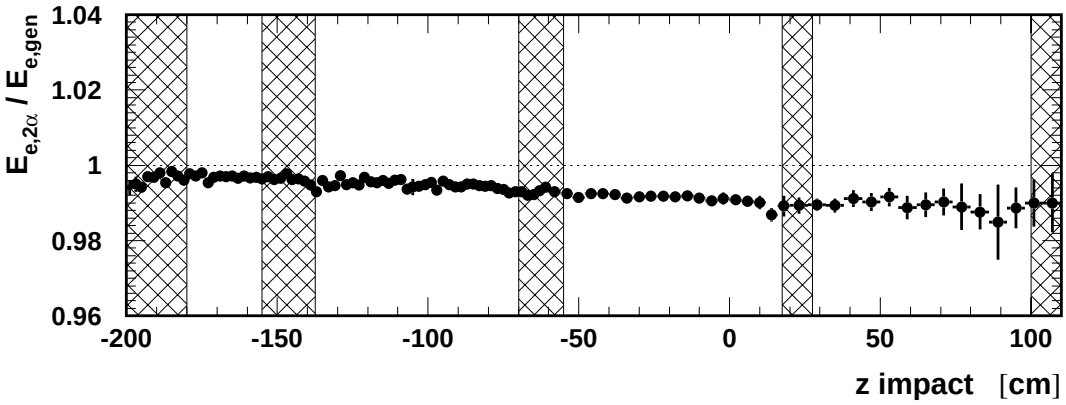

Figure 5.25: Bias of the double angle electron energy w.r.t. the true electron energy as function of the electron z impact position.

5.7.1 Electron energy calibration procedure

Figure 5.26 shows typical calibration histograms of $E_e/E_{e,2\alpha}$ for data and simulation, comparing the calorimetric energy measurement with the double angle prediction. Also

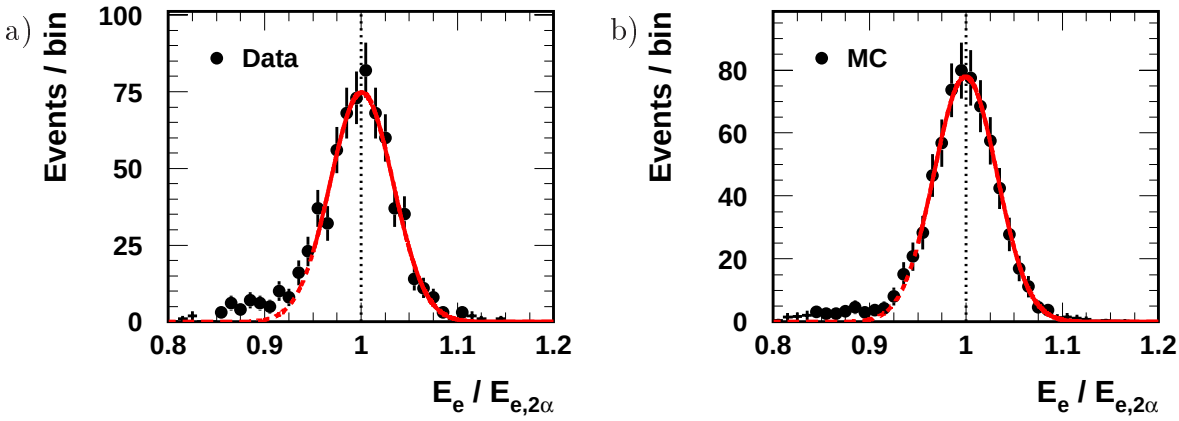

Figure 5.26: Typical calibration histograms of $E_e/E_{e,2\alpha}$ for data (a) and simulation (b). The curve shows a Gaussian function obtained from an asymmetric fit to the distribution.

shown is the respective Gaussian obtained from an asymmetric fit to the distributions from one third of the total height on the leading edge to the total trailing edge. There is a pronounced tail at low $E_e/E_{e,2\alpha}$ values originating from remaining events with radiation. This contribution is irreducible, since e.g. the requirement of cluster-track momentum match would need to be rather tight and disturb the calibration signal.

Thus, the mean value of an asymmetric Gaussian fit is used to determine the (inverse) calibration constant. The errors of the fit results shown in the following contain the error on the mean value of the fit as well as the uncertainty from the definition of the start of the fit at the leading edge.

The energy calibration of the LAr calorimeter proceeds in several steps which are mainly based on the hardware structure of the LAr calorimeter. An overview of the

procedure is given in table 5.12, the details are discussed thereafter.

Electron energy calibration:
1. octant-wise for each wheel
2. z-wise overall
3. z-wise for each half octant
4. time dependent
5. half octant ϕ-wise
6. reiterations to refine

Table 5.12: Individual steps of the electron energy calibration. Steps 1 and 2 are reiterated before each of the steps 3, 4 and 5.

The LAr calorimeter is subdivided into eight wheels each of them containing eight octants. The first calibration step is performed octant-wise for each of the BBE, CB1, CB2 and CB3 wheels. For the very first pass, large areas around the z cracks are excluded to be safe from energy losses as will be discussed for the z-wise calibration. At further reiterations, the standard ϕ and z crack cuts are imposed. Using the electromagnetic energy scale[9] for the electron, figure 5.27 shows the octant-wise $E_e/E_{e,2\alpha}$ ratio. The octant by octant variations in data reach up to 4% in the BBE and CB1

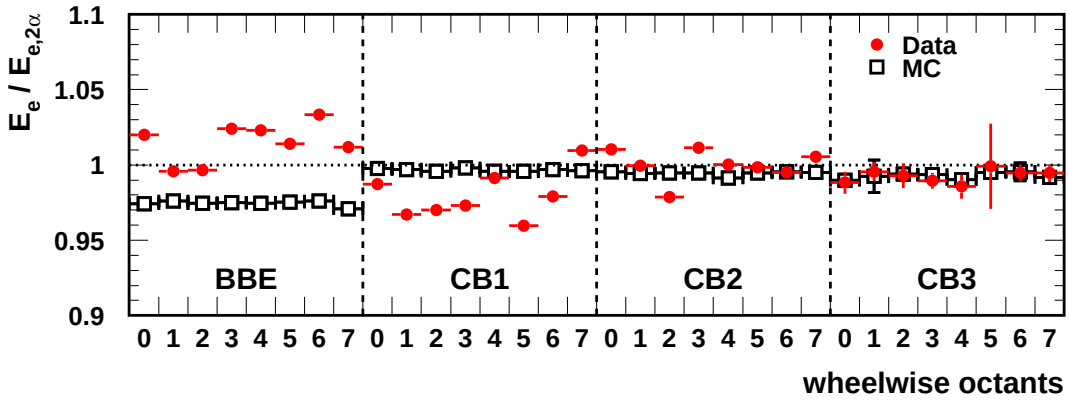

Figure 5.27: Octant-wise electron energy calibration, $E_e/E_{e,2\alpha}$ using the electromagnetic reconstruction scale.

wheels. They are larger than expected, since the reconstructed electromagnetic energy scale is supposed to provide a more accurate energy calibration. The resulting octant-wise calibration factors are applied to the entire octants.

Due to the non-perpendicular angle of incidence, the electron energy reconstruction suffers from losses in the crack regions over a large range in z_{imp}. However, an accurate energy measurement can be obtained by position dependent energy calibration except for clusters located very close to the crack regions. Figure 5.28 shows the z-wise energy calibration, performed independently of ϕ, after the octant-wise correction. Large effects up to 10% and significant disagreement between data and simulation

[9]The electromagnetic energy scale is called E_1 scale and includes dead material corrections.

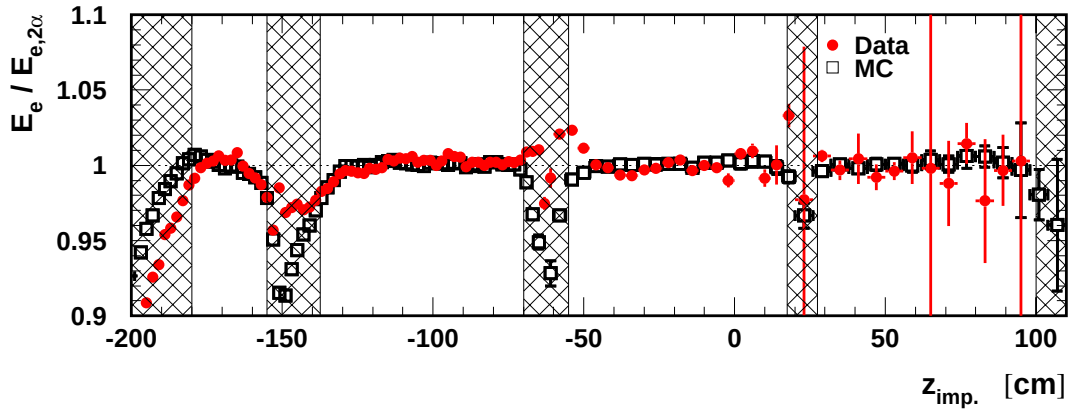

Figure 5.28: z-wise electron energy calibration for data and simulation after the octant-wise correction. The hatched bands indicate the regions around the z cracks, which are cut in the final analysis.

are observed in the LAr z crack regions, which are therefore cut in the cross section analysis. The description of the energy measurement close to the z cracks are improved when using the detailed simulation of the electromagnetic clusters instead of the fast parameterisation. However, in contrary to the data, the detailed simulation shows a significant z dependence of the electron energy response in the CB1 wheel [73]. The effect could not be traced back to a known source and therefore disfavours the use of the detailed simulation.

The first two steps of the electron energy calibration are repeated once to dissolve correlations and to refine the calibration constants.

Next, a z-wise calibration is performed for each half octant, i.e. in 16 divisions in the ϕ direction, two per octant. In order to have sufficient statistics, the z bins are coarser here than in the previous calibration step. Figure 5.29 shows the distributions for two selected half octants. There is a clear z dependence, especially in the BBE

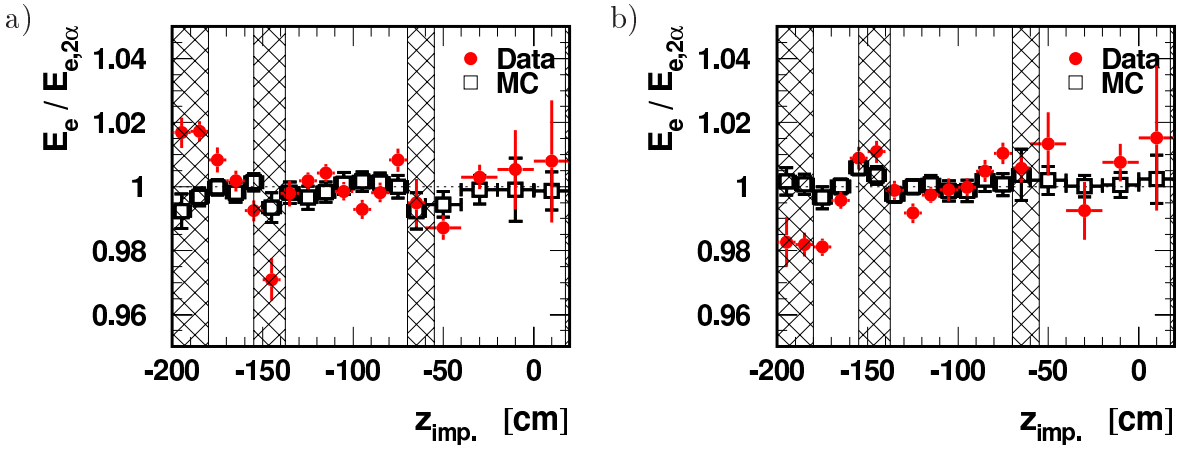

Figure 5.29: z-wise electron energy calibration within a half octant of octant 5 (a) and 7 (b) after the octant and z-wise corrections.

wheel. The observed variations are on the 1% level and reach up to 3% in some regions. The effects may originate from variations in the LAr gap sizes which linearly enter the charge collection and therefore the energy response. The read out cells are fabricated with 2.35 mm LAr gaps to about 2% accuracy [44], that is the same size as observed in the variations of the energy response. On the other hand, these variations should average out since a single read-out cell consists of several active LAr layers and absorber material in-between.

The energy response of the data is investigated for time dependent effects. The cumulative electronegative impurities in the LAr causes a gradual reduction in the charge collection efficiency. Since the time dependence is not corrected for on the reconstruction level, a decrease of the energy response of about 1-2% per year is expected from the analysis of the impurity measurement system [81]. The actual time dependence observed in the data is shown in figure 5.30, reflecting some lack of understanding. The

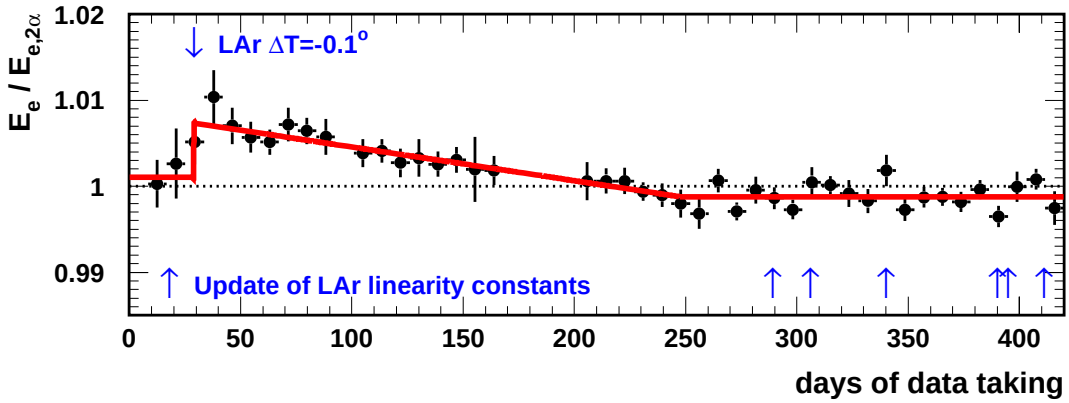

Figure 5.30: Time dependent electron energy response observed in the data. The energy calibration is applied according to the solid line.

rising step at the beginning coincides in time with a decrease of the LAr temperature, but the change of $\Delta T = -0.1°$ should contribute only 0.15% to the energy response. One (no. 2) out of seven LAr purity probes[10] reflects the same jump, while the other probes show a continuous slope. After this step, the energy response decreases in good agreement with the expectation for the LAr impurity. While the LAr probes show a continuous linear decrease, the energy measurement finally gets constant for about 2/3 of the luminosity. At about the time of the level off, the electronic calibration constants constants were updated as indicated by the arrows in figure 5.30. These constants are intended to assure linearity of the electronic chain, though they are not supposed to change the energy scale.

The time dependent electron energy response is visible within statistical precision in all wheels and for instance identical in the upper half ($y > 0$) and in the lower half of the LAr calorimeter. Although not understanding the structure of the time dependent energy response, the effect is corrected in all events as shown in figure 5.30 by the solid line. As expected, no time dependences are found in the simulation.

[10] The LAr purity is monitored by small ionisation chambers which are equipped with a ^{207}Bi source, to check the stability of the ratio of energy loss to collected charge.

Finally, the electron energy response is investigated half octant ϕ-wise. Respecting the symmetry of the cell structure, each octant is 'folded' at the centre (cf. figure 5.12), leading to the remaining angle $\phi_{half\,octant} = |\phi_{octant}|$. The (inverse) calibration factor is shown in figure 5.31 as function of $\phi_{half\,octant}$ for the combined CB1 and CB2 wheels. The cell structure of four cells per half octant is clearly visible for the BBE-

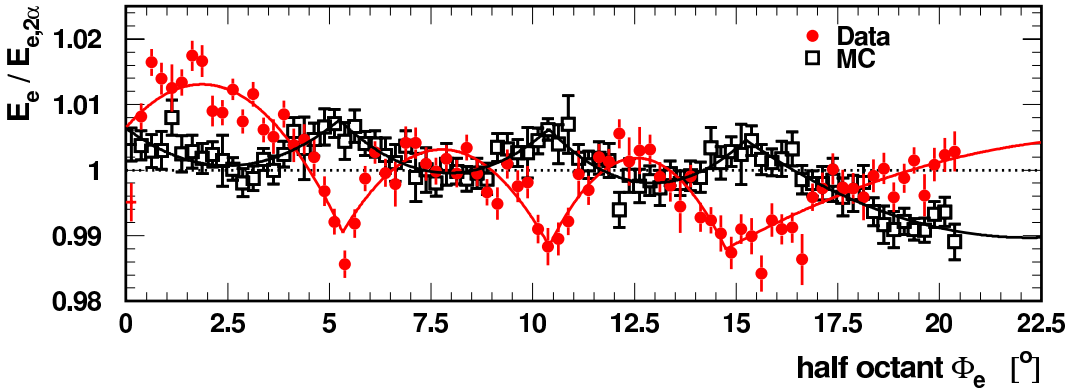

Figure 5.31: Half octant ϕ dependent electron energy calibration. The curves show the respective (inverse) calibration functions applied to data and simulation.

CB2 wheels, where the cell size in ϕ is larger than the typical radial shower extension (cf. section 5.4.1). Almost the same effect but in the opposite direction is observed in the simulation. The origin of the different detector response for electrons entering the centre of a cell or the intersection between two cells could not be found. The cell effect can at least not be based solely on the event reconstruction, which may cause a non-linear cell response, since this would imply the same dependences to data and simulation.

The half octant ϕ-wise calibration is performed in the BBE, CB1 and CB2 wheels. Since within the statistical precision the effects observed in CB2 are compatible with those of CB1, the correction is determined and applied for the combined CB1 and CB2 wheels. The half octant ϕ distribution in the BBE wheel differs significantly from those of CB1 and CB2, especially in the outermost cell next to the ϕ crack. No such effects are visible in the CB3 and more forward wheels where the cell granularity doubles in the ϕ direction.

The whole electron energy calibration is subject to iterations in order to resolve correlations between the different steps. Already after the second iteration, the calibration factors are stable within 0.5%.

Due to the lack of statistics, the electron energy calibration of [27] is taken for the more forward wheels of FB1, FB2 and IF. As is described in detail in [82], the procedure is as well based on neutral current DIS events but is supplemented by elastic QED-Compton events ($ep \to ep\gamma$) and by events from elastic photon-photon interactions ($ep \to epe^+e^-$). Calibration factors are applied for each wheel and for the z crack regions in-between. On top of this, an additional correction of about 1% in data and simulation is applied for the FB1 wheel.

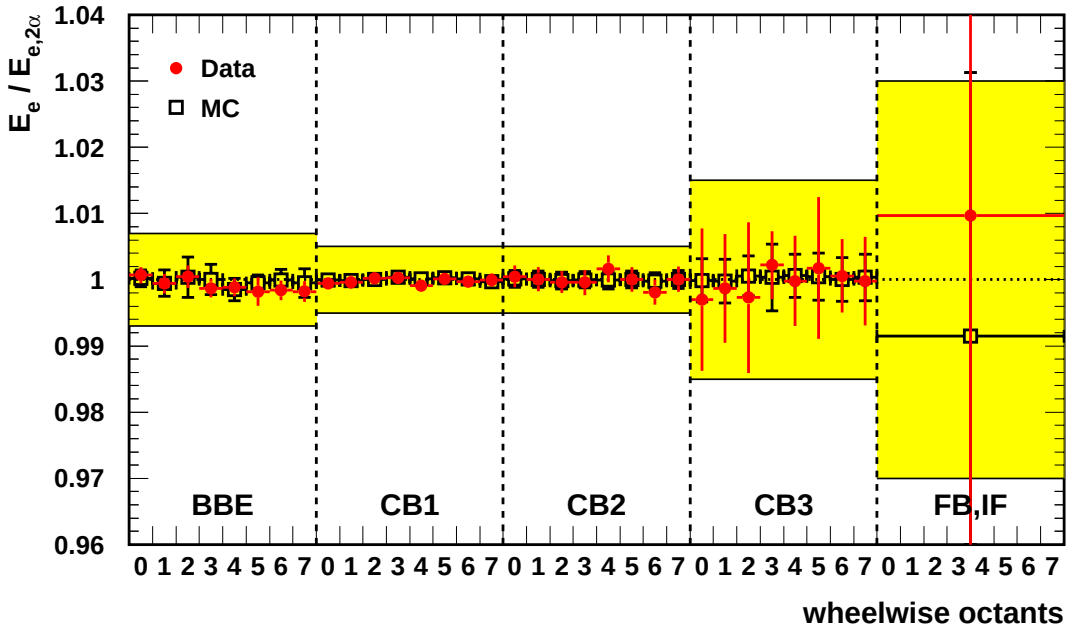

Figure 5.32: Final result of the electron energy calibration as function of wheels and octants. The errors include the error on the mean of the peak fit as well as the uncertainty from the fit method (see text). The yellow band indicates the total systematic uncertainty assigned to the electron energy measurement.

The final result of the electron energy calibration is shown in figure 5.32 as function of the octants. The energy scales of data and simulation agree very well and provide a precise absolute energy scale as predicted by the double angle method. The total systematic uncertainty is illustrated by the yellow band and will be discussed below.

The γ_{had} measurement, which enters the double angle energy prediction, is to first order independent of the hadronic energy scale but is affected by local inhomogeneities in the hadronic energy response. These higher order effects are minimised by iterating electron and hadronic energy calibrations (cf. section 5.8) alternately. Stable results within quoted systematic uncertainties are reached after one iteration.

With the future HERA-II high statistics data sample the electron energy calibration may become refined in the z-ϕ plane, especially in the CB3 and more forward detector region. However, in parts of the central barrel the calibration is already limited by the prediction of the double angle energy and further improvements may require a new approach in the definition of the reference scale.

5.7.2 Electron energy resolution

The resolution of the electron energy is studied for data and simulation using the final energy calibration. Electron test beam measurements with the complete calorimeter set-up yielded an electromagnetic energy resolution of [47]

$$\frac{\sigma(E)}{E} \approx \frac{12\%}{\sqrt{E[\mathrm{GeV}]}} \oplus 1\% \ , \tag{5.7}$$

where $\sigma(E) = \sigma(E_e - E_{true})$ with E_{true} given by the monochromatic beam. The first part takes into account the intrinsic and sampling fluctuations and is called sampling term. The constant term arises from the inter-calibration of the individual calorimeter channels. A third term which is proportional to $1/E$ and represents the noise contribution is neglected in the following.

In contrary to the test beam measurements, the true energy E_{true} of a particle entering the LAr calorimeter is not known in real data from ep collisions. Instead, the electron energy prediction by the double angle method is used as reference, which has at least a better resolution than the calorimetric energy measurement in the selected kinematic range (cf. figure 5.24). To minimise the energy dependence, the quantity

$$\frac{\sigma(E)}{\sqrt{E}} \approx 12\% \oplus 1\% \cdot \sqrt{E}$$

with all energies in GeV is studied in the following. The bias due to the finite resolution of the double angle method is corrected for using the simulation as suggested in [82]:

$$\frac{\sigma(E)}{\sqrt{E[\mathrm{GeV}]}} = \sigma\left(\frac{E_e - E_{2\alpha}}{\sqrt{E_{2\alpha}[\mathrm{GeV}]}}\right) \left[\frac{\sigma\left[(E_e - E_{gen})/\sqrt{E_{gen}[\mathrm{GeV}]}\right]}{\sigma\left[(E_e - E_{2\alpha})/\sqrt{E_{2\alpha}[\mathrm{GeV}]}\right]}\right]_{MC} . \tag{5.8}$$

The results are presented in table 5.13 for different z impact regions of the LAr calorimeter which behave significantly different in terms of electron energy resolution. The resolution $\sigma(E)/\sqrt{E}$ in the data is as accurate as 13-15% in the central area of the BBE-CB2 wheels, while it is significantly worse in the vicinity of the z cracks where part of the cluster energy is lost. The increase in resolution for the CB3 is due to

LAr wheel	LAr z_{imp} region [cm]	$\sigma(E)/\sqrt{E}$ [%]		$\langle E_e \rangle$ [GeV]	*const* [%]	
		Data	MC		Data	MC
BBE (rear)	$z < -180.0$	23.8 ± 1.0	18.1	26.2	4.0	2.7
BBE	$-180.0 \leq z < -155.0$	17.8 ± 0.5	14.8	25.5	2.6	1.7
BBE/CB1	$-155.0 \leq z < -137.5$	20.7 ± 0.6	17.7	25.4	3.3	2.6
CB1 (rear)	$-137.5 \leq z < -120.0$	14.2 ± 0.3	13.1	25.9	1.5	1.0
CB1	$-120.0 \leq z < -70.0$	13.1 ± 0.3	12.2	27.5	1.0	0.5
CB1/CB2	$-70.0 \leq z < -55.0$	18.5 ± 1.0	17.5	30.1	2.6	2.3
CB2	$-55.0 \leq z < 17.5$	14.8 ± 0.3	12.9	35.8	1.4	0.8
CB2/CB3	$17.5 \leq z < 27.5$	18.2 ± 8.3	18.9	47.9	2.0	2.1
CB3	$27.5 \leq z < 100.0$	18.8 ± 1.4	12.7	62.3	1.8	0.5

Table 5.13: Resolution of the electron energy measurement with the LAr calorimeter. $\sigma(E)/\sqrt{E}$ with E in GeV gives the total resolution including the constant term. The resolutions of the simulation are taken before the energy smearing which is performed to adapt the simulation to the data. The last columns contain the constant term for data and simulation assuming a sampling term of 12% and using the mean energy $\langle E_e \rangle$. The shaded regions contain a z crack and are excluded from the cross section measurement.

remaining calibration issues which cannot be addressed with the current statistics of the data. Also shown in the table is the mean electron energy which is used to estimate the constant term of the resolution (cf. equation 5.8), assuming the sampling term of $12\%/\sqrt{E}$ as obtained from test beam measurements. The resulting constant term is presented in the last columns of table 5.13 for data and simulation. In the CB1 wheel a value of 1% is found for the data in well agreement with the test beam results. In the central regions of the other wheels, the constant term is slightly higher. The energy measurement in the BBE suffers from dead material in front of the calorimeter and from the missing hadronic section. In the CB2 and more forward wheels, additional data should allow to reach a 1% constant term as well. The wheel-wise differences in resolution are well reproduced by the simulation which in general yields better resolutions than observed in the data. However, a more detailed investigation would need to include the noise contribution which has been neglected here. To achieve an accurate energy resolution, electrons measured in the z crack regions are rejected from the cross section determination.

Compared to the data, the resolution is overestimated in the simulation. This discrepancy is corrected for in the simulation by smearing the electron energy by the corresponding difference in resolution as function of z impact. Figure 5.33 shows the resolution of $E_e/E_{e,2\alpha}$ as function of z impact for the data as well as for the simulation before and after the adjustment to the resolution of the data. After the correction,

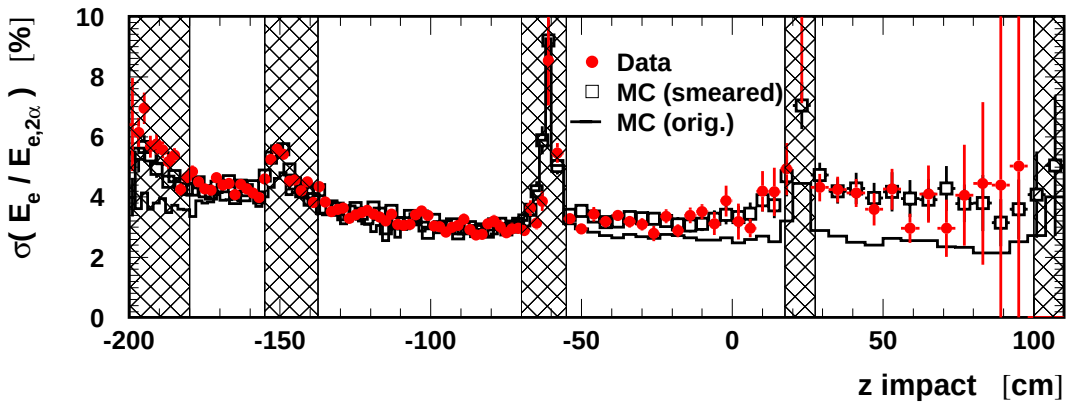

Figure 5.33: Electron energy resolution, defined as the width of $E_e/E_{e,2\alpha}$, as function of the LAr z impact position for data and simulation. The simulation is shown with its intrinsic resolution (histogram) as well as after the adjustment to the resolution of the data (open squares).

the data are well described by simulation. For the FB1 and more forward region, the smearing of the Monte Carlo events is taken from [27].

The final electron energy distributions for data and simulation are shown in figure 5.34 for four different Q^2 regions. Apart from the overall normalisation, the simulation provides an excellent description of the data.

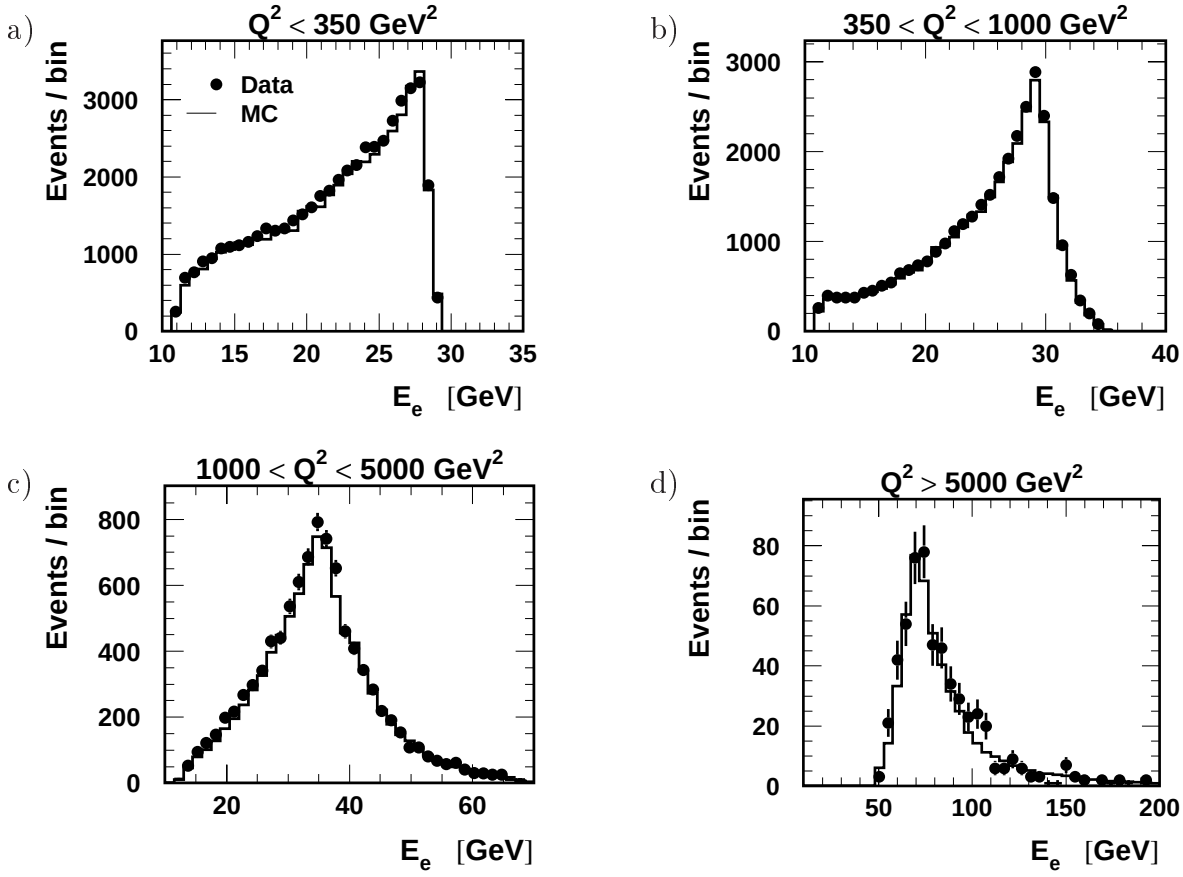

Figure 5.34: Electron energy distributions for data and simulation in four different Q^2 regions. The simulation is normalised to the luminosity of the data.

5.7.3 Systematic uncertainties of the electron energy scale

The systematic uncertainty of the electron energy scale yields one of the dominant contributions to the cross section error and is studied in terms of correlated and uncorrelated errors w.r.t. the cross section measurement. While the correlated part affects all cross section points in the same way, the uncorrelated uncertainty accounts for local deviations in certain detector regions.

The correlated error of the electron energy scale arises from the uncertainty of the reference scale, which affects the energy prediction of all wheels in a similar way. Since the double angle energy prediction is derived from the polar angle measurements of the electron and the hadronic final state (cf. equation 2.38), its accuracy is estimated by varying the input quantities within errors. The error of the electron angle θ_e is taken to be 1 mrad (cf. section 5.6). The inclusive hadron angle γ_{had} is independent of the overall hadronic energy scale (cf. equation 2.21), and is conservatively varied by shifting $(E-p_z)_{had}$ and $p_{T,had}$ independently by the uncorrelated uncertainty of the hadronic energy measurement of 1.7% (cf. section 5.8). The variations lead to very small differences in the double angle energy prediction at the 0.1% level. The studies are performed with Monte Carlo events to have sufficient statistics in all detector

regions. The results are verified within statistical accuracy by the data.

The correlated electron energy uncertainty is estimated to be 0.3%. The improvement compared to the 0.5% correlated error of previous analyses is due to the advanced reconstruction of the electron angle and the hadronic final state.

The uncorrelated uncertainty of the electron energy scale is studied by comparing the octant and z-wise calibration constants derived from different data subsets or with different methods:

- The events are split according to different ranges in y_Σ which implies a strong influence on the double angle energy prediction (cf. figure 5.24b). The sub-samples have $y_\Sigma < 0.1$, $y_\Sigma \in [0.1; 0.3]$ and $y_\Sigma > 0.3$, respectively, and among others correspond to different regions in the electron cluster energy.
  Compared to the overall energy calibration, no systematic effects are found for the three sub-samples, which would indicate an energy dependence of the electron energy scale.
- The events are divided into sub-samples of different ranges in the reconstructed z vertex position. The samples of $z_{vtx} < -10$, $z_{vtx} \in [-10; 10]$ and $z_{vtx} > 10$ cm may reveal a potential bias in the calibration for different incident angles at the same z impact position due to the fixed reference plane of z impact. Within statistical precision, the effects are negligible for events with electrons in the fiducial volume of the cross section measurement. However, variations of up to 1% are observed in the rear part of the BBE and in the z crack region between BBE and CB1, which are however cut in the analysis.
- To study the sensitivity to tails in the $E_e/E_{2\alpha}$ distributions, the calibration constants are taken as the mean value of the $E_e/E_{2\alpha}$ distributions instead of the mean of an asymmetric Gaussian peak fit. Small absolute trends are observed in the BBE (CB1 and CB2) at the 0.5% (0.3%) level with octant by octant fluctuations. In the BBE, the data have larger tails compared to simulation maybe due to leakage, leading to deviations between data and simulation in some octants of about 0.5%. Otherwise the simulation reproduces the effects of the data within 0.3% in the CB1 and CB2 wheels and within 0.7% in the CB3.
- Finally, the electron energy calibration has been tested for different event selections.
  - The additional requirement of a track associated with the electron cluster, which may provide an even cleaner data sample, doesn't change the calibration constants at all. The same is true for variations of the $(E - p_z)$ and z crack cuts.
  - Relaxing the upper y cut to $y_e < 0.9$ and even using the standard selection of the cross section measurement yields an absolute increase of the calibration factors of up to 1.5% in the BBE. However, the simulation still provides an excellent overall description of the data.
  - A NC event sample complementary to the events which have been used for the calibration yields an effect on the calibration constants of 0.5% in the

BBE which increased to 1.0% in the CB1/CB2 and to 1.5% in the CB3. However, the simulation reproduces the data within 0.7% for the BBE-CB2 wheels and 1.5% for CB3.

The relative agreement between data and simulation always stays within the range of the quoted systematic error.

The electron calibration has been proven to be robust and rather insensitive to details in the method or the data selection.

The uncorrelated error of the electron energy measurement is estimated to be 0.63%,0.4%,1.47%,2.98% in the BBE,CB1-CB2,CB3,FB1-IF wheels, where the last value has been taken from [16]. Thus, the total electron energy uncertainty is 0.7% in the BBE, 0.5% in the CB1 and CB2, 1.5% in the CB3, and 3.0% in the FB1 and more forward wheels.

The electron energy calibration has been improved compared to previous analyses and provides smaller systematic uncertainties of the electron energy measurement. As a consequence, the uncertainty of the absolute energy scale is no longer the dominant contribution to the systematic error of the cross section. In addition, the effects of the electron angle measurement and the electron identification become comparable in parts of the phase space, in particular at high y where the electron calibration is most precise.

Further improvements of the electron energy calibration are expected in particular in the central and forward detector region with additional statistics from the HERA-II run. However, since the precision of the absolute electron energy scale is presently limited by the accuracy of the double angle reference scale, new principle methods may have to be introduced to obtain a more precise absolute energy scale.

5.8 Measurement of the Hadronic Final State

The hadronic final state of neutral current events is usually determined in H1 as any energy deposition in the calorimeters not originating from the scattered electron. In the kinematic range considered in this analysis, the largest fraction of hadronic energy flow is measured in the LAr calorimeter as shown in figure 5.35 for the hadronic transverse momentum $p_{T,had}$. It is supplemented by the Spacal calorimeter in the backward direction and by the instrumented iron system to catch up mainly hadronic energy deposits which escape the LAr calorimeter (punch through). In order to avoid systematic dependences on position and time variations of the efficiencies of the tracking system, the hadronic final state is measured solely with the calorimeters without making the attempt to improve the low energy measurements with the help of tracks measured in the central drift chambers.

The quantities of the hadronic final state enter the cross section measurement with minor but not negligible contribution. Most important is the measurement of the hadronic $(E-p_z)_{had}$. The total $(E-p_z)$ of the event visible in the detectors is sensitive to initial state radiation effects. Moreover, the $(E-p_z)$ and the transverse momentum $p_{T,had}$ appear as a ratio in the reconstruction of the inclusive hadronic angle γ_{had} (cf.

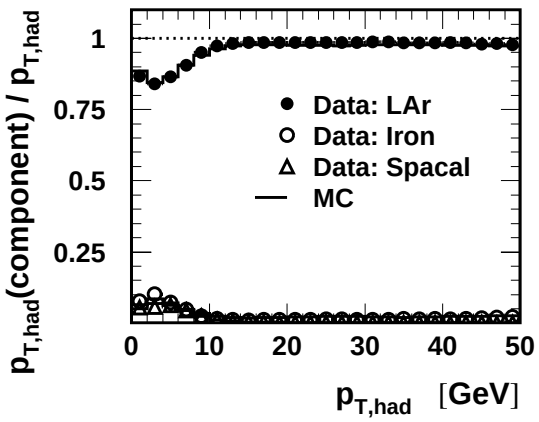

Figure 5.35: Fraction of $p_{T,had}$ contributed by the LAr (full points), Iron (open points) and Spacal (open triangles) calorimeters as function of the total hadronic transverse momentum, $p_{T,had}$. The data are compared to the simulation (histograms).

equation 2.21). Therefore, the measurement of γ_{had} is affected by inhomogeneities of the calorimeter calibration, like wheel-by-wheel or octant-by-octant variations. The uncertainty of the γ_{had} reconstruction dominates the systematic error of the determination of the absolute electron energy scale (cf. section 5.7.3).

Since the kinematic range of this analysis is restricted to $y > 0.05$, the hadronic final state always leaves energy deposits of a sizeable $E - p_z$ contribution within the LAr calorimeter. Therefore, this analysis is rather insensitive to the LAr calorimeter noise. Since the simulation contains measured noise patterns (cf. section 4.4) and since applying noise suppression algorithms implies removing signal contributions and degrading the energy resolution, no noise suppression algorithm is used in the LAr calorimeter in addition to the one on reconstruction level [44].

5.8.1 Energy Weighting in the LAr calorimeter

The energy response to electromagnetically and hadronically interacting particles, the e/π signal ratio, of the H1 LAr calorimeter is measured to be about 1.35 for 10 GeV particles [46] and reflects the non-compensating nature of the calorimeter.

Hadronic showers contain a strongly fluctuating electromagnetic component due to the creation of neutral pions. The energy fraction of this component increases logarithmically with the shower energy. This implies a non-linear energy response for the measurement of hadronic particles. Furthermore, the fluctuations of neutral pion contributions create significant non-Gaussian contributions to the energy measurement, which appear as a constant term of about 4% in the energy resolution function (cf. section 4.2.1). Both difficulties can be overcome by energy weighting, a software method first proposed by the CCFR collaboration and later used in the CDHF experiment to equalise the response of the electromagnetic and hadronic component in a shower [83]. The H1 LAr calorimeter has been designed such that the fine granularity allows to identify the high density energy depositions of the primary electromagnetic component in jets and of the neutral pion component in the hadronic energy deposits. The energy weighting technique exploits the fact that the energy density in the electromagnetic shower component is much larger than for the wide spread pure hadronic component. The following method is applied cell by cell to equalise the response of the calorimeter

due to the electromagnetic and hadronic component in the shower [44]:

$$E_F^i = \omega \cdot E_1^i \quad \text{with} \quad \omega = C_1 \cdot e^{-C_2 \cdot \frac{E_0^i}{V^i}} + C_3 \ , \tag{5.9}$$

where E_0^i and V^i are the energy and volume of a cell, respectively. The weighting function is applied to the dead material corrected energy E_1^i of hadronic objects, if their energy is larger than 10 GeV. The weighting factor ω suppresses the cell energies E_1^i depending on the energy density and contains three parameters, which are determined from detailed Monte Carlo simulations of jets in the H1 LAr calorimeter. C_3 is parameterised as function of the shower energy and the calorimeter location. $C_{1,2}$ are parameterisations of the total shower energy.

For hadronic objects with an energy below 7 GeV the weighting ansatz is replaced by a linear function which corresponds to the signal ratio of electrons and pions in the electromagnetic and hadronic stacks of the LAr calorimeter.

In the energy region between 7 and 10 GeV the parameters are evaluated such that a smooth transition between both methods is obtained.

5.8.2 Improved Hadronic Energy Weighting

The potential of new weighting algorithms has been evaluated using CERN test beam data of an FB1 module. The basic idea [84] was to replace the parameterised functional form in equation 5.9 by tabulated weighting factors depending on the energy density and the energy of the hadronic object. These values were generated using the true energy of the shower tracks in the cells and their measured cell energies in detailed simulation data.

Based on these studies the idea of using weighting tables was followed and an algorithm was developed providing corrections to the true energy scale for the whole H1 LAr calorimeter. The details of the algorithm including results for high and low Q^2 DIS data are described in [85]. The new energy weighting algorithm has been developed in parallel to this analysis and a prototype version is used for the present cross section measurement. A summary of [85] is presented in the following.

The weighting tables are derived with single pions which have been simulated with the detailed simulation (cf. section 4.4). The pion energies are in the range of 0.25 to 300 GeV covering the whole LAr calorimeter. The energy scale of the weighting scheme E_{group} is determined by the sum of connected energy clusters on the E_0 scale in a grid of the azimuth ϕ and the polar angle θ. The true energy of the simulated particle tracks E_{true}^i and the measured energy E_0^i of a cell are used to determine the weighting factors in bins of the energy density ($\log_{10}(E_0^i/V^i)$) and the energy scale ($\log_{10}(E_{group})$). Within each wheel the tables are derived separately for the electromagnetic and hadronic stacks.

The weighting factors are derived such that the reconstructed energy in each cell has the energy of the incident shower particles in that cell. However, zero suppression is applied on the level of the data acquisition as well as topological noise suppression on the reconstruction level [44]. This energy loss E_{loss} is corrected for. In the Monte Carlo simulation the energy loss due to the noise cuts is known on the true scale

and can be parameterised as function of the shower volume of connected clusters. The parameterisations are derived wheel-wise for the electromagnetic and hadronic sections.

No attempt is made in the algorithm to exclude clusters of electromagnetic origin, i.e. electrons or photons.

The following sequence is applied to obtain the measured hadronic energy:

1. Obtain the weighting factor:
   Determine E_{group} as the total energy of connected energy depositions the cell belongs to and the energy density of the cell E_0^i/V^i. This allows to extract the weighting constant.
2. Noise correction:
   Obtain for each group of connected energy the total shower volume and estimate the energy loss due to noise suppression from the parameterisation.
3. Adjustment of the response to single pions in the Monte Carlo simulation:
   The weighted and noise corrected energy is compared to the true energy of the simulated single pions in the LAr calorimeter.
4. Dead material corrections:
   Dead material corrections are applied as implemented in the standard reconstruction software.
5. In situ hadronic energy calibration using *ep* data:
   A wheel-wise hadronic energy calibration is performed with real data and simulated data as described in the following.

The algorithm to reconstruct hadronic energy was derived using simulated data only. Therefore it is not expected that the absolute values of the energy response in data and simulations agree to high precision. In order to improve, both data and simulation are adjusted to the same reference, the precisely calibrated electromagnetic scale (cf. section 5.7). Using the transverse momentum balance of the scattered electron and the hadronic final state in neutral current events, wheel-wise calibration constants are introduced to adjust the hadronic energy scale on average. The quality of the procedure and the errors of the hadronic energy reconstruction are determined by the description of various observables (like p_T, $(E-p_z)$, y_{had}, Q^2) in data by the simulation.

Figure 5.36a shows the p_T balance, $p_{T,had}/p_{T,e}$, as function of the jet energy for the new weighting and for the standard reconstruction. The new algorithm provides a significant improvement of the energy response, especially at energies below ≈ 15 GeV. The decrease at low energies originates mainly from energy losses in the material in front of the LAr calorimeter.

The energy resolution of both reconstruction methods is compared wheel-wise in figure 5.36b in terms of the width of the p_T balance distribution. Clear improvements of the Gaussian shape of the distributions and of the energy resolution are observed. Especially at low energies in the central barrel area the improvements amount to up to 25%.

Furthermore, the observables of the hadronic final state reconstructed with the new weighting algorithm are independent of any kinematical quantities. In particular, no

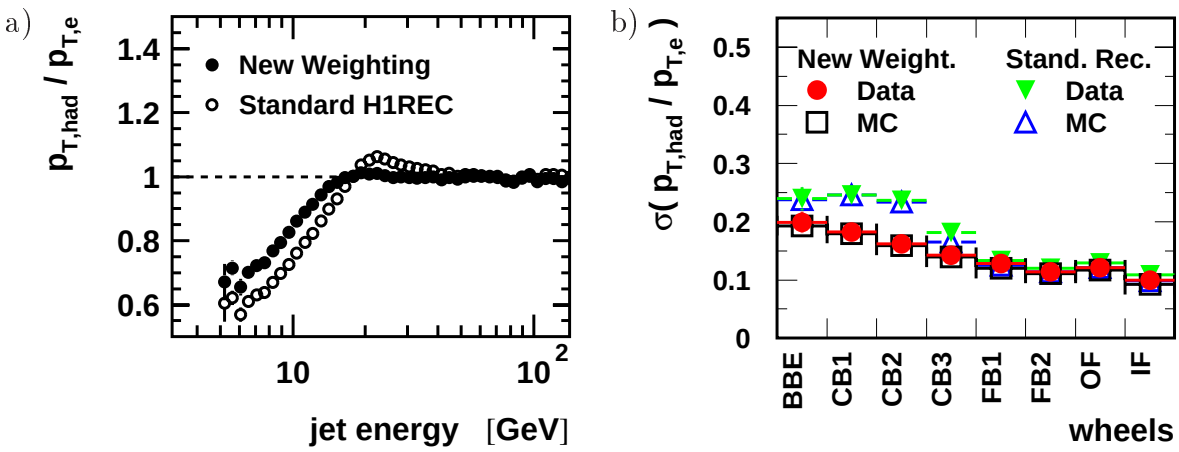

Figure 5.36: a) $p_{T,had}/p_{T,e}$ as function of the jet energy for the new energy weighting and the standard reconstruction. b) Wheel-wise resolution for both methods for data and simulation.

remaining p_T dependence of the energy response is observed. Finally, the new weighting yields excellent agreement between data and simulation at the 1-2% level. For details and further distributions see [85].

5.8.3 Final Hadronic Energy Calibration using *ep* Data

The calibration of the hadronic final state as discussed in the previous section is not able to describe the octant to octant variations in the data which are of the order of a few percent for electromagnetic particles (cf. section 5.7). Furthermore, the relative scale between the electromagnetic and hadronic part of the LAr calorimeter relies on the Monte Carlo simulation. The transverse momentum balance of the electron and the hadronic final state in neutral current events allows the determination of octant- and wheel-wise factors in each calorimeter part by the use of minimisation methods to overcome both deficits.

Events with exactly one electron and one jet are selected to obtain a well defined p_T balance and to allow the proper assignment of the hadronic final state to wheels and octants. $p_{T,had}$ contains wheel- and octant-wise calibration parameters for the electromagnetic and hadronic stacks. In a first step the relative factors between the hadronic and electromagnetic sections of each wheel are evaluated. Aiming for the best energy resolution, the quantity $\Delta p_T/\sigma(p_T)$ is minimised, where

$$\begin{aligned} \Delta p_T &= p_{T,had} - p_{T,e} \ , \\ \sigma(p_T) &\approx \text{const} \cdot \frac{p_{T,e}}{\sqrt{E_{jet}}} \ , \end{aligned} \tag{5.10}$$

to determine the calibration parameters. It is assumed that $\sigma(p_T)/p_T \approx \sigma(E)/E$. The second step adjusts the octant-wise energy response by minimising $\Delta p_T/p_T$.

Figure 5.37a shows the p_T balance for the different LAr calorimeter wheels using all high Q^2 neutral current events entering the cross section measurement. The enlarged event selection partly leads to small deviations of the p_T balance values from one. In

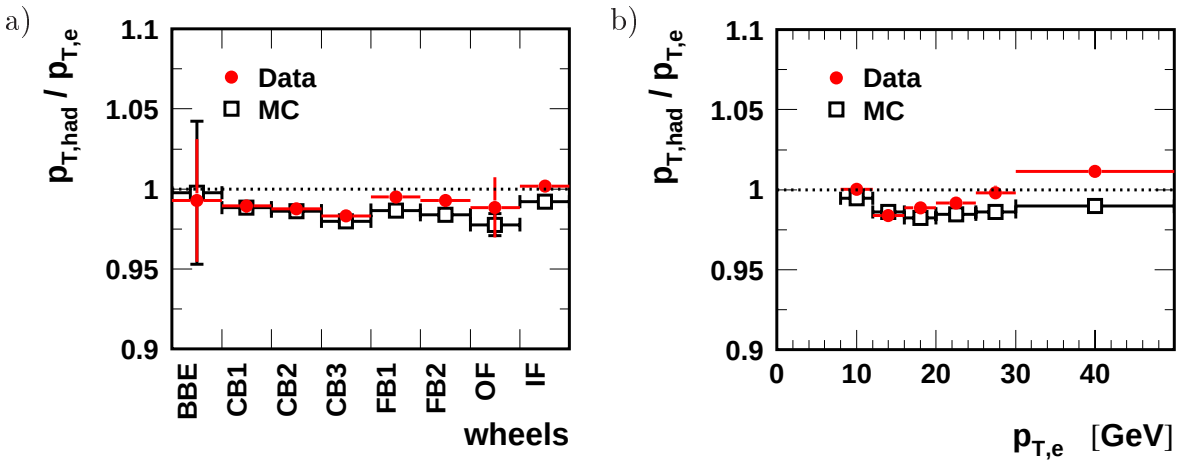

Figure 5.37: Transverse momentum p_t balance with the main contributions in the various LAr calorimeter wheels (a) and as function of p_t^e (b).

addition, the mean values of the peak fits to the p_T balance distributions are shown for each bin, while the calibration procedure adjusted the mean values. However, excellent agreement at the 1% level is observed between data and simulation. The $p_{T,e}$ dependence of the p_T balance is shown in figure 5.37b. Again, the simulation provides a good description of the data. In particular, no large $p_{T,e}$ dependence of the data over Monte Carlo ratio is observed as in [82], which can be attributed to the improvement due to the new energy weighting scheme.

The details of the calibration method and the results are discussed in [85]. The total systematic uncertainty of the energy measurement of the hadronic final state is estimated to be 2% by comparing the description of data and simulation for the p_T and y balances including their dependences on γ_{had}, $p_{T,e}$, y_e, Q^2, m_{jet} and E_{jet}. A correlated error of 1% is assigned due to the error on the electron energy measurement (cf. section 5.7.3).

Spacal calorimeter and instrumented iron

In the kinematic range of this analysis, the Spacal calorimeter provides only little contribution of to the measurement of the hadronic final state. The Spacal longitudinal momentum is shown in figure 5.38. Less than 3% of the events deposit energy in the Spacal calorimeter. The energy contributions in data are well described by simulation. The energy calibration of the Spacal calorimeter has negligible effect on the reconstruction of the hadronic final state. The systematic uncertainty of the Spacal energy calibration is estimated to be 5% and its effect is included in the overall systematic error of the hadronic energy scale.

A similar statement is true for the instrumented iron energy measurement. As shown in figure 5.38b, the data are only reasonably described by simulation. However, the iron serves mainly as tail catcher and measures the contribution of very high energetic particles leaking through the LAr calorimeter. Therefore, the relative contribution of the iron calorimeter is small and the influence of the iron energy calibration on the overall energy measurement of the hadronic final state is negligible.

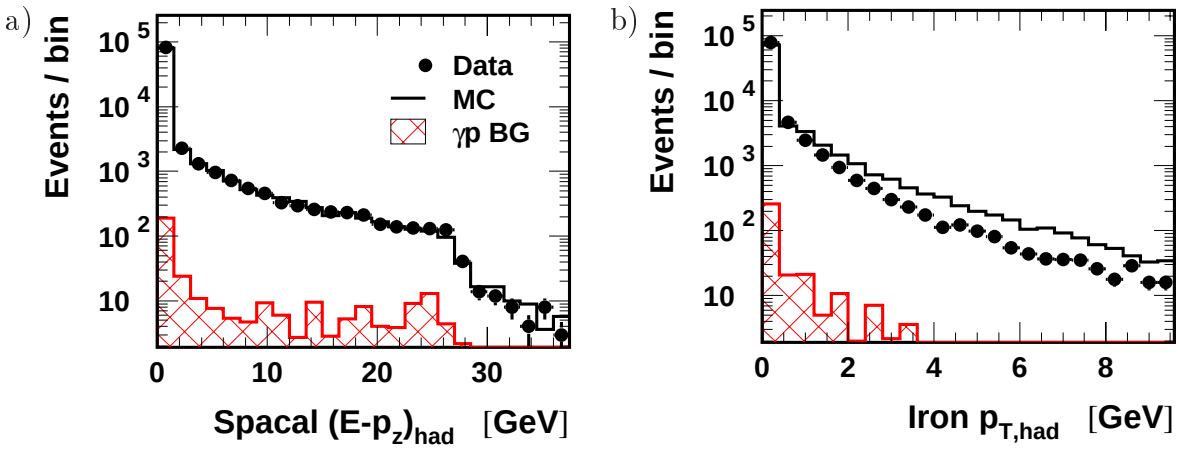

Figure 5.38: Measurements of the Spacal calorimeter $(E - p_z)_{had}$ (a) and the iron $p_{T,had}$ of the hadronic final state. Shown are the distributions for the data (full points), the NC simulation (histogram) and the γp background simulation (hatched). The simulations are normalised to the luminosity of the data.

Chapter 6

Selection of Neutral Current Events

This chapter presents the data selection applied for the inclusive neutral current cross section measurement. The run selection and the luminosity measurement are explained as well as the definition of the acceptance volume of the detector and the treatment of remaining background to ensure high data quality. Finally, the NC selection is summarised and the Monte Carlo simulation is compared to the data.

6.1 Preselection

The data considered in this analysis were taken in the 1999-2000 e^+p running period. The preselection serves a wide range of high Q^2, high p_T and high energy DIS physics. It defines a comprehensive data set which allows to perform all investigations necessary for this analysis. Besides events with identified electron candidates also event samples from other channels, e.g. with high p_T jets, are preselected. Thus redundant and also complementary data samples are provided to ensure that all neutral current events within the considered kinematic range are selected. Double events which appeared in the data sample due to reconstruction defects were purged. The final selection for all channels is the requirement of a reconstructed primary vertex. For efficiency studies, one out of each ten events without a primary vertex is selected as well. The preselection data sample consists of about six million events.

6.2 Run Selection and Luminosity

The data taking is performed in many "runs" which reflect changes in experimental conditions. For this analysis, runs have to be classified as "good" or "medium" according to detector performance, read-out and background conditions.

In addition, all major components of the H1 detector relevant for this analysis have to be fully operational, supplied by nominal high voltage, and must be included in the read-out of the data acquisition. This concerns the LAr calorimeter and trigger, the central drift chambers (CJC1 and CJC2), the luminosity system, the central proportional chambers (CIP/COP) and the time-of-flight detectors (ToF).

To guarantee a certain level of stability during data taking, runs are rejected which correspond to an integrated luminosity of less than 0.2 nb^{-1}.

The run selection is summarised in table 6.1. About 1.8 million data events taken in 6646 runs survive the run selection and enter the further analysis.

run quality	"good" or "medium"
high voltage on and in read-out	LAr, CJC1 and CJC2, lumi, CIP/COP, ToF
run length	$L_{run} > 0.2$ nb^{-1}

Table 6.1: Run selection requirements depending on data taking conditions and operational detector systems.

Time dependent experimental conditions

The 1999-2000 e^+p data taking period is characterised by several run ranges of significantly different experimental conditions. This analysis is mainly affected by changes in the z vertex position due to different beam settings of the HERA collider (cf. figure 6.1) and in the performance of the LAr trigger (cf. section 6.3). Both effects have

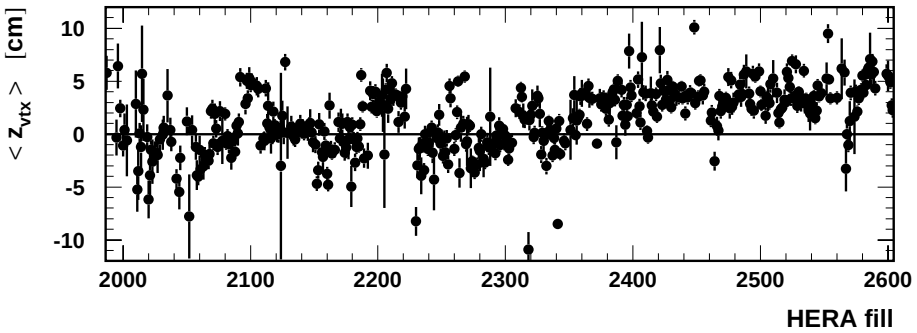

Figure 6.1: Mean z position of the interaction vertex observed for each HERA fill. The variations around the nominal interaction point at $z = 0$ are due to changes in the beam settings.

strong implications on the acceptance of the cross section measurement and thus have to be well described by the simulation.

To account for these time dependent effects, the data are divided into five subsamples as indicated in table 6.2. All detector components relevant for the cross section measurement show stable conditions throughout each run period. This includes the primary vertex efficiency which is not deteriorated by the varying performance of the tracking system (cf. section 5.2).

No attempts have been made to simulate each of these run ranges separately. Instead, an overall Monte Carlo set is used corresponding to constant data taking conditions. In particular, the z vertex distribution is given by a Gaussian of constant mean and width, and a perfect central tracking detector is used. The time dependences of

#	first run	L [pb^{-}1]	$\langle z_{vtx} \rangle$ [cm]	fid. vol.	comment
1	244963	10.3	0.47	1	
2	257590	8.1	0.82	1	broken wire in CJC
3	262144	16.3	0.02	2	start of year 2000
4	269335	20.8	3.25	3	z_{vtx} shift
5	276210	10.5	3.98	4	

Table 6.2: Definition of run periods with significantly different experimental conditions. The respective integrated luminosity L, mean z vertex position and number of fiducial volume definition are shown for each range starting with the specified run number.

the experimental conditions and their correlations are introduced into the simulation by adjusting the Monte Carlo simulation to the data separately for each run period. The simulated events are assigned randomly to the five run ranges such that the event fractions correspond to the respective integrated luminosities in the data. The z vertex distribution is reweighted to that of the data individually for each period (cf. section 5.2). The fiducial volume definition is imposed to both data and simulation of the corresponding run ranges.

Luminosity and Event Yield

The H1 experiment measures the luminosity using the event rate of the well calculable Bethe-Heitler process (cf. section 4.2.6). Since these events are recorded in parallel with the status of all detector systems, the luminosity can be determined for the time periods, where all relevant detector components were operational and the high voltage requirements were fulfilled.

This raw luminosity has to be corrected for the effects of so-called satellite bunches [86]. Due to the bunch structure of the proton beam, ep interactions occur not only close to the nominal interaction point but also occasionally in neighbouring regions which are about 70 cm apart. Due to the restriction of the reconstructed vertex to $|z_{vtx}| < 35$ cm, only a small fraction of events from these satellite bunches enters the event sample of the cross section analysis. However, they contribute to the luminosity measurement, since the interaction point of the almost collinear photon radiation cannot be measured. Therefore, the luminosity is reduced to correspond to the ep interactions within the allowed z_{vertex} range, typically by about 5-10%.

The final data set of the cross section measurement corresponds to an integrated luminosity of [87]

$$\int \mathcal{L}\, dt = 65.99 \text{ pb}^{-1} \ .$$

The uncertainty of the integrated luminosity measurement amounts to 1.5%.

The stability of data taking is monitored by counting the number of selected data events per recorded integrated luminosity. Figure 6.2 shows the event yield with the final selection of this analysis for the entire data set and in addition for the further requirement of $Q^2 > 500$ GeV^2. Indicated are also the five run ranges of the data (cf.

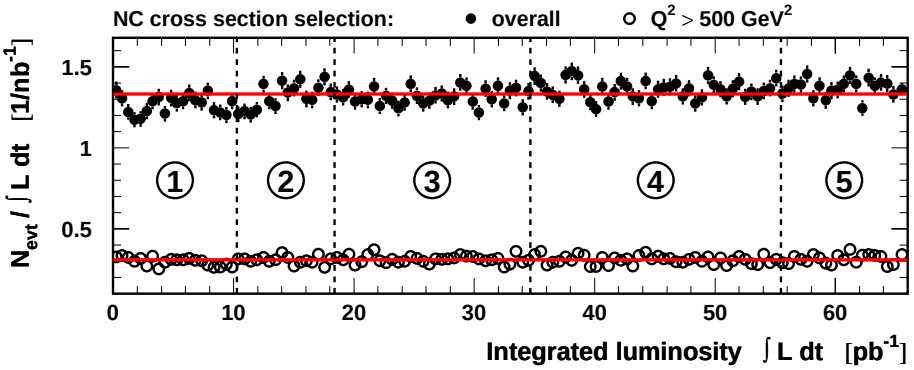

Figure 6.2: Event yield of the final data selection as function of integrated luminosity. The overall data (full points) and those fulfilling in addition $Q^2 > 500$ GeV^2 (open points) are shown. The solid lines indicate the respective average event yield of the complete data set. Each bin contains at least 500 nb^{-1}. Marked and labelled are also the five run periods the data are split into.

table 6.2). The time dependence of the z vertex distribution and of the fiducial volume cuts, which directly affect the acceptance of the measurement, may lead to a different event yield for each period. Within each run range, the event yield is stable and in agreement with statistical fluctuations.

6.3 Trigger and Fiducial Volume Definition

A trigger is needed for a fast and efficient recognition of desired events. Since the event yield is directly proportional to the trigger efficiency, the understanding of the trigger is important for this analysis.

Trigger requirements and efficiency

NC high Q^2 events are triggered essentially by the prominent signature of the scattered electron in the LAr calorimeter. The related subtriggers used for this analysis are s67 and s75 which are both based on LAr trigger elements asking for a minimum energy deposit in the electromagnetic section of the LAr calorimeter as well as on some timing and veto requirements (cf. section 4.3).

The efficiency ϵ_{TE} of a subtrigger or a trigger element (TE) is obtained using a monitor trigger (MT) condition which is independent of the trigger element:

$$\epsilon_{TE} = \frac{\text{number of events triggered by MT and TE}}{\text{number of events triggered by MT}} \,. \tag{6.1}$$

The trigger elements LAr_electron_1 and LAr_electron_2 are monitored by subtrigger s71 (cf. section 4.3), which is mainly based on track information and thus to a very good approximation independent of LAr information.

The efficiencies of the LAr trigger elements depend on the energy of the cluster deposition, showing a pronounced threshold behaviour [82]. A plateau value consistent

with 100% efficiency is reached for electron energies $E'_e > 11$ GeV, which is therefore introduced as event selection cut.

In order to identify inefficient trigger regions of the LAr calorimeter, the trigger efficiency of the LAr_electron_1 trigger element is studied as function of the electron z impact position and azimuth angle ϕ_e as shown in figure 6.3 for $E'_e > 11$ GeV. The

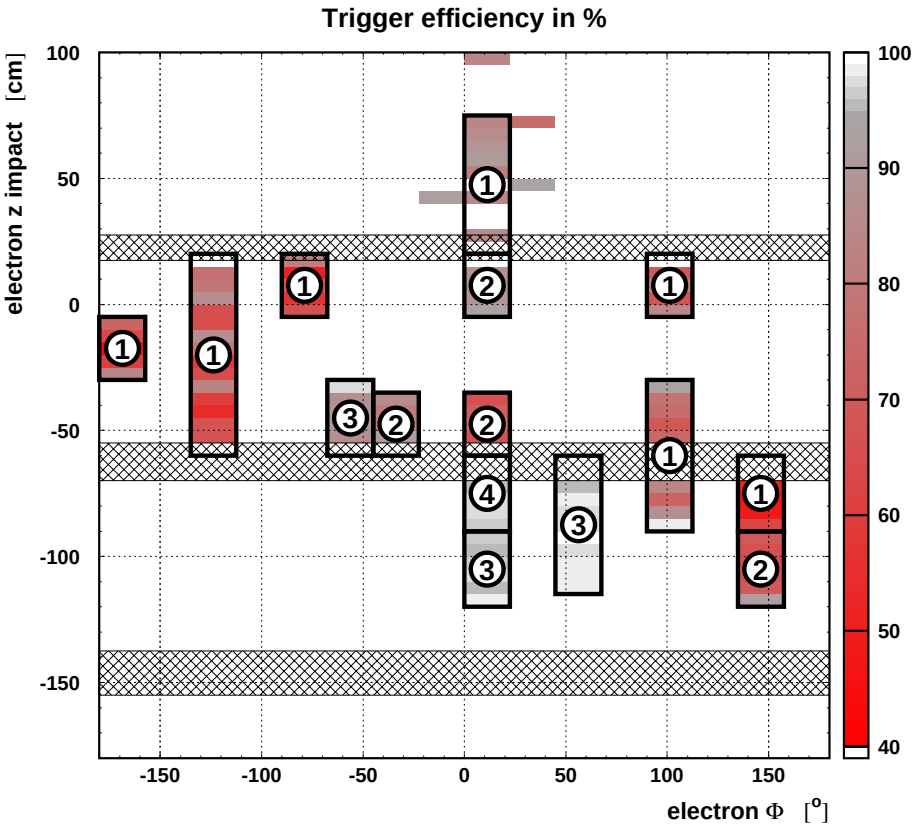

Figure 6.3: Trigger efficiency in the z-ϕ plane of the electron impact position for $E'_e > 11$ GeV. The z cracks (hatched) and the regions of inefficient trigger cells (boxes) are excluded from the analysis. The numbers of the boxes denote the first run period affected (cf. table 6.2).

binning is adapted to the size of the trigger cells, which represent the smallest trigger units of the LAr calorimeter. Most regions are consistent with 100% trigger efficiency. However, there are also areas of significant inefficiencies whose number increases with time. These regions can be attributed to trigger cells, which have been deactivated due to a high noise level, and are excluded from the analysis.

The combination of timing requirements and veto conditions entering subtrigger s67 is also very efficient and yields a total trigger efficiency for neutral current high Q^2 events of above 99.9% for the entire kinematic phase space [88]. The systematic uncertainty on the trigger efficiency is estimated to be 0.3%.

Fiducial volume definition

The fiducial volume cuts ensure the precise measurement of the scattered electron of NC high Q^2 events. The ϕ and z crack regions are excluded to obtain a reliable electron identification (cf. section 5.3), a precise determination of the cluster position (cf. section 5.4), and sufficient resolution of the electron energy measurement (cf. section 5.7). In addition, regions of inefficient LAr trigger cells are excluded from the analysis as function of the time of their appearance (cf. figure 6.3).

The fiducial volume definition is applied using the impact position of the electron which is obtained by linear interpolation between the vertex and the electron cluster position onto a fixed LAr reference plane. In the (x,y) plane of the LAr barrel wheels, the reference surface has an octagon (in the BBE 16-fold polygon) shape with inner radius of 105 cm. The fixed reference surface has the advantage to be independent of the longitudinal shower development of the electron cluster.

6.4 Electron Selection

This section is basically a recapitulation of what has been discussed in section 5.3. The electron identification contains

- a cluster shape analysis indicating an electromagnetically interacting particle,
- an additional isolation w.r.t. hadronic activity to suppress backgrounds, and
- no further validation by requiring an associated track.

The electron identification efficiency in the data ranges between $\sim 99.8\%$ in the CB1 wheel and $\sim 95\%$ in the forward direction and is well reproduced by the simulation. The systematic uncertainty of the electron identification is estimated to be 0.5% for $z_{imp} < 0$ cm and 2% for $z_{imp} \geq 0$ cm.

6.5 Background Rejection

In spite of the clean signature of the scattered electron, background processes may yield a sizeable contribution to the NC event sample. It is differentiated between non-ep background and background which originates from real ep collisions.

Non-ep background

High energetic muons from cosmic rays or the proton beam-halo[1] can cause electromagnetic showers in the LAr calorimeter which may mimic electrons of high transverse momentum.

These events may survive the NC selection requirements, if the muon or a secondary particle leaves a signal in the tracking system which generates a reconstructed event

[1] Halo muons originate from the decay of charged pions produced in proton interactions with the rest gas or the wall of the beam pipe.

vertex or if the muon interaction occurs within the same bunch crossing of a real ep interaction. These events are rare and therefore contribute to the NC event sample most significantly at high Q^2 where the cross section for NC events is small.

Cosmic and halo muons are efficiently rejected using a set of background finding algorithms (QBGFMAR program package, [89]) which identify the events on the basis of their topological patterns of long and narrow signatures in combinations of different detector components:

- Cosmic muons predominantly traverse the detector in vertical direction. They are recognised by
  two opposite muon tracks (instrumented iron) of comparable direction,
  all LAr energy matching the direction of a muon track,
  all LAr energy matching the direction of two opposite iron clusters,
  two CJC tracks of exactly opposite direction, or
  "long" isolated LAr cluster with small electromagnetic energy content.

- Beam-halo muons cross the detector horizontally, almost parallel to the proton beam direction. Their signatures are
  atypical LAr longitudinal energy depositions parallel to the beam line,
  LAr longitudinal pattern matching a deposit in the backward iron endcap,
  horizontal forward muon matching a deposit in the backward iron endcap,
  isolated IF LAr energy matching a deposit in the backward iron endcap, or
  isolated IF LAr energy matching a deposit in the Spacal.

The rejection power of these finders is above 85% for cosmic muons and about 95% for halo muons while the NC signal inefficiencies are below 0.5% [90]. Actually, the background finders reject 0.8% data events and 0.3% simulated events.

Beam-gas and beam-wall interactions may also cause background contributions when the produced particles are scattered into the H1 detector. The typical signatures are energy deposits in the backward detector components accompanied by many tracks which point into the forward direction. The large energy depositions in the backward region lead to large values of the reconstructed $(E-p_z)_{tot}$ of the event. For neutral current events, the nominal $(E-p_z)_{tot}$ is 55 GeV (cf. equation 2.22) and values up to ~ 75 GeV can be reached due to fluctuations in the energy measurement. Thus, a requirement of

$$(E-p_z)_{tot} < 75 \text{ GeV} \tag{6.2}$$

is introduced to reject the remaining background contributions from beam-gas and beam-wall interactions.

Applying the final data selection, the non-ep background is suppressed to a negligible level. This has been verified for random events and in particular for all events with $Q^2 > 10000$ GeV^2 by a visual scan where no background-like events have been found. Potential systematic uncertainties are included in the systematic error of the subtraction of ep-induced background discussed below.

ep-induced background

Photoproduction is the main source of *ep*-induced background which may contribute to the NC event sample. Further contributions arise from low Q^2 DIS events, QED-Compton scattering, and lepton-pair production.

- **Photoproduction and low Q^2 DIS background:** The dominant background contribution is due to photoproduction events, where the scattered electron escapes detection by the main detector through the backward beam pipe and a final state particle is misidentified as an electron. This contribution is efficiently suppressed by the restriction of the measurement to $y_e < 0.9$ and by the additional electron isolation requirement (cf. section 5.3). The latter demands that in a cone of size $R = 1$ around the electron the transverse energy sum $E_{T,had,cone(e)}$ of calorimetric depositions apart from the electron candidate is allowed to be at maximum 10% of the electron transverse momentum $p_{T,e}$.

  A similar rejection is obtained for NC low Q^2 DIS background, where the electron is scattered into the Spacal calorimeter, but again a final state particle is misidentified as an electron. The main contribution comes from events with two jets where one of them fakes the electron and the other accounts for the transverse momentum balance. Due to the $1/Q^4$ dependence of the cross section, this contribution is even further suppressed than that of γp. However, a few events with $Q^2 \sim 1000$ GeV^2 and large $y_e \lesssim 0.9$ have been observed which have a compact energy deposition in the Spacal calorimeter that is not recognised to be an electron. This kind of events is rejected if the Spacal energy deposit is compatible with being the scattered electron of a NC low Q^2 event.
- **Elastic QED-Compton and $\gamma\gamma$ events:** QED-Compton and $\gamma\gamma$ events may pass the NC selection if an electron (or photon) is scattered into the acceptance of the LAr calorimeter. The contribution to the NC data sample is efficiently suppressed by detecting their characteristic signature: They have two localised electromagnetic energy deposits, low track multiplicity, at most small energy deposits in the hadronic section of the LAr calorimeter ($E_{had}/E_{tot} < 15\%$), and no activity in the proton remnant fragmentation region ($\eta > 3$). Furthermore rejected are events which contain only two identified electron (or photon) candidates being well balanced in transverse momentum. As obtained from simulated NC events, the signal inefficiency is below 0.3% while about 95% of the background is excluded. The residual background contribution is negligible.

The only remaining background contribution comes from γp events and is statistically subtracted from the data. At large y, it amounts to about 1-2% on average and increases to almost 5% at highest Q^2. Otherwise the background contribution is negligibly small.

The correct simulation of the background events has been verified with real data for a phase space region which is dominated by photoproduction background. For this purpose, events are selected where the electron is detected in the electron tagger of the luminosity system. The agreement between data and simulation is found to be within 30% which thus is quoted as the systematic uncertainty of the subtracted γp background.

6.6 Final Selection and Control Distributions

The NC selection requirements are summarised below:

- run selection
- events triggered by s67, s71 or s75
- reconstructed primary interaction vertex with $|z_{vtx}| < 35$ cm
- electron identification as electromagnetic particle with additional isolation
- $E'_e > 11$ GeV
- $35 < E - p_z < 75$ GeV
- $0.05 < y_e < 0.9$
- LAr calorimeter acceptance volume, exclude electrons in z and ϕ cracks:
  $z_{e,imp} > -180$ cm,
  $z_{e,imp} \notin [-155; -137.5], [-70; -55], [17.5; 27.5], [100; 120]$ cm,
  $|\mathrm{mod}(\phi_{e,imp}, 45°)| < 2°$
- LAr trigger acceptance volume
- rejection of non-ep background
- rejection of NC low Q^2, elastic QED-Compton and $\gamma\gamma$ events
- visual scan of events with $Q^2 > 10000$ GeV^2

In summary 91423 events are selected and define the data sample for the cross section measurement.

The neutral current event sample is presented in the following to demonstrate that the simulation provides a good description of the data. Thus, the Monte Carlo simulation is suitable to be used for the acceptance correction of the data at the cross section determination which is presented in the following chapter.

In all distributions shown below, the simulations of neutral current and background events are normalised to the luminosity of the data. The error bars represent statistical errors only.

The z vertex distributions of data and simulation have already been shown in figure 5.6, verifying that the simulation reproduces the beam dependences observed in the data.

The variables of the scattered electron are presented in figure 6.4. The energy distribution reveals a sharp maximum for the region of the kinematic peak ($E'_e \approx E_e$) and extends up to values of a few hundred GeV. The spectrum of the polar angle falls rapidly towards small angles reflecting the $1/Q^4$ dependence of the cross section. Apart from an offset in normalisation of about 3% (see below), the data are well described by the simulation. The contamination of γp background appears mainly at low electron energies and extends over the whole range of the polar angle.

Figure 6.5 shows control distributions for the hadronic final state. Good agreement is observed between data and simulation for the transverse momentum $p_{T,had}$ and the

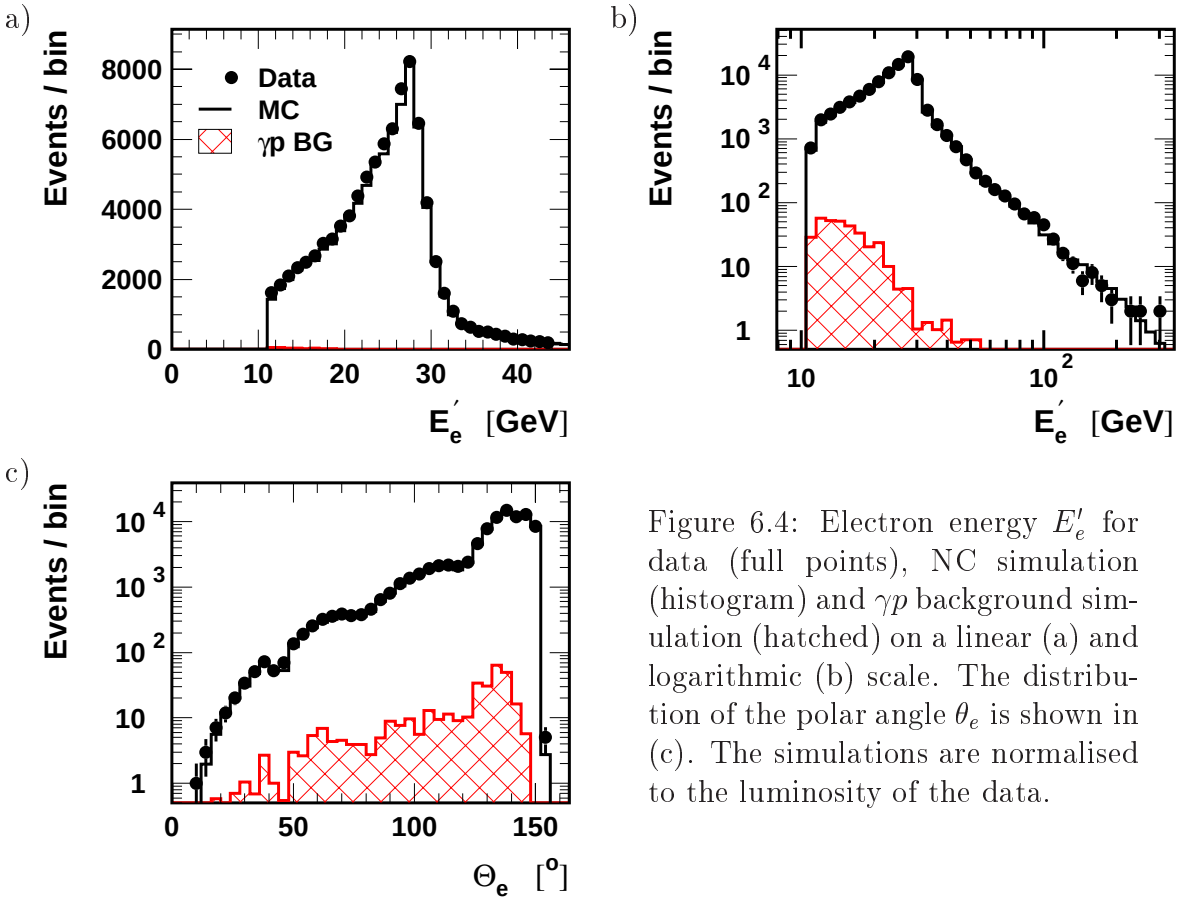

Figure 6.4: Electron energy E'_e for data (full points), NC simulation (histogram) and γp background simulation (hatched) on a linear (a) and logarithmic (b) scale. The distribution of the polar angle θ_e is shown in (c). The simulations are normalised to the luminosity of the data.

inclusive hadron angle γ_{had}. The same is true for the transverse momentum balance between the hadronic final state and the scattered electron $p_{T,had}/p_{T,e}$ which furthermore demonstrates a consistent absolute electromagnetic and hadronic energy scale.

Finally, overall event variables are shown in figure 6.6. For both the total transverse momentum measured with the calorimeters, $p_{T,calo}$, and the total longitudinal momentum balance, $(E-p_z)_{tot}$, the simulation provides a reasonable description of the data. Since the electron has been proven to be well described, the remaining deviations can be attributed to the measurement of the hadronic final. However, the quantities of the hadronic final state only yield a marginal contribution to the cross section measurement. Thus the residual deviations between data and simulation can be neglected.

In order to discuss the absolute normalisation between data and Monte Carlo prediction, figure 6.7 presents the event ratio of data to simulation for the five run periods. Except for the first period, the event yield for the data is significantly higher compared to the prediction by simulation, especially for the fourth run range. However, taking into account the uncertainty of the integrated luminosity of 1.5%, the overall excess is a 2σ effect. Nevertheless, extensive studies have been performed separately for each period. Apart from the time dependent effects which are already considered by the treatment of the four run periods, nothing particular has been found and the deviation could not be traced back to a known source.

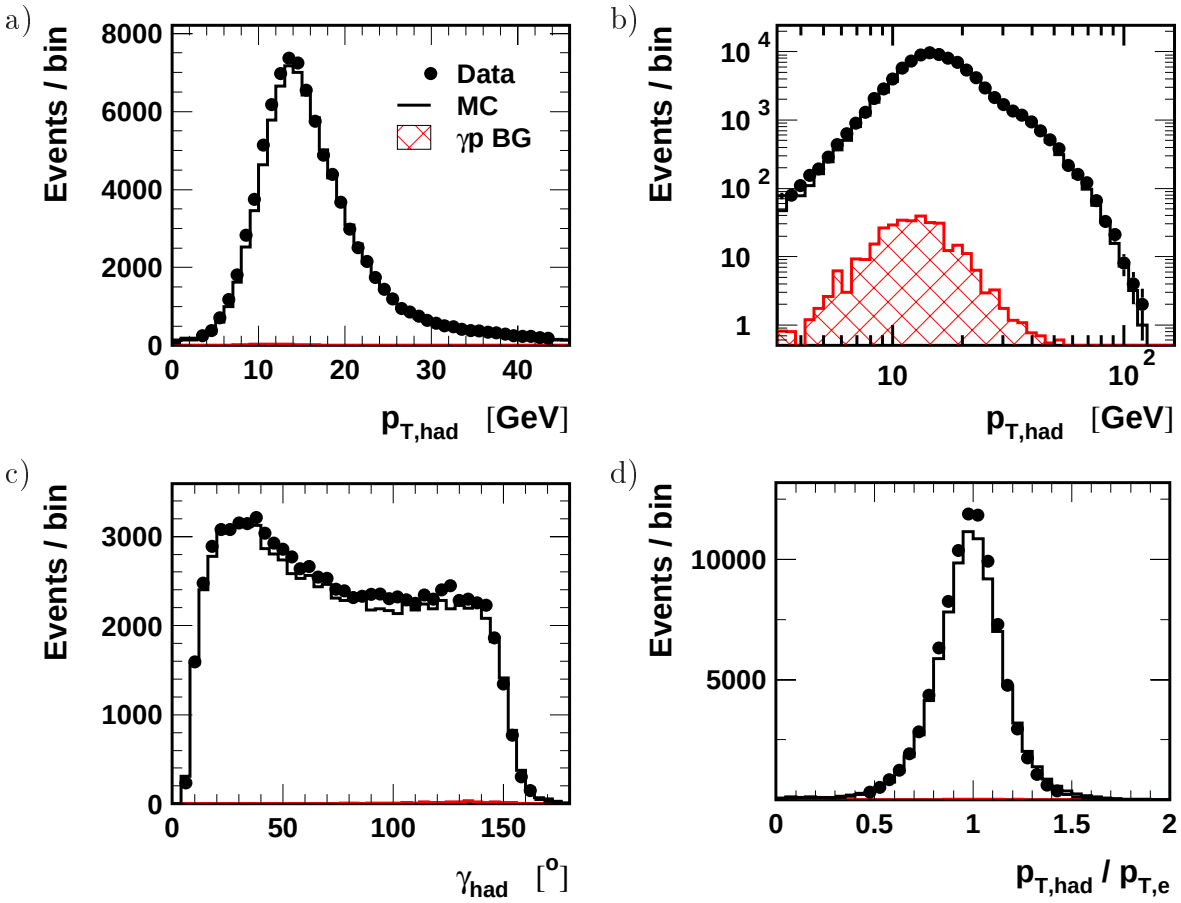

Figure 6.5: Transverse momentum $p_{T,had}$ of the hadronic final state for data (full points), NC simulation (histogram) and γp background simulation (hatched) on a linear (a) and logarithmic (b) scale. The distribution of the inclusive hadron angle γ_{had} is shown in (c), the ratio of the hadronic transverse momentum to that of the electron $p_{T,had}/p_{T,e}$ in (d). The simulations are normalised to the luminosity of the data.

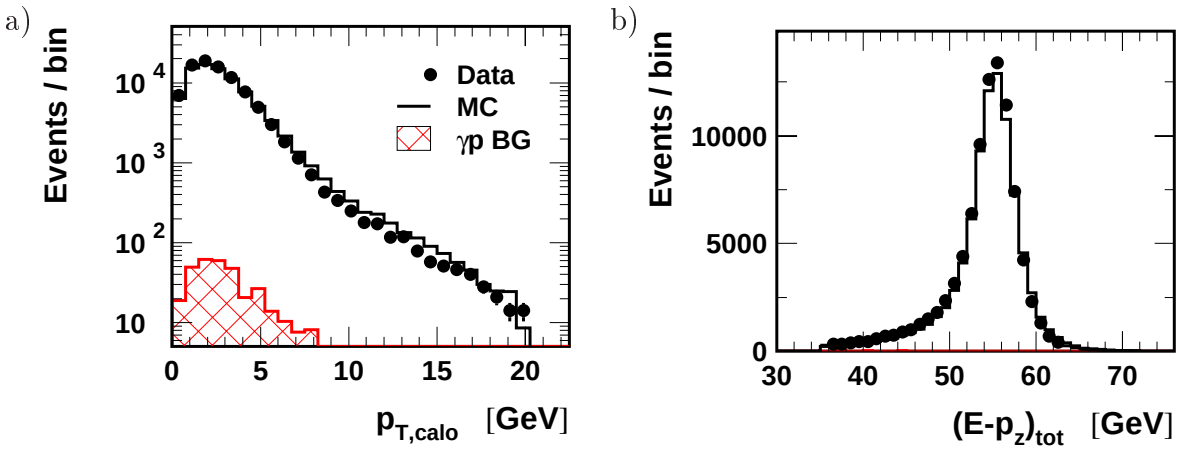

Figure 6.6: Control distributions of the overall event including the scattered electron and the hadronic final state: (a) Total transverse momentum $p_{T,calo}$ measured in the calorimeters for data (full points), NC simulation (histogram) and γp background simulation (hatched). (b) Total longitudinal momentum balance $(E-p_z)_{tot}$ of the event. The simulations are normalised to the luminosity of the data.

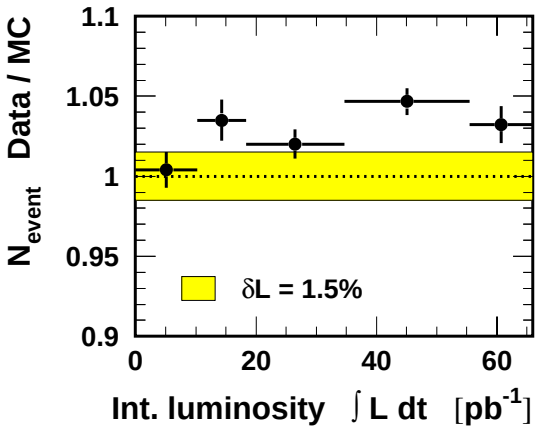

Figure 6.7: Event ratio of data to simulation as function of integrated luminosity, separated into the five run periods of different data taking conditions (cf. table 6.2). The Monte Carlo events are normalised to the luminosity of the data. The yellow band indicates the uncertainty of 1.5% assigned to the luminosity measurement.

Chapter 7

Cross Section Measurement

In this chapter, the determination of the neutral current cross section is presented. The division of the kinematic plane in bins of Q^2 and x is defined and the extraction procedure of the cross section, which is based on the number of events measured in each bin, is described. The effects of the dominant systematic uncertainties on the cross section, which have been determined in the previous chapters, are discussed. Finally, the cross section results are presented and compared to other analyses.

The obtained result provides the foundation for the subsequent search for physics beyond the Standard Model. Hence, the present analysis aims for a comprehensible and systematically well understood cross section measurement. In this context, the focus is put on the high Q^2 region and at least moderate values of x and y.

7.1 Cross Section Measurement Procedure

This section describes the cross section determination. The kinematic plane is divided into bins of Q^2 and x. The cross section is defined by the number of events observed in a bin and the integrated luminosity (cf. equation 4.3). An imperfect detector and radiation effects imply inefficiencies and migrations of reconstructed events between the bins which have to be corrected for.

Binning definition

The cross section is measured in this analysis in bins of Q^2 and x of the kinematic plane. The definition of the bins is visualised in figure 7.1 and follows previous measurements [27, 78]. The bin sizes are chosen according to the statistical precision and the resolution of the Q^2 and x reconstruction provided by the electron (e) method. The resolution is always better than the width of the respective bin [82][1].

Acceptance effects are studied with simulated events which provide both reconstructed and generated true variables. The stability (S) and purity (P) variables are

[1] This statement is true for both the e and $e\Sigma$ reconstruction methods which provide comparable precision in the kinematic range of this analysis.

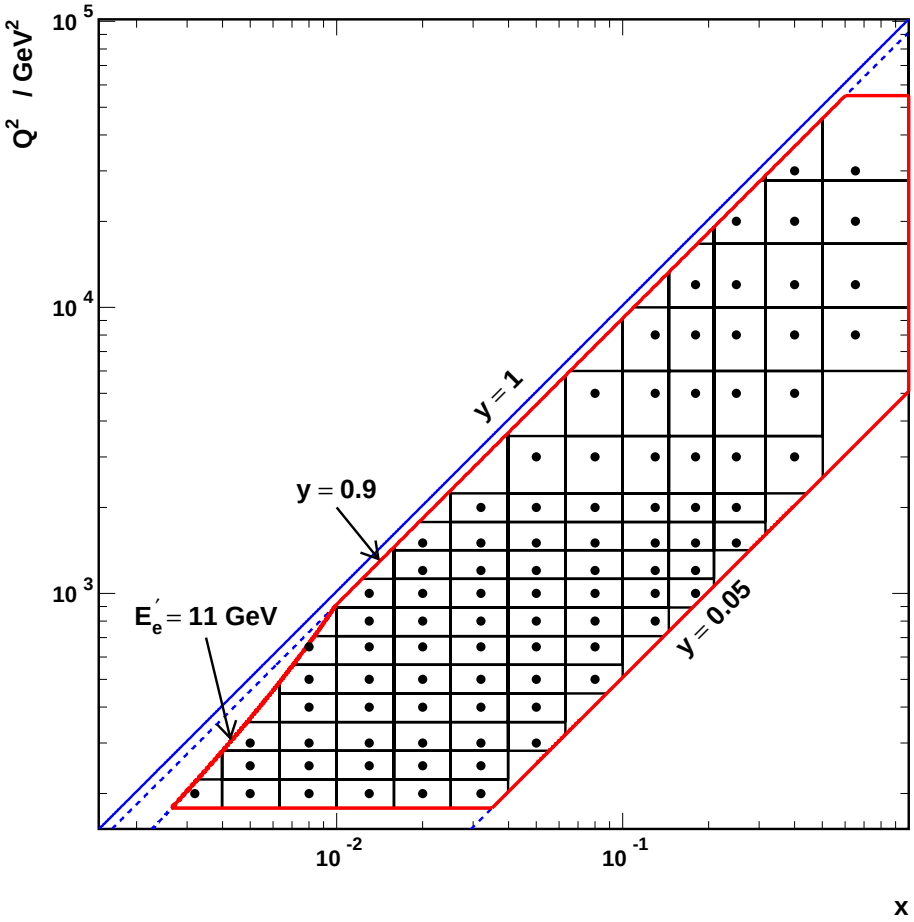

Figure 7.1: Definition of the cross sections bins in the Q^2-x plane. The bin boundaries are indicated by the vertical and horizontal lines, the centres are marked by full points. Also shown are the lower and upper y cuts and the $E'_e = 11$ GeV requirement.

introduced to quantify the migrations between different cross section bins:

$$\begin{aligned} S &= N^{MC}_{rec+gen}/N^{MC}_{gen+sel} \ , \\ P &= N^{MC}_{rec+gen}/N^{MC}_{rec} \ . \end{aligned} \tag{7.1}$$

The stability gives the fraction of selected events which are reconstructed in the same bin they were generated in. In comparison, the purity denotes the fraction of events generated in the same bin they are reconstructed in. With other words, the stability and purity (strictly $1-S$ and $1-P$) quantify the fraction of events migrating out of and into the bin, respectively. They are a measure of the correlations between generated, true variables and their reconstructed values.

For the bins of the cross section measurement, both stability and purity are required to exceed 30%. This allows to apply the acceptance corrections bin by bin to the data as obtained from simulation. The stability and purity are shown in figure 7.2 as determined from simulation using the electron method for the kinematic reconstruction. They both reach large values of 70-80% at low values of x corresponding to large y

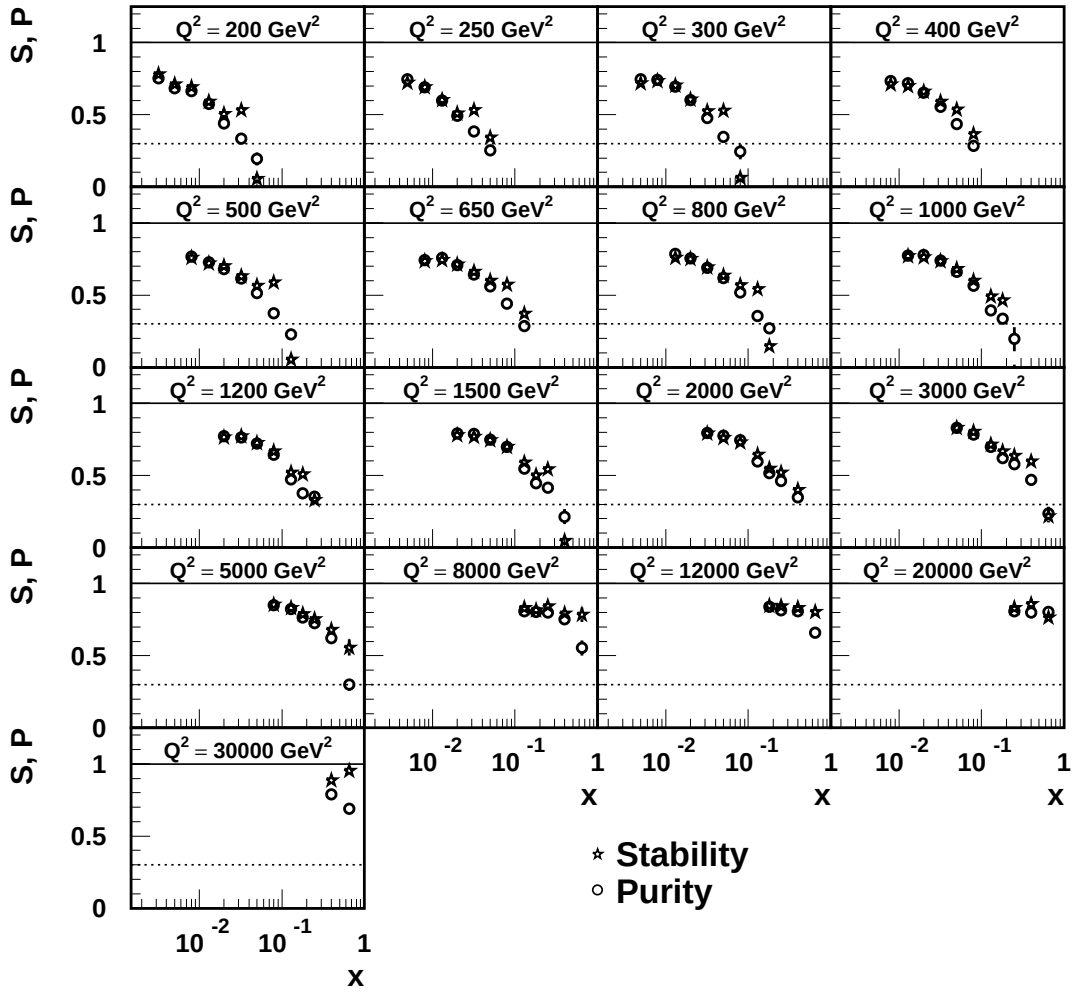

Figure 7.2: Stability and purity of the cross section bins reconstructing the kinematics with the electron method.

where the electron reconstruction method provides excellent resolution (cf. section 2.4). The stability and purity get worse with increasing x, i.e. decreasing y, in particular for y approaching the minimum requirement of $y > 0.05$.

The acceptance of a bin is defined as

$$A = N_{rec}^{MC} / N_{gen}^{MC} \tag{7.2}$$

and quantifies the fraction of reconstructed events compared to all events which were generated in that bin. The acceptance comprises two parts, one is the intrinsic acceptance of the detector, that is where a measurement in principle is possible. The second contribution is given by the efficiency ϵ that an event within the detector acceptance is indeed measured and contains e.g. the electron identification efficiency. Thus, the acceptance A represents the overall probability to measure an event. The acceptance enters directly into the cross section calculation and is larger than 30% as well for all bins of this analysis.

Extraction of the Cross Section

In principle, measuring a cross section is as simple as counting events. However, the number of observed events needs to be corrected to the number of real events given a perfect detector with complete coverage, no cracks, perfect particle recognition, infinite resolution, no background contamination, no radiation contributions and so on. In the present analysis, the cross section is corrected for all these effects bin by bin.

The cross section measured in a single bin in x and Q^2 is defined by

$$\frac{d^2\sigma}{dx\,dQ^2} = \frac{N^{data} - N^{bg}}{\mathcal{L}} \cdot \frac{1}{A} \cdot \delta^{bc} \cdot \frac{1}{1+\delta^{\mathrm{rad}}} \ , \tag{7.3}$$

where

- N^{data} is the number of data events observed in that bin.
- N^{bg} is the number of background events which survive the selection and is estimated by simulation.
- $\mathcal{L}$ denotes the total integrated luminosity of the data.
- A is the acceptance as defined in equation 7.2 and accounts for the detector acceptance and efficiencies.
- δ^{bc} is the bin centre correction and accounts for the finite bin size as well as for the fact that the centre of gravity of the x and Q^2 distributions in general does not agree with the bin centre. It converts the cross section averaged over a bin i of finite size $\Delta x_i = x_{i,max} - x_{i,min}$ and $\Delta Q_i^2 = Q^2_{i,max} - Q^2_{i,min}$ into that at the chosen bin centre position $(x_{i,c}, Q^2_{i,c})$,

$$\delta^{bc} = \frac{\left.\dfrac{d^2\sigma}{dx\,dQ^2}\right|_{x=x_{i,c},Q^2=Q^2_{i,c}}}{\displaystyle\int_{x_{i,min}}^{x_{i,max}} \int_{Q^2_{i,min}}^{Q^2_{i,max}} \frac{d^2\sigma}{dx\,dQ^2}\,dx\,dQ^2} \ .$$

- δ^{rad} contains the radiative QED corrections as discussed in section 2.3.

Whenever accessible, the efficiencies and the acceptances are determined directly from the data and the simulation is adapted accordingly (cf. chapters 5 and 6) to reproduce the data. The acceptance correction is finally taken from the Monte Carlo prediction (cf. equation 7.2),

$$A = A^{MC} \ . \tag{7.4}$$

The bin centre correction is obtained solely from simulation according to

$$\frac{d^2\sigma^{MC}}{dx\,dQ^2} = \frac{N^{MC}_{rec}}{\mathcal{L}^{MC} \cdot A^{MC}} \cdot \delta^{bc} \ , \tag{7.5}$$

where $\mathcal{L}^{MC}$ is the luminosity represented by the Monte Carlo events. The QED radiative corrections are taken into account by using a Monte Carlo simulation which contains radiation processes and comparing to a cross section calculation on born level,

$$\frac{1}{1+\delta^{\text{rad}}} = \frac{\left.\frac{d^2\sigma^{SM}}{dx\,dQ^2}\right|_{\text{Born}}}{\left.\frac{d^2\sigma^{MC}}{dx\,dQ^2}\right|_{\text{rad}}} \; . \tag{7.6}$$

Applying equations 7.4-7.6, the cross section definition of equation 7.3 simplifies to:

$$\frac{d^2\sigma}{dx\,dQ^2} = \frac{N^{data} - N^{bg}}{N^{MC}_{rec}} \cdot \frac{\mathcal{L}^{MC}}{\mathcal{L}} \cdot \left.\frac{d^2\sigma^{SM}}{dx\,dQ^2}\right|_{\text{Born}} \; . \tag{7.7}$$

This procedure defines the cross section measurement for each bin in x and Q^2. It is important to stress that the corrections to the cross section which are obtained from the simulation depend on the cross section input, in particular on the parton densities used for the generation of the Monte Carlo events. That is why for the present analysis, the simulated events are reweighted to the cross section prediction corresponding to the H1 1997 PDF Fit (cf. sections 2.5 and 4.4) which has been proven to reproduce the H1 data [27]. In addition, the control distributions presented in section 6.6 provide confidence that the Monte Carlo simulation is well suited for the determination of the corrections.

7.2 Systematic Uncertainties

The sources of systematic uncertainties relevant for the NC cross section measurement and their actual size have been discussed in the previous chapters. This section describes their implications on the measured cross section.

The systematic uncertainties are separated into correlated and uncorrelated parts w.r.t. the cross section measurement. A correlated error affects the cross section measurement of all bins simultaneously, e.g. the correlated error on the electron energy scale represents a possible overall shift in the absolute energy scale which may imply certain modifications to the cross section result. Of course, correlated errors may lead to different changes to the cross section in different kinematic regions. Contrary, uncorrelated uncertainties reflect local fluctuations or deficiencies and may affect the cross section of each bin separately. The total systematic uncertainty is obtained by adding the individual contributions in quadrature. All errors are assumed to be Gaussian and reflect the 1σ range of a Gaussian distribution.

Determination of the systematic cross section uncertainties

The general implications of various systematic error sources on the cross section measurement concerning efficiency and resolution effects of the detector have been investigated in [74] using a fast parameterisation of the detector response. However, the final

dependences of the cross section are derived directly from the data. Actually, the full simulation is used to minimise the influence of statistical fluctuations and the results are cross-checked with the data.

The implication on the cross section result due to systematic effects is studied for each source of systematic uncertainties. Cross sections are determined by varying a variable according to the estimated systematic error and the corresponding change in cross section is evaluated bin by bin. To minimise the impact of finite statistics and to identify non-linear cross section dependences on the systematic shifts, the variations are performed repeatedly within the typical range covered by the systematic error. The actual systematic error on the cross section is taken from a smooth parameterisation of the observed dependence.

The procedure is illustrated in figure 7.3 for the correlated uncertainty of the electron energy scale for selected bins of the single differential cross section $d\sigma/dQ^2$ using the e method for the kinematic reconstruction. At low Q^2, the cross section decreases

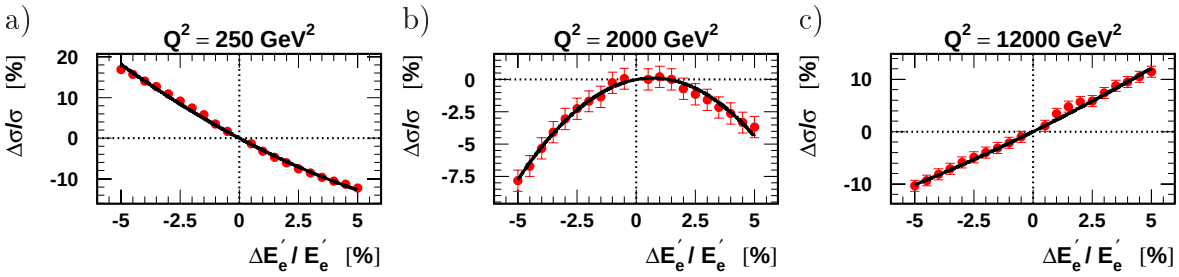

Figure 7.3: Dependence of the single differential cross section $d\sigma/dQ^2$ on systematic shifts of the electron energy scale for $Q^2 = 250$ (a), 2000 (b), and 12000 (c) GeV^2. The solid curves represent the respective fit of a quadratic curve to the points.

with rising energy scale while the opposite dependence is observed at large values of Q^2. At intermediate Q^2, the distribution turns over between both cases showing a strong non-linear behaviour. Here, the cross section measurement is rather independent of the electron energy scale. Even though error propagation (cf. equation 2.26) yields $\delta Q_e^2/Q_e^2 \sim \delta E_e'/E_e'$ and therefore predicts a rising slope, effects of migrations and selection cuts may dominate the cross section dependence.

The cross section dependence is parameterised by a quadratic curve which is required to cross the origin. The value of the function for the estimated size of the systematic error defines the systematic uncertainty of the cross section. For the uncorrelated errors, the mean value is taken from the shifts for positive and negative changes. The correlated uncertainties are given for both directions to provide access to their asymmetric behaviour.

Figure 7.4 shows the cross section dependence on the electron energy scale within the same Q^2 bins as above each for a selected x bin of the double differential cross section $d^2\sigma/dx\,dQ^2$. In addition, the $e\Sigma$ reconstruction method is compared to the e method, revealing clear difference between both methods and indicating the impact of the choice of the reconstruction method. There are tremendous differences in size and shape of the cross section modifications between both reconstructions methods

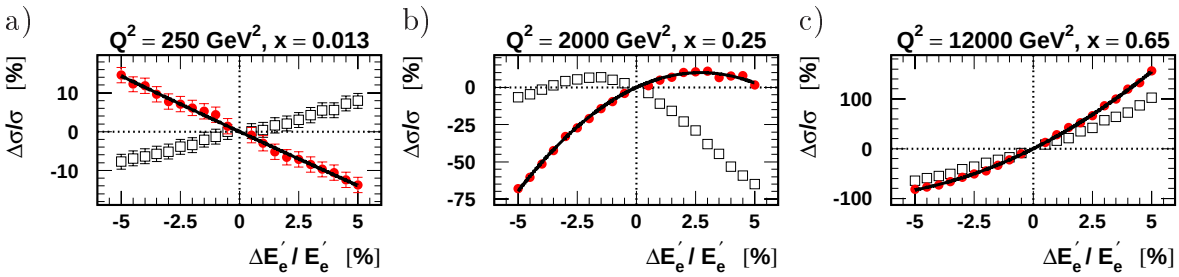

Figure 7.4: (a-c) Dependence of the double differential cross section $d^2\sigma/dx\,dQ^2$ on systematic shifts of the electron energy scale for the same Q^2 bins as in figure 7.3 each for a selected x bin. Shown are the results using the e method (full points) and the $e\Sigma$ method (open squares) for the kinematic reconstruction. The solid curve represents the fit of a quadratic curve to the points of the e method.

and also for each individual method in different parts of the phase space. For given Q^2, the contributions of all x bins average to the result of the single differential cross section. The comparison of the absolute values of figures 7.3 and 7.4 suggests large cancellations between different x bins.

Results of systematic uncertainties

The systematic uncertainties of the NC cross section are presented in the following. They were determined for the e method which is used for the kinematic reconstruction.

- Electron energy scale, cf. section 5.7:
  The total uncertainty of the electron energy scale $\delta^{tot}_{E_e}$ depends on the z impact position of the electron at the surface of the LAr calorimeter and is estimated to be
  0.7% for $z_{imp} \leq -150$ cm (BBE wheel),
  0.5% for $-150 < z_{imp} \leq 20$ cm (CB1,CB2),
  1.5% for $20 < z_{imp} \leq 110$ cm (CB3),
  3.0% for $z_{imp} > 110$ cm (FB1 and more forward).
  The correlated part contributes with 0.3% to the total uncertainty and comes mainly from the possible bias of the calibration method. The corresponding uncertainty of the single differential cross section is of the order of 1-2% at low Q^2, decreases to a negligible level (<0.5%) for $Q^2 \approx 2000$ GeV^2 and reaches 10% at highest Q^2 values. The error of the double differential cross section rises with x from $\lesssim 0.5\%$ to $\sim 1.5\%$ at low and intermediate Q^2 values and reaches up to 40(8)% at $x = 0.65$ and highest Q^2 for the uncorrelated (correlated) part.
- Electron polar angle, cf. section 5.6:
  The correlated uncertainty of the electron polar angle is 1 mrad and 3 mrad for $z_{imp} \leq 0$ and $z_{imp} > 0$ cm, respectively. This leads to systematic error of the cross section measurement of typically 0.5% and increases for $Q^2 \gtrsim 5000$ GeV^2 reaching about 5% for largest values of x.

- Electron identification, cf. section 5.3:
  An uncorrelated uncertainty originates from the electron identification efficiency and is estimated to be 0.5% for $z_{imp} < 0$ cm and 2% for $z_{imp} \geq 0$ cm. This affects the cross section with a systematic uncertainty of 0.5% in the better part of the phase space, approaching 2% for $Q^2 \gtrsim 5000$ GeV^2.
- Hadronic energy scale, cf. section 5.8:
  An uncorrelated error of 1.7% and a correlated error of 1% is assigned to the hadronic energy measurement, resulting in a total systematic uncertainty of 2%. Since the e method is used for the kinematic reconstruction, the impact on the cross section is negligible ($\lesssim 0.1\%$ in general, $\sim 1\%$ at highest Q^2).
- Photoproduction background, cf. section 6.5:
  A 30% correlated uncertainty is assigned to the subtracted photoproduction background. This leads to an average systematic error of 0.5% of the cross section measurement at large values of y and has negligible effect otherwise.
- Trigger efficiency, cf. section 6.3:
  A 0.3% uncorrelated error is considered for the trigger efficiency which converts directly into an uncorrelated systematic uncertainty of 0.3% on the cross section measurement.
- QED radiative corrections, cf. section 2.3:
  Comparisons of different calculations of the QED radiative corrections in the leading log approximation have shown agreement on the few percent level [16, 82]. Thus, an uncorrelated error of 1% is estimated for the QED radiative corrections themselves which propagates directly to the cross section measurement.
- Luminosity measurement, cf. section 6.2:
  The uncertainty on the luminosity measurement has been determined to be 1.5%. It represents a purely correlated error of the cross section of the same size, since the luminosity provides a common normalisation factor for all cross section points.

Systematic effects due to beam energy shifts have been found to be negligible. For a few percent of the data the beam energies are about 0.1% below the nominal value. The statistical uncertainty corresponding to the finite number of Monte Carlo events is treated as uncorrelated systematic error. The tables of the systematic uncertainties for the single and double differential NC cross sections are given in appendix A.

A summary of the systematic error sources is presented in table 7.1 along with their typical implications on the cross section measurement for the majority of the kinematic phase space and in extreme kinematical regions. The uncertainty of the electron energy scale provides the main contribution to the systematic error of the cross section measurement. However, due to the large improvements of the electron energy calibration and also of the electron angle measurement, other sources than the electron reconstruction become of comparable size in parts of the phase space. The QED radiative corrections even yield an increased sensitivity to theoretical issues.

The total correlated and uncorrelated systematic uncertainties are presented in figure 7.5 for the single and double differential cross section measurements. They are compared to the statistical error of the data which increases with Q^2 and x according to

Source	Systematic error contributions [%]		
	general	maximum	
Electron energy (unc.)	$0.5 - 2$	$10 - 40$	for $x = 0.65$
Electron energy (cor.)	$0.5 - 1.5$	8	for $x = 0.65$
Electron polar angle (cor.)	0.5	5	for highest Q^2 and x
Electron ID (unc.)	0.5	2	for $Q^2 \gtrsim 5000$ GeV^2
Hadronic energy (unc./cor.)	0.1	1	for highest Q^2
Background subtraction (cor.)	0	0.5	at high y
Trigger efficiency (unc.)	0.3	0.3	
QED rad. corrections (unc.)	1	1	
Luminosity (cor.)	1.5	1.5	

Table 7.1: Typical and maximum systematic error contributions to the NC cross section.

the cross section prediction. The step-down of the statistical error between $Q^2 = 2000$ and 3000 GeV^2 is due to the change of the bin size (cf. figure 7.1).

The systematic errors dominate the total cross section uncertainty of the single (double) differential cross section for $Q^2 \lesssim 1000(500)$ GeV^2. The total correlated error which is dominated by the 1.5% uncertainty of the luminosity measurement, amounts to about 2% and is almost independent of Q^2 but increases towards high x. The correlated and uncorrelated errors are of similar size in the intermediate Q^2 region. However, the uncorrelated part yields the predominant contribution to the total systematic error, especially at large Q^2 where it is mainly driven by the electron energy scale uncertainty. The double differential systematic uncertainties show clear dependences on x which are averaged out for the single differential case.

Comparison of e and $e\Sigma$ reconstruction methods

In the present analysis, the e method is used for the kinematic reconstruction which relies solely on the energy and angle measurements of the scattered electron. However, the cross section result is obliged to be independent of the reconstruction method.

The $e\Sigma$ method provides an alternative way to reconstruct the event kinematics (cf. section 2.4) and is used to verify the cross section measurement. It depends in addition to the electron variables on the hadronic $(E - p_z)$ measurement and is less sensitive to radiative corrections (cf. figure 2.5). The comparison of the two methods is shown by the corresponding double differential cross sections in figure 7.6. Of course, both results are highly correlated since they rely on the same data set. However, the good agreement between both reconstruction methods provides confidence that the measurements and the radiative corrections are controlled on the level of the systematic uncertainties.

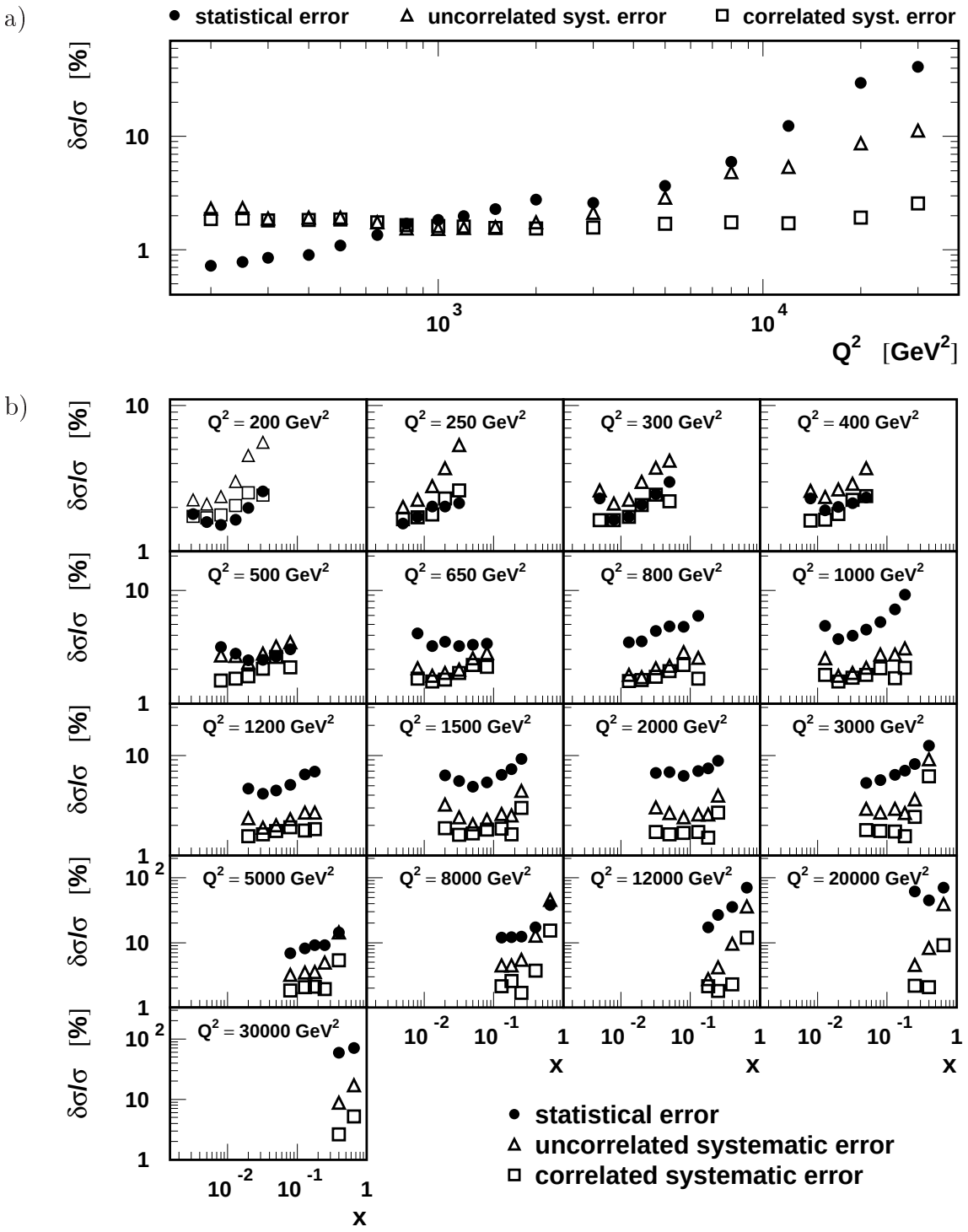

Figure 7.5: Statistical (full points), uncorrelated systematic (open triangles) and correlated systematic (open squares) errors on the single (a) and double (b) differential NC cross section measurements.

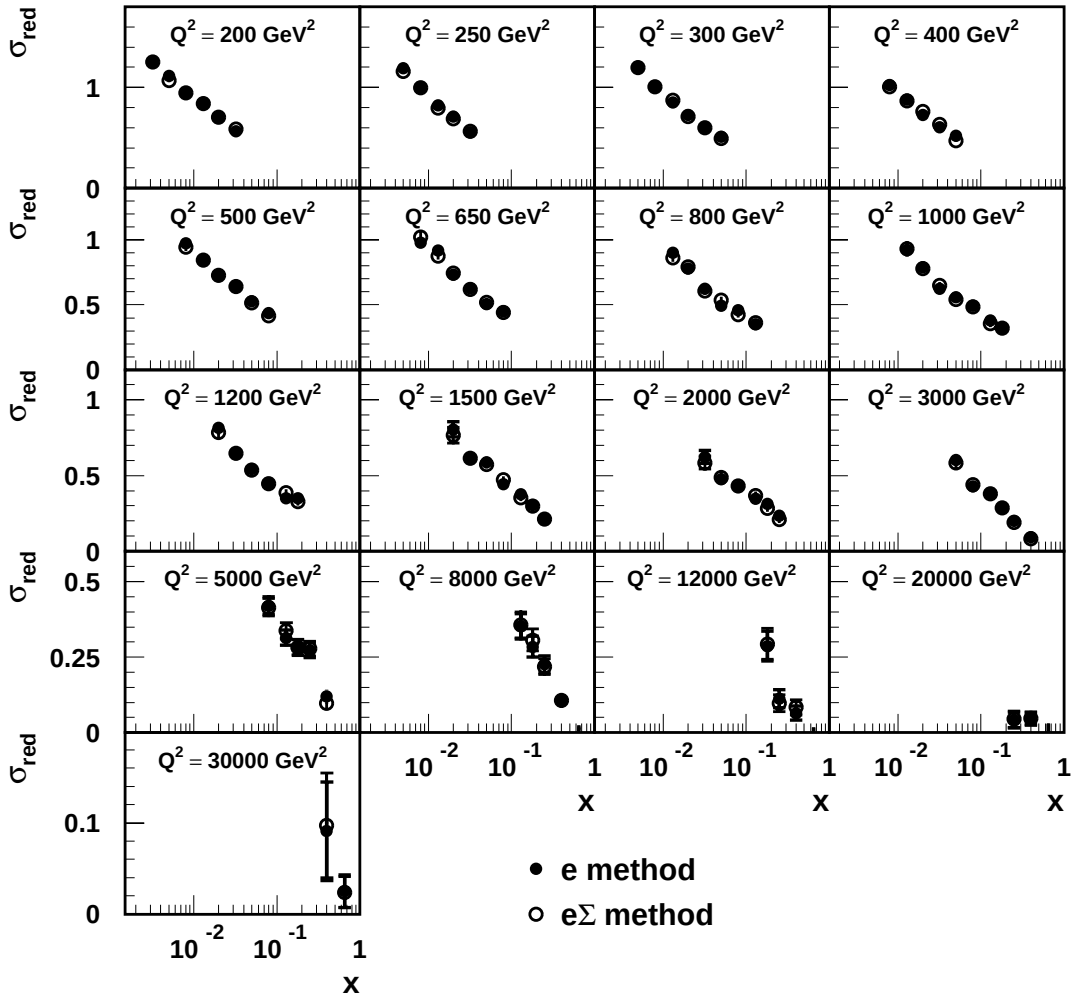

Figure 7.6: Comparison of the reduced NC cross sections as obtained using the e method (full points) and $e\Sigma$ method (open points) for the kinematic reconstruction.

7.3 Cross Section Result

This section presents the single and double differential NC cross section results with full errors as obtained from the present analysis. The data are compared to the Standard Model prediction which is based on the H1 1997 PDF Fit (cf. section 2.5) and which is mainly constrained by low Q^2 data. Due to the insufficient knowledge of the parton densities (cf. section 2.5) no attempt is made to quantify the uncertainty on the Standard Model prediction.

In all figures, the inner and outer error bars represent the statistical and the quadratic sum of statistical and uncorrelated systematic errors, respectively. The correlated uncertainty is shown as shaded band around the Standard Model prediction. The luminosity uncertainty of 1.5% is not included in the error band, since it dominates the correlated systematic uncertainty and simply corresponds to an overall shift of all cross section points.

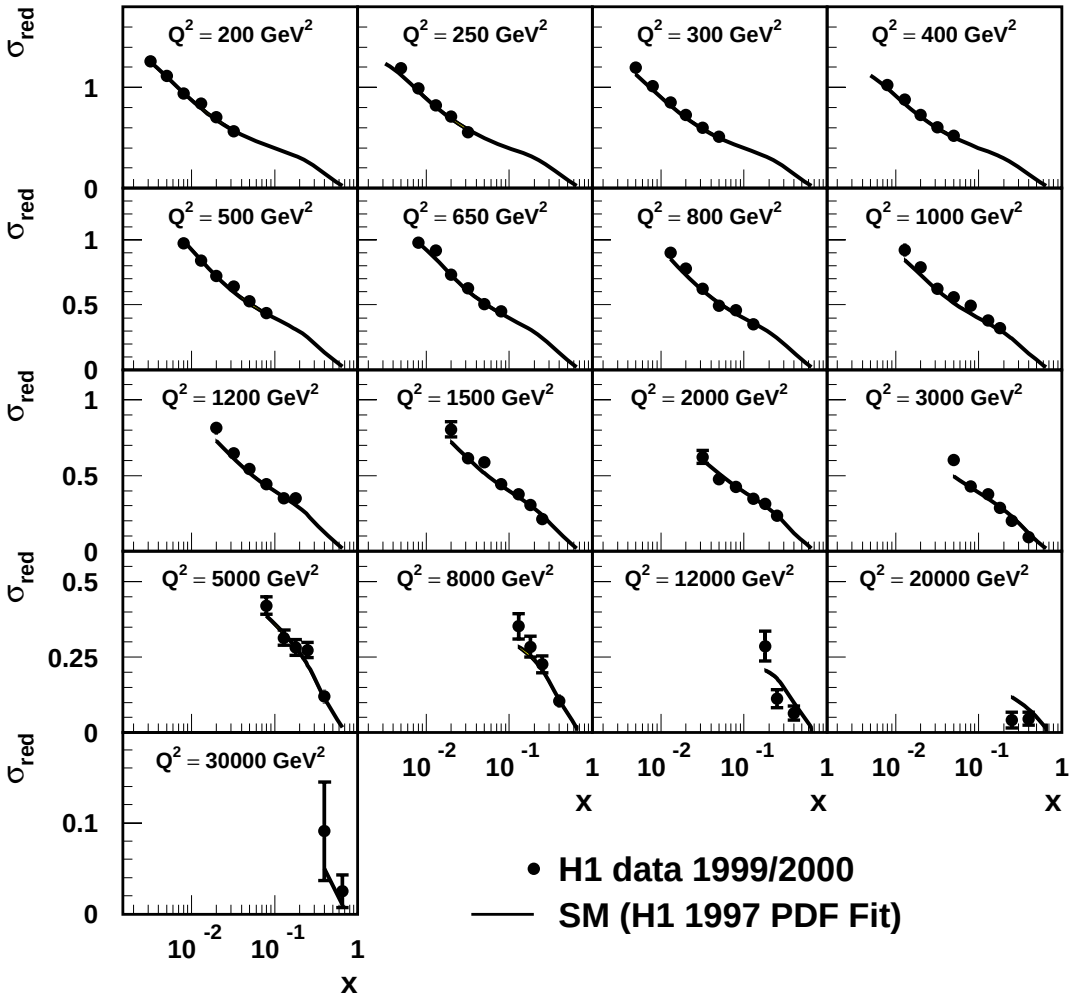

Figure 7.7: The reduced cross section as function of x for different values of Q^2. The data (points) are compared to the Standard Model (SM) prediction (line). The error bars represent the statistical and uncorrelated systematic errors, while the correlated error is hidden within the lines.

Figure 7.7 presents the reduced NC cross section in bins of Q^2 and as function of x. The measurement contains 91 measurement points and covers the kinematic range of $200 \leq Q^2 \leq 30000$ GeV^2 and $0.0032 \leq x \leq 0.65$. The data show the famous, steep rise of the cross section towards low x and are in good agreement with the prediction by the Standard Model. The measurement is statistically limited at highest Q^2 values. Due to the $y > 0.05$ requirement, which is needed to allow a precise reconstruction of the event kinematics, large values of x are only accessible at highest Q^2.

To allow a better evaluation of the reduced cross section data, the ratio of the data to the Standard Model prediction is shown in figure 7.8. In general, the data agree with the Standard Model prediction. Maybe apart from the $Q^2 = 3000$ GeV^2 bins, there are no obvious systematics trends depending on x at fixed Q^2 and the variations within each bin are well consistent with statistical fluctuations. At low and intermediate Q^2 values of $Q^2 < 2000$ GeV^2, the data show an overall offset of about a few percent

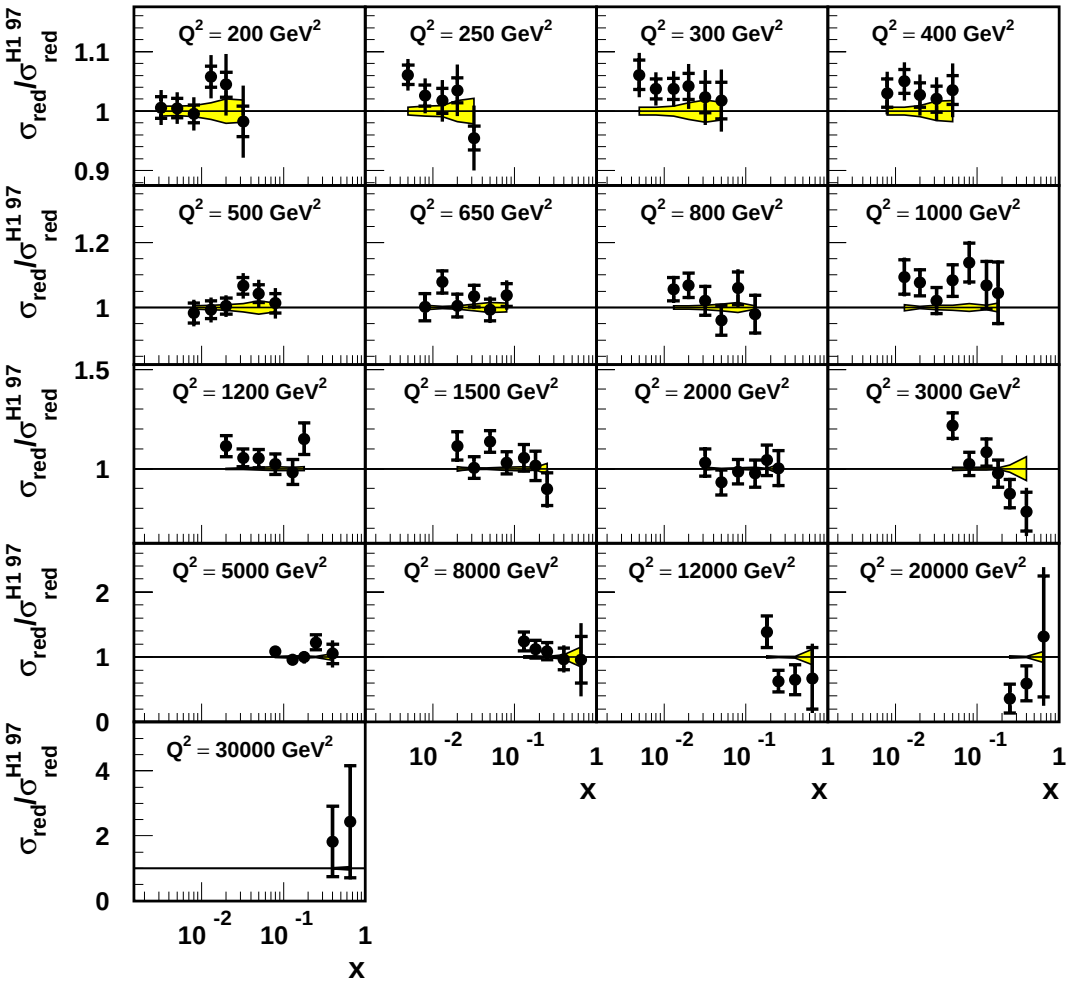

Figure 7.8: Ratio of the NC reduced cross section data to the Standard Model prediction which is based on the H1 1997 PDF Fit ("H1 97"). The error bars represent the statistical and uncorrelated systematic errors, while the correlated error is shown by the shaded band.

above the prediction. However, considering the 1.5% luminosity uncertainty and the unknown error on the Standard Model cross section which is expected to amount to at least a few percent, the observed deviations are found to be not significant.

To quantify the agreement between data and Standard Model prediction, a χ^2 fit has been performed which contains the statistical and systematic cross section errors. The overall fit yields a perfect agreement of $\chi^2 = 90.2$ for 91 data points. However, 62.7 units come from 44 points of the restricted $Q^2 > 1000$ GeV^2 region, indicating some overestimation of the errors at low Q^2 and at the same time some underestimation at large values of Q^2. The missing point may be our ignorance of the uncertainty of the Standard Model prediction which is related to the proton parton densities (cf. section 2.5).

The Standard Model prediction is based on the DGLAP evolution equations which evolve the parton densities for fixed x along Q^2. Thus, the reduced NC cross section

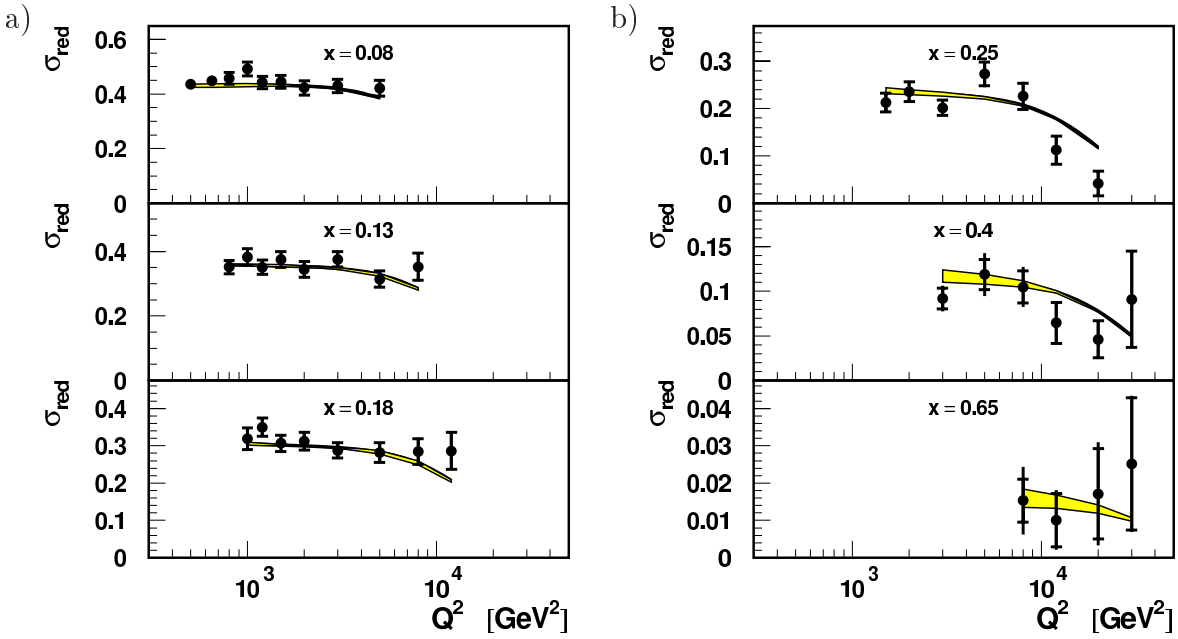

Figure 7.9: NC reduced cross section at high x as function of Q^2. The error bars represent the statistical and uncorrelated systematic errors, while the correlated error is shown by the shaded band.

is shown in figure 7.9 as function of Q^2 for large values of x. In the kinematic region of high x, the valence quarks carry most of the proton momentum. The data are reasonably described by the Standard Model QCD prediction, the χ^2 test yields 48.8 units for 42 data points. The decrease of the cross section at highest Q^2 values is due to the negative interference of the photon with the Z^0 boson.

Figure 7.10 presents the single differential cross section $d\sigma/dQ^2$. The NC cross section falls by six orders of magnitude, reflecting the strong $1/Q^4$ behaviour of the photon exchange contribution to the cross section. A closer look is provided by figure 7.11 showing again the ratio of the measured cross section to the Standard Model expectation. As already seen in the reduced cross section, the data surpass the prediction. In particular at $Q^2 \approx 1000$ GeV^2 the data show a prominent structure which is hard to explain just with the experimental errors of the cross section. However, the data are consistent with an overall shift of about 3% in normalisation. The minimum of the correlated systematic uncertainty at $Q^2 \sim 2000$ GeV^2 reflects the insensitivity of the cross section measurement to the absolute electron energy scale in that kinematic region (cf. figure 7.3).

A lot of further systematic investigations have been performed to look for so far unknown systematic error sources:

- The events of selected bins of the double differential cross section were explicitly scanned for background events.
- The cross section was determined with stronger kinematic requirements and separately for different kinematic regions.

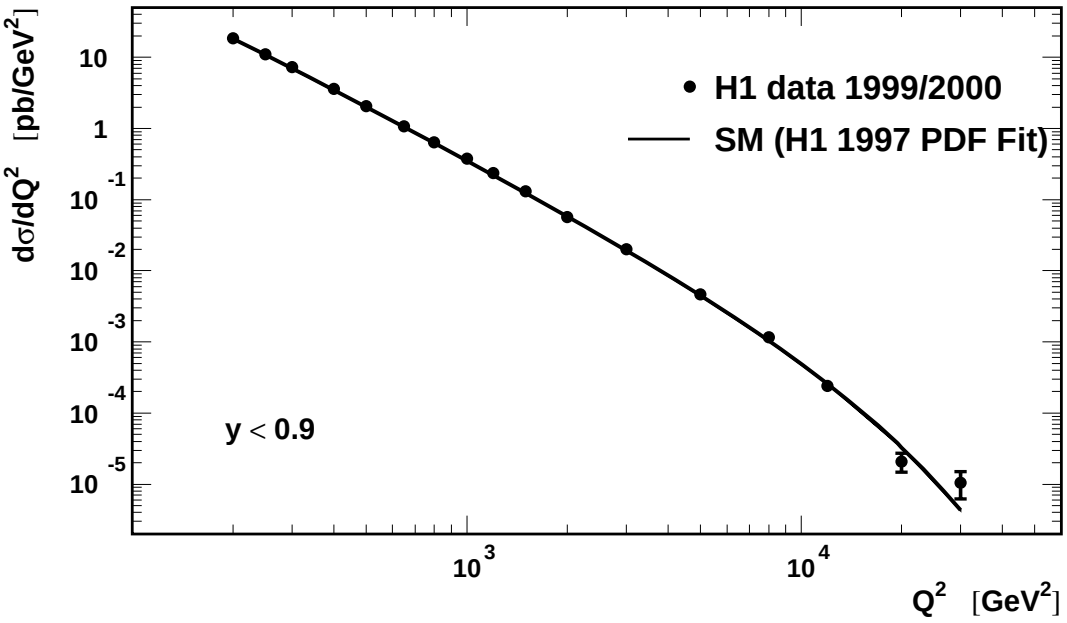

Figure 7.10: Measurement of the single differential NC cross section compared with the Standard Model expectation (solid line). The error bars represent the statistical and uncorrelated systematic errors, while the correlated error is hidden within the line.

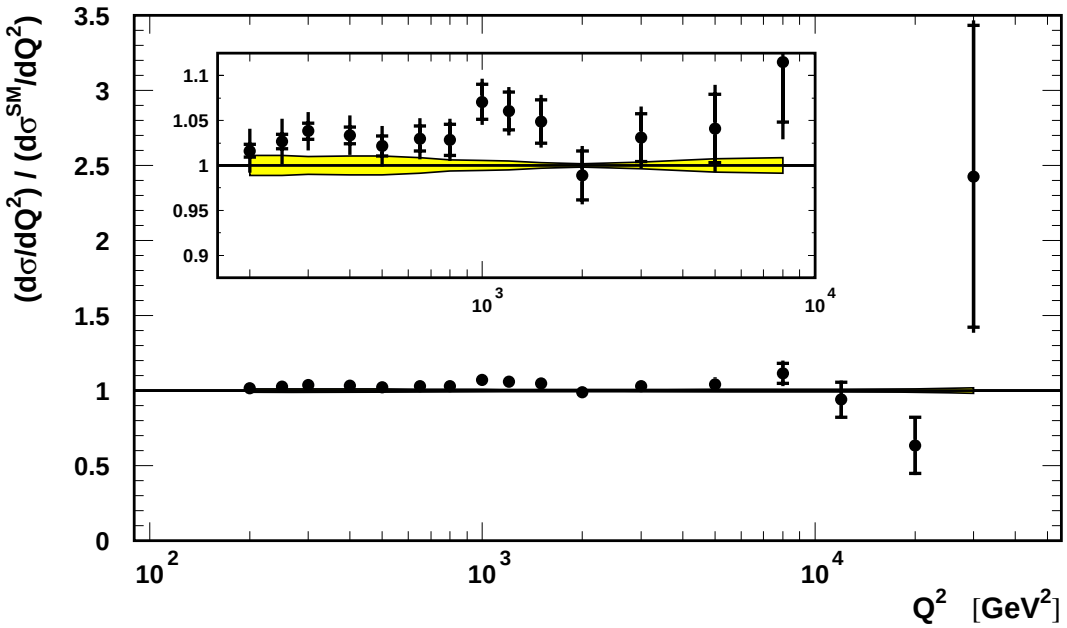

Figure 7.11: NC single differential cross section divided by the Standard Model expectation which is based on the H1 1997 PDF Fit. The error bars represent the statistical and uncorrelated systematic errors, while the correlated error is shown by the shaded band.

- The electron energy calibration was checked extensively going beyond what has been discussed in section 5.7. For instance, local variations at least of the size of the quoted systematic uncertainty were imposed to the energy scale as function of the electron z and ϕ impact positions. However, huge biases are needed to obtain the observed cross section variations. Furthermore, to account for deficits in the double angle reference energy, the energy calibration and the subsequent cross section measurement were restricted to regions of optimum kinematic reconstruction.
- Local effects of the LAr calorimeter structure were investigated, e.g. by studying slices in z_{imp}, tightening z crack cuts and elongating or compressing the LAr coordinates also periodically corresponding to some influence by cell structure.
- Systematic studies were performed of shifts in the z vertex position within the tolerance of the vertex fit. This was motivated by the observation of a few events where the primary vertex is reconstructed solely from the electron track but which have additional hadronic final state tracks pointing to an alternative primary vertex.
- A direct z vertex dependence of the cross section was studied by separately determining the cross section for $z < -7.5$ cm, $-7.5 \leq z < 7.5$ cm and $z \geq 7.5$ cm.

The variations of measurement quantities were performed within their typical uncertainties and partly even exceeding the range of quoted systematic errors. All effects if at all observable were found to be small compared to the size of effects caused by the known the systematic error sources of this analysis. The result of this investigation confirmes the systematic error treatment and provides confidence that no other experimental systematic uncertainties of relevant influence are involved.

Consequently, the prominent variations in the cross section measurement must be attributed to statistical fluctuations or external issues such as the incomplete knowledge of the parton densities of the proton.

7.4 Comparisons to other Measurements

The present NC cross section measurement is compared to the result published recently by H1 on the same data set [16]. Figure 7.12 shows the NC reduced cross section data of both measurements each of them normalised to the cross section prediction based on the H1 1997 PDF Fit. Good agreement is observed between the measurements in normalisation and for the most parts even on details of the bin-by-bin variations. Both results are highly correlated, of course, since they are based on the same data set. However, the measurements are rather independent of each other in terms of the data analysis and in particular of the event reconstruction: The published result is based on the $e\Sigma$ reconstruction method and applies different procedures for the electromagnetic and hadronic energy calibration. In addition the electron z cluster position is measured in the standard way, and the hadronic final state is reconstructed using the original

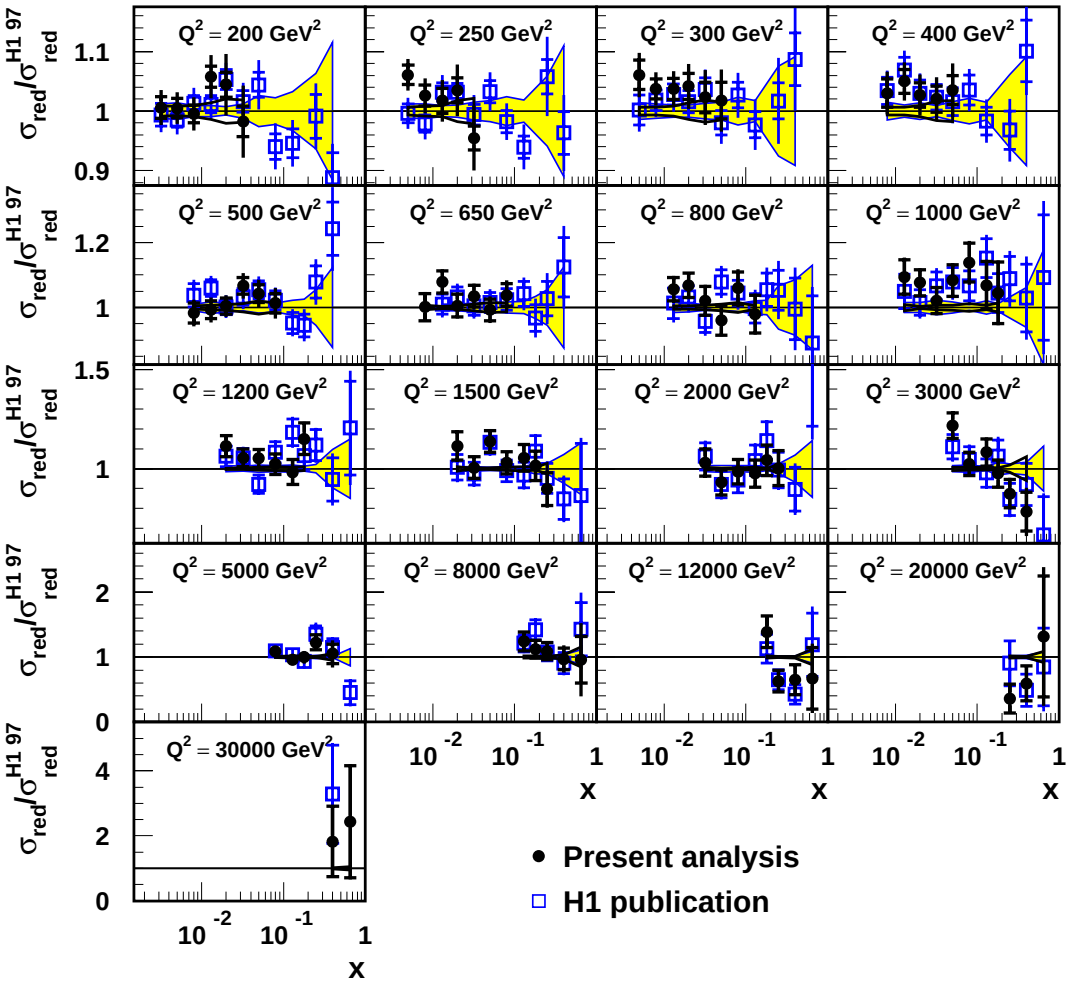

Figure 7.12: Ratio of the NC reduced cross section data to the Standard Model prediction which is based on the H1 1997 PDF Fit (labelled "H1 97"). The present data (full points) are compared to the result published by H1 on the same data set [16] (open squares). The error bars represent the statistical and uncorrelated systematic errors. The correlated error is shown by the shaded band and does not include the luminosity uncertainty of 1.5% which both measurements have in common.

energy weighting procedure. Thus, the comparison provides an appropriate consistency check and confirms a proper data handling.

At low and intermediate Q^2 values, the published measurement extends to the large x region, corresponding to very low values of $y < 0.05$. This range is accessible using the $e\Sigma$ method (cf. section 2.4) for the kinematic reconstruction. However, at very low y, the hadronic final state is restricted to the far forward detector region and the measurement gets quite sensitive to noise contributions of the LAr calorimeter [82]. Its impact on the cross section measurement is reflected by the strong increase of the correlated error towards low y, i.e. large x. Thus, there are even good experimental reasons to omit this region from the present analysis.

7.5 Summary

The present NC cross section measurement benefits from large improvements achieved in the event reconstruction and in particular the measurement of the scattered electron. The typical total precision of the cross section result is about 3% at low Q^2 and 5% for the double differential cross section at $Q^2 \sim 1000$ GeV^2.

Apart from an overall shift in normalisation of about 3%, the present results are in good agreement with the Standard Model QCD prediction and with competitive measurements. The improved treatment of systematic errors takes into account asymmetric uncertainties and will be exploited in the contact interaction fits to the data presented in the following chapter.

Chapter 8

Statistical Analysis

In this chapter, the neutral current cross section measured in the first part of this analysis is investigated to look for the effects of electron-quark contact interactions beyond the present Standard Model. An upper bound on the radius of light quarks and lower limits on the scales of various compositeness models are evaluated applying a χ^2 fit. A novel ansatz is used in the fits to reduce the influence of the uncertainties of the proton parton densities on the results. Finally, the results are compared to searches for contact interactions carried out by other analyses.

Specific emphasis is put here on a careful treatment of systematic errors and of their correlations. Deficits of analyses done so far have been found and eliminated. Of course, as long as there is no signal observed, people in general don't care too much about systematics and take notice only of results with strongest exclusion limits. However, this attitude would change dramatically in the presence of a signal or its experimental hints. The methods developed here will prove useful for future HERA-II high statistics analyses which will reach a new sensitivity to physics beyond the Standard Model.

8.1 Introduction and Fit Method

The compatibility and consistency of a cross section measurement with a prediction based on a theoretical model can be quantified by statistical means. A probability density function $f(x, \alpha)$ with known parameter α predicts the frequency with which random data x will show up in a given range. However, having done a measurement x one generally wants to solve the inverse problem of making inferences about α.

In the present analysis, the frequentist approach is used to determine confidence intervals of α from the observed data. Frequentist methods provide the probability to obtain various data sets for a given hypothesis, i.e. the frequency of measurements from in principle repeatable experiments. In practice, these frequencies are often determined from Monte Carlo experiments.

The method of maximum likelihood is the most general method of parameter estimation. Suppose a set of independently measured quantities x_i which come from a probability density function $f(x_i, \alpha)$, where α is a set of unknown parameters. The method of maximum likelihood consists of finding the set of $\hat{\alpha}$ which maximises the

joint probability density for all data, given by the likelihood function $\mathcal{L} = \prod_i f(x_i, \alpha)$. It is usually easier to maximise the logarithm of this function by solving the equation $\partial \ln \mathcal{L} / \partial \alpha = 0$.

The method of least squares, which will be used in the present analysis for parameter estimation, follows from the maximum likelihood theorem assuming normal distributed measurements y_i at the points x_i with mean $\mu(x_i, \alpha)$ and variance σ_i^2. Then

$$\chi^2 = -2 \ln \mathcal{L} + const = \sum_i \frac{(y_i - \mu(x_i, \alpha))^2}{\sigma_i^2} \tag{8.1}$$

is the χ^2 function which in practice provides easy access to extract the parameters α. Maximising the likelihood function is equivalent to minimising the χ^2 function.

If the point errors $\epsilon_i = y_i - \mu(x_i, \alpha)$ are Gaussian distributed and assuming that the model is correct, the minimum χ^2 of repeated measurements will be distributed as a χ^2 random variable with n_{dof} degrees of freedom. n_{dof} is the number of measurement points minus the number of free parameters entering the prediction and gives the expectation value of a χ^2 distribution. Thus the ratio χ^2/n_{dof} is a measure of the compatibility of the data with the model and yields the Goodness of Fit (GoF). The GoF is typically given as the probability $P(\chi^2 > \chi^2_{data})$ to obtain a measurement which is at least as incompatible with the hypothesis as the data actually observed.

The minimum of equation 8.1 defines the least-squares estimators $\hat{\alpha}$ also for the more general case where the y_i are not Gaussian distributed as long as they are independent. If they are not independent, the estimators are determined by the minimum of

$$\chi^2 = (\mathbf{Y} - \mathbf{M}(\alpha))^T \; V^{-1} \; (\mathbf{Y} - \mathbf{M}(\alpha)) \;\; , \tag{8.2}$$

where $\mathbf{Y}$ and $\mathbf{M}(\alpha)$ are the vectors of the measurements y_i and predictions $\mu(x_i, \alpha)$, respectively, and $V_{i,j} = \mathrm{cov}[y_i, y_j]$ is the covariance matrix.

In many practical cases, the problem is restricted to the situation where the prediction $\mu(x_i, \alpha)$ is a linear function of the parameters α. Minimising χ^2 in this case reduces to solving a system of linear equations. Otherwise, if the problem is non-linear, the χ^2 minimum may be found iteratively. The CERN program MINUIT [91] contains numerical methods to find such solutions reliably and is used in this analysis. In the case of non-Gaussian measurement errors, the GoF probability itself becomes meaningless. However, the minimum χ^2/n_{dof} can be used to quantify the compatibility of the data with different hypotheses.

In the approximation of Gaussian errors, the δ-standard deviation limits on each of the parameters are given by a set α' such that

$$\chi^2(\alpha') = \chi^2_{\min} + \delta^2 \;\; . \tag{8.3}$$

Further information and a comprehensive overview of statistics can be found in [92].

8.1.1 General Approach to Search for Contact Interactions

To search for the effects of contact interactions, the measured cross section data of this analysis are compared to the predictions of the Standard Model including a form factor

or additional couplings introduced by compositeness models. A χ^2 fit is performed to quantify the compatibility of the data with the Standard Model prediction and to derive limits on new physics scales.

Standard Model prediction and new physics

The complete error treatment would in principle need to include the uncertainty of the Standard Model prediction. A considerable contribution is expected from the uncertainty of the parton density functions (PDFs) which provide the basis for the Standard Model cross section calculation (cf. section 2.5). In particular the 'theoretical' error of the PDFs, which for instance accounts for the uncertainty of the x parameterisation of the PDFs, is subject to extensive discussions [25].

The apparent optimal procedure would be fitting contact interactions in parallel with the parton densities to a global set of data points which would require input from other experiments. However, the principle problem of estimating the theoretical error of the PDFs would persist. Thus, the present analysis proceeds differently and uses the Standard Model predictions based on PDFs which are provided by global fit analyses.

At first glance, this approach seems to be inconsistent since the investigation of effects beyond the Standard Model is based on structure functions which may already incorporate additional contributions of new physics. However, the procedure is justified by the fact that the experimental cross section data of the present analysis at highest Q^2 have negligible impact on the global PDF fits which are constrained predominantly by precision low Q^2 fixed target data. In particular at highest x, where the effects of contact interactions are most prominent (cf. diagrams in appendix B), the results of fixed target experiments dominate by far the parton density fits. Contrary to that, the cross section data of the high Q^2 and high x domain at HERA have large sensitivity to the effects of contact interaction. Thus, the global PDF fits and the fit to contact interactions performed in the present analysis effectively decouple.

Nevertheless, the PDF input may play an important role in the search for contact interactions. The Q^2 evolution is experimentally proven to be governed by the DGLAP equations in the kinematic region of $Q^2 \gtrsim 10$ GeV^2. However, the x dependence is not at all predicted by theory and the corresponding PDF uncertainties are rather unknown. Unfortunately, both the Standard Model cross section and the implications due to additional contact interactions depend strongly on x.

Fitting the double differential neutral current cross section

Previous H1 analyses on contact interactions [93, 94, 95] have been performed using the measurement of the single differential neutral current cross section $d\sigma/dQ^2$. In fact, the effects of contact interactions predominantly depend on Q^2 (cf. equation 3.12). However, kinematic effects and the structure function compositions imply additional, rather strong dependences on x and y.

Thus, there are advantages to investigate the double differential cross section, $d^2\sigma/dx\,dQ^2$, for the effects of contact interactions. In particular, it allows

- to resolve different contributions from Standard Model processes, systematic uncertainties and contact interactions in different regions of phase space,
- to avoid explicit contributions from kinematic regions where the systematic errors are large compared to the effects of potential contact interactions,
- to minimise the influence of the x dependence of the PDFs by leaving the normalisation open for each x bin.

The last point deserves some additional explanations. Although contact interactions primarily affect the Q^2 distribution of the cross section, x dependent systematic effects and especially the rather imprecisely known x dependence of the PDFs may yield some fake contribution to the contact interaction signal just by kinematics since high Q^2 corresponds to high x and vice versa. In fact, fixing the x normalisation may imply an artificial change in the Q^2 distribution which is not explained by the Standard Model.

The procedure of normalising each x bin separately exploits the well known Q^2 dependence of the cross section while being rather insensitive to details of the x distribution. Thus, the present analysis performs a fit to the double differential reduced cross section $d^2\sigma/dx\,dQ^2$ taking full benefit of the comprehensive cross section measurement presented in chapter 7.

8.1.2 χ^2 Definition and Error Treatment

The present analysis compares the measured neutral current cross section to the Standard Model expectation including the effects of a finite quark radius or of contact interaction couplings. A simple χ^2 fit is performed which allows the straightforward implementation of systematic errors.

Estimators

The estimator referring to the scale of the various compositeness contact interaction scenarios (cf. section 3.2.3) is chosen to be

$$\frac{\epsilon_{ab}}{\Lambda^2} = \frac{\eta_{ab}}{4\pi} \ . \tag{8.4}$$

It is assumed that only one of the helicity structures dominates, i.e. there is only one scale Λ involved. The estimator $\eta \sim 1/\Lambda^2$ is preferred, since it avoids infinities representing the Standard Model.

For the quark radius fit, the mean-square radius of the electroweak charge distribution, R^2, is taken to be the estimator.

χ^2 function

The χ^2 function comprises the sum over all cross section points i and additional penalties arising from constrained parameters

$$\chi^2 = \sum_i \left(\frac{\sigma_i^{\text{exp}} - \sigma_i^{\text{theo}} \cdot [1 - (f_{\text{norm}} - 1) - \sum_k \Delta\sigma_{ik}^{\text{corr}}(\epsilon_k)]}{\Delta\sigma_i^{\text{exp}}} \right)^2 + \left(\frac{f_{\text{norm}} - 1}{\Delta f_{\text{norm}}} \right)^2 + \sum_k \epsilon_k^2 \ . \tag{8.5}$$

The χ^2 function is composed of:

- $\sigma_i^{\rm exp}$ is the measured cross section.
- $\sigma_i^{\rm theo}$ is the theoretical cross section prediction based on the Standard Model which additionally contains the form factor or coupling contributions for a quark radius or compositeness model and thus depends on R^2 and ϵ_{ab}/Λ^2, respectively.
- $\Delta\sigma_i^{\rm exp}$ is the experimental cross section error including statistical and uncorrelated systematic errors added in quadrature.
- $f_{\rm norm}$ is a fit parameter for the overall normalisation of the data. A deviation in the overall normalisation from one is penalised by the additional χ^2 term which contains the effective pull, i.e. the deviation in units of standard deviations.
- $\Delta f_{\rm norm}$ is the overall normalisation uncertainty given by the error of the luminosity measurement.
- $\Delta\sigma_{ik}^{\rm corr}(\epsilon_k)$ are functions which take into account the correlated systematic error associated with source k. They depend on the fit parameters ϵ_k which are effectively pulls, i.e. deviations in terms of the uncertainty, implied by the corresponding systematic error. The correlated systematic errors considered are the electron energy scale, the electron polar angle and the strong coupling constant as will be discussed below.

As a particular feature of the present analysis, the normalisation parameter is determined individually for each x bin of the cross section measurement:

$$f_{\rm norm} \rightarrow f_{\rm norm}(x) \ . \tag{8.6}$$

These normalisation parameters are constrained by the total cross section sum,

$$\overline{f}_{\rm norm} \cdot \sum_i \sigma_i^{\rm exp} = \sum_i f_{\rm norm}(x_i)\ \sigma_i^{\rm exp} \ , \tag{8.7}$$

where $\overline{f}_{\rm norm}$is the effective overall normalisation.

Table 8.1 summarises the parameters used in the fits:

$f_{\rm norm}(x)$:	x bin-wise normalisation
ϵ_k:	correlated systematic error contributions, considering
	the uncertainties of - the electron energy scale,
	- the electron scattering angle,
	- the strong coupling constant.
R^2 or ϵ_{ab}/Λ^2:	estimators of contact interactions

Table 8.1: Fit parameters used in the fits.

Statistical uncertainties

Depending on the question being addressed, there are are two possibilities to define the statistical errors which enter the χ^2 function by $\Delta\sigma_i^{\text{exp}}$:

- **Statistical error obtained from the data measurement:**
  For the test of the compatibility of the data with a certain hypothesis, e.g. the Standard Model, the experimental statistical error is used in the χ^2 function. The data points thus contribute with the fixed weight $(\Delta\sigma_i^{\text{exp}})^{-2}$ to the χ^2 function, independent of the model prediction and therefore independent of the fit parameters. As a consequence, upward fluctuations of the data w.r.t. the model prediction get a smaller weight (larger statistical error) than downward fluctuations (smaller statistical error), leading to asymmetric χ^2 distributions.
- **Statistical error according to the model expectation:**
  In this case one assumes the validity of a certain model hypothesis, i.e. contact interactions, and determines the probability to observe the measured value. The data points enter with a varying weight depending on the model parameters but independent of fluctuations in the data. This procedure is completely equivalent to the log-likelihood approach.

The statistical error of the data is sometimes referred to as the 'experimental statistical error', the one of the model prediction as the 'theoretical statistical error'.

Systematic uncertainties

The relevant systematic uncertainties of the neutral current cross section measurement were discussed in section 7.2.

The total uncorrelated cross section errors are considered in the χ^2 function by the $\Delta\sigma_i^{\text{exp}}$ term in the denominator being added in quadrature to the statistical error.

The dominant correlated systematic errors are introduced to the χ^2 function by $\Delta\sigma_{ik}^{\text{corr}}(\epsilon_k)$ functions, which modify the model prediction accordingly. They are parameterised by

$$\Delta\sigma_{ik}^{\text{corr}}(\epsilon_k) = \frac{\hat{\sigma}_{i,k}^{+} - \hat{\sigma}_{i,k}^{-}}{2}\,\epsilon_k + \frac{\hat{\sigma}_{i,k}^{+} + \hat{\sigma}_{i,k}^{-}}{2}\,\epsilon_k^2 \;, \tag{8.8}$$

where $\sigma_{i,k}^{\pm}$ denote the positive and negative relative cross section uncertainties corresponding to one sigma deviation of point i and source k as provided in the cross section tables (cf. appendix A). By construction, the asymmetric behaviour of the systematic uncertainties is taken into account.

The relevant experimental correlated systematic errors considered in the χ^2 function are

- the normalisation uncertainty of 1.5%, which yields the dominant and most important error contribution,
- the error of the absolute electron energy scale, which contributes to less extent,
- the error of the electron polar angle measurement which yields even smaller contributions.

The correlated errors of the hadronic energy measurement and of the background subtraction are neglected.

The model prediction also incorporates systematic uncertainties. A considerable systematic error contribution to the predicted cross section is due to the PDF parameterisations. However, due to the separate normalisation of each x bin mainly the error of the Q^2 dependence has to be considered. The Q^2 dependence of the PDFs is predominantly governed by the strong coupling constant, which is measured by many experiments. The strong coupling constant was measured by H1 to be $\alpha_s(M_Z^2) = 0.1150 \pm 0.0017\ ^{+0.0009}_{-0.0005}$ [96], where the first error accounts for experimental uncertainties while the second one reflects model uncertainties. The world average value is quoted as $\alpha_s(M_Z^2) = 0.1172 \pm 0.002$ [92].

The implication on the cross section of a change in α_s of ± 0.002 was derived from a specific set of PDFs provided by MRST2001 [21] and is shown in figure 8.1. An

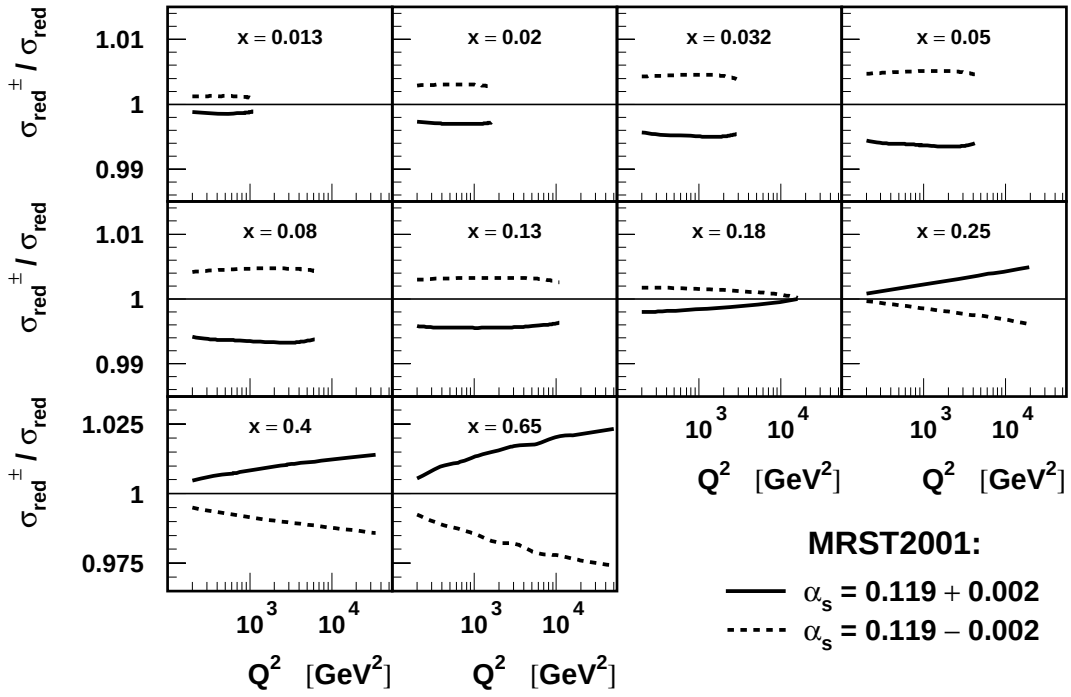

Figure 8.1: Relative deviations of the double differential cross section due to a change in the strong coupling constant $\alpha_s(M_Z) = 0.119 \pm 0.002$.

increase in α_s lowers the cross section at low and intermediate x while the cross section is enhanced at highest x. The effects on the cross section are mostly below 1% and reach about 2% only at highest x and Q^2. They are thus mostly smaller than the experimental correlated systematic uncertainties considered. The relative cross section deviations due to changes in α_s of ± 0.002 are introduced to the χ^2 fit using an additional set of $\Delta\sigma^{\mathrm{corr}}_{i,k}(\epsilon_k)$. The remaining impact of the systematic uncertainties of the PDFs on the Q^2 distribution is supposed to be very small and covered by the uncertainties of α_s and the electron energy scale.

8.2 Fit Optimisation

This section describes the kinematic phase space which is chosen to obtain a regular behaviour of the fit and reliable results. Furthermore, the novel normalisation procedure is investigated and compared to the standard method.

8.2.1 Selection of Cross Section Points

Since systematic uncertainties are always difficult to handle within fits, the present analysis of contact interactions is restricted to a region in phase space, where the cross section measurement is not dominated by systematic effects. The comparison of the statistical and systematic errors of the cross section measurement were shown in figure 7.5. The systematic error dominates the total cross section error for $Q^2 \lesssim 500$ GeV^2.

Moreover, fits were performed comparing the data to the Standard Model prediction for different lower Q^2 requirements. The resulting GoF values are shown in table 8.2 for the one- and two-dimensional fits with overall and x bin-wise normalisation. All

	1 dim. fit			2 dim. fit, overall norm.			2 dim. fit, x bin norm.		
	n_{dof}	$\frac{\chi^2}{n_{dof}}$	GoF [%]	n_{dof}	$\frac{\chi^2}{n_{dof}}$	GoF [%]	n_{dof}	$\frac{\chi^2}{n_{dof}}$	GoF [%]
overall	17	1.010	44.3	91	0.959	59.2	79	0.918	68.2
$Q^2 \geq 250$ GeV^2	16	1.053	39.5	85	0.983	52.3	74	0.933	64.2
$Q^2 \geq 300$ GeV^2	15	1.121	33.0	80	0.991	50.2	69	0.967	55.6
$Q^2 \geq 400$ GeV^2	14	1.192	27.3	74	1.049	36.3	64	1.019	43.4
$Q^2 \geq 500$ GeV^2	13	1.281	21.6	69	1.112	24.4	59	1.085	30.5
$Q^2 \geq 650$ GeV^2	12	1.374	17.0	63	1.166	17.3	53	1.101	28.6
$Q^2 \geq 800$ GeV^2	11	1.499	12.4	57	1.220	12.3	48	1.133	24.4
$Q^2 \geq 1000$ GeV^2	10	1.649	8.7	51	1.273	9.1	42	1.179	19.9

Table 8.2: Fit results for one- and two-dimensional fits with overall and x bin-wise normalisation comparing the data with the Standard Model prediction. Shown are the n_{dof}, χ^2/n_{dof} and GoF values for different lower Q^2 requirements.

fits show an increase of χ^2/n_{dof} with increasing cut on Q^2. As already discussed for the cross section measurement, the systematic errors seem to be overestimated at low Q^2 and underestimated at high Q^2. In these fits, the experimental systematic uncertainties as well as the impact of the α_s error are included. However, there may be still some missing theoretical uncertainties like those of the PDFs.

Compared to the one-dimensional fit, the double differential fits and especially the one with free x normalisation provide a much better description of the data in terms of the χ^2/n_{dof} and GoF values, independent of the selection cut.

To avoid large systematic contributions and to obtain a fair GoF and a strong enough lever arm in Q^2, the fit analysis is restricted to the kinematic region of $Q^2 \geq 500$ GeV^2. Since there are only two data points left in the $x = 0.008$ bin, $x \geq 0.013$ is

required in addition. Finally, 67 cross section points enter the fit procedure with at least 4 data points in each x bin. Figure 8.2 shows the reduced cross section measurement of these points in bins of x as function of Q^2.

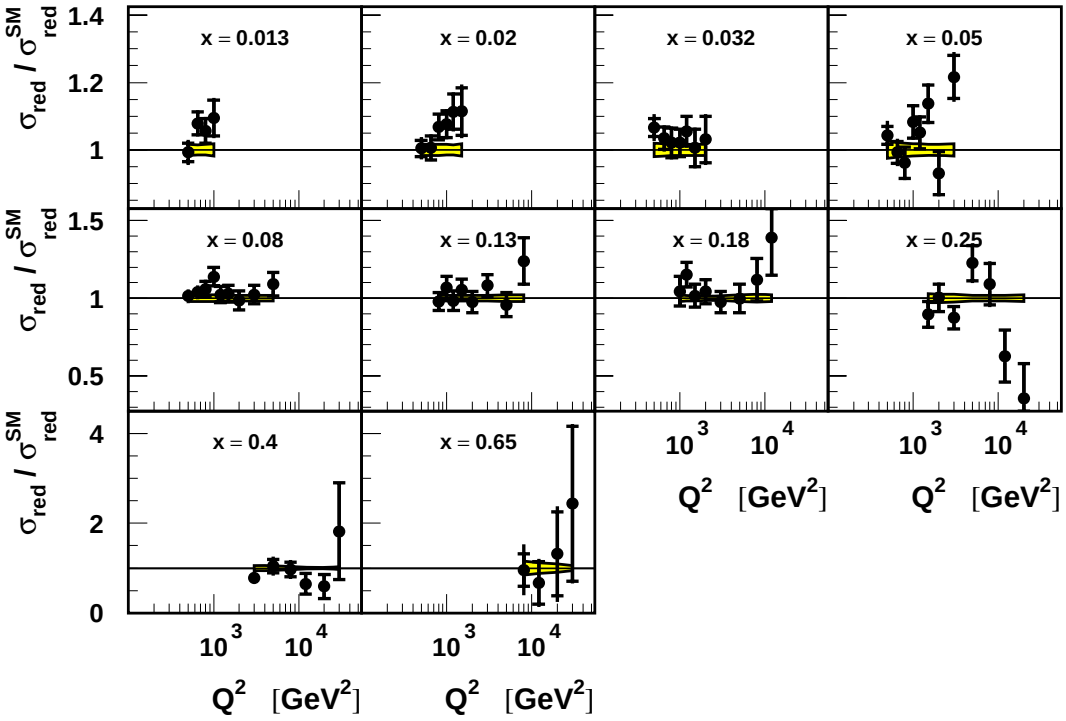

Figure 8.2: Points of the reduced neutral current cross section measurement entering the contact interaction fits. The result is normalised to the Standard Model prediction based on the H1 1997 PDF Fit. The error bars represent the statistical and uncorrelated systematic errors, while the correlated error is shown by the shaded band. The normalisation uncertainty of 1.5% is not included in the errors.

8.2.2 Normalisation Procedure and Parton Density Uncertainties

The normalisation procedure introduced to the χ^2 function has to account for the overall normalisation uncertainty arising from the error of the luminosity measurement. However, there is in addition the possibility to treat other systematic uncertainties by normalising individual subsets of the cross section data. The following procedures are used in this analysis:

1. Overall normalisation: This takes into account the error on the luminosity measurement which is used for the χ^2 penalty term.
2. Normalisation of each x bin separately: Again, the overall normalisation, as constrained by the cross section sum (cf. equation 8.7), considers the error of the luminosity measurement. The variations in the relative normalisation between different x bins are left free without a χ^2 penalty.

The open relative x bin normalisation is motivated by the rather unknown impact of the PDF uncertainties and in particular of their x dependence on the contact interaction fit results. The improvement obtained by this ansatz in the description of the data was already seen in table 8.2. To further evaluate the procedure of free x normalisation, contact interaction fits to the selected data (cf. section 8.2.1) are performed

- for three different fits: Single and double differential fits, the latter with overall normalisation only and in addition with open relative x bin normalisation.
- for various PDF parameterisations: The Standard Model prediction is based on H1 1997, H1 2000, MRST2001, MRST1999, CTEQ6.1 and CTEQ5.
- for all contact interaction coupling combinations of compositeness models (cf. section 3.2.3).

The resulting estimators ϵ/Λ^2 are shown in figure 8.3. Various observations are discussed in the following:

In both the one- and two-dimensional fits with only an overall normalisation parameter, the results tend to prefer a negative value of ϵ/Λ^2. This behaviour can be understood in terms of local or x dependent statistical or systematic effects. Any downward fluctuation of the data favours a model with negative interference w.r.t. the standard model amplitude.

The effect is observed in particular for the double differential case (cf. figure 8.3b). The data of low x bins are about 5% high in normalisation compared to the Standard Model prediction (cf. figure 8.2). Their high statistical weight leads to an overall normalisation of about 2.5% below unity. However, the data of the intermediate x range agree in normalisation with the Standard Model prediction and thus favour a decrease in the predicted cross section induced by the contact interaction model. Just by kinematics, the x dependence is transferred into the Q^2 spectrum for the single differential fit. An exception of the preference of a negative value of ϵ/Λ^2 is the $RL-RR$ coupling combination. It is the $RL - RR^+$ model which provides a reduction of the cross section at highest Q^2 (cf. figure B.13).

The impact of general x dependent systematic effects on the fit result is reduced when applying a normalisation parameter for each x bin separately.

Dependence on the PDF input

A particular x dependence of the cross section is introduced by the PDFs. In fact, large dependences of the fit results on the PDF input are observed for the one-dimensional fit (cf. figure 8.3a). The variations are partly at the 1σ level, in particular for models where only few contact interaction couplings are involved, i.e. for the pure chiral couplings and their pairwise combinations. Also seen are systematic dependences between different PDFs. Some PDFs generally yield results closer to zero (i.e. the Standard Model) while others predict signal-like effects of contact interactions.

Using fits to the double differential cross section with an overall normalisation parameter reduces the sensitivity of the fit results to the choice of the PDF (cf. figure 8.3b). However, some dependences remain, especially for both the H1 1997 and H1 2000 PDF Fit. Compared to the other PDFs they show a different Q^2 dependence for

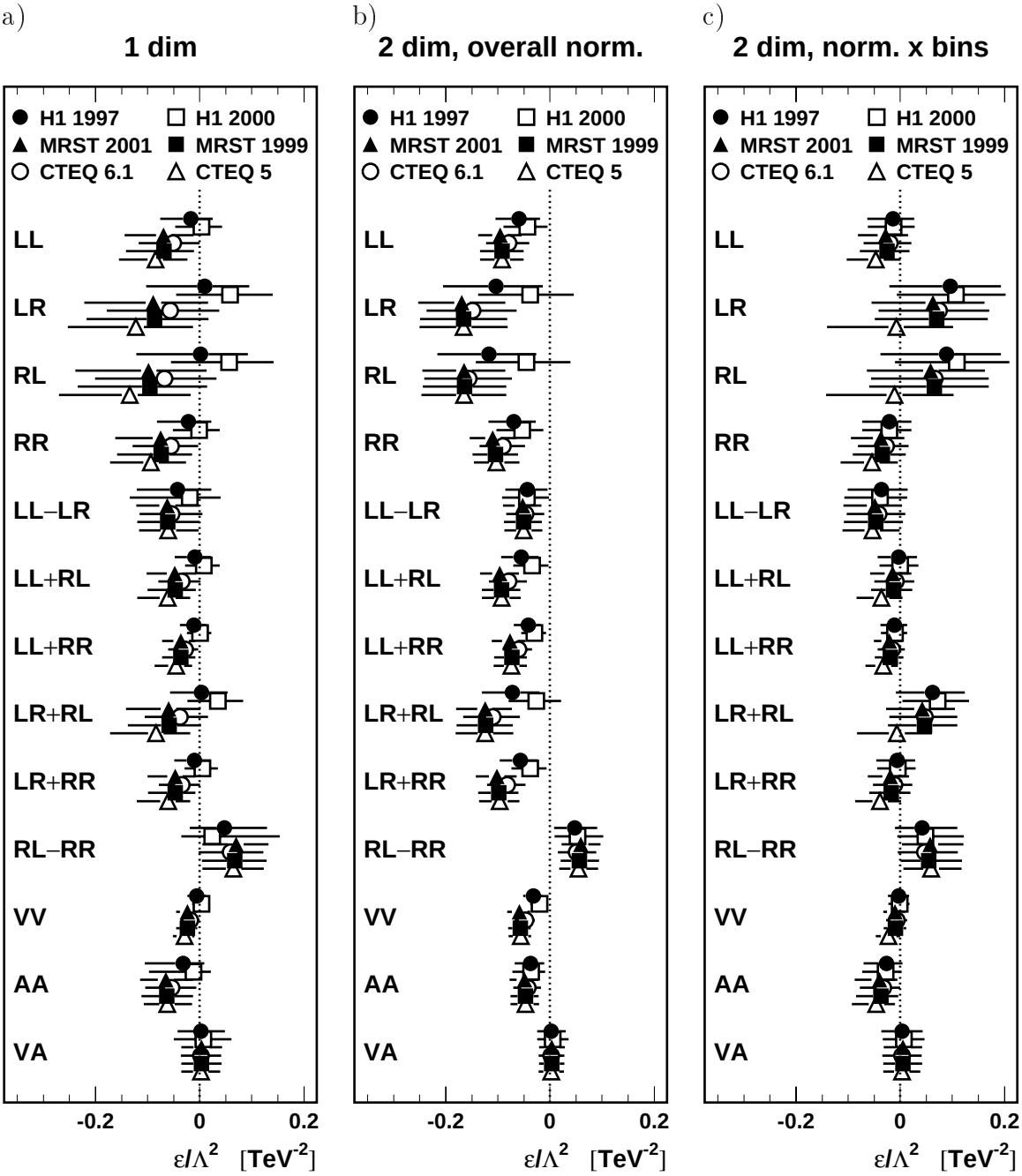

Figure 8.3: Comparison of the χ^2 fit results of ϵ/Λ^2 for different compositeness models and for different parton density parameterisations. The results are shown for fits to the single differential cross section (a) and the double differential cross section applying an overall normalisation parameter (b) and normalising each x bin separately (c). The error bars show the 1σ uncertainty of the fit result including the effects of systematic errors.

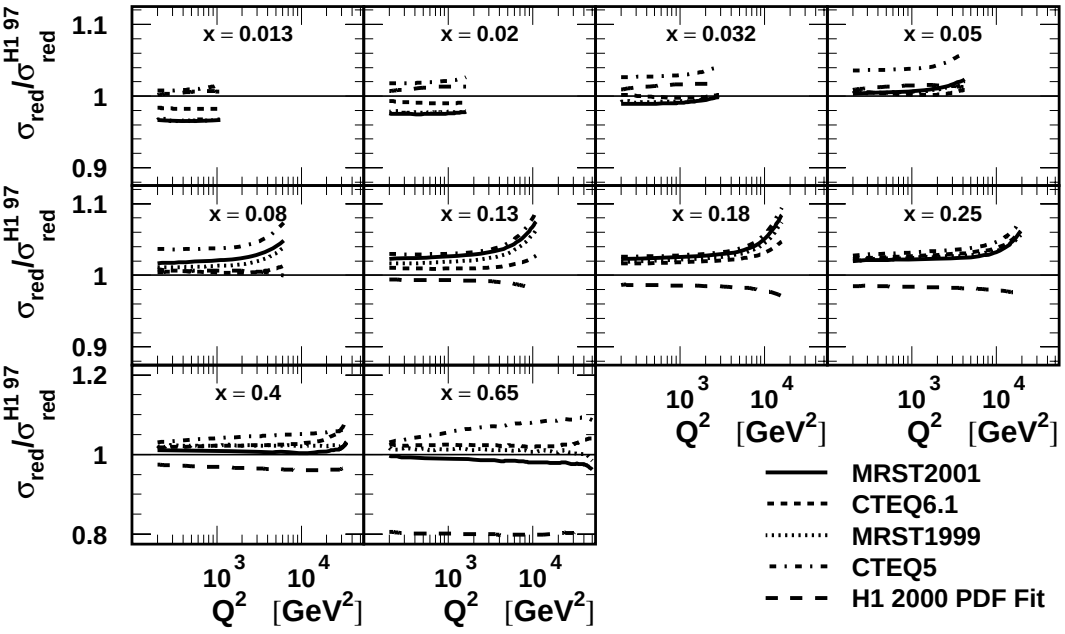

Figure 8.4: Neutral current cross sections derived from different PDF sets. They are normalised to the cross section obtained from the H1 1997 PDF Fit.

intermediate x values as can be seen in figure 8.4 which compares the cross section predictions based on different PDFs. For $0.13 \leq x \leq 0.25$ the H1 PDFs yield a smaller cross section towards high Q^2 compared to the PDFs of global analyses.

Fits to the double differential cross section with open relative normalisation between the x bins provide the lowest sensitivity to the PDF input (figure 8.3c). Apart from the CTEQ5 PDF all results of a given coupling combination are well compatible with each other. Also observed are significant changes in the results between the different normalisation procedures, in particular for the LR, RL and $LR + RL$ models. These changes can be attributed to cross section variations between different x bins these models are particularly sensitive to, since apart from the very high Q^2 region they yield only minor modifications to the Standard Model cross section (cf. figures in appendix B).

For a few contact interaction models, the results of the two-dimensional fit with free x normalisation obtained with the CTEQ5 PDF show distinct deviations compared to the results of all other PDFs. As shown in figure 8.4, the CTEQ5 PDF provides by far the largest cross section in the entire kinematic phase space. Furthermore, a significantly different Q^2 dependence is observed for the largest x bins. Of all PDFs considered here, the CTEQ5 PDF contains least input from HERA high Q^2 data. However, if the HERA high Q^2 data were significantly contributing to the PDF fits, the PDFs including recent HERA data should yield consistent results, but they don't in the one- and plain two-dimensional fits.

Thus, the contact interaction fits to the double differential cross section with a separate normalisation for each x bin yield the most robust procedure which is least sensitive to the PDF input. Moreover using the H1 1997 PDF Fit throughout this analysis, i.e. for the cross section measurement and for the fits, provides a consistent treatment of the Standard Model prediction.

8.2.3 Fits with PDF uncertainties

To obtain another estimate of the impact of the PDF uncertainties, the contact interaction fits were also performed with the PDF sets of MRST2001 [22] and CTEQ6.1 [19]. These analysis groups provide additional parameterisations which reflect the uncertainty contour of the χ^2 minimum of their PDF fit and are suited for use within the framework of linear error propagation (cf. section 2.5).

However, it is important to stress that so far these uncertainties only consider the statistical and systematic experimental errors of the data which are used in the PDF fits. So-called theoretical errors are not yet taken into account due to the lack of knowledge how to derive and how to treat them properly. Nevertheless, these PDF sets were used for systematic checks.

Two approaches were performed:

1. The error PDFs allow to calculate the error on the cross section due to the experimental uncertainties of the PDFs (cf. figure 2.7 on page 24). The resulting cross section changes are found to vary mainly as function of x but to be rather independent of Q^2 at fixed x. Contact interaction fits were performed where the relative normalisation of the x bins was allowed to vary within the corresponding cross section error given by the error PDFs.
2. The error PDF sets provide the cross section modifications for each eigenvector representation of the Hessian matrix obtained in the PDF fits (cf. section 2.5). Instead of allowing for the relative normalisation of each x bin, the contributions of the cross section changes obtained from these eigenvector PDF sets are fitted simultaneously within the contact interaction fit.

The fit results of both procedures are very similar to those obtained by the two-dimensional fit with an overall normalisation parameter only (cf. figure 8.3b). This may indicate that the PDF error treatment is still incomplete as expected since the theoretical uncertainties are not included.

8.2.4 Final normalisation procedure

The previous discussion confirms the approach to investigate the Q^2 dependence of the double differential neutral current cross section for each x bin separately. The final fit procedure allows the free relative normalisation between the x bins and accounts only for an effective overall normalisation.

Finally, the sensitivity to potential effects of contact interactions is investigated. The error bars of figure 8.3 already indicate that the final fit procedure provides comparable sensitivity as the one-dimensional fit. The χ^2 scans as function of ϵ/Λ^2 for different contact interaction coupling combinations are compared in figure 8.5 for the one- and two-dimensional fits with overall and x bin-wise normalisation. The width of the curves is a measure of the sensitivity. In general, highest sensitivity is obtained for models with multiple coupling contributions which lead to large cross section modifications. The sensitivity to the LR and RL models is low since they imply only small cross section changes for at least moderate compositeness scales Λ. The favoured

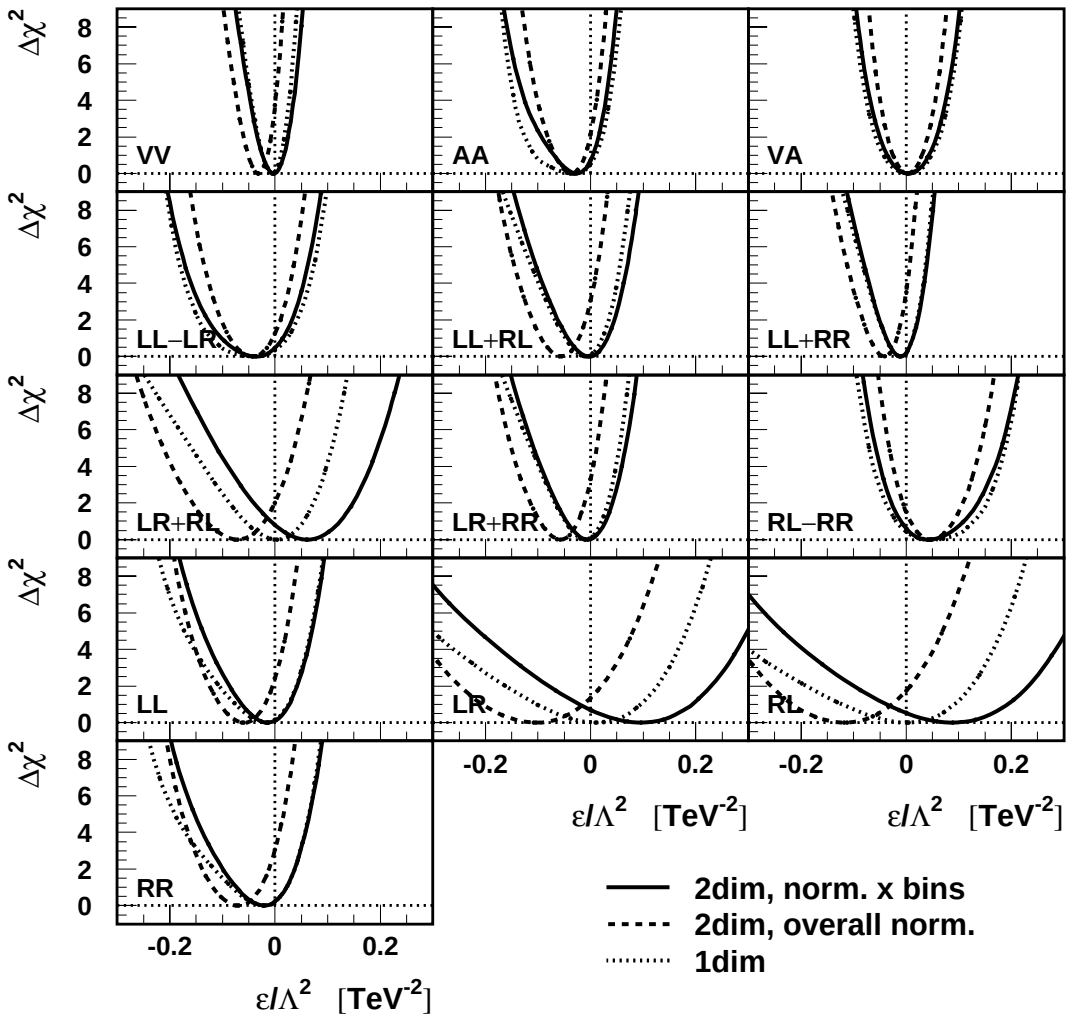

Figure 8.5: $\Delta\chi^2 = \chi^2 - \chi^2_{\text{min}}$ distribution as function of ϵ/Λ^2 for the different contact interaction coupling combinations. The results of the double differential fits with x bin-wise normalisation (solid line) are compared to the single (dotted line) and double differential (dashed line) fits applying only an overall normalisation. The cross section prediction is based on the H1 1997 PDF Fit.

procedure with free x normalisation yields comparable and partly even increased sensitivity compared to the one-dimensional fit. The two-dimensional fit with an overall normalisation parameter only provides the best sensitivity but introduces additional systematic dependences.

By construction of the fit, the results include the effects of systematic uncertainties. However, the fit considers only the dominant sources, and relies on several assumptions, in particular on the assignment of correlated and uncorrelated systematic errors. To check the influence of the systematic error treatment on the fit results the correlated systematic uncertainty of the electron energy measurement was considered individually for each wheel of the LAr calorimeter. Moreover, the correlated systematic error of the electron polar angle measurement was subdivided for the forward and backward detector regions. Negligible effects on the fit results were obtained compared to the original procedures.

8.3 Fit Result – Compatibility with the Standard Model

This section presents the fit results for the kinematic range of $Q^2 \geq 500$ GeV^2 and $x \geq 0.013$. Since the search for the effects of new physics is based on the prediction of the Standard Model, the data are first compared to the Standard Model alone without any contact interactions.

Including experimental statistical and systematic errors, the fit yields $\chi^2 = 64.4$ for 58 degrees of freedom, translating into a GoF probability of 26.4%. The overall normalisation is 0.977 and found to be compatible with the overall experimental uncertainties within 2σ. The relative normalisation between the x bins ranges from 0.98 at low x to about 1.1−1.2 at highest x. The pulls of the correlated systematic errors are close to zero. The correlations between the fit parameters are about 50% without large point-to-point correlations.

Very similar results are found using the alternative PDFs like the H1 2000 PDF Fit, CTEQ6.1, MRST2001 and MRST1999. They only differ slightly in the normalisation of the x bins. The fit with CTEQ5 yields an improved $\chi^2 = 60$ with an overall normalisation of unity.

Thus, there is good agreement of the data with the Standard Model hypothesis, allowing to test the compatibility of the data with the predictions of contact interactions.

The compatibility of the data with the Standard Model within the different contact interaction scenarios is tested by determining the estimators R^2 and ϵ/Λ^2 for the quark radius and compositeness hypotheses, respectively. For this procedure, the fit is performed using statistical errors from the data observation (cf. section 8.1.2). R^2 is allowed to become negative and both $\epsilon = +1$ and $\epsilon = -1$ models of the compositeness coupling combinations are treated within the same fit.

For the quark radius fit, the χ^2 function is shown in figure 8.6 together with the systematic dependences of electron energy scale and scattering angle, strong coupling constant and overall normalisation. As expected, the normalisation shows a distinct negative correlation with R^2, since the cross section prediction decreases with rising R^2. The remaining correlations are rather small.

The χ^2 dependence of ϵ/Λ^2 of the compositeness models was shown in figure 8.5. All scenarios are found to be well compatible with the Standard Model prediction of $\epsilon/\Lambda^2 = 0$. Some scenarios, for instance the AA and $LL - LR$ models, show an asymmetric χ^2 behaviour. This can be attributed to cancellations of the contact interaction contributions with the Standard Model amplitudes which, depending on the sign of ϵ, allow significant cross section changes only at very large Q^2 or for rather low scales Λ (cf. figures in appendix B). No secondary minima are observed, i.e. the χ^2 distributions show a monotonic rise in both directions around the minimum. This means in particular, that for the specific models of interference sign opposite to the fit result the best value of the estimators is $\epsilon/\Lambda^2 = 0$.

The results on R^2 and ϵ/Λ^2 are presented in figure 8.7. The errors represent the total 1 and 2σ uncertainties corresponding to $\Delta\chi^2 = 1$ and 4, respectively. All contact

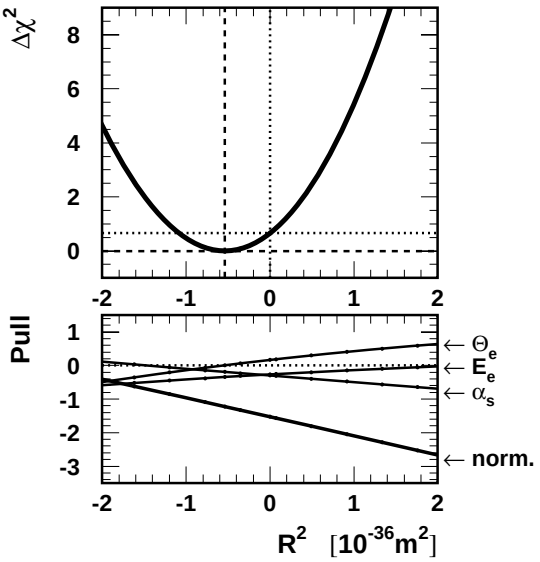

Figure 8.6: $\Delta\chi^2 = \chi^2 - \chi^2_{\text{min}}$ distribution (upper plot) and the effective pulls of the correlated parameters (lower plot) as function of R^2 for the quark radius fit.

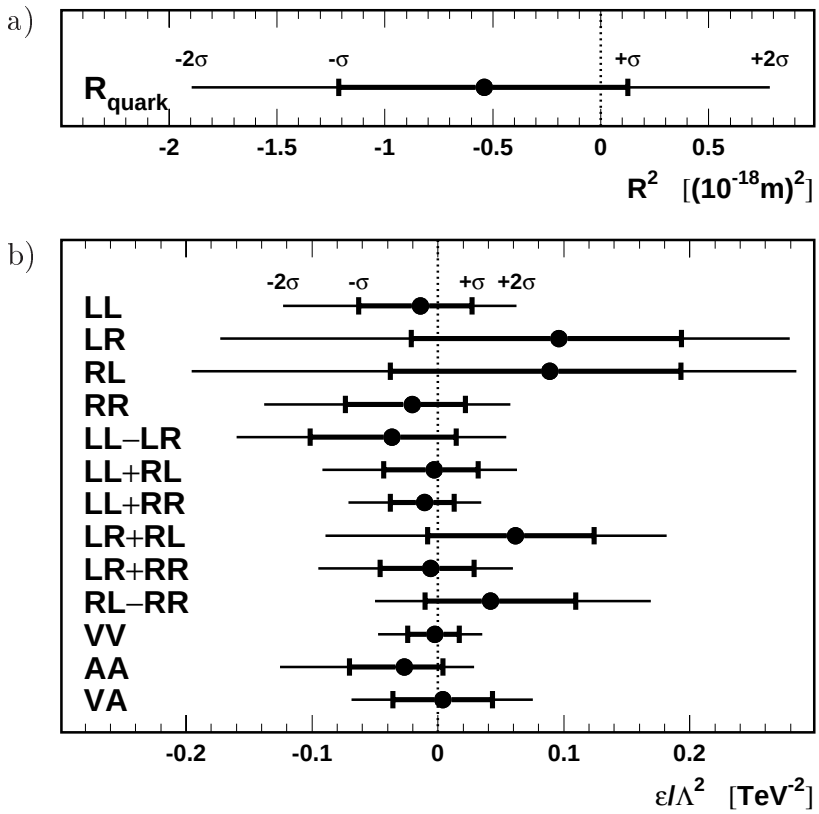

Figure 8.7: χ^2 fit results of the parameters R^2 for the quark radius (a) and ϵ/Λ^2 for compositeness models (b). The inner and outer error bars represent one and two standard deviations, respectively, as obtained using experimental statistical and systematic errors. Each coupling combination of figure (b) represents two contact interaction models of $\epsilon = \pm 1$.

interaction models are in good agreement with the Standard Model prediction which is always obtained within one standard deviation.

Assuming Gaussian errors, the compatibility of the data with different contact interaction hypotheses is measured by the GoF probability $P_{GoF}(\chi^2 > \chi^2_{\min})$ of expecting a χ^2 value larger than the one obtained from the data. The values of P_{GoF} are given in table 8.3 with the χ^2 fit results for all contact interaction models, including the quark radius. The GoF probability is about 25% for all hypotheses, indicating consistency of

	χ^2 fit to $d^2\sigma/dx\,dQ^2$ with free relative x bin normalisation				
	New physics estimator	n_{dof}	χ^2/n_{dof}	P_{GoF} [%]	P_{SM} [%]
SM	-	58	1.110	26.4	-
R_{quark}	$R^2 = (-0.54 \pm 0.67)10^{-36}$ m^2	57	1.118	25.2	10.5
LL	$\epsilon/\Lambda^2 = (-0.014 \pm 0.044)$ TeV^{-2}	57	1.127	23.7	62.7
LR	$\epsilon/\Lambda^2 = (\ 0.096 \pm 0.105)$ TeV^{-2}	57	1.117	25.4	11.9
RL	$\epsilon/\Lambda^2 = (\ 0.089 \pm 0.113)$ TeV^{-2}	57	1.120	24.9	13.9
RR	$\epsilon/\Lambda^2 = (-0.021 \pm 0.047)$ TeV^{-2}	57	1.125	24.0	59.8
VV	$\epsilon/\Lambda^2 = (-0.003 \pm 0.020)$ TeV^{-2}	57	1.129	23.5	68.0
AA	$\epsilon/\Lambda^2 = (-0.027 \pm 0.036)$ TeV^{-2}	57	1.116	25.4	44.4
VA	$\epsilon/\Lambda^2 = (\ 0.004 \pm 0.042)$ TeV^{-2}	57	1.129	23.5	28.7
$LL - LR$	$\epsilon/\Lambda^2 = (-0.037 \pm 0.059)$ TeV^{-2}	57	1.121	24.7	50.3
$LL + RL$	$\epsilon/\Lambda^2 = (-0.003 \pm 0.037)$ TeV^{-2}	57	1.129	23.5	69.9
$LL + RR$	$\epsilon/\Lambda^2 = (-0.011 \pm 0.025)$ TeV^{-2}	57	1.126	24.0	58.6
$LR + RL$	$\epsilon/\Lambda^2 = (\ 0.061 \pm 0.066)$ TeV^{-2}	57	1.115	25.6	10.5
$LR + RR$	$\epsilon/\Lambda^2 = (-0.006 \pm 0.037)$ TeV^{-2}	57	1.129	23.5	67.7
$RL - RR$	$\epsilon/\Lambda^2 = (\ 0.042 \pm 0.061)$ TeV^{-2}	57	1.119	25.1	48.1

Table 8.3: Results of the fits to the Standard Model (SM) prediction, the quark radius and various compositeness models. The errors of the estimators represent the parabolic error obtained from the corresponding χ^2 fit. The P_{SM} probability is derived from Monte Carlo experiments and corresponds to models with ϵ of the same sign as the ϵ/Λ^2 fit result.

the models with the data. The introduction of additional physics beyond the Standard Model cannot improve the fit quality.

Since the models provide an appropriate description of the data, a frequentist approach is used to quantify the compatibility of the data with the different model predictions. The Monte Carlo experiment procedure is used, which is introduced in section 8.4.1 for the limit determination. For the quark radius and for compositeness models (of specific sign of ϵ) with $1/\Lambda^2 \neq 0$, Monte Carlo experiments are used to estimate the probability P_{SM}, that statistical or systematic effects in an experiment with the Standard Model cross section would produce a value of $1/\Lambda^2$ larger than the one obtained from the data. In this case, the statistical error entering the fit is taken from the Standard Model prediction. The results are given in the last column of table 8.3.

The probabilities to measure the data assuming the Standard Model hypotheses ranges between 10 and 70%. Rather low probabilities are obtained for contact interac-

tion models of positive ϵ/Λ^2 results, suggesting some preference of the fit for negative values of the estimators in the absence of a clean signal. However, the Standard Model probabilities P_{SM} don't indicate significant amplitudes for any of the contact interaction scenarios considered. Limits will thus be determined on the effects of contact interactions.

8.4 Limits for New Physics Scales

This section introduces methods to determine limits on contact interactions scales and presents the limits on the quark radius and compositeness scales.

8.4.1 Limit Determination

The procedure used for the limit determination assumes the validity of a certain model hypothesis, i.e. contact interactions, and determines the probability to observe the model parameter as measured in the data. In this case, the statistical error is taken from the model prediction.

$\Delta\chi^2$ Method

An obvious way to derive limits from a χ^2 fit is the $\Delta\chi^2$ method, which provides a central confidence interval according to equation 8.3. The procedure is illustrated in figure 8.8. Since the data were found to be in agreement with the Standard Model

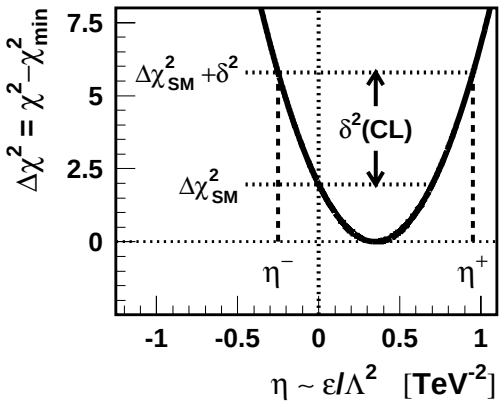

Figure 8.8: Illustration of the limit determination using the statistical χ^2 method. The curve represents an arbitrary χ^2 function. The lower and upper limits, η^- and η^+, are obtained from $\Delta\chi^2 = \Delta\chi^2_{\mathrm{SM}} + \delta^2$, where δ specifies the standard deviations.

prediction, the deviations from the Standard Model, i.e. non-zero ϵ/Λ^2 values, are attributed to statistical fluctuations. Therefore, the limits are derived with respect to the Standard Model χ^2 value, χ^2_{SM}.

However, the probabilistic interpretation becomes problematic in case of secondary minima and asymmetric shapes of the χ^2 curves as actually observed. To avoid this problems, a frequentist approach is used for the determination of the contact interaction limits.

Monte Carlo Experiment Method

The limits on the contact interaction scales are determined applying a frequentist approach on the basis of Monte Carlo experiments. The procedure is explained in the following for the evaluation of limits on compositeness scales but applies identically to the quark radius.

1. Generate a Monte Carlo cross section for the prediction of a specific contact interaction model with scale parameter Λ_{true}.
2. Smear the Monte Carlo cross section according to the experimental uncorrelated and correlated systematic uncertainties, assuming Gaussian behaviour of the errors.
3. Smear the Monte Carlo cross section according to the statistical error given by the predicted number of events using Poisson statistics.
4. Analyse the Monte Carlo event in the same way as the data, with the statistical errors taken from the prediction and including all systematic errors to obtain the best fitted value Λ_{fit}.
5. Repeat steps 1 to 4 numerous times for fixed Λ_{true}.
6. Repeat steps 1 to 5 for different values of Λ_{true}.

For each input scale Λ_{true}, the fit results Λ_{fit} of the Monte Carlo experiments yield a probability distribution to obtain some scale Λ. The limits on the contact interaction scales are derived by comparing the Monte Carlo experiments to the actual data fit result Λ_{data}. The lower limit on Λ at 95% confidence level is defined as that value Λ_{true} where 95% of the Monte Carlo experiments produce values of Λ_{fit} which are smaller than Λ_{data}. The procedure is illustrated in figure 8.9 in terms of $\eta \sim \epsilon/\Lambda^2$ for the case of $\epsilon = +1$. The lower limit on Λ corresponds to an upper limit on $|\eta|$. Considering both

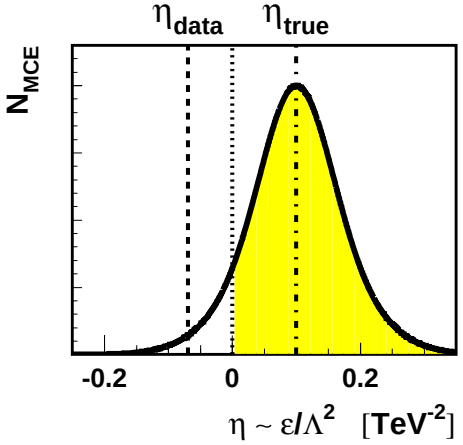

Figure 8.9: Illustration of the limit determination using MC experiments. The curve represents the fit results η_{fit} of many MC experiments for a given value η_{true}. In this example, the confidence level for the scenario of positive ϵ corresponds to the shaded area fraction starting at $\eta = 0$, which is the data result for the $\epsilon = +1$ compositeness model.

signs of ϵ, the upper (lower) limit on η at 95% confidence level is defined according to that value Λ_{true} where 95% of the Monte Carlo experiments produce values of η_{fit} which are larger (smaller) than η_{data}. The value is taken for η_{data} which corresponds to the specific model of sign ϵ which is actually tested. This means that $\eta_{data} = 0$, if

the data fit result has opposite sign compared to ϵ, since the χ^2 curves of the data fits shown a monotonic increase without secondary minima.

8.4.2 Quark radius

A finite quark radius, which is represented by the root of the mean squared radius of the electroweak charge distribution, is introduced to the neutral current cross section by a form factor ansatz (cf. section 3.1). Assuming point-like electrons, the upper bound on the quark radius is determined to be

$$\boxed{R_{\text{quark}} < 1.1 \times 10^{-18} \text{ m (CL=95\%)}.}$$

The limit is valid for the light quarks which yield the dominant contribution to neutral current ep scattering at HERA.

The result is compatible to other measurements. A recent H1 publication quotes $R_{\text{quark}} < 1.0 \times 10^{-18}$ m [95], investigating the single differential cross sections $d\sigma/dQ^2$ of all H1 data of the HERA-I run. The TeVatron experiments D0 and CDF derived very similar bounds from Drell-Yan e^+e^- and $\mu^+\mu^-$ production in $p\overline{p}$ scattering, assuming point-like leptons. Using an identical form factor ansatz, the LEP experiment L3 derived the most stringent upper limit so far of $R_{\text{quark}} < 4.2 \times 10^{-19}$ m [97] from the hadronic cross section measurement on the Z^0 resonance.

The form factor approach provides clean and direct access to the spatial extension of fermions without further model assumptions. A point-like electron is a conservative assumption, which is however motivated by stringent limits obtained from the $(g-2)$ experiments searching for anomalous magnetic moments. Allowing form factors for both electrons and quarks, the limits get stronger since the cross section is then proportional to f^4 instead of f^2. Moreover, the exchange bosons are treated as point-like, which is quite natural for the elementary photons but may be less obvious in the case of the massive Z^0 boson.

A complementary approach is the investigation of hadronic Z^0 decays performed by the LEP experiments. Their search for contributions of anomalous magnetic dipole moments to the $Z^0 q\overline{q}$ vertex yields comparable upper bounds of the order of $R_{\text{quark}} < 10^{-18}$ m on the size of the light quarks [32]. However, these analyses strongly rely on model assumptions, for instance whether the anomalous magnetic moments depend linearly or quadratically on the fermion mass.

8.4.3 Compositeness

The description and implementation of compositeness models in the framework of Standard Model neutral current ep scattering were discussed in section 3.2. Contact interaction fits were performed to confront the cross section measurement with various compositeness models represented by coupling combinations and the sign of the interference with the Standard Model amplitude. The lower limits on the compositeness scales Λ are presented in figure 8.10. The limits range from 1.5 to 4.8 TeV depending on the chiral structure.

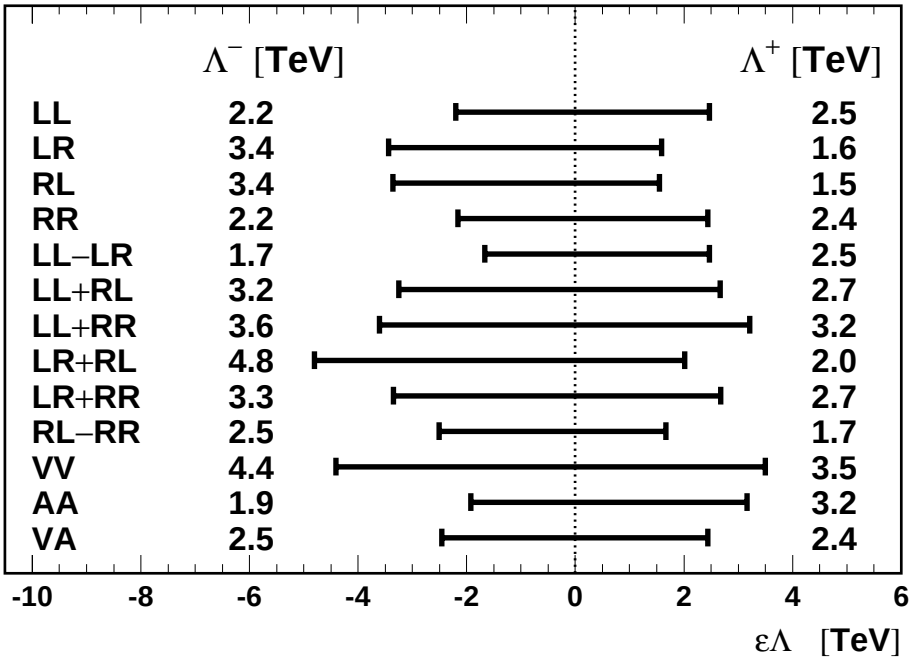

Figure 8.10: Result of the fit analysis: Exclusion limits (CL=95%) on the compositeness scales Λ^+ and Λ^- for different coupling combinations.

The strongest limits are obtained for the $LL+RR$, $LR+RL$, VV and AA models, where multiple chiral couplings enter with the same sign. The LL and RR models and the LR and RL models are almost indistinguishable in unpolarized DIS scattering. The cases with limits below 2 TeV correspond to parameter combinations where the pure contact interaction contributions and the terms of interference with the Standard Model amplitudes approximately cancel.

For most of the coupling combinations, higher bounds are found for models with negative interference. This behaviour can be attributed to the tendency of the cross section to rise towards highest Q^2 in some x bins (cf. figure 8.2).

Very asymmetric limits are observed for the LR, RL, $LR+RL$ and AA coupling combinations, where the model with the interference sign of the weak limit yields significant modifications to the cross section only at low values of Λ (cf. figures in appendix B). The results are found to be consistent with the χ^2 observations of figure 8.7.

Comparison with other results

Electron-quark compositeness is searched for by many experiments. They approach the four-fermion interaction from different sides as illustrated in figure 8.11. The HERA experiments exploit deep inelastic ep scattering as in the present analysis. LEP analyses investigate the $e^+e^- \to q\overline{q}$ hadronic cross section measurement and forward-backward asymmetries in fermion pair production. The TeVatron experiments study Drell-Yan lepton-pair production ($q\overline{q} \to l\overline{l}$) at high dielectron invariant mass.

Table 8.4 shows a comparison of the compositeness results presented in this thesis

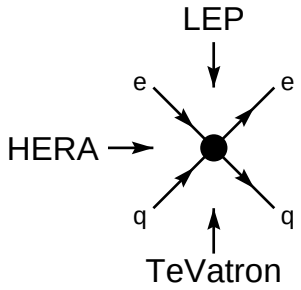

Figure 8.11: Access to electron-quark contact interactions for HERA, LEP and TeVatron experiments.

Compositeness couplings		This analysis [TeV]	H1 [TeV]	ZEUS [TeV]	LEP [TeV]	TeVatron [TeV]
LL	Λ^+	2.47	2.8	-	5.4	3.3
	Λ^-	2.20	1.6	-	6.2	4.2
LR	Λ^+	1.59	3.3	-	3.8	3.4
	Λ^-	3.44	1.9	-	4.4	3.6
RL	Λ^+	1.55	3.3	-	2.7	3.3
	Λ^-	3.36	2.0	-	6.4	3.7
RR	Λ^+	2.44	2.8	-	3.9	3.3
	Λ^-	2.16	2.2	-	4.4	4.0
VV	Λ^+	3.50	5.3	4.7	6.4	4.9
	Λ^-	4.41	5.5	5.0	7.1	6.1
AA	Λ^+	3.17	2.5	2.6	7.2	4.7
	Λ^-	1.92	4.1	3.7	7.9	5.5
VA	Λ^+	2.44	2.9	2.5	-	-
	Λ^-	2.45	3.0	2.6	-	-
$LL-LR$	Λ^+	2.47	-	1.8	-	3.9
	Λ^-	1.67	-	2.8	-	4.5
$LL+RL$	Λ^+	2.67	-	3.4	-	-
	Λ^-	3.25	-	3.1	-	-
$LL+RR$	Λ^+	3.21	3.7	2.9	6.7	4.2
	Λ^-	3.61	3.9	2.8	7.4	5.1
$LR+RL$	Λ^+	2.01	4.4	4.0	3.4	3.9
	Λ^-	4.80	4.4	4.3	7.1	4.4
$LR+RR$	Λ^+	2.67	-	3.5	-	-
	Λ^-	3.35	-	3.3	-	-
$RL-RR$	Λ^+	1.67	-	2.8	-	4.0
	Λ^-	2.51	-	1.7	-	4.3

Table 8.4: Comparison of the present limit results on compositeness scales with other analyses from HERA, LEP and TeVatron.

with the corresponding limits reported by other analyses. All limits shown assume flavour symmetry, i.e. couplings to all three generations of quarks. The sensitivity to contact interactions is at scales Λ of a few TeV.

The limits published recently by H1 [95], labelled 'H1', are based on the investigation of the single differential cross sections $d\sigma/dQ^2$ of the entire data sets of the

HERA-I run. They found comparable or slightly stronger limits. For the LR, RL and AA models the published analysis derived asymmetric limits with the stronger limit for the opposite interference signs as observed in the present analysis. This can be attributed to the bias of the one-dimensional fit performed by the published analysis to negative values of ϵ/Λ^2 as discussed in section 8.2.2 and shown in figure 8.3.

A similar opposite behaviour is observed between the present analysis and the ZEUS publication [98], which is based on an unbinned log-likelihood technique using solely the shape of the (x,y)-distribution of the neutral current cross section. Here oppositely strong exclusion limits are assigned to the AA, $LL-LR$ and $RL-RR$ models. This may suggest that the ZEUS analysis suffers from PDF dependences as well. Otherwise, the ZEUS limits are comparable to the H1 results.

The LEP experiments ALEPH [99], L3 [97] and OPAL [100] also have reported on contact interactions. The 'LEP' results in table 8.4 give the stongest limits for each coupling combination (both signs) obtained by any of the three experiments. Where available, the LEP results exceed the limits obtained in the present analysis and mostly yield the strongest limits at all reaching scales of $6-8$ TeV. However, the predominance is basically due to the assumption of flavour symmetric compositeness structures. The LEP experiments are mainly sensitive to second- and third-generation quarks. Actually, the LEP limits for compositeness models which couple only to first-generation quarks [100] are very similar to the HERA and TeVatron results.

The TeVatron experiments provide limits on the energy scale of quark-electron compositeness with common constituents. The 'TeVatron' limits, which show the results of the D0 experiment [101], are similar or slighly stronger compared to the HERA results.

The contact interaction constraints at HERA and TeVatron are insensitive to possible contributions from second- and third-generation quarks and thus rather independent of the assumption of flavour symmetry. If flavour universality is imposed, the LEP experiments sets stringent constraints on compositeness scales reaching about 8 TeV. Otherwise, the HERA, LEP and TeVatron experiments yield comparable and in some cases complementary sensitivity to the various contact interaction models.

Further discussions on comparisons and combinations of experimental results can be found in [102].

Chapter 9

Summary and Outlook

In this thesis, the measurement of the inclusive neutral current cross section for deep inelastic e^+p scattering and the subsequent search for electron-quark contact interactions is presented. The analysis is performed in the kinematic phase space of large momentum transfers where potential effects of new physics are expected to be seen first. This study presents an improved treatment of systematic effects and novel fitting methods in data reconstruction and in their interpretation. Both will prove useful in the analyses of future high statistics HERA data.

Cross section measurement

The cross section analysis is based on e^+p data taken in 1999 and 2000 with the H1 experiment at HERA. The available centre-of-mass energy was $\sqrt{s} \approx 319$ GeV and the data correspond to an integrated luminosity of 66 pb^{-1}.

Substantial improvements were obtained for the reconstruction of neutral current high Q^2 events. In particular, the precise measurement of the scattered electron is established using solely calorimetric information. Exploiting the full capabilities of the H1 Liquid Argon calorimeter the electron scattering angle is measured with a precision of 1 mrad and the uncertainty of the electron energy measurement is as low as 0.5% in most of the kinematic phase space. The comprehensive electron energy calibration procedure yields an energy resolution approaching $\sigma(E)/E = 12\%/\sqrt{E[\mathrm{GeV}]} \oplus 1\%$ as obtained from test beam measurements. In addition, the application of a new hadronic energy weighting algorithm allows the precise reconstruction of the hadronic final state without large kinematic dependences.

The inclusive single and double differential neutral current cross sections $d\sigma/dQ^2$ and $d^2\sigma/dx\,dQ^2$ are measured in the kinematic range of $200 \leq Q^2 \leq 30000$ GeV^2, $0.0032 \leq x \leq 0.65$ and $0.05 < y < 0.9$. The typical total precision of the cross section result is about 3% at low Q^2, where systematic uncertainties are the dominant contribution. The statistical error limits the accuracy of the single differential cross section for $Q^2 \gtrsim 1000$ GeV^2 and the double differential cross section for $Q^2 \gtrsim 500$ GeV^2. Compared to the Standard Model prediction the data are found to be about 3% high in overall normalisation. Considering statistical and systematic errors of the measurement the deviation corresponds to a 2σ effect. However, theoretical uncertainties of the

Standard Model prediction are not included, since they are not completely available. Otherwise the present results are in good agreement with the Standard Model QCD prediction and with comparable measurements.

In parts of the kinematic phase space, especially at large Q^2 and x, further improvements are expected with high statistics HERA-II data. In other regions the precision of the cross section measurement is already limited by systematic uncertainties. In addition, the measurements become sensitive to theoretical issues. In particular, a better understanding of the uncertainties of the parton density parameterisations would be desirable.

Contact interaction analysis

The measured cross section is further investigated to look for potential effects of electron-quark contact interactions associated with scales far beyond the HERA centre-of-mass energy. The Standard Model is extended including a finite quark radius or electron-quark compositeness. The former is considered by a Dirac form factor ansatz, the latter by a model independent approach of different chiral coupling combinations. These types of contact interactions primarily imply modifications to the Q^2 dependence of the Standard Model cross section.

In order to obtain reliable results, a novel χ^2 fit is introduced to compare the data with the model predictions. In particular the fit

- is performed to the double differential neutral current cross section to resolve the different kinematic dependences of Standard Model processes, systematic uncertainties and contact interactions;
- is restricted to the kinematic range of $Q^2 \geq 500$ GeV^2 and $x \geq 0.013$ to reduce the impact of systematic uncertainties on the results;
- allows the separate normalisation of different x bins to reduce the influence of x dependent systematic effects on the Q^2 distribution, accounting especially for the rather imprecisely known x dependence of the parton density parameterisations.

Estimators are evaluated to quantify the compatibility of the cross section measurement with the Standard Model prediction including the extensions due to contact interactions.

No significant indications are found for any of the contact interaction scenarios considered. The probability that the fitted contact interaction parameter is obtained from the Standard Model process is typically 50% and always larger than 10%. Limits are thus determined on the quark radius and on compositeness scales using a frequentist approach. The upper bound on the radius of light quarks is determined to be $R_{\text{quark}} < 1.1 \times 10^{-18}$ m (CL=95%). The lower limits on electron-quark compositeness scales range from 1.5 to 4.8 TeV depending on the chiral coupling contributions. The results exhibit a sensitivity to contact interactions comparable and partly complementary to that of other analyses performed at HERA, LEP or TeVatron.

Further data from the HERA-II run will improve the sensitivity by adding statistics in the region of highest Q^2 values. However, the systematic dependences remain and

need to be improved from both the experimental and the theoretical side. Future analyses may also include the charged current cross section, which is ignored so far due to low statistics and large systematic errors compared to the neutral current interactions. Nevertheless, since the Standard Model charged current interaction is already maximum selective concerning chiral couplings, this channel may provide high sensitivity to specific coupling combinations. Moreover, the HERA-II run will deliver longitudinally polarised lepton beams, which will increase the sensitivity to some compositeness models and will be of extraordinary importance to identify potential signals.

Closing words

Although formulated more than ten years ago, the following citation from [4] concisely describes the present situation in high energy physics:

> "The Standard Model is a remarkable theory, representing the culmination of modern scientific attempts to understand the laws of Nature. While appreciating the power of the Standard Model, it is nonetheless appropriate to look forward to the discovery of new physics from the next layer of reality."

Appendix A

Tables of Cross Section Results

Q^2 [GeV^2]	$d\sigma/dQ^2$ [pb/GeV^2]	δ_{stat} [%]	δ_{unc} [%]	δ_{cor} [%]	δ_{sys} [%]	δ_{tot} [%]	$\delta_{cor}^{E_e^+}$ [%]	$\delta_{cor}^{E_e^-}$ [%]	$\delta_{cor}^{\theta_e^+}$ [%]	$\delta_{cor}^{\theta_e^-}$ [%]	$\delta_{cor}^{E_h^+}$ [%]	$\delta_{cor}^{E_h^-}$ [%]	$\delta_{cor}^{Bg^+}$ [%]	$\delta_{cor}^{Bg^-}$ [%]
200	1.860×10^{1}	0.7	2.3	1.1	2.5	2.6	-0.9	0.9	-0.7	0.6	0.0	0.0	-0.1	0.1
250	1.105×10^{1}	0.8	2.3	1.1	2.6	2.7	-0.9	0.9	-0.6	0.6	0.0	0.0	-0.1	0.1
300	7.221×10^{0}	0.8	1.9	1.0	2.1	2.3	-0.8	0.8	-0.5	0.6	0.0	0.0	-0.1	0.1
400	3.581×10^{0}	0.9	1.9	1.0	2.2	2.4	-0.8	0.8	-0.6	0.6	0.0	0.0	0.0	0.0
500	2.048×10^{0}	1.1	1.9	1.1	2.2	2.5	-0.8	0.8	-0.7	0.6	0.0	0.0	-0.1	0.1
650	1.077×10^{0}	1.4	1.7	0.8	1.9	2.4	-0.7	0.7	-0.5	0.5	0.0	0.0	-0.1	0.1
800	0.639×10^{0}	1.7	1.5	0.6	1.7	2.4	-0.5	0.5	-0.3	0.4	0.0	0.0	-0.1	0.1
1000	0.378×10^{0}	1.8	1.5	0.6	1.6	2.4	-0.4	0.4	-0.3	0.3	0.0	0.0	-0.2	0.2
1200	0.235×10^{0}	2.0	1.6	0.5	1.6	2.6	-0.3	0.3	-0.4	0.3	0.0	-0.1	-0.1	0.1
1500	0.130×10^{0}	2.3	1.6	0.3	1.6	2.8	-0.2	0.1	-0.2	0.3	0.0	0.0	-0.1	0.1
2000	0.573×10^{-1}	2.8	1.7	0.2	1.8	3.3	0.1	-0.1	-0.1	0.2	0.0	0.0	-0.1	0.1
3000	0.198×10^{-1}	2.6	2.1	0.4	2.2	3.4	0.3	-0.3	-0.2	0.2	0.1	-0.1	-0.1	0.1
5000	0.464×10^{-2}	3.7	2.9	0.8	3.0	4.7	0.4	-0.4	-0.6	0.7	0.0	0.0	-0.1	0.1
8000	0.116×10^{-2}	6.0	4.8	0.9	4.9	7.8	0.8	-0.8	-0.3	0.3	0.0	-0.1	-0.2	0.2
12000	0.241×10^{-3}	12.4	5.4	0.8	5.4	13.6	0.7	-0.7	-0.4	0.4	0.0	-0.1	-0.3	0.3
20000	0.209×10^{-4}	29.7	8.7	1.1	8.8	31.0	0.9	-0.9	0.1	0.0	0.2	-0.2	-0.5	0.5
30000	0.105×10^{-4}	41.4	11.2	1.8	11.4	43.0	1.4	-1.4	0.3	-0.4	0.5	-0.6	-1.1	1.1

Table A.1: The NC e^+p cross section $d\sigma/dQ^2$ for $y < 0.9$, shown with statistical (δ_{stat}), uncorrelated systematic (δ_{unc}), correlated systematic (δ_{cor}), total systematic (δ_{sys}) and total (δ_{tot}) errors. The table also provides the contributions to the correlated systematic error from a respective positive and negative variation of one standard deviation of the error on the electron energy ($\delta_{cor}^{E_e^\pm}$), the electron polar angle ($\delta_{cor}^{\theta_e^\pm}$), the hadronic energy ($\delta_{cor}^{E_h^\pm}$) and the background subtraction ($\delta_{cor}^{Bg^\pm}$). The normalisation uncertainty of 1.5% is not included in the errors.

Q^2 [GeV^2]	x	y	$\widetilde{\sigma}$	δ_{stat} [%]	δ_{sys} [%]	δ_{tot} [%]	δ_{unc} [%]	$\delta_{unc}^{E_e}$ [%]	$\delta_{unc}^{E_h}$ [%]	δ_{cor} [%]	$\delta_{cor}^{E_e^+}$ [%]	$\delta_{cor}^{E_e^-}$ [%]	$\delta_{cor}^{\theta_e^+}$ [%]	$\delta_{cor}^{\theta_e^-}$ [%]	$\delta_{cor}^{E_h^+}$ [%]	$\delta_{cor}^{E_h^-}$ [%]	$\delta_{cor}^{Bg^+}$ [%]	$\delta_{cor}^{Bg^-}$ [%]
200	0.0032	0.615	1.257	1.8	2.4	3.0	2.2	0.7	0.1	0.9	-0.4	0.4	-0.4	0.2	0.0	0.0	-0.7	0.7
200	0.0050	0.394	1.113	1.6	2.3	2.8	2.1	0.7	0.0	0.8	-0.4	0.4	-0.6	0.7	0.0	0.0	-0.1	0.1
200	0.0080	0.246	0.940	1.5	2.5	3.0	2.4	1.3	0.0	0.9	-0.7	0.7	-0.7	0.6	0.0	0.0	0.0	0.0
200	0.0130	0.151	0.837	1.6	3.3	3.7	3.0	2.1	0.0	1.4	-1.0	1.1	-0.9	0.9	0.0	0.0	0.0	0.0
200	0.0200	0.098	0.707	2.0	4.9	5.3	4.5	3.8	0.0	2.0	-1.9	1.9	-0.6	0.6	0.0	0.0	0.0	0.0
200	0.0320	0.062	0.564	2.6	5.9	6.4	5.6	4.8	0.0	1.9	-1.8	1.8	-0.5	0.3	0.0	0.0	0.0	0.0
250	0.0050	0.492	1.192	1.6	2.1	2.6	2.0	0.5	0.1	0.7	-0.3	0.3	-0.6	0.5	0.0	0.0	-0.3	0.3
250	0.0080	0.308	0.988	1.7	2.4	3.0	2.2	0.8	0.0	0.8	-0.6	0.6	-0.5	0.7	0.0	0.0	0.0	0.0
250	0.0130	0.189	0.821	2.0	3.0	3.6	2.8	1.6	0.0	1.0	-0.8	0.8	-0.5	0.4	0.0	0.0	0.0	0.0
250	0.0200	0.123	0.712	2.0	4.1	4.6	3.7	2.9	0.0	1.7	-1.5	1.6	-0.8	0.8	0.0	0.0	0.0	0.0
250	0.0320	0.077	0.554	2.1	5.7	6.1	5.3	4.8	0.1	2.1	-2.0	2.0	-0.7	0.7	0.0	0.0	0.0	0.0
300	0.0050	0.591	1.199	2.3	2.7	3.6	2.6	0.5	0.1	0.7	-0.3	0.3	-0.3	0.4	-0.1	0.0	-0.4	0.4
300	0.0080	0.369	1.013	1.6	2.2	2.8	2.1	0.6	0.0	0.7	-0.4	0.4	-0.5	0.5	0.0	0.0	-0.1	0.1
300	0.0130	0.227	0.850	1.7	2.4	3.0	2.2	0.7	0.1	0.8	-0.6	0.6	-0.6	0.6	-0.1	0.1	0.0	0.0
300	0.0200	0.148	0.726	2.1	3.3	3.9	3.0	1.8	0.0	1.4	-1.3	1.4	-0.5	0.6	0.0	0.0	0.0	0.0
300	0.0320	0.092	0.599	2.5	4.2	4.9	3.7	2.6	0.1	1.9	-1.7	1.7	-0.7	0.9	0.0	0.0	0.0	0.0
300	0.0500	0.059	0.510	3.0	4.4	5.4	4.2	2.9	0.1	1.5	-1.4	1.4	-0.6	0.5	0.0	-0.1	0.0	0.0
400	0.0080	0.492	1.022	2.3	2.7	3.5	2.6	0.2	0.0	0.6	-0.2	0.2	-0.6	0.6	0.0	0.0	-0.1	0.1
400	0.0130	0.303	0.877	1.9	2.5	3.1	2.4	0.6	0.1	0.7	-0.4	0.4	-0.5	0.6	0.0	0.0	0.0	0.0
400	0.0200	0.197	0.729	2.0	2.8	3.5	2.7	1.3	0.1	1.0	-0.8	0.8	-0.5	0.6	0.0	0.0	0.0	0.0
400	0.0320	0.123	0.606	2.1	3.3	4.0	2.9	1.6	0.1	1.6	-1.4	1.5	-0.8	0.7	0.0	0.0	0.0	0.0
400	0.0500	0.079	0.523	2.3	4.1	4.7	3.7	2.6	0.0	1.8	-1.6	1.6	-0.7	0.8	0.0	0.0	0.0	0.0
500	0.0080	0.615	0.978	3.1	2.7	4.2	2.6	0.3	0.2	0.5	-0.2	0.1	-0.2	0.1	0.1	-0.1	-0.5	0.5
500	0.0130	0.379	0.840	2.8	2.7	3.9	2.6	0.8	0.0	0.7	-0.5	0.5	-0.6	0.5	0.0	0.0	-0.1	0.1
500	0.0200	0.246	0.722	2.4	2.4	3.4	2.3	0.5	0.1	0.8	-0.5	0.5	-0.7	0.5	0.0	0.0	0.0	0.0
500	0.0320	0.154	0.639	2.4	3.0	3.9	2.8	1.6	0.1	1.3	-1.1	1.2	-0.6	0.5	-0.1	0.0	0.0	0.0
500	0.0500	0.098	0.530	2.6	3.8	4.6	3.2	2.2	0.1	2.0	-1.7	1.8	-0.9	1.0	0.0	0.0	0.0	0.0
500	0.0800	0.062	0.436	3.0	3.7	4.8	3.5	2.4	0.1	1.4	-1.0	0.9	-1.0	0.9	0.0	0.0	0.0	0.0

Table A.2: The NC e^+p reduced cross section $\widetilde{\sigma}(x, Q^2)$, shown with statistical (δ_{stat}), systematic (δ_{sys}) and total (δ_{tot}) errors. Also shown are the total uncorrelated systematic errors (δ_{unc}) and two of its contributions: the electron energy error ($\delta_{unc}^{E_e}$) and the hadronic energy error ($\delta_{unc}^{E_h}$). The effect of the other uncorrelated systematic errors is included in δ_{unc}. The table also provides the correlated systematic error (δ_{cor}) and its contributions from a respective positive and negative variation of one standard deviation of the error on the electron energy ($\delta_{cor}^{E_e^\pm}$), the electron polar angle ($\delta_{cor}^{\theta_e^\pm}$), the hadronic energy ($\delta_{cor}^{E_h^\pm}$) and the background subtraction ($\delta_{cor}^{Bg^\pm}$). The normalisation uncertainty of 1.5% is not included in the errors. The table continues on the next two pages.

Q^2 [GeV^2]	x	y	$\widetilde{\sigma}$	δ_{stat} [%]	δ_{sys} [%]	δ_{tot} [%]	δ_{unc} [%]	$\delta_{unc}^{E_e}$ [%]	$\delta_{unc}^{E_h}$ [%]	δ_{cor} [%]	$\delta_{cor}^{E_e^+}$ [%]	$\delta_{cor}^{E_e^-}$ [%]	$\delta_{cor}^{\theta_e^+}$ [%]	$\delta_{cor}^{\theta_e^-}$ [%]	$\delta_{cor}^{E_h^+}$ [%]	$\delta_{cor}^{E_h^-}$ [%]	$\delta_{cor}^{Bg^+}$ [%]	$\delta_{cor}^{Bg^-}$ [%]
650	0.0080	0.800	0.982	4.2	2.2	4.7	2.0	0.2	0.2	0.7	-0.2	0.2	-0.1	0.1	0.1	-0.1	-0.7	0.7
650	0.0130	0.492	0.920	3.2	1.8	3.7	1.8	0.5	0.1	0.4	-0.3	0.3	-0.2	0.3	0.1	0.0	-0.1	0.1
650	0.0200	0.320	0.731	3.5	1.9	4.0	1.9	0.7	0.1	0.6	-0.4	0.4	-0.3	0.4	0.0	0.0	0.0	0.0
650	0.0320	0.200	0.626	3.2	2.2	3.9	2.0	1.1	0.0	1.0	-0.8	0.8	-0.5	0.5	0.0	0.0	0.0	0.0
650	0.0500	0.128	0.508	3.3	2.9	4.4	2.5	1.9	0.1	1.5	-1.4	1.4	-0.6	0.6	0.0	0.0	0.0	0.0
650	0.0800	0.080	0.448	3.4	3.1	4.6	2.8	2.2	0.0	1.4	-1.2	1.1	-0.8	0.6	0.0	0.0	0.0	0.0
800	0.0130	0.606	0.901	3.5	1.9	3.9	1.8	0.3	0.1	0.5	-0.2	0.2	-0.2	0.2	0.1	-0.1	-0.4	0.4
800	0.0200	0.394	0.781	3.5	1.8	4.0	1.7	0.2	0.1	0.5	-0.3	0.3	-0.3	0.4	0.0	-0.1	-0.1	0.1
800	0.0320	0.246	0.622	4.4	2.2	4.9	2.0	0.9	0.1	0.7	-0.6	0.7	-0.3	0.3	0.0	0.0	0.0	0.0
800	0.0500	0.158	0.494	4.8	2.4	5.4	2.1	1.1	0.0	1.1	-1.0	1.0	-0.5	0.5	0.0	0.0	0.0	0.0
800	0.0800	0.098	0.457	4.8	3.2	5.7	2.8	2.1	0.0	1.5	-1.4	1.4	-0.6	0.6	0.0	0.0	0.0	0.0
800	0.1300	0.061	0.352	5.9	2.6	6.5	2.5	1.4	0.1	0.6	0.0	-0.2	-0.6	0.6	0.0	0.0	0.0	0.0
1000	0.0130	0.757	0.923	4.9	2.7	5.5	2.5	0.4	0.2	0.9	-0.2	0.2	-0.1	0.1	0.1	-0.1	-0.9	0.9
1000	0.0200	0.492	0.790	3.7	1.8	4.1	1.8	0.3	0.1	0.3	-0.2	0.2	-0.1	0.2	0.1	0.0	-0.2	0.2
1000	0.0320	0.308	0.625	4.0	1.9	4.4	1.9	0.6	0.0	0.6	-0.5	0.5	-0.4	0.4	0.0	0.0	0.0	0.0
1000	0.0500	0.197	0.558	4.5	2.2	5.0	2.1	0.8	0.1	0.8	-0.7	0.7	-0.3	0.4	0.0	0.0	0.0	0.0
1000	0.0800	0.123	0.492	5.2	3.0	6.0	2.7	1.8	0.0	1.3	-1.1	1.2	-0.6	0.6	0.0	0.0	0.0	0.0
1000	0.1300	0.076	0.382	6.8	2.8	7.3	2.7	1.2	0.0	0.6	-0.6	0.4	-0.4	0.4	0.0	0.0	0.0	0.0
1000	0.1800	0.055	0.319	9.1	3.4	9.7	3.1	1.0	0.1	1.4	1.2	-1.5	-0.4	0.3	0.0	-0.1	0.0	0.0
1200	0.0200	0.591	0.814	4.7	2.4	5.2	2.4	0.4	0.1	0.3	-0.2	0.2	0.1	0.0	0.1	-0.1	-0.2	0.2
1200	0.0320	0.369	0.647	4.2	1.9	4.6	1.9	0.5	0.0	0.4	-0.3	0.3	-0.3	0.3	0.0	0.0	0.0	0.0
1200	0.0500	0.236	0.542	4.5	2.1	5.0	2.0	0.7	0.1	0.7	-0.6	0.6	-0.4	0.4	0.0	-0.1	0.0	0.0
1200	0.0800	0.148	0.442	5.1	2.5	5.7	2.3	1.3	0.1	1.1	-0.9	0.9	-0.5	0.5	0.0	0.0	0.0	0.0
1200	0.1300	0.091	0.351	6.4	2.8	7.0	2.7	1.4	0.0	0.9	-0.7	0.6	-0.6	0.5	0.0	0.0	0.0	0.0
1200	0.1800	0.066	0.350	6.9	2.9	7.5	2.7	0.4	0.1	1.0	0.8	-1.1	-0.3	0.3	0.1	-0.1	0.0	0.0
1500	0.0200	0.738	0.805	6.3	3.4	7.2	3.2	0.5	0.1	1.1	-0.1	0.1	-0.7	0.8	0.1	-0.1	-0.8	0.8
1500	0.0320	0.462	0.616	5.5	2.4	6.0	2.4	0.6	0.1	0.3	-0.3	0.3	0.2	-0.2	0.0	0.0	-0.1	0.1
1500	0.0500	0.295	0.587	4.9	2.1	5.3	2.0	0.5	0.0	0.5	-0.4	0.5	-0.1	0.1	0.0	0.0	0.0	0.0
1500	0.0800	0.185	0.444	5.4	2.4	5.9	2.3	1.1	0.0	0.8	-0.8	0.8	-0.3	0.3	0.0	0.0	0.0	0.0
1500	0.1300	0.114	0.375	6.4	2.8	7.0	2.6	1.2	0.0	1.0	-0.9	0.8	-0.6	0.6	0.0	0.0	0.0	0.0
1500	0.1800	0.082	0.307	7.2	2.6	7.7	2.5	0.4	0.0	0.6	0.3	-0.5	-0.4	0.5	0.0	0.0	0.0	0.0
1500	0.2500	0.059	0.213	9.3	5.1	10.6	4.4	3.4	0.0	2.6	2.4	-2.7	0.2	-0.2	0.0	0.0	0.0	0.0
2000	0.0320	0.615	0.623	6.7	3.1	7.4	3.0	0.2	0.2	0.7	-0.1	0.1	-0.6	0.6	0.1	-0.1	-0.2	0.2
2000	0.0500	0.394	0.477	6.8	2.7	7.3	2.6	0.0	0.1	0.2	-0.1	0.1	-0.1	0.2	0.0	-0.1	-0.1	0.1
2000	0.0800	0.246	0.423	6.2	2.5	6.7	2.4	0.6	0.0	0.5	-0.5	0.5	0.0	0.0	0.0	0.0	0.0	0.0
2000	0.1300	0.151	0.345	7.0	2.7	7.5	2.6	0.9	0.1	0.7	-0.7	0.7	-0.3	0.3	0.1	0.0	0.0	0.0
2000	0.1800	0.109	0.312	7.5	2.6	7.9	2.6	0.5	0.0	0.1	0.1	-0.1	-0.1	0.1	0.0	0.0	0.0	0.0
2000	0.2500	0.079	0.236	8.8	4.5	9.9	4.0	2.8	0.0	2.2	2.1	-2.3	0.3	-0.3	0.0	0.0	0.0	0.0

Table A.2: Continuation from the previous page. See page 160 for explanations.

Q^2 [GeV^2]	x	y	$\tilde{\sigma}$	δ_{stat} [%]	δ_{sys} [%]	δ_{tot} [%]	δ_{unc} [%]	δ^{Ee}_{unc} [%]	δ^{Eh}_{unc} [%]	δ_{cor} [%]	$\delta^{E^+_e}_{cor}$ [%]	$\delta^{E^-_e}_{cor}$ [%]	$\delta^{\theta^+_e}_{cor}$ [%]	$\delta^{\theta^-_e}_{cor}$ [%]	$\delta^{E^+_h}_{cor}$ [%]	$\delta^{E^-_h}_{cor}$ [%]	$\delta^{Bg^+}_{cor}$ [%]	$\delta^{Bg^-}_{cor}$ [%]
3000	0.0500	0.591	0.604	5.3	3.0	6.1	2.9	0.7	0.1	0.8	-0.2	0.2	-0.7	0.8	0.1	-0.1	-0.1	0.1
3000	0.0800	0.369	0.430	5.7	2.8	6.3	2.7	0.6	0.1	0.7	-0.2	0.2	-0.6	0.7	0.0	0.0	0.0	0.0
3000	0.1300	0.227	0.376	6.4	3.0	7.0	2.9	1.1	0.1	0.8	-0.5	0.5	-0.5	0.6	0.0	0.0	0.0	0.0
3000	0.1800	0.164	0.287	7.0	2.7	7.5	2.7	0.5	0.0	0.4	-0.3	0.2	-0.4	0.2	0.0	0.0	0.0	0.0
3000	0.2500	0.118	0.202	8.2	4.1	9.2	3.6	2.4	0.1	1.9	1.6	-1.8	0.8	-0.8	0.1	-0.1	0.0	0.0
3000	0.4000	0.074	0.092	12.5	10.9	16.6	9.1	8.4	0.1	5.9	5.0	-5.0	3.1	-3.2	0.0	0.1	0.0	0.0
5000	0.0800	0.615	0.421	6.9	3.3	7.6	3.2	0.6	0.1	0.8	-0.1	0.1	-0.8	0.9	0.0	0.0	-0.1	0.1
5000	0.1300	0.379	0.314	8.1	3.7	8.9	3.5	1.3	0.1	1.4	-0.3	0.3	-1.3	1.4	0.0	0.0	0.0	0.0
5000	0.1800	0.273	0.282	9.2	3.8	9.9	3.5	0.4	0.1	1.5	-0.2	0.3	-1.4	1.5	0.1	-0.1	0.0	0.0
5000	0.2500	0.197	0.273	9.2	5.1	10.5	4.9	3.2	0.1	1.2	0.7	-0.8	-0.8	1.0	0.1	0.0	0.0	0.0
5000	0.4000	0.123	0.119	14.3	15.2	20.9	14.4	13.6	0.1	5.0	4.0	-4.0	3.0	-3.1	0.0	0.0	0.0	0.0
8000	0.1300	0.606	0.352	12.0	4.7	12.8	4.5	1.1	0.1	1.4	0.2	-0.2	-1.3	1.4	0.0	0.0	-0.3	0.3
8000	0.1800	0.438	0.284	12.2	4.9	13.2	4.4	0.8	0.1	2.0	-0.3	0.3	-2.1	2.0	0.0	0.0	-0.1	0.1
8000	0.2500	0.315	0.226	12.3	5.5	13.5	5.5	3.4	0.1	0.8	0.7	-0.8	-0.1	0.1	-0.1	0.0	0.0	0.0
8000	0.4000	0.197	0.105	17.1	13.1	21.6	12.7	11.5	0.1	3.2	2.4	-2.5	1.9	-2.2	0.1	-0.1	0.0	0.0
8000	0.6500	0.121	0.015	37.8	48.0	61.1	45.5	44.2	0.4	15.2	9.5	-9.0	12.3	-11.7	0.3	-0.2	0.0	0.0
12000	0.1800	0.656	0.286	17.3	3.1	17.6	2.8	0.6	0.2	1.4	0.0	0.0	-1.3	1.4	0.1	-0.1	-0.4	0.4
12000	0.2500	0.473	0.112	26.7	4.3	27.1	4.2	3.0	0.1	1.0	0.3	-0.3	-1.0	1.0	0.0	-0.1	0.0	0.0
12000	0.4000	0.295	0.065	35.4	9.8	36.7	9.7	9.1	0.1	1.3	1.3	-1.3	0.2	-0.3	0.0	-0.1	0.0	0.0
12000	0.6500	0.182	0.010	70.7	37.9	80.2	36.0	35.2	0.3	11.7	7.3	-7.0	9.3	-9.2	-0.1	0.2	0.0	0.0
20000	0.2500	0.788	0.042	62.0	4.8	62.2	4.5	3.2	0.3	1.5	0.3	-0.3	-1.1	1.4	0.2	-0.2	-0.8	0.8
20000	0.4000	0.492	0.046	45.2	8.4	46.0	8.3	7.7	0.4	1.0	0.9	-1.0	-0.1	-0.1	0.2	-0.3	-0.2	0.2
20000	0.6500	0.303	0.017	70.7	40.1	81.3	39.1	38.9	0.2	8.8	4.6	-4.5	7.7	-7.5	0.1	-0.2	0.0	0.0
30000	0.4000	0.738	0.091	59.4	9.0	60.1	8.8	7.5	0.5	2.1	0.6	-0.6	-1.2	1.1	0.3	-0.3	-1.6	1.6
30000	0.6500	0.454	0.025	70.7	17.7	72.9	17.1	16.2	1.8	4.4	2.8	-2.8	3.2	-3.3	1.0	-1.1	0.0	0.0

Table A.2: Continuation from the previous pages. See page 160 for explanations.

Appendix B

Contact Interaction Cross Sections

This appendix presents the double differential reduced cross sections of the contact interaction models investigated in this analysis. The cross sections are normalised to the Standard Model predictions without contact interaction contributions. All cross sections are calculated using the H1 1997 PDF Fit. Shown are the respective models for coupling scales of $\epsilon\Lambda = \pm 1,3,5$ and 10 TeV and for x bins with $x \geq 0.013$.

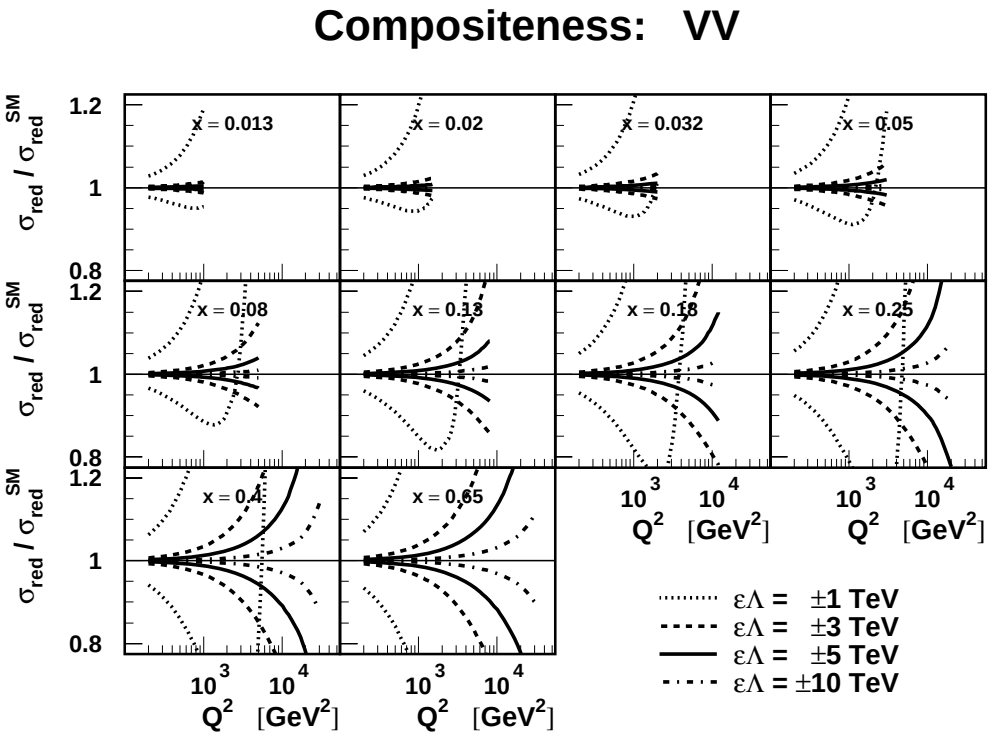

Figure B.1: Reduced cross section for the compositeness model VV compared to the Standard Model prediction.

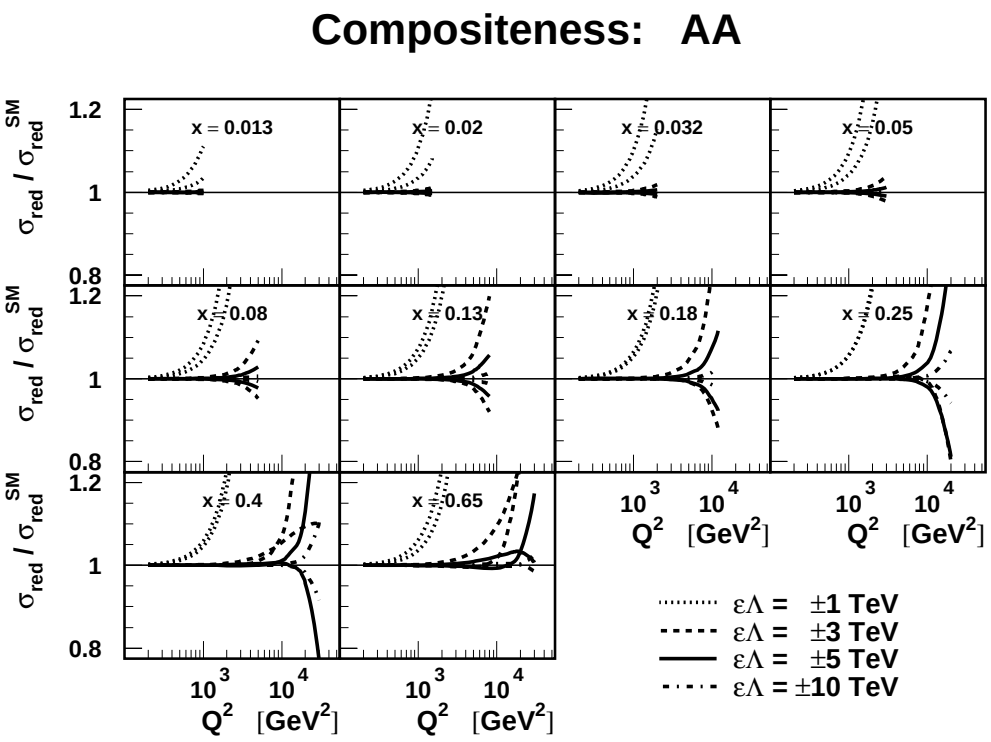

Figure B.2: Reduced cross section for the compositeness model AA compared to the Standard Model prediction.

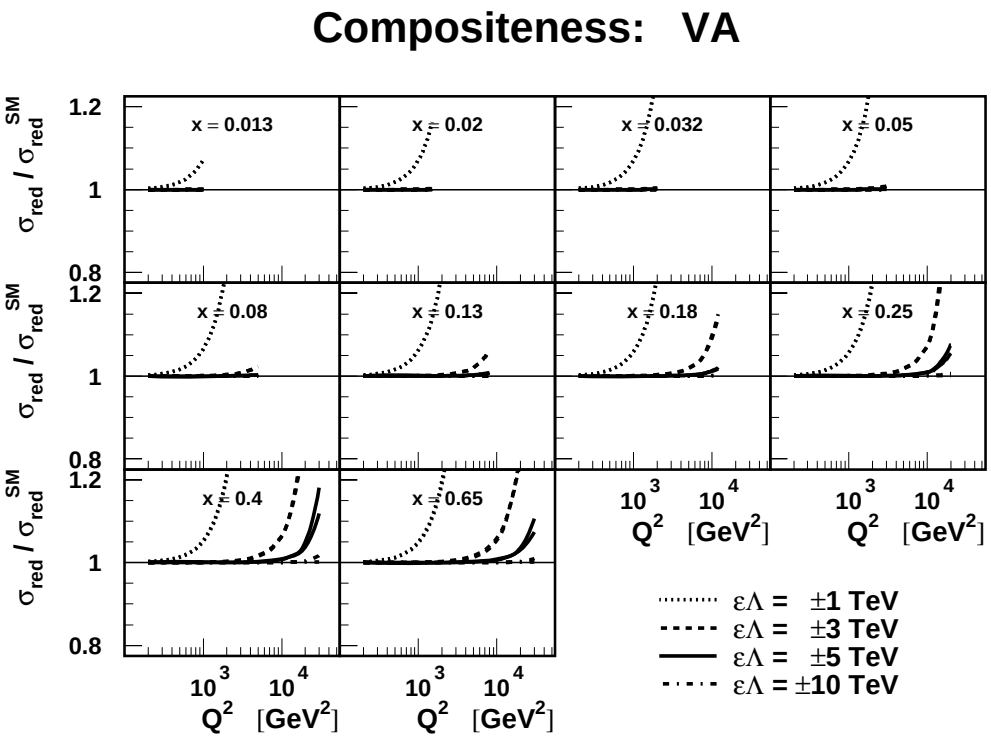

Figure B.3: Reduced cross section for the compositeness model VA compared to the Standard Model prediction.

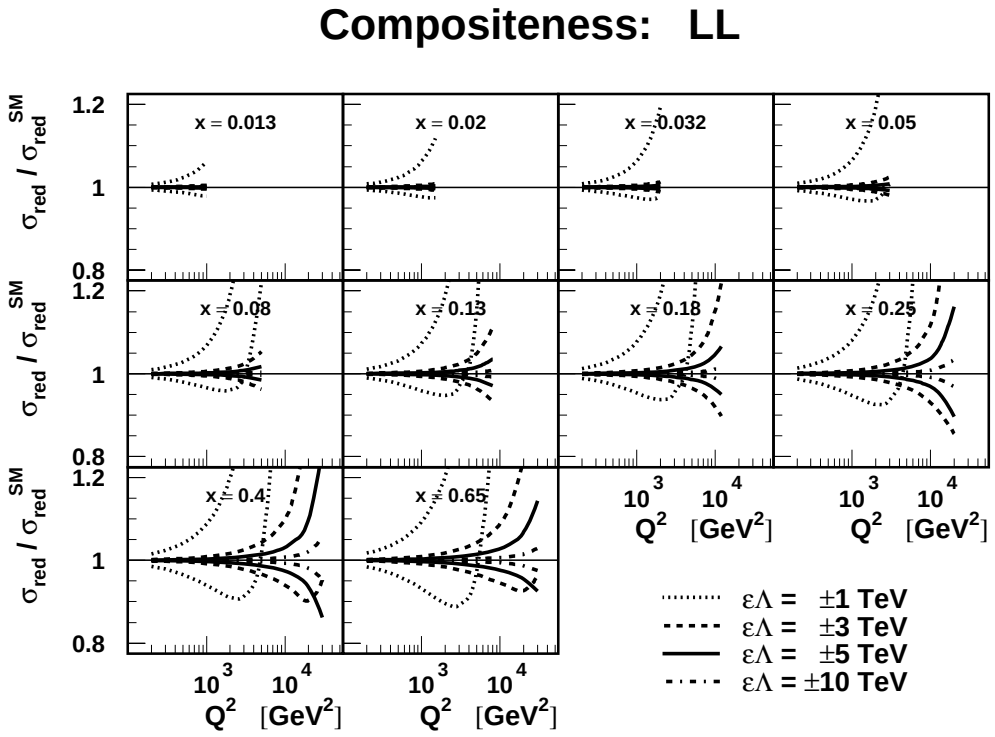

Figure B.4: Reduced cross section for the compositeness model LL compared to the Standard Model prediction.

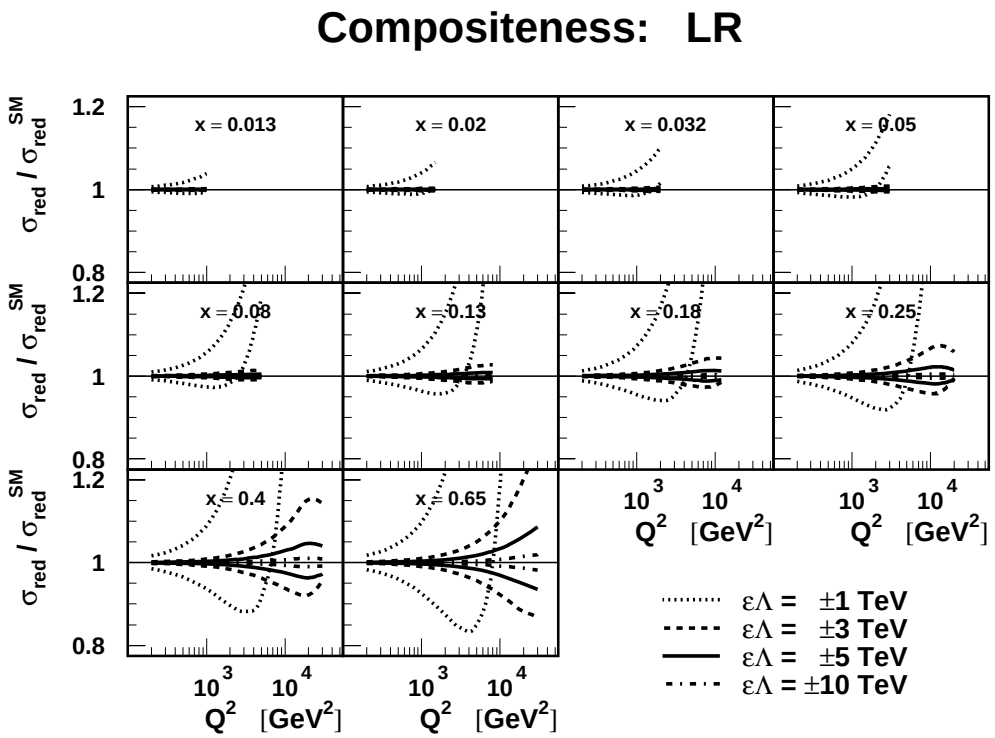

Figure B.5: Reduced cross section for the compositeness model LR compared to the Standard Model prediction.

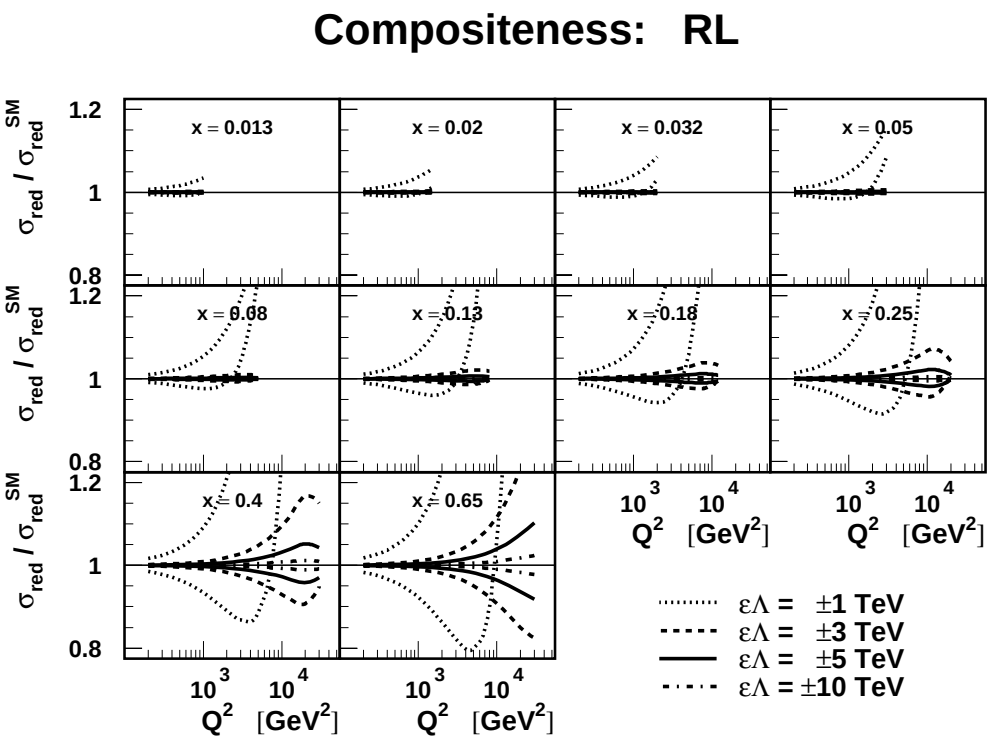

Figure B.6: Reduced cross section for the compositeness model RL compared to the Standard Model prediction.

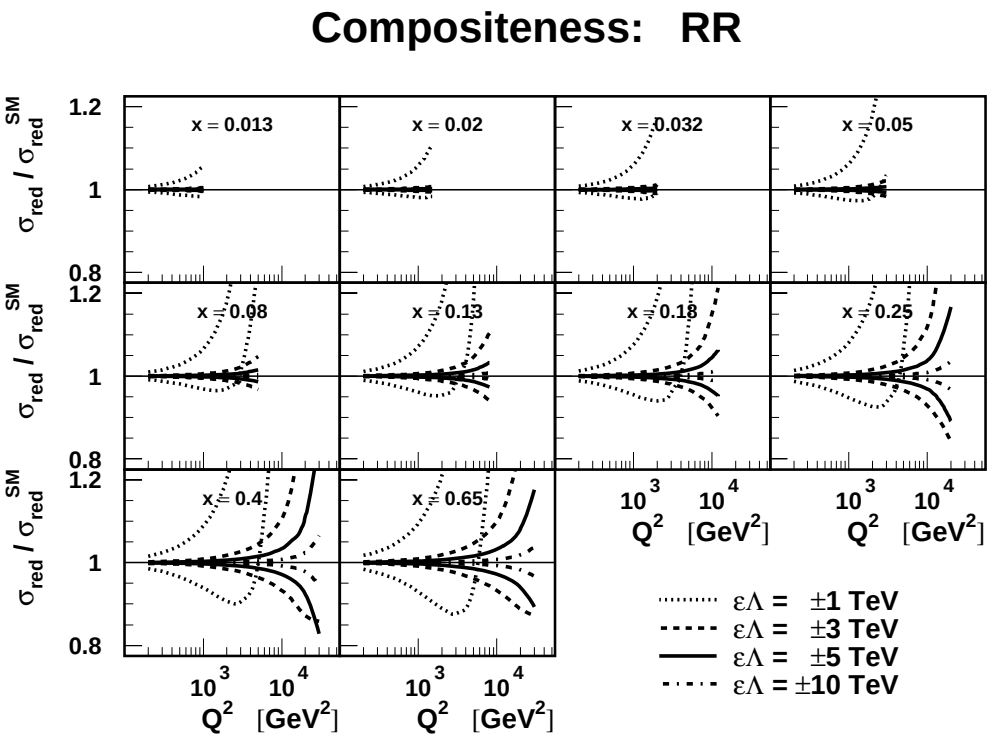

Figure B.7: Reduced cross section for the compositeness model RR compared to the Standard Model prediction.

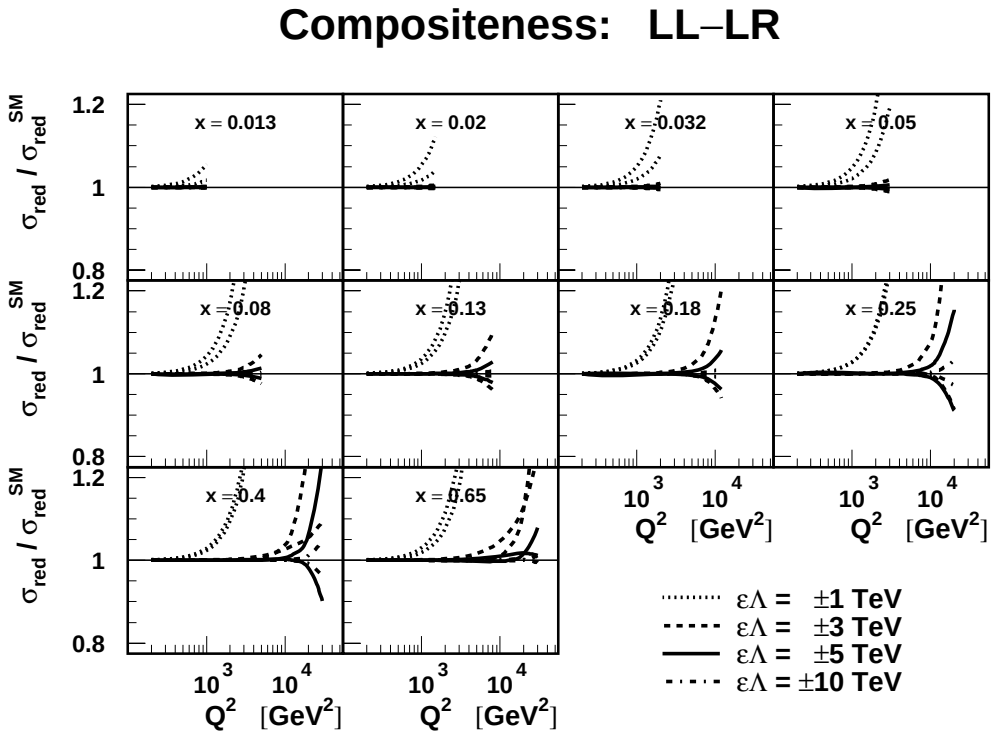

Figure B.8: Reduced cross section for the compositeness model $LL - LR$ compared to the Standard Model prediction.

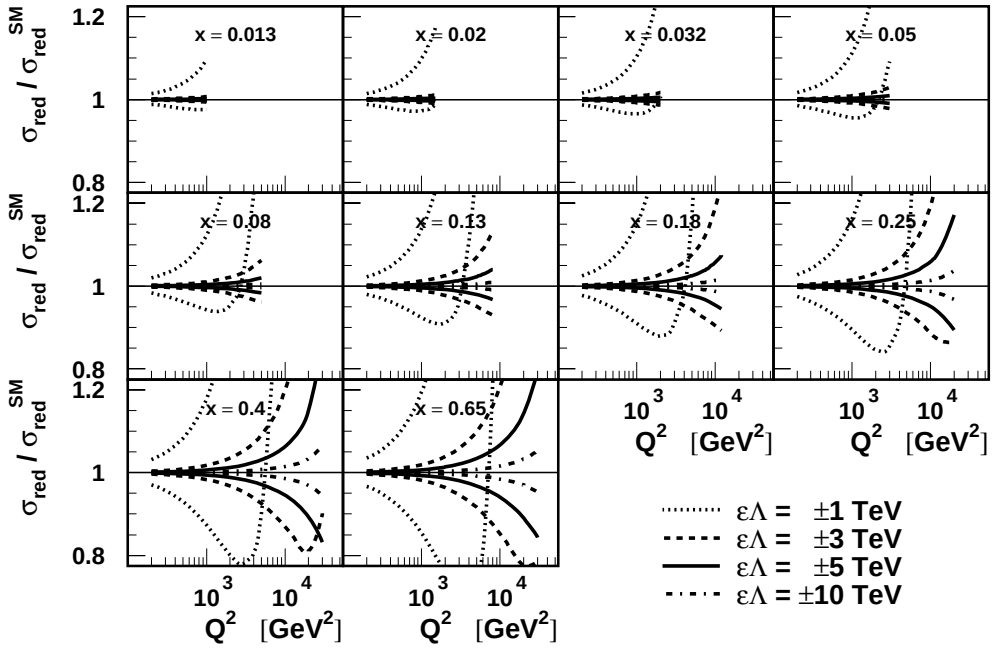

Figure B.9: Reduced cross section for the compositeness model $LL + RL$ compared to the Standard Model prediction.

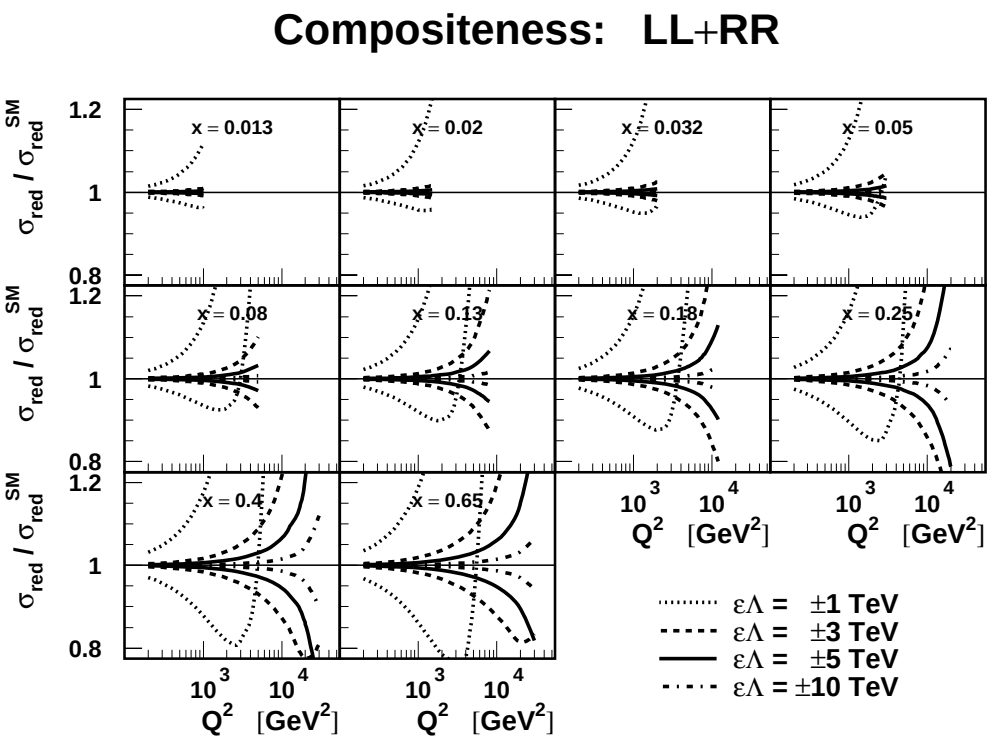

Figure B.10: Reduced cross section for the compositeness model $LL + RR$ compared to the Standard Model prediction.

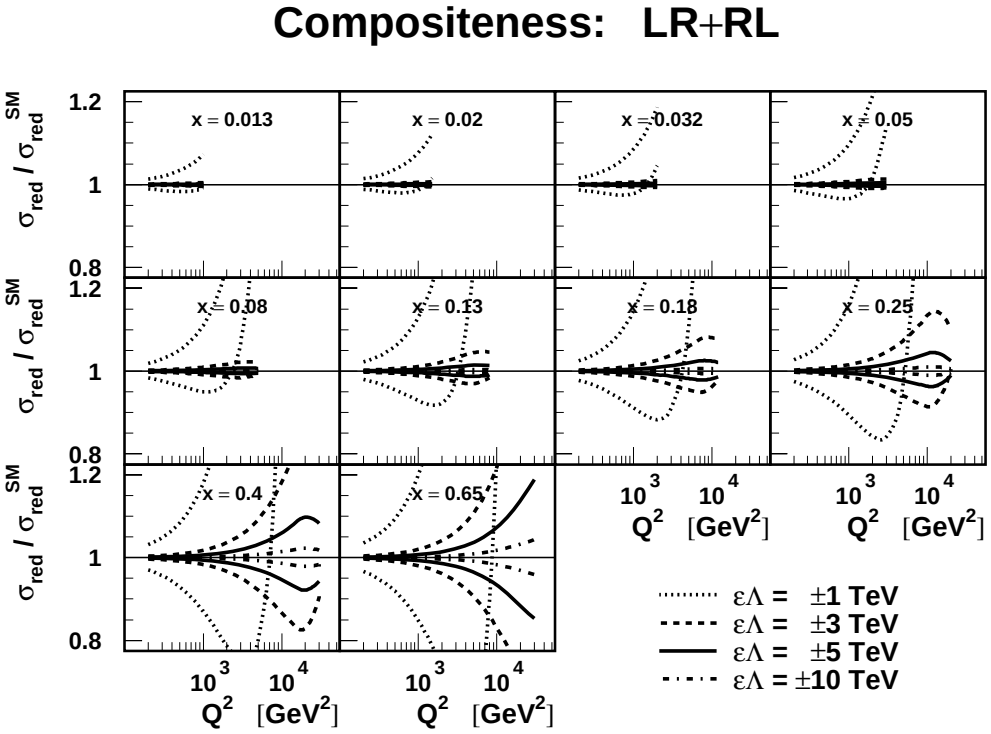

Figure B.11: Reduced cross section for the compositeness model $LR + RL$ compared to the Standard Model prediction.

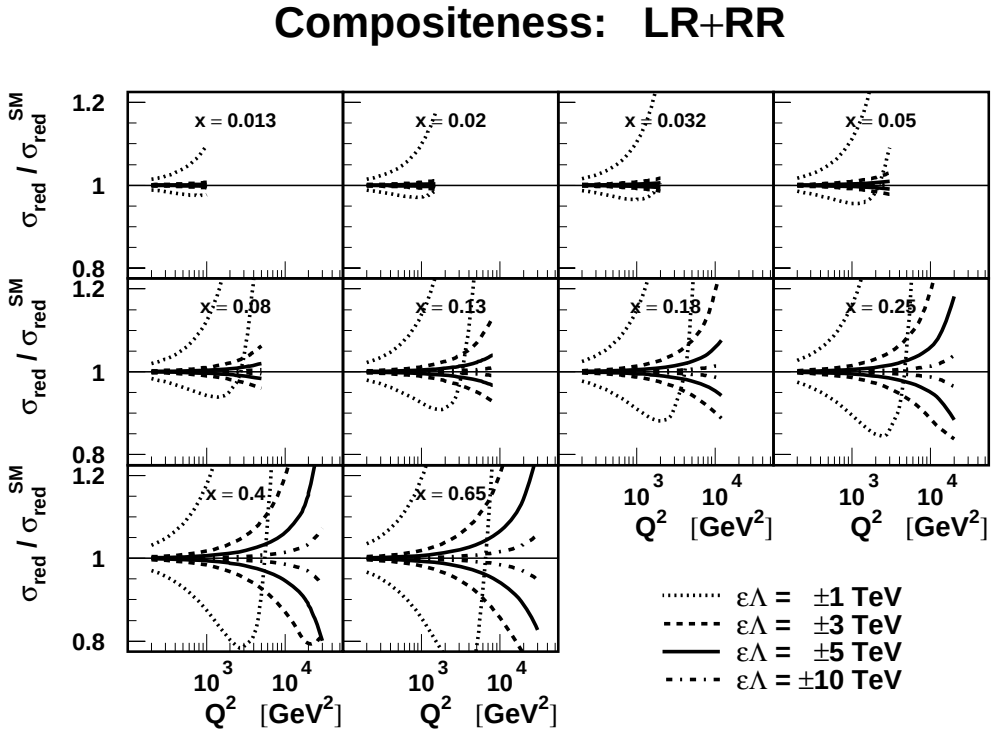

Figure B.12: Reduced cross section for the compositeness model $LR + RR$ compared to the Standard Model prediction.

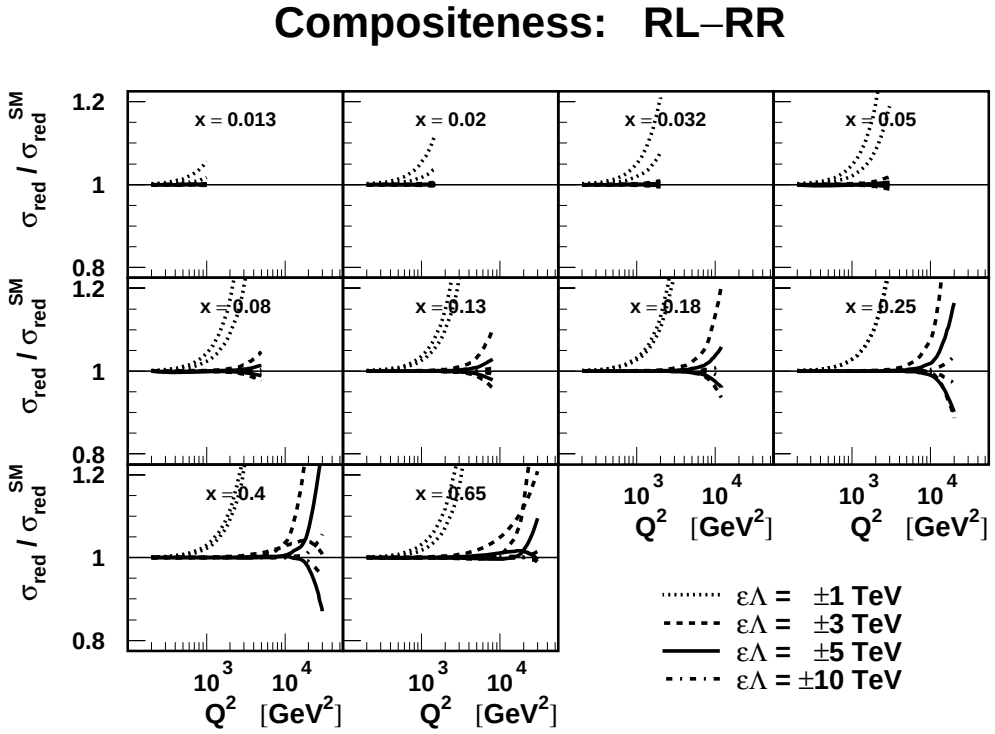

Figure B.13: Reduced cross section for the compositeness model $RL - RR$ compared to the Standard Model prediction.

List of Figures

List of Tables

Bibliography

[1] F. Halzen and A. D. Martin, "Quarks And Leptons: An Introductory Course In Modern Particle Physics," Wiley, New York, 1984

[2] O. Nachtmann, "Phenomena And Concepts Of Elementary Particle Physics. (In German)," Vieweg, Braunschweig, 1986

[3] R. K. Ellis, W. J. Stirling and B. R. Webber, "QCD And Collider Physics," Cambridge Monogr. Part. Phys. Nucl. Phys. Cosmol. **8** (1996) 1.

[4] J. F. Donoghue, E. Golowich and B. R. Holstein, "Dynamics Of The Standard Model," Cambridge Monogr. Part. Phys. Nucl. Phys. Cosmol. **2** (1992) 1.

[5] J. I. Friedman and H. W. Kendall, "Deep Inelastic Electron Scattering," Ann. Rev. Nucl. Part. Sci. **22** (1972) 203.

[6] R. Brock *et al.* [CTEQ Collaboration], "Handbook of perturbative QCD," Rev. Mod. Phys. **67** (1995) 157.

[7] V. N. Gribov and L. N. Lipatov, "Deep Inelastic E P Scattering In Perturbation Theory," Yad. Fiz. **15** (1972) 781 [Sov. J. Nucl. Phys. **15** (1972) 438].

[8] Y. L. Dokshitzer, "Calculation Of The Structure Functions For Deep Inelastic Scattering And E+ E- Annihilation By Perturbation Theory In Quantum Chromodynamics. (In Russian)," Sov. Phys. JETP **46** (1977) 641 [Zh. Eksp. Teor. Fiz. **73** (1977) 1216].

[9] G. Altarelli and G. Parisi, "Asymptotic Freedom In Parton Language," Nucl. Phys. B **126** (1977) 298.

[10] G. Altarelli, R. K. Ellis and G. Martinelli, "Leptoproduction And Drell-Yan Processes Beyond The Leading Approximation In Chromodynamics," Nucl. Phys. B **143** (1978) 521 [Erratum-ibid. B **146** (1978) 544].

[11] W. A. Bardeen, A. J. Buras, D. W. Duke and T. Muta, "Deep Inelastic Scattering Beyond The Leading Order In Asymptotically Free Gauge Theories," Phys. Rev. D **18** (1978) 3998.

[12] A. Arbuzov, D. Y. Bardin, J. Bluemlein, L. Kalinovskaya and T. Riemann, "HECTOR 1.00 - A program for the calculation of QED, QCD and electroweak corrections to ep and lN deep inelastic neutral and charged current scattering," Comput. Phys. Commun. **94** (1996) 128 [arXiv:hep-ph/9511434].

[13] H. Spiesberger *et al.*, "Radiative corrections at HERA," CERN-TH-6447-92 *Contribution to Workshop on Physics at HERA, Hamburg, Germany, Oct 29-30, 1991, Vol. 2, p. 798.*

[14] J. Blumlein, "HELIOS 1.00: A Program to calculate leading log QED corrections to e p scattering," PHE-91-016

[15] A. Kwiatkowski, H. Spiesberger and H. J. Mohring, "Heracles: An Event Generator For E P Interactions At Hera Energies Including Radiative Processes: Version 1.0," Comput. Phys. Commun. **69** (1992) 155.

[16] C. Adloff *et al.* [H1 Collaboration], "Measurement and QCD analysis of neutral and charged current cross sections at HERA," arXiv:hep-ex/0304003.

[17] U. Bassler and G. Bernardi, "On the kinematic reconstruction of deep inelastic scattering at HERA: The Sigma method," Nucl. Instrum. Meth. A **361** (1995) 197 [arXiv:hep-ex/9412004].

[18] U. Bassler and G. Bernardi, "Structure function measurements and kinematic reconstruction at HERA," Nucl. Instrum. Meth. A **426** (1999) 583 [arXiv:hep-ex/9801017].

[19] J. Pumplin, D. R. Stump, J. Huston, H. L. Lai, P. Nadolsky and W. K. Tung, "New generation of parton distributions with uncertainties from global QCD analysis," JHEP **0207** (2002) 012 [arXiv:hep-ph/0201195].

[20] D. Stump, J. Huston, J. Pumplin, W. K. Tung, H. L. Lai, S. Kuhlmann and J. F. Owens, "Inclusive jet production, parton distributions, and the search for new physics," arXiv:hep-ph/0303013.

[21] A. D. Martin, R. G. Roberts, W. J. Stirling and R. S. Thorne, "MRST2001: Partons and alpha(s) from precise deep inelastic scattering and Tevatron jet data," Eur. Phys. J. C **23** (2002) 73 [arXiv:hep-ph/0110215].

[22] A. D. Martin, R. G. Roberts, W. J. Stirling and R. S. Thorne, "Uncertainties of predictions from parton distributions. I: Experimental errors," Eur. Phys. J. C **28** (2003) 455 [arXiv:hep-ph/0211080].

[23] J. Pumplin *et al.*, "Uncertainties of predictions from parton distribution functions. II: The Hessian method," Phys. Rev. D **65** (2002) 014013 [arXiv:hep-ph/0101032].

[24] R. S. Thorne *et al.*, "Questions on uncertainties in parton distributions," J. Phys. G **28** (2002) 2717 [arXiv:hep-ph/0205233].

[25] R. S. Thorne, "Uncertainties on parton related quantities," J. Phys. G **28** (2002) 2705 [arXiv:hep-ph/0205235].

[26] A. D. Martin, R. G. Roberts, W. J. Stirling and R. S. Thorne, "Uncertainties of predictions from parton distributions. II: Theoretical errors," arXiv:hep-ph/0308087.

[27] C. Adloff *et al.* [H1 Collaboration], "Measurement of neutral and charged current cross-sections in positron proton collisions at large momentum transfer," Eur. Phys. J. C **13** (2000) 609 [arXiv:hep-ex/9908059].

[28] A. C. Benvenuti *et al.* [BCDMS Collaboration], "A High Statistics Measurement Of The Proton Structure Functions F(2) (X, Q**2) And R From Deep Inelastic Muon Scattering At High Q**2," Phys. Lett. B **223** (1989) 485.

[29] M. Arneodo *et al.* [New Muon Collaboration.], "Measurement of the proton and the deuteron structure functions, F2(p) and F2(d)," Phys. Lett. B **364** (1995) 107 [arXiv:hep-ph/9509406].

[30] H. L. Lai *et al.* [CTEQ Collaboration], "Global QCD analysis of parton structure of the nucleon: CTEQ5 parton distributions," Eur. Phys. J. C **12** (2000) 375 [arXiv:hep-ph/9903282].

[31] A. D. Martin, R. G. Roberts, W. J. Stirling and R. S. Thorne, "Parton distributions and the LHC: W and Z production," Eur. Phys. J. C **14** (2000) 133 [arXiv:hep-ph/9907231].

[32] G. Kopp, D. Schaile, M. Spira and P. M. Zerwas, "Bounds on radii and magnetic dipole moments of quarks and leptons from LEP, SLC and HERA," Z. Phys. C **65** (1995) 545 [arXiv:hep-ph/9409457].

[33] C. N. Leung, S. T. Love and S. Rao, "Low-Energy Manifestations Of A New Interaction Scale: Operator Analysis," Z. Phys. C **31** (1986) 433.

[34] W. Buchmuller, B. Lampe and N. Vlachos, "Contact Interactions And The Callan-Gross Relation," Phys. Lett. B **197** (1987) 379.

[35] P. Haberl, F. Schrempp and H. U. Martyn, "Contact Interactions And New Heavy Bosons At Hera: A Model Independent Analysis," *Contribution to Workshop on Physics at HERA, Hamburg, Germany, Oct 29-30, 1991, Vol. 2, p. 1133.*

[36] G. Altarelli, J. R. Ellis, G. F. Giudice, S. Lola and M. L. Mangano, "Pursuing interpretations of the HERA large-Q**2 data," Nucl. Phys. B **506** (1997) 3 [arXiv:hep-ph/9703276].

[37] V. D. Barger, K. m. Cheung, K. Hagiwara and D. Zeppenfeld, "Global study of electron quark contact interactions," Phys. Rev. D **57** (1998) 391 [arXiv:hep-ph/9707412].

[38] E. Eichten, K. D. Lane and M. E. Peskin, "New Tests For Quark And Lepton Substructure," Phys. Rev. Lett. **50** (1983) 811.

[39] H. Harari, "A Schematic Model Of Quarks And Leptons," Phys. Lett. B **86** (1979) 83.
M. A. Shupe, "A Composite Model Of Leptons And Quarks," Phys. Lett. B **86** (1979) 87.
H. Fritzsch and G. Mandelbaum, "Weak Interactions As Manifestations Of The Substructure Of Leptons And Quarks," Phys. Lett. B **102** (1981) 319.

[40] A. Deandrea, "Atomic parity violation in cesium and implications for new physics," Phys. Lett. B **409** (1997) 277 [arXiv:hep-ph/9705435].

[41] C. S. Wood, S. C. Bennett, D. Cho, B. P. Masterson, J. L. Roberts, C. E. Tanner and C. E. Wieman, "Measurement Of Parity Nonconservation And An Anapole Moment In Cesium," Science **275** (1997) 1759.

[42] I. Abt *et al.* [H1 Collaboration], "The H1 detector at HERA," Nucl. Instrum. Meth. A **386** (1997) 310.

[43] I. Abt *et al.* [H1 Collaboration], "The Tracking, calorimeter and muon detectors of the H1 experiment at HERA ," Nucl. Instrum. Meth. A **386** (1997) 348.

[44] B. Andrieu *et al.* [H1 Calorimeter Group Collaboration], "The H1 liquid argon calorimeter system," Nucl. Instrum. Meth. A **336** (1993) 460.

[45] W. J. Willis and V. Radeka, Nucl. Instrum. Meth. **120** (1974) 221.

[46] B. Andrieu *et al.* [H1 Calorimeter Group Collaboration], "Results from pion calibration runs for the H1 liquid argon calorimeter and comparisons with simulations," Nucl. Instrum. Meth. A **336** (1993) 499.

[47] B. Andrieu *et al.* [H1 Calorimeter Group Collaboration], "Beam tests and calibration of the H1 liquid argon calorimeter with electrons," Nucl. Instrum. Meth. A **350** (1994) 57.

[48] R. D. Appuhn *et al.* [H1 SPACAL Group Collaboration], "The H1 lead/scintillating-fibre calorimeter," Nucl. Instrum. Meth. A **386** (1997) 397.

[49] T. Nicholls *et al.* [H1 SPACAL Group Collaboration], "Performance of an electromagnetic lead / scintillating fiber calorimeter for the H1 detector," Nucl. Instrum. Meth. A **374** (1996) 149.

[50] J. Ebert, "The H1-Tail Catcher Hardware and Software Performance," Internal Report, H1-IN-448, 1995

[51] H1 Muon Group, "Beam Calibration of the H1 Tail Catcher at CERN," Internal Report, H1-IN-197, 1991

[52] C. Wissing, A. Beglarian, P. Biddulph, M. Fleischer, "The H1 ToF system in 1996 and 1997," Internal Report, H1-IN-533, 1998

[53] H. Bethe and W. Heitler, "On The Stopping Of Fast Particles And On The Creation Of Positive Electrons," Proc. Roy. Soc. Lond. A **146** (1934) 83.

[54] H1 Collaboration, "Luminosity Measurement in the H1 Experiment at HERA," Paper submitted to the 28th International Conference on High Energy Physics, ICHEP'96, Warsaw, Poland, 1996

[55] T. Carli *et al.*, "Performance of the H1 Lar Trigger in 1994," Internal Report, H1-IN-445, 1995

[56] B. Reisert, "Electron proton scattering at high momentum transfers at the H1-experiment at HERA. (In German)," MPI-PHE-2000-26

[57] G. A. Schuler and H. Spiesberger, "Django: The Interface For The Event Generators Heracles And Lepto," *Contribution to Workshop on Physics at HERA, Hamburg, Germany, Oct 29-30, 1991, Vol. 3, p. 1419.*

[58] G. Ingelman, A. Edin and J. Rathsman, "LEPTO 6.5 - A Monte Carlo Generator for Deep Inelastic Lepton-Nucleon Scattering," Comput. Phys. Commun. **101** (1997) 108 [arXiv:hep-ph/9605286].

[59] B. Andersson, G. Gustafson, L. Lonnblad and U. Pettersson, "Coherence Effects In Deep Inelastic Scattering," Z. Phys. C **43** (1989) 625.

[60] L. Lonnblad, "ARIADNE version 4: A Program for simulation of QCD cascades implementing the color dipole model," Comput. Phys. Commun. **71** (1992) 15.

[61] B. Andersson, "The Lund String Model," In Durham 1984, Proceedings, Antiproton 1984, 447, 1986.

[62] T. Sjostrand, "High-energy physics event generation with PYTHIA 5.7 and JETSET 7.4," Comput. Phys. Commun. **82** (1994) 74.

[63] W. Buchmuller and G. Ingelman (eds.), "Monte Carlo Generators," Workshop on Physics At Hera, Hamburg, Germany, Oct 29-30, 1991, Vol. 3.

[64] A. T. Doyle, G. Grindhammer, G. Ingelman and H. Jung, "Monte Carlo Generators For Hera Physics. Proceedings, Workshop, Hamburg, Germany, 1998-1999," DESY-PROC-1999-02

[65] A. D. Martin, W. J. Stirling and R. G. Roberts, "Parton distributions updated," Phys. Lett. B **306** (1993) 145 [Erratum-ibid. B **309** (1993) 492].

[66] M. Gluck, E. Reya and A. Vogt, "Photonic parton distributions," Phys. Rev. D **46** (1992) 1973.

[67] A. Courau and P. Kessler, "QED Compton scattering in high-energy electron - proton collisions," Phys. Rev. D **46** (1992) 117.

[68] J. A. M. Vermaseren, "Two Photon Processes At Very High-Energies," Nucl. Phys. B **229** (1983) 347.

[69] S. P. Baranov, O. Duenger, H. Shooshtari and J. A. M. Vermaseren, "Lpair: A Generator For Lepton Pair Production," *Contribution to Workshop on Physics at HERA, Hamburg, Germany, Oct 29-30, 1991, Vol. 3, p. 1478.*

[70] J. Meyer, "Guide for the H1 simulation program H1SIM," Internal H1 Software Note 03-11/89, DESY, 1989.

[71] R. Brun, F. Bruyant, M. Maire, A. C. McPherson and P. Zanarini, "Geant3," CERN-DD/EE/84-1, 1987.

[72] S. Peters, "Die parametrisierte Simulation elektromagnetischer Schauer," MPI-PhE/92-13, Ph.D. Thesis, MPI Munich, 1992.
M. Rudowicz, "Hadronische Schauersimulation für den H1-Detektor," MPI-PhE/92-14, Ph.D. Thesis, MPI Munich, 1992.

[73] M. Ellerbrock, J. Marks, C. Risler and C. Schwanenberger, "Tuning of Electromagnetic Showers in H1FAST," Internal Report, in preparation.

[74] D. Emschermann, "Auswirkungen systematischer Detektoreffekte auf die Messungen der tief-inelastischen *ep*-Streuung," Diploma Thesis, Heidelberg, 2001

[75] P. Bruel, "Recherche d'interactions au-delà du Modèle Standard à HERA," Ph.D. Thesis, Univ. Paris XI, Orsay, 1998

[76] L. A. del Pozo, Ph.D. Thesis, University of Cambridge, Cambridge (1993) RALT-002.

[77] M. H. Seymour, "Searches for new particles using cone and cluster jet algorithms: A Comparative study," Z. Phys. C **62** (1994) 127.

[78] C. Adloff *et al.* [H1 Collaboration], "Measurement of neutral and charged current cross sections in electron proton collisions at high Q**2," Eur. Phys. J. C **19** (2001) 269 [arXiv:hep-ex/0012052].

[79] B. Andrieu *et al.* [H1 Calorimeter Group Collaboration], "Electron / pion separation with the H1 LAr calorimeters," Nucl. Instrum. Meth. A **344** (1994) 492.

[80] G. Grindhammer, M. Rudowicz and S. Peters, "The Fast Simulation Of Electromagnetic And Hadronic Showers," Nucl. Instrum. Meth. A **290** (1990) 469.

[81] E. Barrelet *et al.* [H1 Calorimeter Group Collaboration], "A purity monitoring system for the H1 liquid argon calorimeter," Nucl. Instrum. Meth. A **490** (2002) 204 [arXiv:hep-ex/0111066].

[82] B. Heinemann, "Measurement of charged current and neutral current cross sections in positron proton collisions at $\sqrt{s} \approx 300$ GeV," DESY-THESIS-1999-046

[83] H. Abramowicz *et al.*, "The Response And Resolution Of An Iron Scintillator Calorimeter For Hadronic And Electromagnetic Showers Between 10-Gev And 140-Gev," Nucl. Instrum. Meth. **180** (1981) 429.

[84] C. Issever, "Entwicklung eines alternativen Gewichtsverfahrens für das H1-Kalorimeter," Diploma Thesis, Dortmund, 1996

[85] M. Ellerbrock, J. Marks, "A New Hadronic Energy Weighting Algorithm," Internal Report, in preparation.

[86] S. Levonian and A. Panitch, "Treatment of the Proton Satellite Bunches in 1994 Data," Internal Report H1-IN-454, 1995

[87] S. Levonian, Luminosity Summary Tables, http://www-h1.desy.de/h1det/lumi/summary_tables/summary.html

[88] B. Reisert, Private communication, Hamburg, 2001

[89] E. Chabert *et al.*, "QBGFMAR: An Updated Phan Package for Cosmic and Halo Muon Topological Rejection in High P_T Physics Analysis," Internal Report, H1-IN-556, 1998

[90] I. Negri *et al.*, "A Minimal Comprehensive Set of Muon Background Topological Finders for High P_T Physics Analysis," Internal Report, H1-IN-498, 1996

[91] F. James and M. Roos, "MINUIT – Function Minimization and Error Analysis," CERN D506 (Long Writeup). Available from the CERN Program Library Office, CERN-IT Division, CERN, CH-1211, Geneva 23, Switzerland.

[92] K. Hagiwara *et al.* [Particle Data Group Collaboration], "Review Of Particle Physics," Phys. Rev. D **66** (2002) 010001.

[93] S. Aid *et al.* [H1 Collaboration], "Leptoquarks and compositeness scales from a contact interaction analysis of deep inelastic e+- p scattering at HERA," Phys. Lett. B **353** (1995) 578 [arXiv:hep-ex/9504008].

[94] C. Adloff *et al.* [H1 Collaboration], "Search for compositeness, leptoquarks and large extra dimensions in e q contact interactions at HERA," Phys. Lett. B **479** (2000) 358 [arXiv:hep-ex/0003002].

[95] C. Adloff *et al.* [H1 Collaboration], "Search for new physics in e+- q contact interactions at HERA," Phys. Lett. B **568** (2003) 35 [arXiv:hep-ex/0305015].

[96] C. Adloff *et al.* [H1 Collaboration], "Deep-inelastic inclusive e p scattering at low x and a determination of alpha(s)," Eur. Phys. J. C **21** (2001) 33 [arXiv:hep-ex/0012053].

[97] M. Acciarri *et al.* [L3 Collaboration], "Search for manifestations of new physics in fermion pair production at LEP," Phys. Lett. B **489** (2000) 81 [arXiv:hep-ex/0005028].

[98] J. Breitweg *et al.* [ZEUS Collaboration], "Search for contact interactions in deep inelastic e+ p $\to$ e+ X scattering at HERA," Eur. Phys. J. C **14** (2000) 239 [arXiv:hep-ex/9905039].

[99] R. Barate *et al.* [ALEPH Collaboration], "Study of fermion pair production in e+ e- collisions at 130-GeV to 183-GeV," Eur. Phys. J. C **12** (2000) 183 [arXiv:hep-ex/9904011].

[100] G. Abbiendi *et al.* [OPAL Collaboration], "Tests of the standard model and constraints on new physics from measurements of fermion pair production at 189-GeV at LEP," Eur. Phys. J. C **13** (2000) 553 [arXiv:hep-ex/9908008].

[101] B. Abbott *et al.* [D0 Collaboration], "Measurement of the high-mass Drell-Yan cross section and limits on quark-electron compositeness scales," Phys. Rev. Lett. **82** (1999) 4769 [arXiv:hep-ex/9812010].

[102] K. m. Cheung, "Constraints on electron quark contact interactions and implications to models of leptoquarks and extra Z bosons," Phys. Lett. B **517** (2001) 167 [arXiv:hep-ph/0106251].

Acknowledgement

I am very thankful to everyone who supported me on all the way up to the finish of this thesis. There are certainly a lot of people I owe gratitude to, and I would like to apologise to those I forgot to name here. I wish to thank cordially:

- My supervisor Prof. Franz Eisele for the interesting topic and the opportunity to continue the work in his group after my diploma thesis. I am very thankful for his excellent guidance and support, allowing to find my own way to research.
- Prof. Johanna Stachel for her kind willingness to act as second referee of this thesis.
- Jörg Marks for his great support not only in computing issues but in particular in the whole business of understanding and calibrating the LAr calorimeter. Thank you for always having time for me, for taking over the proof-reading of 'the' chapter and in particular for your friendship which I appreciate a lot.
- All my further colleagues in the H1 group Heidelberg, Olaf Behnke, Jochen Dingfelder, Christian Gerlich, Christoph Werner, David Emschermann, Gerhard Brandt, Matthias Mozer, Stefan Schenk, Roger Wolf for the teamwork and the pleasant working atmosphere. Special thanks go to Jochen and Olaf who contributed a good deal to the contents and style of this thesis.
- Everyone in the H1 Collaboration. All members of the ex-HIP and the nELAN group, especially Eram Rizvi and Burkard Reisert for a great cooperation. And all my colleagues at DESY, just to name a few: Frank-Peter Schilling, Sebastian Schätzel, Johannes Haller, Nicolas Keller and Christian Schwanenberger.
- All members of the Physics Institute for offering a pleasant atmosphere I enjoyed to work in.
- My family and friends for their understanding when I did not have time.
- My loved Sabine and my son Lennart, my largest treasure, for their patience and for the beautiful time so far and still to come.

My special gratitude belongs to my parents and my sister for their loving care and support – and much more words cannot say.

This thesis was funded by the Graduiertenkolleg "Experimental Methods of Nuclear and Particle Physics" of the German Research Society (DFG).